A study of enzymatic methyl transfer catalysed by COMT: mechanism and structural biology

A thesis submitted to the University of Manchester for the degree of Doctor of Philosophy
in the Faculty of Science and Engineering

2018

Sylwia Czarnota

School of Chemistry

Table of Contents

Word count: 48,847

Abbreviations

Arg (R) – arginine

Asp (D) – aspartic acid

BMRB – biological magnetic resonance bank

BPTI - bovine pancreatic trypsin inhibitor

COMT – catechol-*O*-methyltransferase

Cys (C) – cysteine

DFT – density functional theory

DNA - deoxyribonucleic acid

dsDNA - double stranded deoxyribonucleic acid

DTT – dithiothreitol

E·S – enzyme-substrate

E·TS – enzyme-transition state

Gln (Q) - glutamine

Glu (E) – glutamic acid

His (H) – histidine

HSQC - heteronuclear single quantum correlation

Lys (K) – lysine

MB-COMT- membrane-bound catechol-*O*-methyltransferase

MD – molecular dynamics

MES - 2-(*N*-morpholino)ethanesulfonic acid

Met (M) – methionine

MM/MD – molecular mechanics/molecular dynamics

MPD - 2-methyl-2,4-pentanediol

MT - methyltransferase

NAC – near attack conformation

NMR – nuclear magnetic resonance

NOE – nuclear Overhauser effect

PDB – protein data bank

PEG – polyethylene glycol

Pro (P) - proline

QM/MM – quantum mechanics/molecular mechanics

RF – radiofrequency

SAH (AdoHcy) - S-adenosyl-L-homocysteine

SAM (AdoMet) - S-adenosyl-L-methionine

S-COMT- soluble catechol-*O*-methyltransferase

SDS-PAGE - sodium dodecyl sulfate polyacrylamide gel electrophoresis

Ser (S) - serine

Thr (T) – threonine

TROSY - transverse relaxation optimized spectroscopy

Trp (W) – tryptophan

TSA – transition state analogue

TSP - trimethylsilyl propanoic acid

Tyr (Y) – tyrosine

Val (V) – valine

Abstract of thesis

Looking at protein structure and studying changes in active site geometry is a fundamental step to understand how enzymes work, how the reaction proceeds and it gives absolutely essential background for potential drug design and development. Enzymes that transfer methyl groups (methyltransferases, MTs) are exciting targets for therapeutic intervention in a range of disorders. COMT (catechol-*O*-methyltransferase) is a model system for the study of enzyme-catalysed methyl transfer, but is also a very important drug target, as inhibition of this enzyme is a strategy for the treatment of a range of neurological disorders including Parkinson's disease, depression and schizophrenia.

This thesis primarily concerns the use of nuclear magnetic resonance (NMR) spectroscopy to study the reactant and transition state analogue (TSA) of human S-COMT. To achieve that, firstly, two NMR backbone assignments of COMT ternary complexes were determined. One with sinefungin, a fungal-derived inhibitor that possesses transition state-like charge on the transferring methyl group; and the second with S-Adenosyl-L-methionine (SAM), which is the major methyl donor for MTs, naturally present in organisms. Two X-ray crystal structures of the same complexes were obtained in high resolution. Comparisons between these complexes were done with the aid of computational studies, identifying subtle conformational differences in the active sites of the two ternary complexes. Results were consistent between all three methods, leading to the conclusion of active site "compaction" and electrostatic stabilization between the transferring methyl group and "equatorial" residues that are orthogonal to the donor-acceptor coordinate. High pressure NMR (up to 2500 bar) was next used to probe protein flexibility and rigidity, as well as NMR relaxation measurements, to study dynamics of the backbone. Both indicated high stability of the protein and showed that the majority of the protein is highly ordered. Those methods also indicated C-terminus stabilisation, most likely due to the dimer interface occurring there, which could be the focus of future work.

Declaration

No portion of the work referred to in the thesis has been submitted in support of an application for another degree or qualification of this or any other university or other institute of learning.

Copyright statement

In memory of two Hearts,
who passed away last summer

Acknowledgements

First and foremost I would like to thank my principal supervisor, Dr Sam Hay, for his help, guidance and time whenever I needed. Thank you Sam for providing me with kind references, so I can proceed to the next step in my career. I am grateful to Professor Jon Waltho for all fruitful discussions and support, and for helping me to continue in Manchester by supporting a fellowship with C4X Discovery. I thank Professor Nigel Scrutton for the opportunity to work in his famous lab. I am grateful to Dr Matt Cliff for his patience and help. I would like to acknowledge the guidance and paper corrections I received from Dr Nicky Baxter. Thanks to Dr Colin Levy for teaching me crystallography.

I would like to thank Dr Dearg Brown for being a coach, manager and friend. Thanks for the MAGIC project - it all brought a real magic to my life. Many thanks to Michiyo Sakuma, Shirley Tait and Marina Golovanova for teaching me the basic lab techniques, especially protein purification, which I'd never done before but am now fully confident in. Hanan Messiha – thanks for all the coffees together, for listening to me, for understanding. Thanks for the encouragement and all the kind words. Rich Tunnicliffe – thanks for helping in the lab and helping with Linux. Andreea Iorgu and Matja Zalar – thanks for being close and for all the discussions. Matja and Jack, perhaps I will see you in the US someday? Zhalgas Serimbetov – many thanks for your help with relaxation. Thanks for being in touch, even 3500 miles away. Thanks for all Whatsapp chats and recordings.

Thanks to C4X Discovery, especially Martin Watson for signing the contract with BBSRC, so I'm still paid when finishing my thesis. Thanks to Zoltan Takacs (however not in C4X anymore) for the relaxation workshop. Thanks to Hugh Dannatt, especially for sharing your thesis with me! Thanks to Jan-Christoph Westermann for virtual screening training and Jon Holmes for MD. Thanks to Wojtek Augustyniak for all chats.

I have to say that the time spent in Manchester was really the best time in my life and taught me a lot. Amazing and tough experiences. During my PhD I experienced two births, two deaths (this thesis is half-dedicated to my mum, God rest her soul, and half to my lost child), and real hospitality and friendship. I have to thank my neighbourhood. Nicci, Lizzie, Laila, Jamie (and Jamie's mum) – I love you so much!

Thanks for adopting me to your community. Thanks for sharing laughs and tears. Thanks for praying together! Many thanks to the Polish Church community, especially Dorota Semaniszyn, for understanding me and sharing feelings. Thanks to Joanna Jarosz for all the phone calls. Thanks to all my friends from Poland for remembering about me! Paulina Stolarska, Ania Goral – thank you. Thanks to my family, especially my sister Agnieszka and my dad.

And finally, Łukasz, my husband, I won't be able to do it without you! Love you so much (more than neighbours, don't worry). Thanks for all the support.

Thanks to my kids, Daniel and Kacper. Maybe one day you will read it. I love you. It wouldn't be the same without you.

Thanks to all the people who helped me to get to where I am.

Sylwia Czarnota

6th December 2018 *("Mikołajki")*

Alternative format for submission and authorship details

This thesis has been presented and submitted in a journal format. It consists of five chapters. Chapter 1 is the general introduction, while Chapter 2, Chapter 3 and Chapter 4 are drafts of manuscripts written for publication. Chapter 5 consists of preliminary work that can be investigated and continued in the future. The manuscript presented in Chapter 2 has already been published, while drafts of manuscripts in the next two chapters are soon to be submitted. Chapter 6 of the thesis provides a conclusion to the studies reported and anticipation for the future work.

Authors

S.C. – Sylwia Czarnota; S.H. – Sam Hay; M.J.C. – Matthew Cliff; N.J.B. – Nicola Baxter; J.P.W. – Jonathan Waltho; N.S.S. – Nigel Scrutton; C.W.L. – Colin Levy; L.O.J. – Linus Johannissen; A.L. Wilson – Alex Wilson

Chapter 2

S.C. performed the expression and purification as described in the experimental section. S.C. prepared the NMR samples. M.J.C. assisted in setting up the NMR experiments and in analysing the NMR data. S.C. performed the analysis and the resonance assignments. N.J.B. assisted in assessing the quality of the assignments of the reported complexes and made valuable contributions to increase the extent of the assignments. S.C. wrote the first draft of the manuscript. N.J.B. made a significant contribution to the final draft of the manuscript. N.J.B., M.J.C., J.P.W., N.S.S. and S.H. each contributed by providing invaluable feedback and review of the work done.

Chapter 3

S.C. performed the expression and purification of the protein samples. C.L. and S.C. set up the crystallisation trials and performed the sitting drop experiments. S.C. and C.L. processed and refined the X-ray data. C.L. carried out final refinements of the crystal structures and deposited them in PDB. S.C. prepared the NMR samples. M.J.C. assisted in setting up the NMR experiments and in analysing the NMR data. S.C. wrote the first draft of the NMR and X-ray crystallography sections of the manuscript. L.J.O.

performed MD calculations and analysis. A.L.W. performed initial DFT calculations of COMT active site cluster models. L.J.O. continued DFT calculations and wrote the first draft of the computational section of the manuscript. S.H made a significant contribution to the final draft of the manuscript. S.H., N.J.B., M.J.C., J.P.W. and N.S.S. each contributed by providing invaluable feedback and review of the work done.

Chapter 4

S.C. performed the expression and purification of the protein samples. S.C. prepared the NMR samples. N.J.B assisted in recording the initial high pressure experiments on the NMR spectrometer. M.J.C. assisted in recording the high pressure experiments on the NMR spectrometers. S.C. analysed the data with help of M.J.C. S.C. wrote the first draft of the manuscript. M.J.C. and S.H contributed significantly to the final draft of the manuscript. S.H., M.J.C., J.P.W., N.J.B. and N.S.S. each contributed by providing invaluable feedback and review of the work done.

Chapter 5

S.C. performed the expression and purification of the protein samples. S.C. prepared the NMR samples. M.J.C. assisted in recording the relaxation measurements on the NMR spectrometers. S.C. analysed the relaxation data. M.J.C. helped to analyse the NMR data. S.C. carried out the Model-free analysis using the *Relax* software program. M.J.C. carried out the Model-free analysis using in-house Python scripts. S.C. wrote the first draft of the manuscript. M.J.C. contributed significantly to the final draft of the manuscript. S.H., M.J.C., J.P.W. and N.S.S. each contributed by providing invaluable feedback and review of the work done.

1. – Introduction

1.1 The methyltransferase family

Methyltransferases (MTases, EC 2.1.1.-) are a large group of enzymes that all methylate small molecules and macromolecules and are involved in biosynthesis, metabolism, protein repair and other biological processes [1, 2]. They are subdivided into main five classes, distinguished by different structural folds. The major class (Class I), contains a structural motif called a Rossman fold, based on a seven-strand twisted β-sheet structure for binding S-adenosyl-L-methionine (AdoMet, SAM) [3]. Class II possesses a long, central, antiparallel β-sheet surrounded by groups of helices at either ends. Class II MTases bind to SAM in a shallow groove on the surface of the domain [4]. Class III contains a SAM-binding site between the two αβα domains and a groove in the N-terminal domain, which is proposed to be the active-site cleft [1, 5]. Class IV consist of SPOUT MTases, characterized by α/β knot fold. This class was first described based on the primary sequence and predicted secondary structural similarities of bacterial SpoU and TrmD methyltransferases. Class IV methylate RNA [6]. Class V contain a SET domain, which was originally identified as part of a larger conserved region present in the Drosophila Trithorax protein and was subsequently identified in the Drosophila Su(var)3-9 and 'Enhancer of zeste' proteins, from which the acronym SET was derived. This family includes a number of histone lysine MTases involved in transcriptional control through chromatin structural modification [7]. MTases can also be grouped by the different substrate preference. Then, four groups can be distinguished: protein methyltransferases (PMTs), DNA/RNA methyltransferases, non-SAM dependent methyltransferases and natural product methyltransferases (NPMTs) [8-11]. All MTases can also be classified according to the substrate atom that accepts the methyl group. Usually it is oxygen (54% of EC subclass), nitrogen (23%) or carbon (18%). Sulphur accepts the methyl group only in 3% cases among all MTases and other acceptors, such as halides, are also possible, but rare [11].

The vast majority of MTases belong to the Rossmann-like fold (Class I). Substrate-bound complexes have been determined mainly for this class. COMT (EC 2.1.1.6), catechol-*O*-methyltransferase, is a pharmacologically relevant example of the Class I MTases. It plays an important role in the metabolism of catechol

neurotransmitters and inhibition of COMT is a medically important target (see following section 1.1.1).

Class	Topology diagram	PDB	X-ray crystal structure
Class I	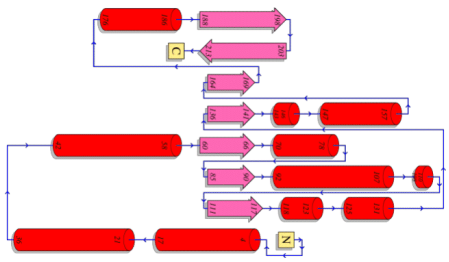	6I3C	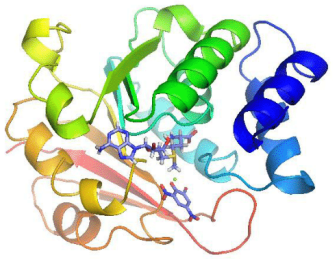
Class II	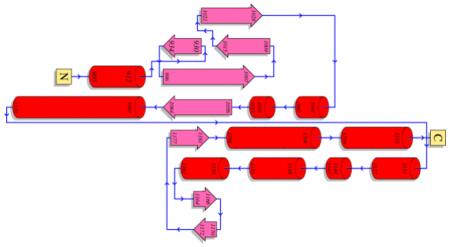 (domain 1)	1MSK	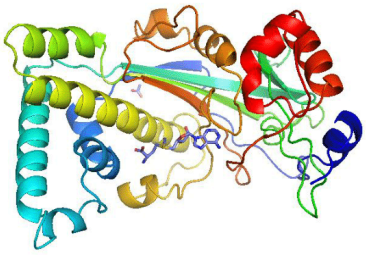
Class III	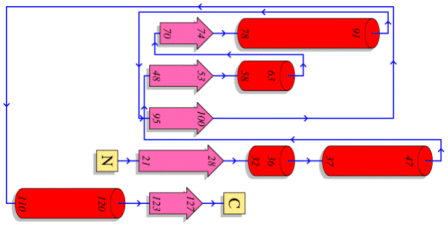 (domain 1)	1CBF	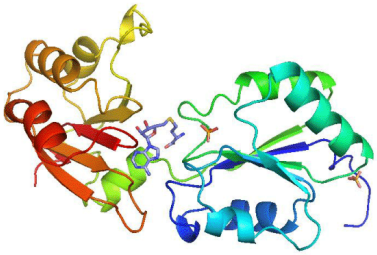
Class IV	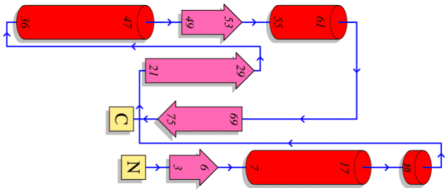 (domain 1)	1GZ0	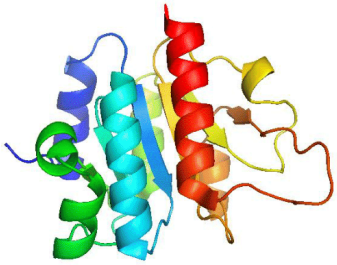
Class V	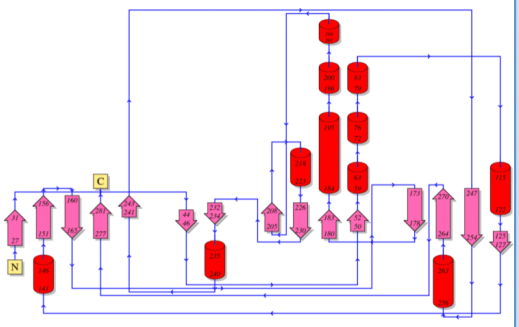	1ML9	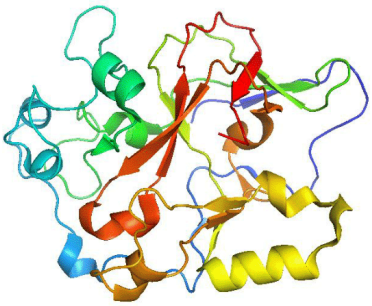

Table 1. The structures of the five classes of MTases. In each case a representative topology diagram and a crystallographic structure is shown. Diagrams rendered using PDBsum [12].

1.1.1 The model system: Catechol-*O*-methyltransferase (COMT)

COMT was purified and characterized initially by Axelrod and Tomchick [13]. COMT is a ubiquitous bisubstrate magnesium-dependent enzyme, occurring in plants, animals and microorganisms [14]. It catalyses the transfer of a methyl group from its cofactor SAM to one of the phenolic hydroxyl groups in a catechol substrate, preferentially the 3-hydroxyl in an S_N2-type reaction [15, 16] (**Figure 1**).

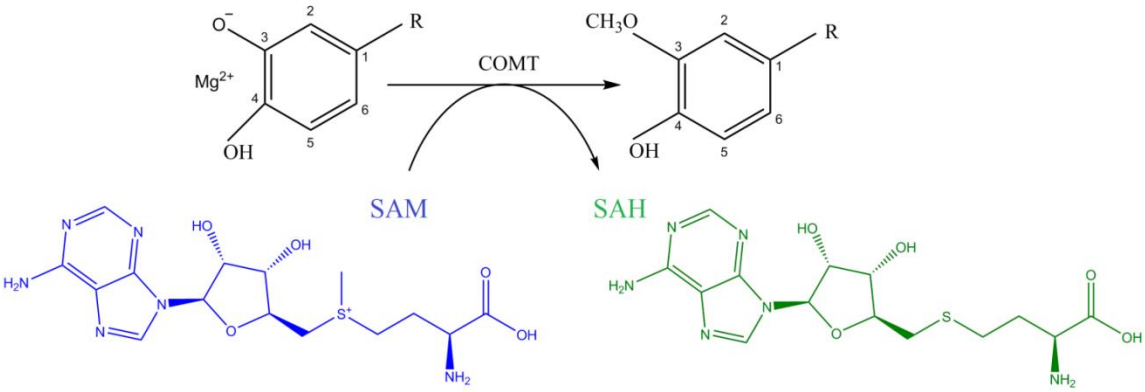

Figure 1. The O-methylation of the catechol substrate catalysed by COMT. SAM: S-adenosyl-L-methionine, SAH: S-Adenosyl-L-homocysteine [17].

The O-methylation of catechols shows regioselectivity [18]. *In vivo* it is almost exclusively to the 3-hydroxyl (meta) of the catechol ring, while *in vitro* also 4-methoxy (para) product formation can be found [19]. The magnitude of the ratio of the *O*-methylated products is dependent upon the concentration of divalent cation, the pH of the medium, and the nature and position of the substituents on the catechol ring [20]. Physiological substrates of COMT are catecholamine neurotransmitters such as dopamine, noradrenaline, adrenaline and their metabolites (**Figure 2**) [21]. COMT also inactivates catecholic steroids like 2-hydroxyestradiol (catechol estrogen) and a large number of other catechol compounds, as well as neuroactive drugs such as L-Dopa and α-methyldopa and isoproterenol [22, 23].

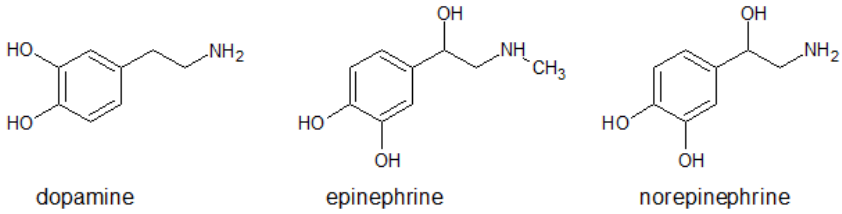

Figure 2. Structures of dopamine, epinephrine (adrenaline) and norepinephrine (noradrenaline).

COMT inhibition is a way of treating schizophrenia, depression, Parkinson's disease and other dopamine deficiency-related diseases [24]. In humans there are two isoforms of this enzyme, soluble cytoplasmatic COMT (S-COMT), which is mainly intracellular and is expressed in the liver and kidneys, and membrane-bound form (MB-COMT), predominating in the brain, which has a 50 amino acid extension at the N-terminus [25]. Rat and human S-COMT both contain 221 amino acids and the molecular masses are 24.8 kDa for the rat enzyme and 24.4 kDa for the human enzyme. The corresponding molecular masses for MB-COMT are 29.6 and 30 kDa for the rat and human enzymes [26]. Rat S-COMT is relatively 'slow' enzyme with turnover number of 24 per minute [27]. There are some differences between human and rat COMT, although they share 81% sequence identity. In general, they have different substrate specificities and human S-COMT contains a common single nucleotide Val-Met polymorphism (G → A substitution) at position 108 (158 in MB-COMT) and also three additional solvent-exposed cysteine residues (C95, C173, C188), which can cause protein aggregation by disulfide bond formation [28, 29]. S-COMT possesses about 15 times higher K_m values for catecholamines than MB-COMT and also has lower affinity for the coenzyme S-adenosyl-L-methionine [22]. Genetic studies have demonstrated that both soluble and membrane-bound isoforms of COMT are coded by a single gene, using two separate promoters, assigned to chromosome 22 band q11.2 in humans [30].

1.1.2 Structure, reaction mechanism and substrates/inhibitors

Rat S-COMT was crystallized by Vidgren et al. in 1991, who then solved the structure in 1994 [31]. The critical atomic structures have been described in details by Vidgren and Ovaska in 1997 [32]. S-COMT has a typical α/β fold, eight α-helices and seven β-sheets. The sheet contains five parallel β-strands and one antiparallel β-hairpin. The C-terminal part consists of two antiparallel β-strands, while the N-terminus is composed of α-helices. The active site of COMT, which is located in the outer surface of the enzyme, includes SAM binding domain and the actual catalytic site situated in the vicinity of the Mg^{2+} ion (**Figure 3**) [31].

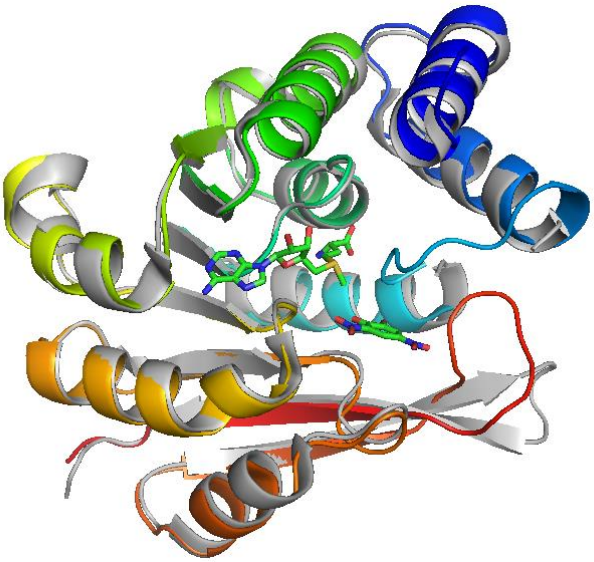

Figure 3. X-ray crystal structures of S-COMT in the apo state (PDB: 4PYI; grey colour) versus S-COMT:SAM:DNC:Mg^{2+} complex (PDB: 6I3C; coloured in a rainbow gradient: N-terminus in blue to C-terminus in red).

The active site of the enzyme consists of two distinct parts: the co-enzyme-binding motif and the catalytic site situated in the vicinity of the Mg^{2+} ion. SAM binds only when the enzyme is complexed with the Mg^{2+} ion, but there is no direct interaction of the SAM with the magnesium. The order in which the substrates bind is: Mg^{2+} binds first, followed by SAM and then by the catechol substrate [33]. SAH (S-Adenosyl-L-homocysteine) is the last product to dissociate from the enzyme [27]. The role of magnesium is to make the hydroxyl groups of the catechol substrate more easily ionisable [16]. A lysine residue (Lys144) in COMT accepts the proton from the substrate hydroxyl group, and subsequently the methyl group from SAM is transferred to the hydroxyl group [31]. Key active-site residues are: Val42, His142, Asp141, Trp38 and Trp143. The carboxyl oxygens of SAM are hydrogen-bonded to Val42 and water. The adenine part of SAM structure has favourable van der Waals contacts with His142 (also Trp143 and Ile91). The Mg^{2+} ion is octahedrally coordinated by six ligands: water, two hydroxyl groups of catechol and side-chain oxygens of Asp141, Asp169 and Asn170 (**Figure 4**). Trp38, Trp143 and Pro174 keep the planar catechol ring in the correct position, by forming the hydrophobic “walls”. In case of the inhibitor, DNC (3,5-dinitrocatechol), the 5-nitro group is sandwiched between Pro174 and Trp38 [34, 35].

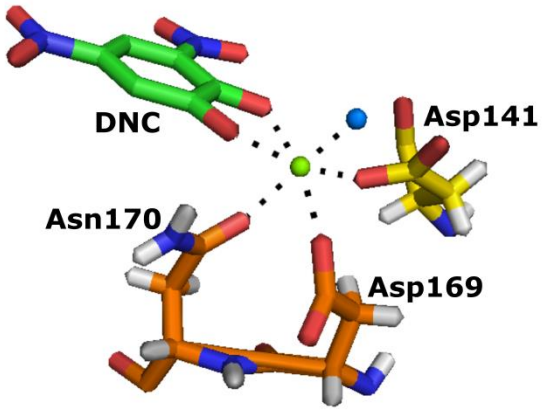

Figure 4. Magnesium coordination in COMT:DNC:SAM:Mg^{2+} complex. The magnesium ion is represented as a green sphere, and the coordinated water molecule is represented as a blue sphere (PDB: 6I3C).

3,5-dinitrocatechol as mentioned before, is a tight-binding inhibitor of COMT [36, 37]. The inhibitor binds to the catalytic site in a para orientation, with the two catechol hydroxyls coordinating the Mg^{2+} ion. The nitro group fits tightly at one end of the binding pocket, forming favourable van der Waals interactions with the indole ring of Trp143. One oxygen atom of the nitro group is buried by the protein near the amino group of Lys144, whereas the other oxygen is partially solvated. The benzene ring of DNC forms edge-to-face π-π interactions with Trp38, which is an important residue for high affinity binding of catechols. Substitution of Trp38 by arginine reduced the affinity of catechol compounds by 10~1000-fold [38].

Another important residue highlighted by Klinman and Zhang is Tyr68. Tyr68 is positioned directly above SAM, with a short distance between the sulphur atom of SAM and the C_β of Tyr68 (**Figure 5**). It has an important role in achieving the catalytically optimal alignment of the methyl donor (SAM) in relation to its ionized acceptor. Klinman and Zhang have mutated the Tyr68 residue showing that it influences methyl donor-acceptor distance and catalytic efficiency [39].

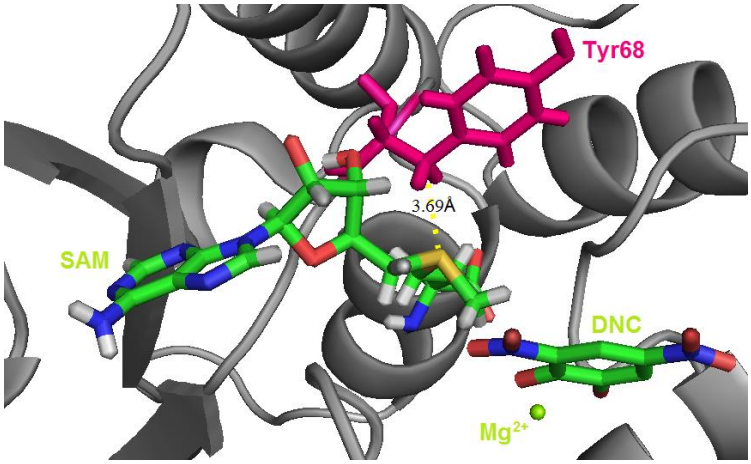

Figure 5. Active site of human S-COMT with highlighted Tyr68 residue (magenta). PDB: 6I3C.

A common polymorphism of the human COMT gene coding for a thermolabile activity was described for the first time in 1979 by Scanlon, Raymond and Weinshilboum. It has been reported that there are two alleles, responsible for "low" and "high" enzyme activity, $COMT^{L}$ and $COMT^{H}$, respectively [40]. Human S-COMT contains a single nucleotide Val-Met polymorphism (G → A substitution) at position 108 (158 in MB-COMT), that was mentioned above. While the two proteins have similar kinetic properties, the $Met^{108/158}$ form of COMT has a lower thermostability and activity than $Val^{108/158}$. Shield et al. reported T_{50} (temperatures resulting in 50% inactivation) values of 53.7 ± 0.1ºC for the 108V protein and 49.7 ± 0.3ºC for the 108M protein [41]. Crystal structures of human Val108 and Met108 S-COMT were solved by the Rutherford group in 2008 (**Figure 6**). Residue 108 is located approximately 16 Å from the active site in a short, stable loop between α5 and β3. Replacing Val108 with the larger methionine residue leads to greater solvent exposure and heightened packing interactions between Met108 and helices α2, α4 (especially with Arg78) and α5. In humans, the 108M allele has been associated with increased risk for breast cancer, schizophrenia, alcoholism and obsessive-compulsive disorder. Individuals with that allele may suffer from a higher level of dopamine in the brain due to decreased deactivation of the neurotransmitter [28, 42].

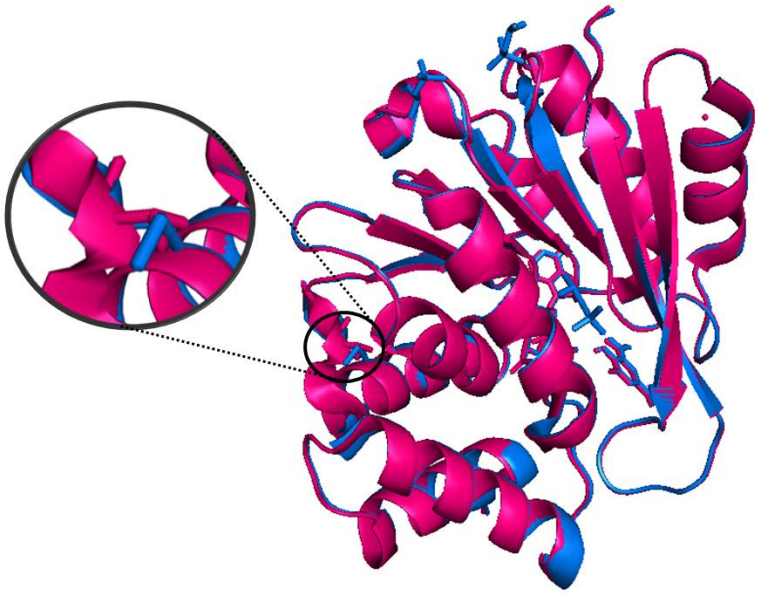

Figure 6. S-COMT Val-Met polymorphism represented as an overlay between 108V (PDB: 3BWM) structure (pink colour) and 108M (PDB: 3BWY) structure (blue colour). Residue 108 is circled and zoomed.

In a large number of published X-ray structures of ternary complexes of COMT with substrate-like catechol inhibitors, a surprisingly short C⋯O (methyl-to-catechol oxygen) bond has been detected, with length about 2.7Å, which is less than the expected van der Waals distance. Klinman pointed out that all of the interrogated structures contain inhibitors with electron withdrawing groups that will lower the pK_a of one of the catechol OH groups, which results in the binding of the anionic form of inhibitor [39]. She also postulated active site compaction/compression, the compact arrangement of active site residues and reactants that affords the tunneling-ready state [43].

1.1.3 S-Adenosyl-L-methionine and analogues

S-Adenosyl-L-methionine (SAM, AdoMet) is a universal biological cofactor, discovered by Cantoni in 1953 [44]. It takes part in methyltransferase reactions that transfer the active methyl group of SAM to methyl acceptor molecules, including catecholamines, phospholipids, nucleic acids, proteins and polysaccharides. It is one of the most important methyl group donors in mammalian tissues [45].

In 2006, Blackburn, Couture, Hauk and others examined SAM and three SAM analogues to investigate their interactions during methyl transfer, thermodynamic

parameters for the binding and their crystal structures after binding to pLSMT (pea Rubisco large subunit methyltransferase) [7]. Structures of SAM and SAM analogues are presented in **Figure 7**.

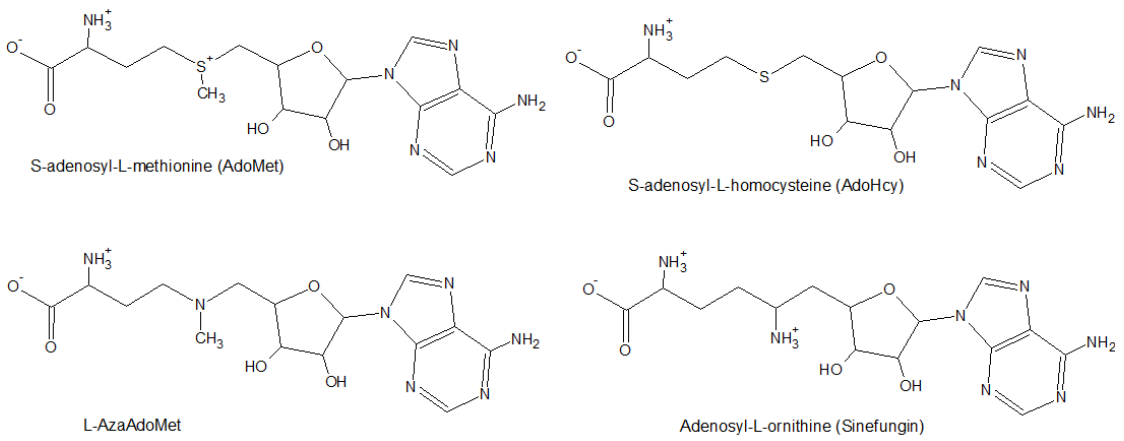

Figure 7. Structures of AdoMet (SAM), AdoHcy (SAH), L-AzaAdoMet and Sinefungin.

In 2012, Struck et al. used aziridine SAM analogues and sulfonium and selenonium SAM analogues for the SMILing DNA approach (Sequence-specific Methyltransferase-Induced Labelling of DNA). They also replaced the methyl group of natural SAM with alternative alkyl, alkenyl, alkynyl and further functionalised chains [46]. More recently, the amino-functionalised SAM has also been used in single-molecule optical mapping of DNA, which allows linear dsDNA to be fluorescently labelled at specific sites [47, 48].

In this project, sinefungin (also known as Adenosyl-L-ornithine), a fungal-derived nucleoside SAM-analogue possessing an amine group in place of the methylsulfonium moiety, was widely used. Sinefungin is an antifungal and antiviral antibiotic isolated from *Streptomyces griseolus*, and it is naturally occurring structural analogue of SAM/SAH. It inhibits transmethylation reactions related to proteins, DNA, RNA and other molecules. [49, 50]. Inhibition of COMT is medically relevant and complexes with inhibitors are more stable over time. Also, protein-inhibitor studies are often used at the initial stage and at the optimization phase of drug-development [51], thus this work is focused on COMT:inhibitor complexes.

1.2 Protein dynamics

The old and classic "lock-and-key" model treats proteins as static molecules that interact with ligands if they have appropriate shape and size. That hypothesis was proposed more than 100 years ago [52]. Since then enzymology has made enormous progress and we know that proteins are not static, but dynamic and they can interconvert between different conformations on varying timescales. Local motions, including loop motions, side-chain rotations and bond vibrations occur on the fast timescale (fs-ns). Global motions, such as ligand binding, protein folding and domain rearrangement occur on the slower timescales (up to seconds) [53]. Different NMR experiments are suited to study dynamics on different timescale (**Figure 8**). Selected NMR experiments will be explained further in the next chapter.

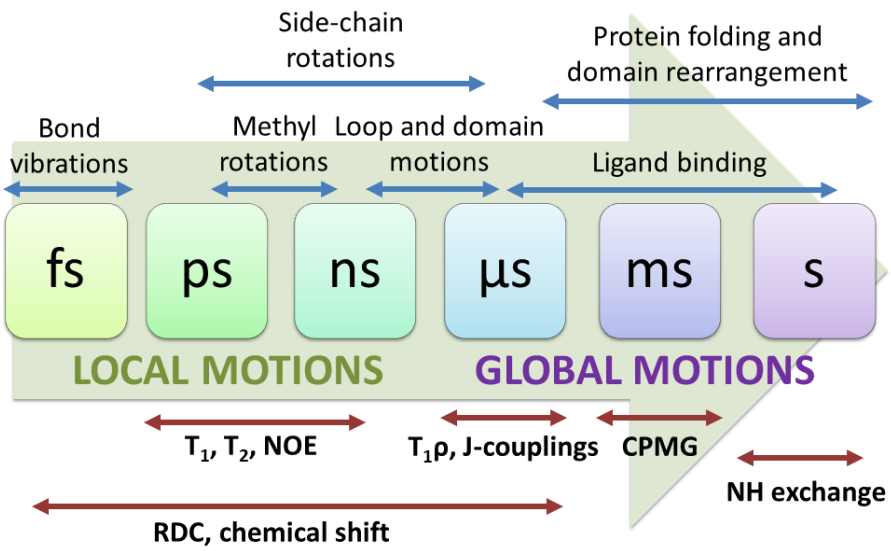

Figure 8. Timescale of protein motions. At the top of the picture possible motions are indicated. At the bottom NMR experiments are shown to probe these motions. Figure adapted from [53].

1.2.2. Computational studies of COMT

Molecular dynamics (MD) is a computer simulation method for studying how molecules move, deform and interact over time. It is used for structure studies, thermodynamic and dynamics. Currently, a typical simulation might have a system size of around 10^5-10^6 atoms and simulate 10's – 1000's ns of dynamics. It can provide information about macromolecular stability, conformational and allosteric properties,

dynamics in enzyme activity, properties of complexes, protein association, hydration, folding and much more [54].

Klinman and Zhang used MD and QM/MM (quantum mechanics/molecular mechanics) simulations several times in COMT study, which supported the proposal of active site compaction. Their results also implicated a critical role of Tyr68 (mentioned before) in achieving the catalytically optimal alignment of SAM in relation to the ionized catecholate acceptor [39, 55]. On the other hand, QM/MM calculations of KIE (kinetic isotope effects) by the William's group, does not support the compression hypothesis [56]. Bruice and Lau used MD simulations to study the active site of COMT. They have found that the physical properties of the enzyme are very similar when containing catecholate or the transition state. They suggest that the catalytic power of COMT in going from E·S (enzyme-substrate) to E·TS (enzyme-transition state) is due to the ability of the active site to arrange the reactants into conformers that mimics the transition state [57]. In other MD studies on the enzyme complexed with cofactor and substrate, Bruice et al. showed that the attacking methyl of SAM and the O^- of the catechol were in a near attack configuration (NAC). A NAC is an energy minimum structure that must be formed geometrically before reaching a TS in a reaction pathway. They pointed out that the opposing charges of SAM and Asp141 form a stabilizing interaction which orient the cofactor into a NAC. Their results support the proposition declaring that factors like desolvation and bringing together the nucleophile and electrophile in the correct position play an important role in the catalytic efficiency of COMT [58]. However, Warshel et al used EVB (the empirical valence bond approach) to determine reaction free energies, as well as MM/MD simulations, and they argued against compaction and NACs in favour of electrostatic preorganisation [59]. Recently, Klinman and Martinez used QM/MM to calculate transition state free energy ($\Delta G^{\ddagger}$). The value they calculated, of 16 kcal/mol, was in a good agreement with the experimental value of 18 kcal/mol [60]. Computational methods were also used to study COMT regioselectivity for several compounds, confirming preferences of meta *O*-methylation [61].

MD is mentioned here as a complementary technique. All MD calculations presented in Chapter 3 were done by Dr Linus O. Johannissen, not by the PhD candidate.

1.3 NMR - Nuclear Magnetic Resonance

1.3.1 Principles of NMR

The first NMR signal was observed independently in 1945 by Purcell and Bloch [62-64], who were both awarded the Nobel Prize for physics in 1952. The first low resolution NMR instrument appeared on the market in 1953, which was a continuous wave (CW) NMR spectrometer. In the beginning, the magnetic fields for NMR instruments were between 1.41 T (60 MHz) and 2.35 T (100 MHz). Superconducting magnets with a high resolution were produced after 1970. Currently, a 1 GHz NMR instrument is available for use at the European Centre for High Field NMR (CRMN) in Lyon, France [65], and higher resolution magnets are also being developed [66].

In an NMR experiment, the sample is placed in a static magnetic field B_0, applied in a direction defined as z-axis. In the absence of a magnetic field the proton spin states have the same energy. In an external magnetic field B_0 the magnetic moment μ of the nuclear particles will orient parallel or antiparallel with B_0. This causes a movement of precession of the nuclear dipoles around the z-axis, analogous to a gyroscope in a gravitational field. The frequency of the precession, which is known as Larmor frequency, is proportional to the strength of the magnetic field:

$$\omega = \gamma B \qquad (1.1)$$

where γ is the proportionality constant called the gyromagnetic ratio.

Parallel and antiparallel orientations of nuclear spin states have different energy. Energy separation between the states is called nuclear Zeeman splitting (**Figure 9**). The number of energy levels equals $2I + 1$, where I is the nuclear spin quantum number. The energy shift is determined by magnetic quantum number, m, which is an interval including 0 ranging from $-I$ to I in integer steps ($m=1/2$ and $m=-1/2$ for $I=1/2$). The most common for NMR are nuclei with $I=1/2$, so with only two possible energy levels. Energy level (energy state) with $m=1/2$ is denoted α ("spin up"), while the state with $m=-1/2$ is denoted β ("spin down"). Only energy transitions in which m changes by one ($\Delta m=\pm 1$) are allowed in NMR. Often for theoretical explanations the quantum number M is used, which is found by adding up the m values for each of the spins ($M=m_1+m_2$). Then the selection rule is that $\Delta M=\pm 1$ and it is called a single-quantum transition. Zero-quantum

and double-quantum transitions are not allowed by the usual selection rule, but are possible in case of relaxation (see chapter 1.3.4.1 The Solomon equations).

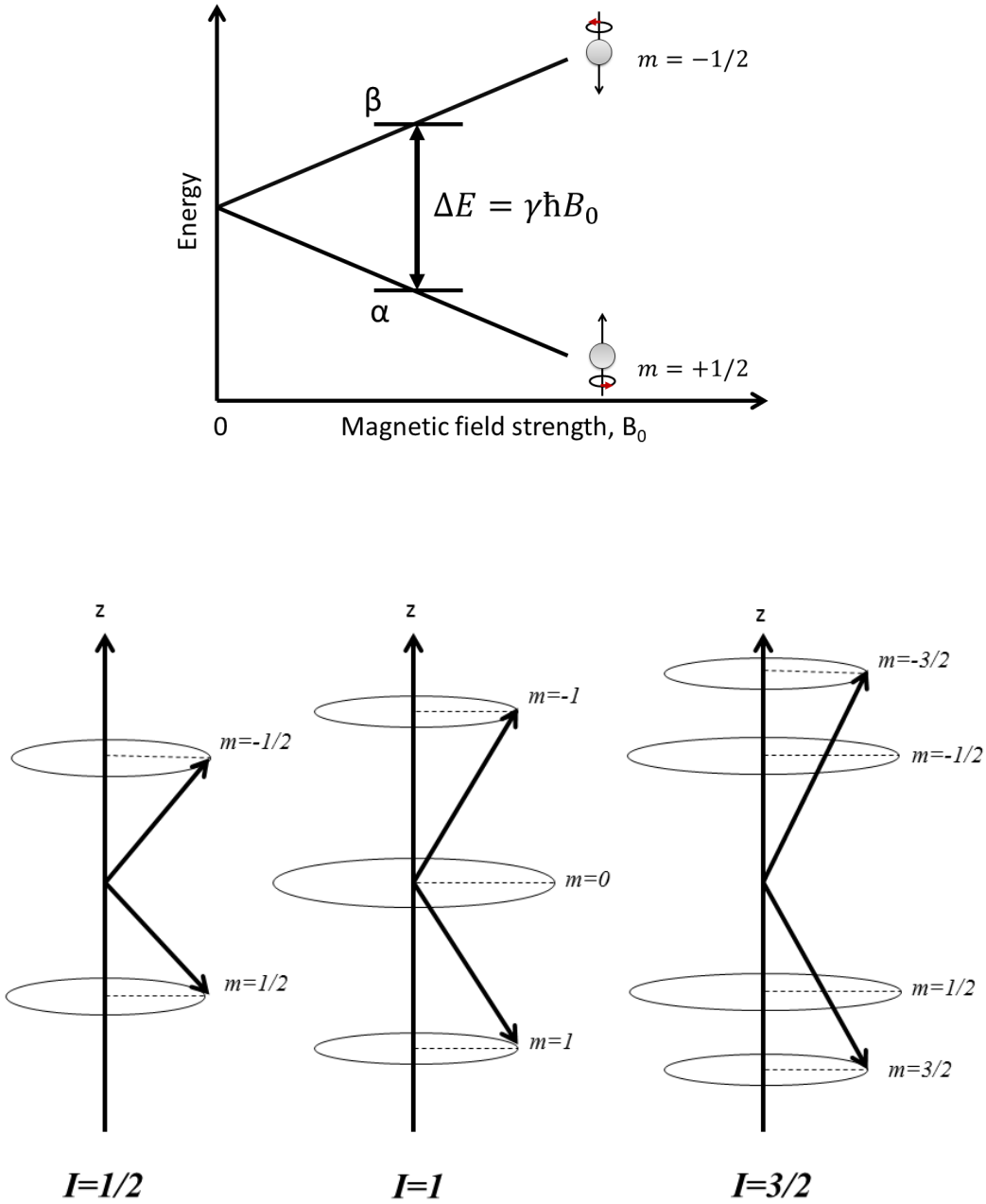

Figure 9. NMR energy level diagram. (top): The splitting of the degenerate nuclear energy levels under an applied magnetic field. The grey spheres represent atomic nuclei which are either aligned with (low energy) or against (high energy) the magnetic field. Figure adapted from ref. [67] (bottom): Energy level diagram showing the breakdown of nuclear spin degeneracy upon the application of magnetic field for I=1/2 (left) I=1(middle) and I=3/2 (right). The magnitude is denoted by the arrow while the projection along the z-axis is denoted by the circle.

The Boltzmann distribution says that the most stable and lowest energy state in a system will be the most populated at equilibrium. The nuclear magnetic dipoles oriented with B_0 have the lowest energy. The difference with dipoles oriented against is small, but although minor, that small difference in population results in a net magnetization. Net nuclear magnetic moment, which is the sum of the dipole moments of identical spins, is called magnetization (*M*, different from the quantum number *M*), and it is represented by a vector parallel to the static magnetic field. The length of the *M* vector is proportional to the population difference between the parallel and antiparallel dipolar moments.

$$M = \sum_i \mu_i \qquad (1.2)$$

$$\mu = \gamma \hbar \sqrt{I(I+1)} \qquad (1.3)$$

where $\hbar = h/2\pi$; h is Planck's constant (h=6.63 x 10^{-34} J·s), γ is the gyromagnetic ratio, I is the nuclear spin quantum number.

The precession of the magnetization vector is what we detect in an NMR experiment, but due to interference form B_0, the precession rate of the nuclei cannot be measured while the net magnetization is along the z-axis (longitudinal, aligned along the static field axis B_0). To overcome that, the NMR experiment consists of a radiofrequency (RF) pulses to rotate the net magnetization onto the xy-plane (90° NMR pulse, **Figure 10**). The RF pulse is coherent across the sample, which means that it affects all the spins.

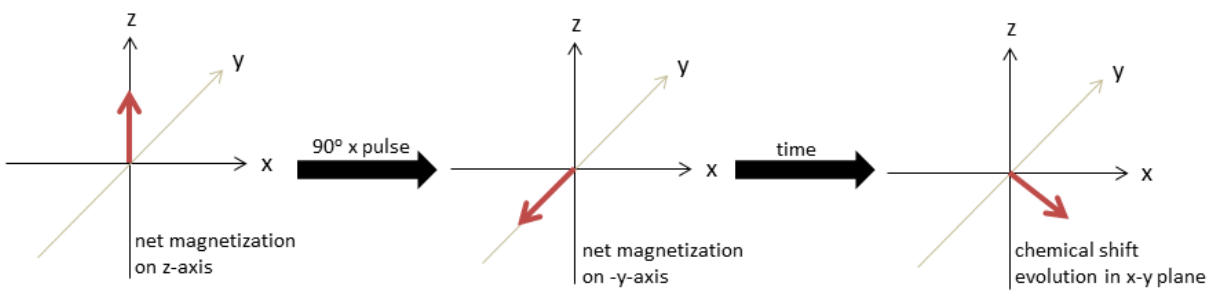

Figure 10. 90° NMR pulse. The diagram represents the net magnetization of the sample (red arrow) on the z-axis, the effect of the 90° pulse and the chemical shift evolution in the x-y plane after application of the 90° pulse.

Precession while the RF field is on causes the magnetization to move away from the B_0 axis, and leaves a transverse component of magnetization (M_{xy}) when the RF field is off. The transverse magnetization created due to the RF pulse precesses about B_0 at a frequency ν given by the Larmor equation:

$$\nu = \frac{\gamma}{2\pi}|B_0| = \frac{1}{h}\left[E_\beta - E_\alpha\right] \qquad (1.4)$$

where E_α and E_β are energies of α and β nuclear spin states.

All nuclear spins with magnetic properties (non-zero quantum number *I*) can be studied by NMR. All nuclei with an odd mass number have magnetic properties, because they have an unpaired proton. Nuclei with an even mass number and an odd atomic number (e.g. ^{2}H, ^{14}N) also have magnetic properties. The most popular nuclei studied by NMR are ^{1}H, ^{13}C, ^{15}N, ^{19}F and ^{31}P. When the quantum number is I=0, then the magnetic moment μ also is zero, and the nucleus does not have magnetic properties (e.g. ^{12}C, ^{16}O) [67-71].

The one-dimensional NMR spectrum shows amplitude as a function of frequency. To gain this spectrum, the excited nuclei generate a signal detected in the time domain, which is then converted to the frequency domain using Fourier transformation. A 1-D pulse sequence contains two parts: preparation and detection, separated by an excitation pulse (**Figure 11**A) [72]. First, preparation delay allows the spins to come to equilibrium. Typically, it takes a few seconds. Then, high power radiofrequency (RF) is applied. This excites a transient signal FID (free induction decay) which lasts between 50 ms and a few seconds. Finally, Fourier transformation of FID gives the spectrum. The two-dimensional NMR spectrum is obtained after carrying out two Fourier transformations on a matrix of data. The 2-D pulse sequence contains four parts: preparation, evolution, mixing and detection (**Figure 11**B). In the 3-D pulse evolution and mixing steps are doubled (**Figure 11**C).

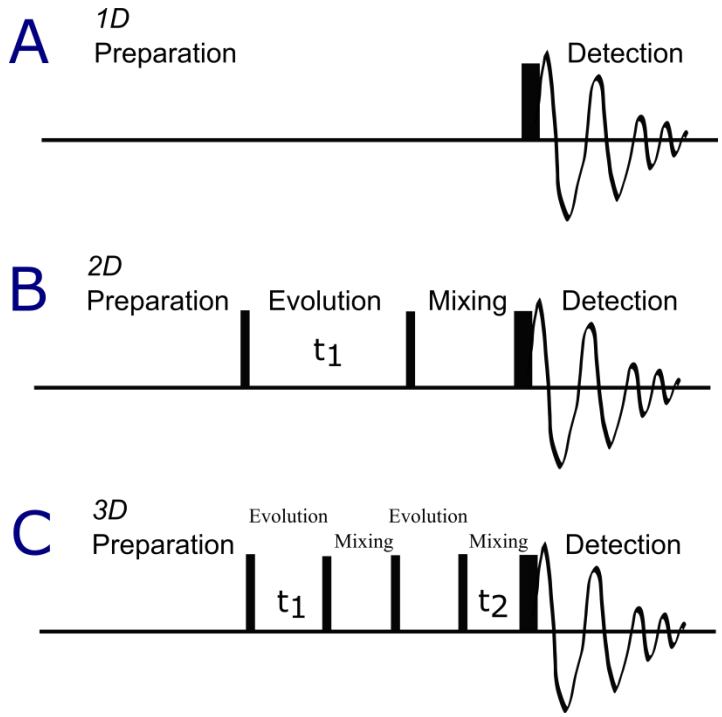

Figure 11. The distinct time periods of a generic 1-D, 2-D and 3-D NMR pulse sequence. Figure adapted from Rinaldi (2004) [73].

Evolution is a delay for mapping of chemical shifts, mixing is a time during which through-bond (COSY-type) or through-space (NOESY-type) couplings are allowed to interact. The most popular 2D NMR experiments are homonuclear: COSY (Correlation Spectroscopy), NOESY (Nuclear Overhauser Effect Spectroscopy), TOCSY (Total Correlation Spectroscopy) and heteronuclear: HSQC (Heteronuclear Single Quantum Correlation) and HMQC (Heteronuclear Multiple-Quantum Correlation). The differences between them are acquisition and processing parameters (**Table 2**). Adapted from ref. [74].

		Spectrum	Pulse Sequence
Homonuclear	**COSY**	Spectrum contains the shifts and J-couplings spins along the f_1 and f_2 axes.	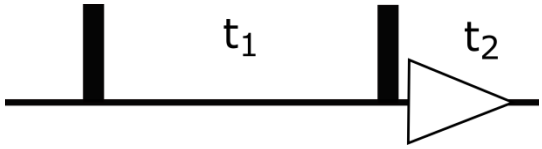
	NOESY	Spectrum similar to COSY but the cross peaks are generated not by coherence transfer through couplings, but by cross relaxation.	
	TOCSY	Coupling between two spins in the spectrum is indicated by the presence of a cross-peak multiplet.	
Heteronuclear	**HMQC**	The spectrum contains ^1H chemical shift along the f_2 axis and the chemical shift of other nucleus along the f_1 axis.	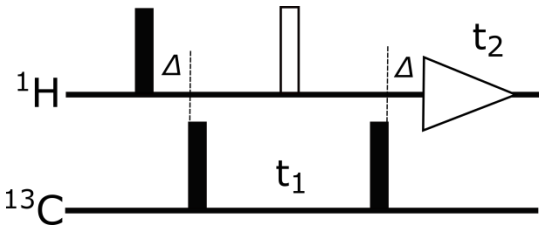
	HSQC	The same spectrum as HMQC but differing in the way the relaxation affects the experiment (different pulse sequence).	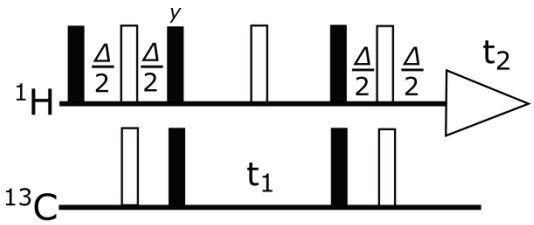

Table 2. Comparison of different types of NMR experiments. Figures adapted from ref.[74].

Often TROSY (Transverse Relaxation Optimized Spectroscopy) is used instead of HSQC due to HSQC limitation for large proteins or nucleic acids. TROSY data collection employs an HSQC measurement with neither ^{1}H nor ^{15}N decoupling elements as well as other elements which suppress the broad lines of the doublets and retain the sharp lines. For large proteins (≥30 kDa) at high field there is a significant sensitivity and resolution advantage compared to a conventional HSQC. However, in the case of proteins that are larger than approximately 40-50 kDa, the observed signal-to-noise ratio will be higher than that found in a standard HSQC spectrum because of the narrower linewidth of the observed peak. It should be noted that the TROSY cross peaks are shifted by ½ $^{1}J_{HN} \approx 45$Hz in both the ^{15}N and $^{1}H^{N}$ dimensions and the NH_2 proton resonances do not appear as in HSQC spectra. Other characteristics of TROSY are similar to that of HSQC as are their applications and experimental setups. [72, 74, 75].

1.3.2 Protein NMR

The first nuclear magnetic resonance experiments with biological macromolecules were reported more than 50 years ago [76, 77]. In the 1980s NMR studies began to determine the three dimensional structure of small isotopically labelled proteins in a solution and used this structural information to study catalysis, assembly and ligand binding etc. [78, 79]. Unlike crystallography, NMR experiments are carried under potentially physiological conditions and therefore are not hampered by the ability or the inability of a protein to crystallize. Today many different triple and quadruple resonance NMR measurements are used and their applications are not limited to proteins in solution, rather, they also include nucleic acids and proteins in the solid state [80]. Recently, several high dimensional strategies have been proposed of up to seven dimensions which are especially useful for studying intrinsically disordered proteins [81].

1.3.3 High pressure NMR

Proteins in a solution are not rigid; rather, they exist in a many different conformations. A protein molecule in a solution fluctuates not only in terms of energy, but also in volume. This fluctuation may involve the folded conformer as well as

partially folded or unfolded conformers. Application of pressure acts simply to stabilize the lower volume unfolded state relative to the higher volume folded state, thus shifting the equilibrium towards unfolding. As a result, the population of a lower volume conformer will increase under pressure. For a protein of a given stability, the ease with which pressure does this task depends on the magnitude of the difference in volume between these two states. High pressure experiments allow for the detection and analysis of the structures and thermodynamic stability of high-energy sub-states in proteins (normally, their populations are too low to be detected by conventional spectroscopic techniques). [82-84].

Pressure effects are governed by Le Chatelier's principle, which provides that at equilibrium a system tends to minimise the effect of any external factor by which it is perturbed. Consequently, an increase in pressure favours the reduction of the volume of a system [85].

$$\Delta G = -RTlnK = \Delta E + p\Delta V - T\Delta S \qquad (1.5)$$

Where ΔG, ΔE, ΔV, ΔS are changes in: free energy, internal energy, volume and entropy; R is the gas constant, T is the temperature, K is the equilibrium constant and p is the pressure.

The difference in conformer population can be expressed by the pressure-dependent Boltzmann distribution:

$$\frac{P_2}{P_1} = exp\left(\frac{-(\Delta G + p\Delta V)}{RT}\right) \qquad (1.6)$$

where P_1 and P_2 are populations of the different states in a thermodynamic equilibrium [86].

The protein volume in a solution is the sum of three main components: the volume of the individual atoms, the volume of the internal cavities due to the imperfect atomic packing within the tertiary structure and a contribution due to the solvation of peptide bonds and amino acid side chains. Protein compressibility is mostly determined by the compression of the internal cavities [87].

Chemical shifts are sensitive to pressure changes. The Akasaka group showed in 1998 that hydrogen bonds are shortened by pressure and indicated that the NH proton shift of a few hertz at the ^{1}H resonance frequency of 750 MHz corresponds to an

average linear compression of the hydrogen bond by 0.001 Å. They claimed that 'free' NH protons, which are actually bonded to solvent water, are more sensitive to pressure than hydrogen-bonded to carbonyls [88]. Baxter et al. observed that most N and HN nuclei in the R3 domain of talin move to higher resonance frequencies at elevated pressure (the lower field region). Compression results in increased polarisation of the H-N bond, causing the chemical shifts of HN and N to move to higher frequencies as the amide proton becomes increasingly deshielded and the amide nitrogen becomes increasingly shielded [86]. Similar behaviour in pressure dependence patterns was observed in PETNR [89]. The majority of residues usually show approximately linear pressure-dependent chemical shift changes. Unusual curved pressure titration data suggests that an alternative conformation is present with a high population and that alternative conformers have different chemical shifts and/or compressibility compared to the basic conformer. Large-scale conformational exchange typically slows at high pressure [86, 90]. Akasaka claimed that large cavities that can hold water molecules are the cause of shift nonlinearity with increasing pressure [91]. Additional examples and discussion of high pressure NMR studies are given in Chapter 4.

1.3.4 Relaxation

Relaxation is the process by which the net magnetisation perturbed by RF pulses returns to the equilibrium state along the z-axis. The magnetization relaxes back using two processes: T_1 spin-lattice longitudinal relaxation along the static magnetic field B_0 direction (relaxation in the z-direction) and T_2 spin-spin transverse relaxation in the transverse plane perpendicular to the field direction (relaxation in the x-y plane). During T_1 relaxation, the nuclei exchange energy with the surroundings or with the environment (lattice), while there is no energy exchange with the lattice during T_2 relaxation. T_2 is less than or equal to T_1, since the return of magnetization to the z-direction inherently causes loss of magnetization in the x-y plane. T_1 is static itself, T_2 precesses at the Larmor frequency ν (1.4). The rate at which the magnetization returns to the z-axis is called the relaxation rate constant R_1 $(R_1=1/T_1)$, while the rate at which coherence is lost between the spins in the x-y plane is called R_2 $(R_2=1/T_2)$. Nuclear spin relaxation measurements probe molecular dynamics, because molecular dynamics produce time dependences in the forces that act on nuclear spins. The various nuclear spin relaxation

times (T_1, T_{1rho}, T_2) refer to the characteristic time scales for the build-up or decay of various states of nuclear spin order. Typical T_1 values range from 1s for proteins to tens of seconds for small molecules [71, 92, 93].

1.3.4.1 The Solomon equations

The Solomon equations explain possible transitions in dipolar relaxation. If a molecule contains two spins, *I* and *S*, that are close enough together for dipole-dipole coupling, but are not scalar coupled ($J_{IS}=0$), then there are four energy levels and all transitions are possible in case of dipolar relaxation (**Figure 12**). Each transition has a different rate constant associated with it. The rate constants for the two allowed *I* spin transitions will be denoted $W_I^{(1)}$ and $W_I^{(2)}$, and similar for the *S* spin transitions $W_S^{(1)}$ and $W_S^{(2)}$. There are also transitions that involve the simultaneous flip of both spins, W_0 $(\alpha\beta\leftrightarrow\beta\alpha)$, which is a zero-quantum transition ($\Delta M=0$) and W_2 $(\alpha\alpha\leftrightarrow\beta\beta)$, which is a double-quantum transition ($\Delta M=2$).

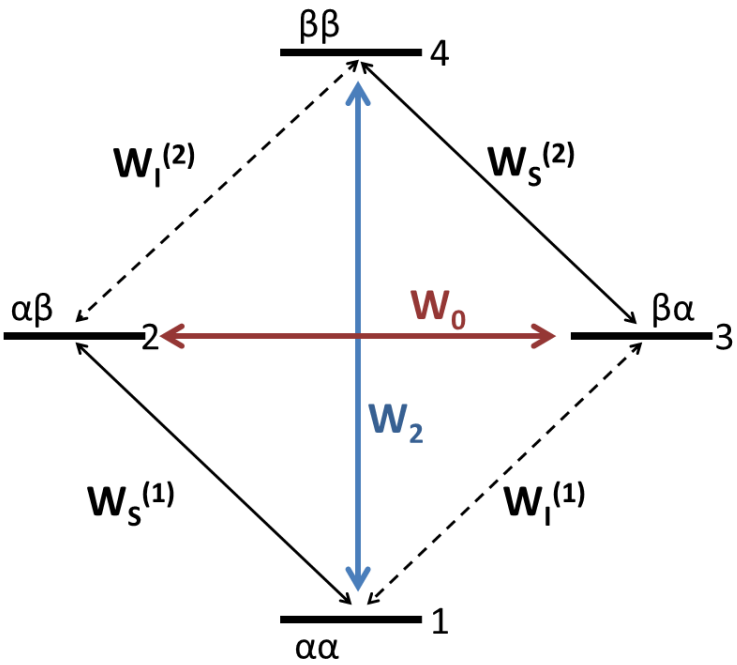

Figure 12. Energy level diagram for a two-spin system showing allowed transitions (black) and the relaxation induced transitions (coloured).

The frequency for the double-quantum transition corresponds to the sum of the frequencies of the individual spins, while the zero-quantum frequencies are formed from the difference of their corresponding frequencies. For homonuclear spin systems the

zero-quantum frequencies are very low (kHz range) and the double-quantum frequencies are very high.

Equations for the flow of population as a function of time for the four energy levels presented in **Figure 12** are:

$$\frac{dn_1}{dt} = -W_S^{(1)}(n_1 - n_1^0) - W_I^{(1)}(n_1 - n_1^0) - W_2(n_1 - n_1^0) + W_S^{(1)}(n_2 - n_2^0) + W_I^{(1)}(n_3 - n_3^0) + W_2(n_4 - n_4^0) \quad (1.7)$$

$$\frac{dn_2}{dt} = -W_S^{(1)}(n_2 - n_2^0) - W_I^{(2)}(n_2 - n_2^0) - W_0(n_2 - n_2^0) + W_S^{(1)}(n_1 - n_1^0) + W_I^{(2)}(n_4 - n_4^0) + W_0(n_3 - n_3^0) \quad (1.8)$$

$$\frac{dn_3}{dt} = -W_I^{(1)}(n_3 - n_3^0) - W_S^{(2)}(n_3 - n_3^0) - W_0(n_3 - n_3^0) + W_I^{(1)}(n_1 - n_1^0) + W_S^{(2)}(n_4 - n_4^0) + W_0(n_2 - n_2^0) \quad (1.9)$$

$$\frac{dn_4}{dt} = -W_S^{(2)}(n_4 - n_4^0) - W_I^{(2)}(n_4 - n_4^0) - W_2(n_4 - n_4^0) + W_S^{(2)}(n_3 - n_3^0) + W_I^{(2)}(n_2 - n_2^0) + W_2(n_1 - n_1^0) \quad (1.10)$$

Where $(n_i\text{-}n_i^0)$ is the population difference from equilibrium. If the observed intensities of I and S are proportional to their spin z-magnetizations I_Z and S_Z, then:

$$I_Z = (n_1 - n_3) + (n_2 - n_4) \quad (1.11)$$

$$S_Z = (n_1 - n_2) + (n_3 - n_4) \quad (1.12)$$

And finally:

$$\frac{dI_Z}{dt} = -\left(W_I^{(1)} + W_I^{(2)} + W_2 + W_0\right)I_Z - (W_2 - W_0)S_Z - (W_I^{(1)} - W_I^{(2)})2I_ZS_Z \quad (1.13)$$

$$\frac{dS_Z}{dt} = -(W_2 - W_0)I_Z - \left(W_S^{(1)} + W_S^{(2)} + W_2 + W_0\right)S_Z - (W_S^{(1)} - W_S^{(2)})2I_ZS_Z \quad (1.14)$$

$$\frac{d2I_ZS_Z}{dt} = -\left(W_I^{(1)} - W_I^{(2)}\right)I_Z - \left(W_S^{(1)} - W_S^{(2)}\right)S_Z - (W_I^{(1)} + W_I^{(2)} + W_S^{(1)} + W_S^{(2)})2I_ZS_Z \quad (1.15)$$

These three equations are known as Solomon equations. The main conclusion from Solomon's work is that the magnetization on the *I* spin depends on the *S* spin. This phenomenon, by which the magnetizations of the two different spins are connected, is called cross relaxation and leads to nuclear Overhauser effect [71, 74, 94].

1.3.4.2 Nuclear Overhauser Effect (NOE)

The nuclear Overhauser Effect (NOE) is a phenomenon that measures how perturbation by saturation or inversion of one resonance in an NMR spectrum affects the net intensities of other resonances in the spectrum. The resonances that change their intensities are close in space to those directly affected by the perturbation; simplifying NOE occurs through space, not chemical bonds. If the two coupled spins are protons (usually the amide proton and the H_α proton of the preceding residue), then the NOE measurement can be used to obtain inter-proton distances for structure determination. This is frequently done by NOESY (nuclear Overhauser effect spectroscopy). In NOESY spectra, cross-peaks appear between nuclei closer than 6Å in space and the intensity of that cross-peak is proportional to the distance between the two nuclei. If the two coupled spins are two different atoms, like ^{15}N-^{1}H group, then the effect is referred to as the heteronuclear NOE (hetNOE or hnNOE) and probe internal motions of macromolecules. The NOE effect is defined as the change in the overall intensity of one resonance that occurs when another resonance is saturated and it is expressed as the fractional enhancement:

$$\eta = f_I\{S\} = \frac{I_{sat} - I_{ref}}{I_{ref}} \quad (1.16)$$

where η is the NOE enhancement factor, I_{sat} is the intensity of the peak in the saturated spectrum and I_{ref} is the intensity of the peak in the reference spectrum.

Particularly for heteronuclear cases, the NOE is calculated by the simple equation:

$$\eta = \frac{I_{sat}}{I_{ref}} = f_I\{S\} + 1 \quad (1.17)$$

Detection of an appreciable NOE indicates that there is a relatively short internuclear distance between two spins, generally less than 5-6 Å. Recently, one of the most significant uses for heteronuclear NOE measurements together with T_1 and T_2 relaxation values is the determination of local flexibility in macromolecules. Typically, for each ^{15}N resonance in a labelled protein, the corresponding T_1, T_2 (or $T_{1\rho}$) and ^{1}H-^{15}N steady-state NOE is measured, and then data are analysed using a suitable formalism, for example 'model-free' formalism of Lipari and Szabo (see next chapter 1.2.4.3). The ^{15}N T_1 and T_2 relaxation rates and the ^{1}H-^{15}N steady-state NOE can be calculated as a function of spectral density $J(\omega)$. Spectral density function is the probability function of finding motions at a given angular frequency ω. For a protein in solution, $J(\omega)$ depends on overall motion of the protein and internal motion of the ^{1}H-^{15}N bond vector.

$$J(\omega) = \frac{2\tau_c}{1 + (\omega\tau_c)^2} \qquad (1.18)$$

where τ_c is the rotational correlation time, that characterized tumbling. It is the average time it takes for a molecule to rotate 1 radian (~57.296^{o}).

$$1/T_1 = d^2[J(\omega_H - \omega_N) + 3J(\omega_N) + 6J(\omega_H + \omega_N)] + c^2 J(\omega_N) \qquad (1.19)$$

$$1/T_2 = 0.5d^2[4J(0) + J(\omega_H - \omega_N) + 3J(\omega_N) + 6J(\omega_H) + 6J(\omega_H + \omega_N)] + 1/6c^2[3J(\omega_N) + 4J(0)] + R_{ex} \qquad (1.20)$$

$$NOE = 1 + \left(\frac{\gamma_H}{\gamma_N}\right) d^2[6J(\omega_H + \omega_N) - J(\omega_H - \omega_N)]T_1 \qquad (1.21)$$

where the constants c^2 and d^2 are defined as:

$$c^2 = \left(\frac{2}{15}\right)\gamma_N^2 H_0^3(\sigma_\parallel - \sigma_\perp)^2 \qquad (1.22)$$

$$d^2 = 0.1\gamma_H^2\gamma_N^2 h^2/(4\pi^2)\left(\frac{1}{r_{NH}^3}\right)^2 \qquad (1.23)$$

where γ_H and γ_N are the gyromagnetic ratios of the ^{1}H and ^{15}N nuclei, ω_H and ω_N are the Lamor frequencies, r_{NH} is the internuclear ^{1}H-^{15}N distance for amides (~1.02Å), H_0 is the magnetic field strength, $\sigma_{/\!/}$ and $\sigma_\perp$ are the parallel and perpendicular components of the ^{15}N chemical shift tensor, respectively. R_{ex} is the chemical exchange relaxation rate,

incorporated to describe the effects that mainly result from the conformation exchange averaging and is an indicator of motions on micro to millisecond timescales [71, 95-98].

1.3.4.3 Model-free analysis

The experimental relaxation data obtained from NMR measurements are interpreted on a residue-by-residue basis and they are commonly related to motional parameters using several approaches, most common are model-free approach and spectral density mapping. Spectral density mapping provides direct access to protein dynamics with no assumptions as to the nature of the molecule or its dynamic behaviour. It involves solving equations for relaxation rates expressed in terms of spectral density. Six independent relaxation rates are measured and then the values of spectral densities are determined by solving a set of equations. The major challenge of the spectral density mapping is the fact that various types of interactions contribute to relaxation in real systems. As a consequence, values of multiple auto- and cross-correlated spectral density functions at several frequencies contribute to the measured relaxation rates, which greatly increases the number of unknown parameters in the spectral density mapping analysis [99]. Model-free approach provides an alternative to direct determination of the spectral density. According to this formalism, the spectral density function is calculated as:

$$J(\omega) = \frac{S^2\tau_m}{1+\omega^2\tau_m^2} + (1-S^2)\tau/(1+\omega^2\tau^2) \qquad (1.24)$$

where τ_m is the autocorrelation time (the overall tumbling correlation time of the entire molecule, in other words it is the overall motion of the protein), ω is Lamor frequency and S^2 is the square of the Lipari and Szabo generalised order parameter. $1/\tau = 1/\tau_e + 1/\tau_m$, where τ_e is the effective correlation time describing the ^1H-^{15}N bond vector internal motion, reflecting the picosecond to nanosecond timescale of motion. If the internal motion is very rapid, τ_e approaches zero. When τ_e is much smaller than τ_m, then the equation is simplified to:

$$J(\omega) = \frac{S^2\tau_m}{1+\omega^2\tau_m^2} \qquad (1.25)$$

The S^2 order parameter describes the geometric extent of the internal motion relative to the molecular frame. In other words, the order parameter reflects the amplitude of the

motion and the correlation time is an indication of the time scale of that motion. S^2 equal to 1 implies complete rigidity (a perfectly rigid sphere) and no internal motions, while S^2 equal to 0 implies the internal motion is isotropic relative to the molecular frame, means random internal motions occur and the molecule is completely flexible.

The original model-free theory [95, 96] describes a single internal motion using the two parameters S^2 and τ_e. That theory was extended by Clore et al. in 1990 [100] to include internal motions on two distinct timescales with the faster timescale described by S^2_f and τ_f, and the slower timescale described by S^2_s and τ_s. The two order parameters are related by the equation:

$$S^2 = S_f^2 \cdot S_s^2 \qquad (1.26)$$

The current strategy of model-free approach involves:

1. Estimation of the correlation time for overall tumbling (τ_m) from the T_1/T_2 ratio for a selected subset of the residues. T_1 and T_2 are recalculated to R_1 and R_2, which are relaxation rates calculated as:

$$R_1 = \frac{d^2}{4}[J(\omega_H - \omega_N) + 3J(\omega_N) + 6J(\omega_H + \omega_N)] + \frac{c^2}{3}J(\omega_N) \qquad (1.27)$$

$$R_2 = \frac{d^2}{8}[4J(0) + 3J(\omega_N) + J(\omega_H - \omega_N) + 6J(\omega_H) + 6J(\omega_H + \omega_N)] + \frac{c^2}{18}[3J(\omega_N) + 4J(0)] + R_{ex} \qquad (1.28)$$

2. Nonlinear least-squares fits to the observed relaxation data are performed using various subsets of the possible optimised parameters (**Table 3**). The fitting is repeated five times, once for each of the five model-free models.
3. Model-selection criteria are used for deciding which choice of variable optimized parameters is appropriate for each residue.
4. Value of τ_m may be re-optimized using the selected diffusion model.
5. The uncertainties in all of the estimated parameters are determined by Monte Carlo simulations for error propagation.

Diffusion Model	Optimized parameters
1 – local τ_m	S^2 ($\tau_e = 0$, $R_{ex} = 0$, $S^2_f = 1$)
2 – sphere	S^2, τ_e ($R_{ex} = 0$, $S^2_f = 1$)
3 – prolate spheroid	S^2, R_{ex} ($\tau_e = 0$, $S^2_f = 1$)
4 – oblate spheroid	S^2, τ_e, R_{ex} ($S^2_f = 1$)
5 - ellipsoid	S^2, τ_e, S^2_f ($R_{ex} = 0$)

Table 3. Nomenclature for subsets of optimized parameters in diffusion models of the model-free approach.

There are few model-free assumptions which can also be a source of errors. Firstly, the model-free approach assumes that intramolecular motions are independent of molecular overall rotation. Conventional model-free protocols assume that the protein does not aggregate during NMR relaxation studies. Usually, the parameters of a ^{15}N nucleus (^{15}N CSA – chemical shift anisotropy, which is a measure of the largest deviation in chemical shift from the average value and ^{15}N-^{1}H distance) are kept fixed, assumed to be the same for all ^{15}N nuclei in the protein [98, 101-104]. In reality there are various effects that can lead to fluctuations in the magnetic field. One is chemical shift anisotropy (CSA, mentioned above), which is the result of non-spherical distribution of electrons around the nucleus. In solution NMR, the anisotropy of the chemical shift is averaged out by fast molecular tumbling and only a single isotropic chemical shift value is observed. CSA is the dependence of the chemical shift on the orientation of the bond vector relative to the external magnetic field and it may induce the relaxation of the ^{15}N nucleus [105]. Another source of fluctuation is dipolar coupling. Dipolar coupling arises when the magnetic field of one nuclear spin affects the local magnetic field of another spin, for instance, the magnetic field generated by the amide nitrogen causes an additional field at the amide proton. The strength of this field is orientation and distance depended [93].

Model-free analysis has been used for many different proteins, including barnase [106], calmodulin [107], nitrophorin [108], calbindin [109], ribonuclease [110] etc. Several

studies revealed quite restricted backbone motions in highly ordered regions in proteins, with the amplitudes of S^2 up to ~0.87, whereas significantly lower S^2 are often observed in the flexible unstructured regions, such as loops and terminal tails. The associated time scales (τ_e or τ_f) are in the 1–100 ps range for protein-core elements and slower, up to several nanoseconds (τ_s) in the flexible regions [111].

1.2.4.4. Relaxation dispersion

Relaxation dispersion experiments refer to study motions on µs-ms time scales. The main experimental techniques for quantifying chemical exchange on these time scales are Carr-Purcell-Meiboom-Gill (CPMG) relaxation dispersion [112] and $R_{1\rho}$ relaxation dispersion [113]. Processes that occur on that slow time scale are in particular: enzyme catalysis, folding, binding, domain reorientation and allosteric regulation [53]. In a relaxation dispersion experiment, the spins are subject to a transverse magnetic field while in the transverse plane (x-y). The observed spin-spin relaxation rate depends on both the chemical exchange rate (R_{ex}) and the strength of the applied field. It is possible to measure exchange rate constant (k_{ex}) without relying on any other information. In practice, the transverse relaxation rate, R_2, is measured at a number of different field strengths (ν_{CPMG}) and the exchange rate is obtained by fitting the measured dispersion curve to theoretical models [93]. When ν_{CPMG} is large, the effective transverse relaxation rate is small as the exchange is quenched. The CPMG uses spin-echo pulse sequences to average the differences in precession frequencies between the spins of interest in the conformational states which are exchanging. The $R_{1\rho}$ relaxation dispersion experiment uses spin-locking to average the effects of chemical exchange during a fixed relaxation period. Relaxation dispersion experiments have been widely used in characterising minor states of proteins (for example, with populations of only 1-10% in solution) and intermediates formed during the folding process [114, 115].

1.4 Aims

The overall objective of this project is to characterise the fast timescale dynamics and mechanistic details of catechol-*O*-methyltransferase (COMT) during its catalytic trajectory with the aid of NMR (including high pressure NMR and NMR relaxation) and X-ray crystallography. We aim to determine if compressive motions are a principal feature of methyl transfer reactions, focussing on the reaction catalysed by COMT. Initial aims of the project include production and purification of stable isotopically-labelled protein, optimisation of NMR experiments and backbone assignment. Next aim of the work is to solve protein structures using X-ray crystallography. We aim to study COMT in physiologically relevant complex with SAM (S-Adenosyl-L-methionine) and its derivative sinefungin, which possesses transition state-like charge on the transferring group and can be used as a transition state analog. Both complexes will be examined and compared by NMR, crystallography and computational methods (including DFT calculations and molecular dynamics). Dynamics studies includes acquisition of the NMR spin relaxation measurements at two field strengths (600 MHz and 800 MHz) and analysis of the data using the Model-free approach. High pressure NMR ^{1}H-^{15}N HSQC experiments will be recorded in the range of 1 bar to 2500 bar pressure at 500 bar increments. The application of pressure and relaxation measurements will allow probing protein rigidity and any conformational exchange/transition, if occurs.

References

1. Schubert, H.L., R.M. Blumenthal, and X. Cheng, *Many paths to methyltransfer: a chronicle of convergence.* Trends in biochemical sciences, 2003. **28**(6): p. 329-335.
2. Petrossian, T.C. and S.G. Clarke, *Uncovering the human methyltransferasome.* Molecular & Cellular Proteomics, 2011. **10**(1): p. M110. 000976.
3. Martin, J.L. and F.M. McMillan, *SAM (dependent) I AM: the S-adenosylmethionine-dependent methyltransferase fold.* Current opinion in structural biology, 2002. **12**(6): p. 783-793.
4. Dixon, M.M., et al., *The structure of the C-terminal domain of methionine synthase: presenting S-adenosylmethionine for reductive methylation of B12.* Structure, 1996. **4**(11): p. 1263-1275.
5. Schubert, H.L., et al., *The X-ray structure of a cobalamin biosynthetic enzyme, cobalt-precorrin-4 methyltransferase.* Nature Structural Biology, 1998. **5**: p. 585.
6. Tkaczuk, K.L., et al., *Structural and evolutionary bioinformatics of the SPOUT superfamily of methyltransferases.* Biomedical Central Bioinformatics, 2007. **8**(1): p. 73.
7. Couture, J.F., et al., *Catalytic roles for carbon-oxygen hydrogen bonding in SET domain lysine methyltransferases.* Journal of Biological Chemistry, 2006. **281**(28): p. 19280-7.
8. Siedlecki, P. and P. Zielenkiewicz, *Mammalian DNA methyltransferases.* Acta Biochimica Polonica-English edition-, 2006. **53**(2): p. 245.
9. Lan, J., et al., *DNA methyltransferases and methyl-binding proteins of mammals.* Biochimica et Biophysica Acta, 2010. **42**(4): p. 243-252.
10. Rana, A.K. and S. Ankri, *Reviving the RNA world: an insight into the appearance of RNA methyltransferases.* Frontiers in genetics, 2016. **7**: p. 99.
11. Liscombe, D.K., G.V. Louie, and J.P. Noel, *Architectures, mechanisms and molecular evolution of natural product methyltransferases.* Natural Product Reports, 2012. **29**(10): p. 1238-1250.
12. Laskowski, R.A., et al., *PDBsum: Structural summaries of PDB entries.* Protein Science, 2018. **27**(1): p. 129-134.
13. Axelrod, J. and R. Tomchick, *Enzymatic O-methylation of epinephrine and other catechols.* Journal of Biological Chemistry, 1958. **233**(3): p. 702-5.
14. Mannisto, P.T., et al., *Characteristics of catechol O-methyl-transferase (COMT) and properties of selective COMT inhibitors.* Progress in Drug Research, 1992. **39**: p. 291-350.
15. Masjost, B., et al., *Structure-based design, synthesis, and in vitro evaluation of bisubstrate inhibitors for catechol O-methyltransferase (COMT).* Chemistry, 2000. **6**(6): p. 971-82.

16. Zheng, Y.-J. and T.C. Bruice, *A Theoretical Examination of the Factors Controlling the Catalytic Efficiency of a Transmethylation Enzyme: Catechol O-Methyltransferase.* Journal of the American Chemical Society, 1997. **119**(35): p. 8137-8145.

17. Lundstrom, K., et al., *Cloning, expression and structure of catechol-O-methyltransferase.* Biochimica et Biophysica Acta, 1995. **1251**(1): p. 1-10.

18. Law, B.J.C., et al., *Effects of Active-Site Modification and Quaternary Structure on the Regioselectivity of Catechol-O-Methyltransferase.* Angewandte Chemie International Edition, 2016. **55**(8): p. 2683-2687.

19. Creveling, C., et al., *Catechol O-methyltransferase: III. m-and pO-methylation of catecholamines and their metabolites.* Molecular Pharmacology, 1970. **6**(6): p. 691-696.

20. Creveling, C., et al., *Catechol O-methyltransferase: IV. Factors affecting m-and p-methylation of substituted catechols.* Molecular Pharmacology, 1972. **8**(4): p. 398-409.

21. Guldberg, H.C. and C.A. Marsden, *Catechol-O-methyl transferase: pharmacological aspects and physiological role.* Pharmacological Reviews, 1975. **27**(2): p. 135-206.

22. Lotta, T., et al., *Kinetics of human soluble and membrane-bound catechol O-methyltransferase: a revised mechanism and description of the thermolabile variant of the enzyme.* Biochemistry, 1995. **34**(13): p. 4202-10.

23. Ball, P., et al., *Interactions Between Estrogens and Catechol Amines III. Studies on the Methylation of Catechol Estrogens, Catechol Amines and other Catechols by the Catechol-O-Methyltransferase of Human Liver.* The Journal of Clinical Endocrinology & Metabolism, 1972. **34**(4): p. 736-746.

24. Harrison, S.T., et al., *Synthesis and Evaluation of Heterocyclic Catechol Mimics as Inhibitors of Catechol-O-methyltransferase (COMT).* American Chemical Society Medicinal Chemistry Letters, 2015. **6**(3): p. 318-23.

25. Salminen, M., et al., *Molecular cloning and characterization of rat liver catechol-O-methyltransferase.* Gene, 1990. **93**(2): p. 241-7.

26. Tilgmann, C. and N. Kalkkinen, *Purification and partial characterization of rat liver soluble catechol-O-methyltransferase.* Federation of European Biochemical Societies Letters, 1990. **264**(1): p. 95-9.

27. Schultz, E. and E. Nissinen, *Inhibition of rat liver and duodenum soluble catechol-O-methyltransferase by a tight-binding inhibitor OR-462.* Biochemistry and Pharmacology, 1989. **38**(22): p. 3953-6.

28. Rutherford, K., et al., *Crystal structures of human 108V and 108M catechol O-methyltransferase.* Journal of Molecular Biology, 2008. **380**(1): p. 120-30.

29. Tunbridge, E.M., P.J. Harrison, and D.R. Weinberger, *Catechol-o-methyltransferase, cognition, and psychosis: Val158Met and beyond.* Society of Biological Psychiatry, 2006. **60**(2): p. 141-51.

30. Tenhunen, J., et al., *Genomic organization of the human catechol O-methyltransferase gene and its expression from two distinct promoters.* European Journal of Biochemistry, 1994. **223**(3): p. 1049-59.

31. Vidgren, J., L.A. Svensson, and A. Liljas, *Crystal structure of catechol O-methyltransferase.* Nature, 1994. **368**(6469): p. 354-8.

32. Vidgren, J., et al., *Catechol 0-methyltransferase*, in *S-Adenosylmethionine-Dependent Methyltransferases*. 2011, World Scientific. p. 55-91.

33. Jeffery, D.R. and J.A. Roth, *Kinetic reaction mechanism for magnesium binding to membrane-bound and soluble catechol O-methyltransferase.* Biochemistry, 1987. **26**(10): p. 2955-8.

34. Vidgren, J., et al., *Crystallization and preliminary X-ray investigation of a recombinant form of rat catechol O-methyltransferase.* Proteins, 1991. **11**(3): p. 233-6.

35. Mannisto, P.T. and S. Kaakkola, *Catechol-O-methyltransferase (COMT): biochemistry, molecular biology, pharmacology, and clinical efficacy of the new selective COMT inhibitors.* Pharmacological Reviews, 1999. **51**(4): p. 593-628.

36. Huo, C., et al., *Proteasome inhibition in human breast cancer cells with high catechol-O-methyltransferase activity by green tea polyphenol EGCG analogs.* Bioorganic and medicinal chemistry, 2010. **18**(3): p. 1252-1258.

37. Kiss, L.E. and P. Soares-da-Silva, *Medicinal chemistry of catechol O-methyltransferase (COMT) inhibitors and their therapeutic utility.* Journal of Medicinal Chemistry, 2014. **57**(21): p. 8692-717.

38. Piedrafita, F., et al., *Inhibition of catechol-O-methyltransferase by N-(3, 4-dihydroxyphenyl) maleimide.* Journal of enzyme inhibition, 1990. **4**(1): p. 43-50.

39. Zhang, J., et al., *Mediation of donor–acceptor distance in an enzymatic methyl transfer reaction.* Proceedings of the National Academy of Sciences, 2015: p. 201506792.

40. Scanlon, P.D., F.A. Raymond, and R.M. Weinshilboum, *Catechol-O-methyltransferase: thermolabile enzyme in erythrocytes of subjects homozygous for allele for low activity.* Science, 1979. **203**(4375): p. 63-65.

41. Shield, A., et al., *Human catechol O-methyltransferase genetic variation: gene resequencing and functional characterization of variant allozymes.* Molecular psychiatry, 2004. **9**(2): p. 151-160.

42. Rutherford, K., et al., *The 108M Polymorph of Human Catechol O-Methyltransferase Is Prone to Deformation at Physiological Temperatures.* Biochemistry, 2006. **45**(7): p. 2178-2188.

43. Klinman, J.P. and A. Kohen, *Hydrogen Tunneling Links Protein Dynamics to Enzyme Catalysis.* Annual Review of Biochemistry, 2013. **82**(1): p. 471-496.

44. Cantoni, G.L., *S-adenosylmethionine; A new intermediate formed enzymatically from L-methionine and adenosinetriphosphate.* Journal of Biological Chemistry, 1953. **204**(1): p. 403-416.

45. Salvatore, F. and A. nazionale dei Lincei, *The Biochemistry of Adenosylmethionine: Proceedings of an International Symposium on the Biochemistry of Adenosylmethionine, Sponsored by the Accademia Nazionale Dei Lincei, Held in Rome, Italy May 21-26, 1974*. 1977: Columbia University Press.

46. Struck, A.W., et al., *S-adenosyl-methionine-dependent methyltransferases: highly versatile enzymes in biocatalysis, biosynthesis and other biotechnological applications.* Chembiochem, 2012. **13**(18): p. 2642-55.

47. Neely, R.K., et al., *DNA fluorocode: A single molecule, optical map of DNA with nanometre resolution.* Chemical Science, 2010. **1**(4): p. 453-460.

48. Neely, R.K., J. Deen, and J. Hofkens, *Optical mapping of DNA: Single-molecule-based methods for mapping genomes.* Biopolymers, 2011. **95**(5): p. 298-311.

49. Borchardt, R.T., et al., *Sinefungin, a potent inhibitor of S-adenosylmethionine: Protein O-methyltransferase.* Biochemical and Biophysical Research Communications, 1979. **89**(3): p. 919-924.

50. Vedel, M., et al., *The antifungal antibiotic sinefungin as a ver y active inhibitor of methyltransferases and of the transformation of chick embryo fibroblasts by rous sarcoma virus.* Biochemical and Biophysical Research Communications, 1978. **85**(1): p. 371-376.

51. Ishima, R., *Protein-Inhibitor Interaction Studies Using NMR.* Applications of NMR spectroscopy, 2015. **1**: p. 143-181.

52. Fischer, E., *Einfluss der Configuration auf die Wirkung der Enzyme.* Berichte der deutschen chemischen Gesellschaft, 1894. **27**: p. 2985-2993.

53. Henzler-Wildman, K. and D. Kern, *Dynamic personalities of proteins.* Nature, 2007. **450**(7172): p. 964.

54. Adcock, S.A. and J.A. McCammon, *Molecular Dynamics: Survey of Methods for Simulating the Activity of Proteins.* Chemical Reviews, 2006. **106**(5): p. 1589-1615.

55. Zhang, J. and J.P. Klinman, *Enzymatic methyl transfer: role of an active site residue in generating active site compaction that correlates with catalytic efficiency.* Journal of the American Chemical Society, 2011. **133**(43): p. 17134-7.

56. Ruggiero, G.D., et al., *QM/MM Determination of Kinetic Isotope Effects for COMT-Catalyzed Methyl Transfer Does Not Support Compression Hypothesis.* Journal of the American Chemical Society, 2004. **126**(28): p. 8634-8635.

57. Lau, E.Y. and T.C. Bruice, *Comparison of the Dynamics for Ground-State and Transition-State Structures in the Active Site of Catechol O-Methyltransferase.* Journal of the American Chemical Society, 2000. **122**(30): p. 7165-7171.

58. Lau, E.Y. and T.C. Bruice, *Importance of correlated motions in forming highly reactive near attack conformations in catechol O-methyltransferase.* Journal of the American Chemical Society, 1998. **120**(48): p. 12387-12394.

59. Lameira, J., et al., *Methyltransferases do not work by compression, cratic, or desolvation effects, but by electrostatic preorganization.* Proteins: Structure, Function, and Bioinformatics, 2015. **83**(2): p. 318-330.

60. Kulik, H.J., et al., *How Large Should the QM Region Be in QM/MM Calculations? The Case of Catechol O-Methyltransferase.* The Journal of Physical Chemistry B, 2016. **120**(44): p. 11381-11394.

61. Cao, Y., et al., *Computational Studies of the Regioselectivities of COMT-Catalyzed Meta-/Para-O Methylations of Luteolin and Quercetin.* The Journal of Physical Chemistry B, 2014. **118**(2): p. 470-481.

62. Koenig, S.H., *II Rabi, F. Bloch, EM Purcell, and the History of NMR and Relaxometry.* Encyclopedia of Nuclear Magnetic Resonance, Historical Perspectives, 1996. **1**: p. 437.

63. Bloch, F., W.W. Hansen, and M. Packard, *Nuclear Induction.* Physical Review, 1946. **69**(3-4): p. 127-127.

64. Purcell, E.M., H.C. Torrey, and R.V. Pound, *Resonance Absorption by Nuclear Magnetic Moments in a Solid.* Physical Review, 1946. **69**(1-2): p. 37-38.

65. Balci, M., *Basic 1H-and 13C-NMR spectroscopy*. 2005: Elsevier.

66. Bascuñán, J., et al., *A 1.3-GHz LTS/HTS NMR Magnet–A Progress Report.* IEEE transactions on applied superconductivity : a publication of the IEEE Superconductivity Committee, 2011. **21**(3 Pt 2): p. 2092-2095.

67. Spyros, A. and P. Dais, *NMR spectroscopy in food analysis*. 2012: Royal Society of Chemistry.

68. Günther, H., *NMR spectroscopy: basic principles, concepts and applications in chemistry*. 2013: John Wiley & Sons.

69. Carbajo, R.J. and J.L. Neira, *NMR for Chemists and Biologists*. 2013: Springer.

70. Hore, P.J., *Nuclear magnetic resonance*. 2015: Oxford University Press, USA.

71. Neuhaus, D. and M.P. Williamson, *Nuclear Overhauser Effect in Structural and Conformational Analysis*. 2000: Wiley-vch.

72. Simpson, J.H., *Organic structure determination using 2-D NMR spectroscopy: a problem-based approach*. 2011: Academic Press.

73. Rinaldi, P.L., *Three-dimensional solution NMR spectroscopy of complex structures and mixtures.* Analyst, 2004. **129**(8): p. 687-699.

74. Keeler, J., *Understanding NMR spectroscopy*. 2011: John Wiley & Sons.

75. Shekhtman, A. and D.S. Burz, *Protein NMR techniques*. 2012: Humana Press.

76. Wüthrich, K., *Protein structure determination in solution by NMR spectroscopy.* Journal of Biological Chemistry, 1990. **265**(36): p. 22059-22062.

77. Wüthrich, K., *The way to NMR structures of proteins.* Nature Structural Biology, 2001. **8**: p. 923.

78. Arseniev, A., et al., *Three-dimensional structure of rabbit liver [Cd7] metallothionein-2a in aqueous solution determined by nuclear magnetic resonance.* Journal of molecular biology, 1988. **201**(3): p. 637-657.

79. Kaptein, R., et al., *Protein structures from NMR.* Biochemistry, 1988. **27**(15): p. 5389-5395.

80. Zhao, X., *Protein structure determination by solid-state NMR*, in *NMR of Proteins and Small Biomolecules*. 2011, Springer. p. 187-213.

81. Żerko, S. and W. Koźmiński, *Six- and seven-dimensional experiments by combination of sparse random sampling and projection spectroscopy dedicated*

for backbone resonance assignment of intrinsically disordered proteins. Journal of Biomolecular NMR, 2015. **63**(3): p. 283-290.

82. Royer, C.A., *Why and How Does Pressure Unfold Proteins?*, in *High Pressure Bioscience: Basic Concepts, Applications and Frontiers*, K. Akasaka and H. Matsuki, Editors. 2015, Springer Netherlands: Dordrecht. p. 59-71.

83. Kamatari, Y.O., et al., *High-pressure NMR spectroscopy for characterizing folding intermediates and denatured states of proteins.* Methods, 2004. **34**(1): p. 133-143.

84. Akasaka, K., *High Pressure NMR Spectroscopy*, in *High Pressure Bioscience: Basic Concepts, Applications and Frontiers*, K. Akasaka and H. Matsuki, Editors. 2015, Springer Netherlands: Dordrecht. p. 707-721.

85. Solaz Portolés, J.J. and J. Quílez Pardo, *Thermodynamics and the Le Chatelier's principle.* Revista Mexicana de Fisica, 1995, vol. 41, num. 1, p. 128-138, 1995.

86. Baxter, N.J., et al., *Pressure-Dependent Chemical Shifts in the R3 Domain of Talin Show that It Is Thermodynamically Poised for Binding to Either Vinculin or RIAM.* Structure, 2017. **25**(12): p. 1856-1866. e2.

87. Mozhaev, V.V., et al., *High pressure effects on protein structure and function.* Proteins-Structure Function and Genetics, 1996. **24**(1): p. 81-91.

88. Li, H., H. Yamada, and K. Akasaka, *Effect of Pressure on Individual Hydrogen Bonds in Proteins. Basic Pancreatic Trypsin Inhibitor.* Biochemistry, 1998. **37**(5): p. 1167-1173.

89. Guerriero, A., *Variable pressure NMR analyses to assess compressive motion in PETNR and catalytically germane PETNR: Ligand complexes*. 2012, University of Manchester, UK.

90. Williamson, M.P., *Pressure-dependent conformation and fluctuation in folded protein molecules*, in *High Pressure Bioscience*. 2015, Springer. p. 109-127.

91. Akasaka, K., *Probing Conformational Fluctuation of Proteins by Pressure Perturbation.* Chemical Reviews, 2006. **106**(5): p. 1814-1835.

92. Tycko, R., *Nuclear magnetic resonance probes of molecular dynamics*. Vol. 8. 1994: Springer Science & Business Media.

93. Rule, G.S. and T.K. Hitchens, *Fundamentals of protein NMR spectroscopy*. Vol. 5. 2006: Springer Science & Business Media.

94. Solomon, I., *Relaxation processes in a system of two spins.* Physical Review, 1955. **99**(2): p. 559.

95. Lipari, G. and A. Szabo, *Model-free approach to the interpretation of nuclear magnetic resonance relaxation in macromolecules. 1. Theory and range of validity.* Journal of the American Chemical Society, 1982. **104**(17): p. 4546-4559.

96. Lipari, G. and A. Szabo, *Model-free approach to the interpretation of nuclear magnetic resonance relaxation in macromolecules. 2. Analysis of experimental results.* Journal of the American Chemical Society, 1982. **104**(17): p. 4559-4570.

97. Neuhaus, D., *Nuclear overhauser effect.* eMagnetic Resonance, 2007.

98. Jin, C., et al., *Sequence specific collective motions in a winged helix DNA binding domain detected by 15N relaxation NMR.* Biochemistry, 1998. **37**(17): p. 6179-6187.

99. Peng, J.W. and G. Wagner, *Mapping of spectral density functions using heteronuclear NMR relaxation measurements.* Journal of Magnetic Resonance (1969), 1992. **98**(2): p. 308-332.

100. Clore, G.M., et al., *Deviations from the simple two-parameter model-free approach to the interpretation of nitrogen-15 nuclear magnetic relaxation of proteins.* Journal of the American Chemical Society, 1990. **112**(12): p. 4989-4991.

101. d'Auvergne, E.J. and P.R. Gooley, *Optimisation of NMR dynamic models I. Minimisation algorithms and their performance within the model-free and Brownian rotational diffusion spaces.* Journal of Biomolecular NMR, 2007. **40**(2): p. 107.

102. d'Auvergne, E.J. and P.R. Gooley, *Optimisation of NMR dynamic models II. A new methodology for the dual optimisation of the model-free parameters and the Brownian rotational diffusion tensor.* Journal of Biomolecular NMR, 2008. **40**(2): p. 121-33.

103. d'Auvergne, E.J. and P.R. Gooley, *The use of model selection in the model-free analysis of protein dynamics.* Journal of Biomolecular NMR, 2003. **25**(1): p. 25-39.

104. Andrec, M., G.T. Montelione, and R.M. Levy, *Estimation of Dynamic Parameters from NMR Relaxation Data using the Lipari–Szabo Model-Free Approach and Bayesian Statistical Methods.* Journal of Magnetic Resonance, 1999. **139**(2): p. 408-421.

105. Cavanagh, J., et al., *Protein NMR spectroscopy: principles and practice*. 1995: Elsevier.

106. Sahu, S.C., et al., *Backbone dynamics of free barnase and its complex with barstar determined by 15N NMR relaxation study.* Journal of Biomolecular NMR, 2000. **18**(2): p. 107-118.

107. Barbato, G., et al., *Backbone dynamics of calmodulin studied by nitrogen-15 relaxation using inverse detected two-dimensional NMR spectroscopy: the central helix is flexible.* Biochemistry, 1992. **31**(23): p. 5269-5278.

108. Muthu, D., et al., *NMR Studies of the Dynamics of Nitrophorin 2 Bound to Nitric Oxide.* Biochemistry, 2013. **52**(45): p. 7910-7925.

109. Akke, M., et al., *Effects of ion binding on the backbone dynamics of calbindin D9k determined by nitrogen-15 NMR relaxation.* Biochemistry, 1993. **32**(37): p. 9832-9844.

110. Fushman, D., O. Ohlenschläger, and H. Rüteijans, *Determination of the backbone mobility of ribonuclease T1 and its 2' GMP complex using molecular dynamics simulations and NMR relaxation data.* Journal of Biomolecular Structure and Dynamics, 1994. **11**(6): p. 1377-1402.

111. Fushman, D., *Determining protein dynamics from ^{15}N relaxation data by using DYNAMICS.* Methods in molecular biology (Clifton, N.J.), 2012. **831**: p. 485-511.

112. Loria, J.P., M. Rance, and A.G. Palmer, *A relaxation-compensated Carr− Purcell− Meiboom− Gill sequence for characterizing chemical exchange by NMR spectroscopy.* Journal of the American Chemical Society, 1999. **121**(10): p. 2331-2332.

113. Akke, M. and A.G. Palmer, *Monitoring macromolecular motions on microsecond to millisecond time scales by R1ρ− R1 constant relaxation time NMR spectroscopy.* Journal of the American Chemical Society, 1996. **118**(4): p. 911-912.

114. Korzhnev, D.M. and L.E. Kay, *Probing invisible, low-populated states of protein molecules by relaxation dispersion NMR spectroscopy: an application to protein folding.* Accounts of Chemical Research, 2008. **41**(3): p. 442-451.

115. Bouvignies, G., et al., *Solution structure of a minor and transiently formed state of a T4 lysozyme mutant.* Nature, 2011. **477**(7362): p. 111.

2. - ^{1}H, ^{15}N, ^{13}C backbone resonance assignments of human soluble catechol-*O*-methyltransferase in complex with S-adenosyl-L-methionine and 3,5-dinitrocatechol

Published in: Biomolecular NMR Assignments

First published: 15th December 2016

Authors: Sylwia Czarnota[a], Nicola J. Baxter[a,b], Matthew J. Cliff[a], Jonathan P. Waltho[a,b], Nigel S. Scrutton[a], Sam Hay[a]

[a]Manchester Institute of Biotechnology and School of Chemistry, The University of Manchester, 131 Princess Street, Manchester, M1 7DN, United Kingdom

[b]Krebs Institute for Biomolecular Research, Department of Molecular Biology and Biotechnology, The University of Sheffield, Firth Court, Western Bank, Sheffield, S10 2TN, United Kingdom

DOI: 10.1007/s12104-016-9720-9

Abstract

Catechol-*O*-methyltransferase (COMT) is an enzyme that plays a major role in catechol neurotransmitter deactivation. Inhibition of COMT can increase neurotransmitter levels, which provides a means of treatment for Parkinson's disease, schizophrenia and depression. COMT exists as two isozymes: a soluble cytoplasmic form (S-COMT), expressed in the liver and kidneys and a membrane-bound form (MB-COMT), found mostly in the brain. Here we report the backbone ^{1}H, ^{15}N and ^{13}C chemical shift assignments of S-COMT in complex with S-adenosyl-L-methionine, 3,5-dinitrocatechol and Mg^{2+}. Assignments were obtained by heteronuclear multidimensional NMR spectroscopy. In total, 97% of all backbone resonances were assigned in the complex, with 205 out of a possible 215 residues assigned in the ^{1}H-^{15}N TROSY spectrum. Prediction of solution secondary structure from a chemical shift analysis using the TALOS+ webserver is in good agreement with published X-ray crystal structures.

Keywords

Enzyme, S-adenosyl-L-methionine, Backbone resonance assignment, Transverse relaxation optimized spectroscopy, Triple-labelled Protein

Biological context

Catechol-*O*-methyltransferase (COMT, EC 2.1.1.6) is a ubiquitous bisubstrate magnesium-dependent enzyme found in plants, animals and microorganisms. It catalyses the transfer of a methyl group from S-adenosyl-L-methionine (SAM) to one of the hydroxyl oxygen atoms (preferentially the 3-hydroxyl) in a catechol substrate [1]. Physiological substrates of COMT are catecholamine neurotransmitters such as dopamine, noradrenaline, adrenaline and their metabolites. COMT also methylates catecholic steroids such as 2-hydroxyestradiol as well as a range of other catecholic compounds including neuroactive drugs such as L-dopa, α-methyldopa and isoproterenol [2-4]. COMT inhibition is a means of treating Parkinson's disease, schizophrenia and depression [5-7]. There are two isoforms of human COMT: soluble cytoplasmic COMT (S-COMT), which is mainly intracellular, and a membrane-bound form (MB-COMT), which has a single-span helix contained within a 50 amino acid extension at the N-terminus. Genetic studies have demonstrated that both soluble and membrane-bound isoforms of human COMT are coded by a single gene, using two separate promoters, assigned to chromosome 22q11.2 [8]. However, S-COMT possesses

K_m values for catecholamines that are ~15 times higher than those reported for MB-COMT, and in addition has a lower affinity for the SAM cofactor [9]. Several X-ray crystal structures have been solved for COMT enzymes from a range of organisms together with different substrate / inhibitor complexes. S-COMT has a single domain α/β-folded structure with eight α-helices and seven β-sheets. The N-terminal region is composed of three α-helices, the central section has five α-helices arranged around a 5-stranded parallel β-sheet, while the C-terminal part consists of two antiparallel β-strands. The active site is located on the outer surface of the enzyme and includes a SAM binding pocket and a substrate binding site situated in the vicinity of a bound catalytic Mg^{2+} ion [10].

Methods and experiments

Protein expression and purification

The human S-COMT construct used in this study has a 12 residue hexa-histidine tag and cloning sequence positioned at the N-terminus (MHHHHHHENLYFQG…). The canonical S-COMT sequence begins at Q1 and here the canonical S-COMT numbering system is used throughout. This construct also contains valine (rather than methionine) at the allelic polymorphism position located at residue 108 of S-COMT [11, 12]. A synthetic, codon-optimised human S-COMT gene cloned into a pEX-A2 plasmid was purchased from Eurofins Genomics. This gene was then cloned into a pET21a plasmid for expression purposes. ^{2}H,^{15}N,^{13}C-labelled protein was expressed using *E. coli* strain BL21(DE3) (Stratagene) in a defined isotopically labelled minimal medium, following the protocol of Reed et al. (2003). The cells were grown at 37 ºC with shaking until $A_{600\ nm}$ reached 0.6-0.8, were cooled to 30 ºC and induced by adding isopropyl-β-D-thiogalactopyranoside (IPTG) to a final concentration of 0.4 mM. Cells were harvested 12-14 hours after induction using centrifugation at ~6,000 rpm for 20 minutes at 4 ºC. The cell pellet was collected and stored at -20 ºC until further use. All purification steps were performed at 4 ºC. Harvested cells were allowed to thaw and were then resuspended in cell lysis buffer comprising 50 mM sodium phosphate, 300 mM NaCl, 10 mM imidazole, pH 7.4 and containing cOmplete™, Mini, EDTA-free protease inhibitor tablets (Roche) (1 tablet per 50 mL of buffer), 10 µg/mL DNase and 10 mM $MgCl_2$. Cells at a concentration of ~100 mg of cell pellet/mL were lysed on ice by sonication for 15 cycles of pulsation for 15 seconds with 45 second intervals. The cell

extract was then separated by ultracentrifugation at ~48,000 *g* (20,000 rpm) for 30 min at 4 ºC in a Beckman Coulter J26-XP Avanti centrifuge using rotor JA 25.50. The supernatant was then filtered using 0.45 µm syringe filters (Sartorius Mechatronics UK Ltd) before loading onto a 5 mL His-Trap FF affinity Ni-sepharose column (GE Healthcare) connected to an AKTA purification system (GE Healthcare) that had been previously washed with at least 5 column volumes of filtered and degassed water and equilibrated by washing with 10 column volumes of filtered and degassed cell lysis buffer. Proteins bound to the Ni resin were eluted with a gradient of 10-300 mM imidazole in cell lysis buffer over 16 column volumes or with a 2-step elution comprising 8 column volumes of 10 mM imidazole in cell lysis buffer and then 8 column volumes of 300 mM imidazole in cell lysis buffer. Fractions showing S-COMT content, observed as a peak in UV absorbance at 280 nm, were pooled, checked for purity by SDS-PAGE, concentrated by VivaSpin (10,000 MWCO, GE Healthcare) and loaded onto a Superdex 75 26/60 size exclusion column (Fisher Scientific) connected to an AKTA purification system. The column was washed with at least 1.5 column volumes of filtered and degassed water and equilibrated with 2 column volumes of filtered and degassed gel filtration buffer (50 mM Tris-HCl buffer pH 7.5 containing 50 mM NaCl and 10 mM DTT) prior to use. S-COMT was eluted with 2 column volumes of gel filtration buffer, and then checked for purity by SDS-PAGE. Chromatograms (280 nm detection) monitoring the size exclusion purification show two separated peaks, which correspond to monomeric and dimeric S-COMT as confirmed by native gel electrophoresis and mass spectrometry (not shown). The fraction of monomer was typically 40-80% of total purified S-COMT. The monomeric form of the protein was used for further investigations. Once purified, back exchange to amide protium atoms in perdeuterated S-COMT was promoted by overnight incubation in 50 mM Tris-HCl, 10 mM DTT, pH 9.0 at 25 ºC, followed by VivaSpin-mediated buffer exchange at 4 ºC into 50 mM Tris-HCl, 10 mM DTT, 50 mM NaCl, pH 7.5. Protein concentrations were estimated by absorbance at 280 nm measured with a NanoDrop (ε_{280} = 24785 M^{-1} cm^{-1}) and Bio-Rad protein concentration assays, following the manufacturers' protocols. NMR experiments were performed on S-COMT samples obtained within 1 day of purification. The stable isotopically-labelled compounds $^{15}NH_4Cl$ (99%), $^{13}C_6$,$^{2}H_7$-D-Glucose (U-$^{13}C_6$, 99%; 1,2,3,4,5,6,6-d_7 97-98%) and $^{2}H_2O$ (99.8%) were purchased from Goss Scientific. All other reagents, including S-adenosyl-L-methionine (SAM)

and 3,5-dinitrocatechol (DNC) were purchased with the highest purity available from Sigma-Aldrich (Dorset, UK) and used as received.

NMR experiments

All NMR measurements were performed at 298 K, using standard pulse sequences on an 800 MHz Bruker Avance III NMR spectrometer fitted with a TCI cryoprobe equipped with Z gradients and TopSpin software version 3.2 housed in the Manchester Institute of Biotechnology. NMR samples containing 0.5 mM ^{2}H,^{15}N,^{13}C-labelled human S-COMT, 5 mM SAM, 5 mM DNC and 2.5 mM $MgCl_2$ in 50 mM Tris-HCl buffer, 50 mM NaCl, 10 mM DTT, 2 mM NaN_3, pH 7.5 were loaded into 5-mm diameter NMR tubes. $^{2}H_2O$ was added to the protein samples (10% v/v) to allow a deuterium lock and 0.5% v/v trimethylsilyl propanoic acid (TSP) was added as a reference signal. ^{1}H chemical shifts were referenced relative to the internal TSP signal, whereas ^{15}N and ^{13}C chemical shifts were indirectly referenced using nuclei-specific gyromagnetic ratios. For the backbone ^{1}H, ^{15}N and ^{13}C resonance assignment, standard Bruker ^{1}H-^{15}N TROSY and TROSY-based 3D HNCA, HNCACB, HN(CO)CACB, HN(CA)CO and HNCO spectra were acquired using non-uniform sampling with a multidimensional Poisson Gap scheduling strategy with sinebell weighting [13]. A 30 Hz (0.4 ppm) resolution in the carbon dimension was obtained after processing. The HNCO spectrum, with one peak per residue in the carbon dimension was obtained with 230 hypercomplex points, whereas spectra with two peaks per residue (HNCA, HN(CO)CACB, HN(CA)CO) were obtained with 460 hypercomplex points and the HNCACB spectrum with four peaks per residue was obtained with 920 hypercomplex points.

Resonance assignments and data deposition

Backbone $^{1}H_N$, ^{15}N, $^{13}C_\alpha$, $^{13}C_\beta$ and $^{13}C'$ chemical shifts were assigned for S-COMT in the S-COMT:SAM:DNC:Mg^{2+} complex using standard triple resonance methodology [14]. Spectra were processed with TopSpin software version 3.2. Peak picking and frequency matching was performed within CCPNMR Analysis version 2.4 [15] and the backbone assignments were checked independently using a simulated annealing algorithm employed by the "asstools" assignment program [16]. The backbone ^{1}H, ^{15}N

and ^{13}C chemical shifts have been deposited in the BioMagResBank (http://www.bmrb.wisc.edu/) under the BMRB accession code 26848.

Excluding the ten proline residues and the first eight residues of the N-terminal cloning tag from the 233-residue S-COMT protein sequence, 205 out of a total of 215 residues were assigned in the ^{1}H-^{15}N TROSY spectrum of the S-COMT:SAM:DNC:Mg^{2+} complex (**Figure 1**). In total, 97% of all backbone resonances were assigned (95% of $^{1}H_N$, 95% of ^{15}N, 98% of $^{13}C_\alpha$, 97% of $^{13}C_\beta$ and 98% of $^{13}C'$ nuclei). There is evidence for exchange dynamics occurring on a slow NMR timescale due to the presence of duplicate spin systems in the ^{1}H-^{15}N TROSY and 3D correlation spectra. *Cis-trans* proline isomerisation at P221 is the most likely source of conformational dynamics responsible for spin system duplication at A219 and G220. There is also spin system duplication for Q1 and G2, where the cloning tag meets the S-COMT sequence.

There are ten residues that remain unassigned in the ^{1}H-^{15}N TROSY spectrum (D3, G43, D44, G47, V53, Q58, M76, G83, S187 and G214). From the crystal structure (PDB: 3BWM; [17], **Figure 2**), D3, Q58, G83, S187 and G214 are located at the surface of the protein, mostly in solvent exposed loops, and as a consequence the ^{1}H-^{15}N TROSY correlations are likely to be attenuated beyond detection by fast exchange with solvent. Several residues in the third α-helix (G43-Q58) and fourth α-helix (G70-R78) have ^{1}H-^{15}N TROSY peak intensities that are broadened by conformational exchange; specifically these are: K48, I49, D51, I54, E56, V74, R75 and A77. Such exchange behaviour points to dynamics occurring on the millisecond timescale in this region of the protein, which are the likely source of the broadening beyond detection of the ^{1}H-^{15}N TROSY correlations of G43, D44, G47, V53 and M76. An overlay of S-COMT crystal structures (PDB: 4PYI, 3A7E, 3BWM, 4PYQ, 4P7J) shows that the last turn of the second α-helix (C33-K36) and the first turn of the third α-helix (G43-K46) have positional heterogeneity resulting from the active site loop (E37-V42) occupying alternative conformations. One consequence of these conformational differences requires that the sidechain donors of R75 coordinate the sidechain acceptors of D44 and D51 differently, which might account for the exchange broadening behaviour observed for these residues, together with residues in their immediate vicinity.

The secondary structure content of S-COMT was predicted by uploading the backbone $^{1}H_N$, ^{15}N, $^{13}C_\alpha$, $^{13}C_\beta$ and $^{13}C'$ chemical shifts of the S-COMT:SAM:DNC:Mg^{2+} complex

to the TALOS+ webserver (Shen et al. 2009). **Figure 3** compares the predicted secondary structure for the solution complex with the secondary structure observed in the crystal form of the complex. These data are in very good agreement, which indicates that the solution conformation is very similar to the protein structure observed in crystals, and provides confidence in the assignments of the S-COMT:SAM:DNC:Mg^{2+} complex.

Acknowledgements

This research was supported by a European Commission Marie Curie Fellowship (S.C. Grant number: PITN-GA-2013-ITN 606831) and the Biotechnology and Biological Sciences Research Council (N.J.B. Grant number: BB/M021637/1). N.S.S. received funding as an Engineering and Physical Sciences Research Council (EPSRC) Established Career Fellow (EP/J020192/1).

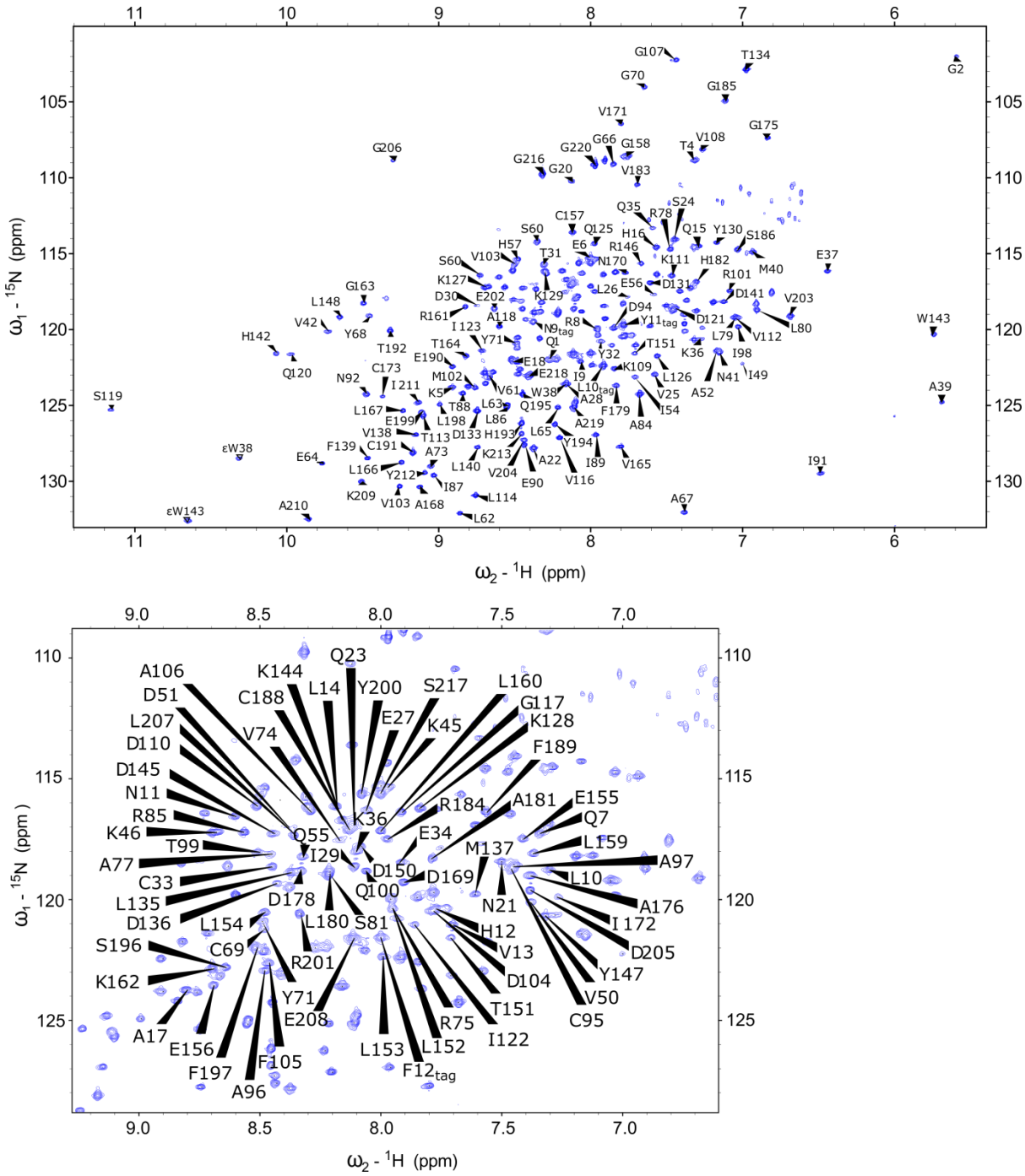

Figure 1. 2D ^{1}H-^{15}N TROSY spectrum of the human S-COMT:SAM:DNC:Mg^{2+} complex recorded at pH 7.5 and 298 K. The assignments of backbone amide resonances are indicated by residue type and sequence number, following the canonical S-COMT nomenclature. Residues of the cloning sequence are referred to by their residue type and position in the cloning tag together with a tag indicator (e.g. $N9_{tag}$).

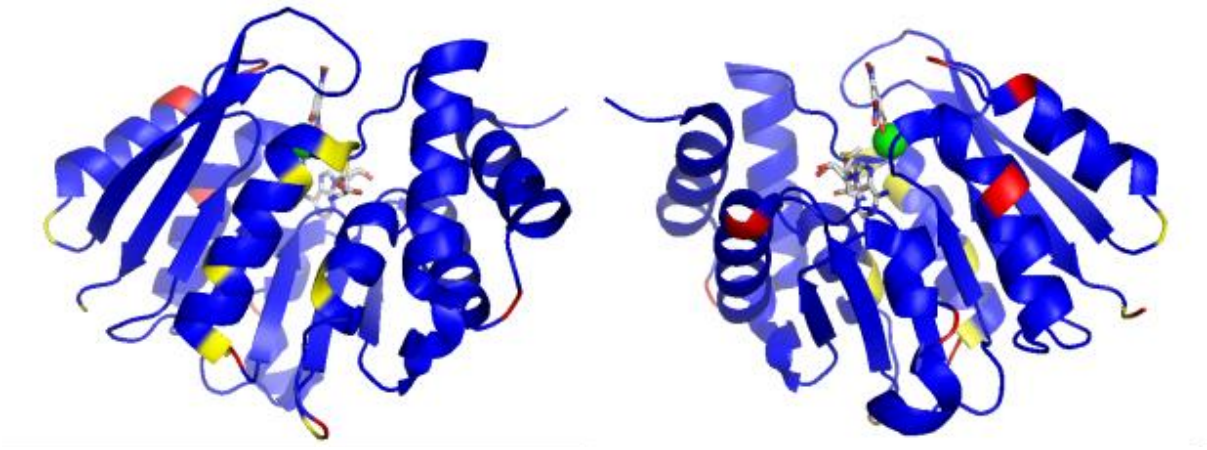

Figure 2. Two orthogonal representations of the backbone assignments mapped onto the X-ray crystal structure of the human S-COMT:SAM:DNC:Mg^{2+} complex (PDB: 3BWM; [17]). Assigned residues are coloured blue, proline residues are coloured red, and all unassigned residues are coloured yellow. SAM and DNC are shown as CPK-coloured sticks and the magnesium ion is indicated as a green sphere.

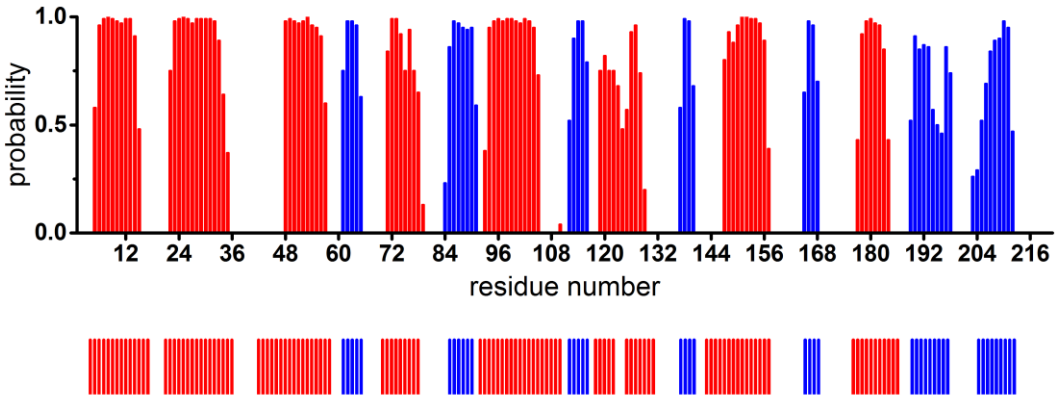

Figure 3. Backbone secondary structure prediction of S-COMT in the S-COMT:SAM:DNC:Mg^{2+} complex obtained with TALOS+ [18] using the backbone $^{1}H_{N}$, ^{15}N, $^{13}C_{\alpha}$, $^{13}C_{\beta}$ and $^{13}C'$ chemical shifts. The secondary structure prediction is shown as red bars for α-helices and blue bars for β-strands, with the height of the bars representing the probability of the secondary structure assigned by the software. The secondary structure derived from the X-ray crystal structure of the human S-COMT:SAM:DNC:Mg^{2+} complex (PDB: 3BWM; [17]) is reported below the panel in the same colour representation.

References

1. Mannisto, P.T. and S. Kaakkola, *Catechol-O-methyltransferase (COMT): biochemistry, molecular biology, pharmacology, and clinical efficacy of the new selective COMT inhibitors.* Pharmacological Reviews, 1999. **51**(4): p. 593-628.
2. Ball, P., et al., *Interactions Between Estrogens and Catechol Amines III. Studies on the Methylation of Catechol Estrogens, Catechol Amines and other Catechols by the Catechol-O-Methyltransferase of Human Liver.* The Journal of Clinical Endocrinology & Metabolism, 1972. **34**(4): p. 736-746.
3. Borchardt, R.T., *N-and O-methylation.* Enzymatic basis of detoxication, 1980. **2**: p. 43-62.
4. Guldberg, H.C. and C.A. Marsden, *Catechol-O-methyl transferase: pharmacological aspects and physiological role.* Pharmacological Reviews, 1975. **27**(2): p. 135-206.
5. Fava, M., et al., *Open study of the catechol-O-methyltransferase inhibitor tolcapone in major depressive disorder.* Journal of Clinical Psychopharmacology, 1999. **19**(4): p. 329-35.
6. Harrison, S.T., et al., *Synthesis and Evaluation of Heterocyclic Catechol Mimics as Inhibitors of Catechol-O-methyltransferase (COMT).* American Chemical Society Medicinal Chemistry Letters, 2015. **6**(3): p. 318-23.
7. Kiss, L.E. and P. Soares-da-Silva, *Medicinal chemistry of catechol O-methyltransferase (COMT) inhibitors and their therapeutic utility.* Journal of Medicinal Chemistry, 2014. **57**(21): p. 8692-717.
8. Tenhunen, J., et al., *Genomic organization of the human catechol O-methyltransferase gene and its expression from two distinct promoters.* European Journal of Biochemistry, 1994. **223**(3): p. 1049-59.
9. Lotta, T., et al., *Kinetics of human soluble and membrane-bound catechol O-methyltransferase: a revised mechanism and description of the thermolabile variant of the enzyme.* Biochemistry, 1995. **34**(13): p. 4202-10.
10. Vidgren, J., L.A. Svensson, and A. Liljas, *Crystal structure of catechol O-methyltransferase.* Nature, 1994. **368**(6469): p. 354-8.
11. Lachman, H.M., et al., *Association of codon 108/158 catechol-O-methyltransferase gene polymorphism with the psychiatric manifestations of velo-cardio-facial syndrome.* American Journal of Medical Genetics, 1996. **67**(5): p. 468-72.
12. Rutherford, K., et al., *The V108M mutation decreases the structural stability of catechol O-methyltransferase.* Biochimica and Biophysica Acta, 2008. **1784**(7-8): p. 1098-105.
13. Hyberts, S.G., S.A. Robson, and G. Wagner, *Exploring signal-to-noise ratio and sensitivity in non-uniformly sampled multi-dimensional NMR spectra.* Journal of Biomolecular NMR, 2013. **55**(2): p. 167-78.
14. Gardner, K.H. and L.E. Kay, *The use of 2H, 13C, 15N multidimensional NMR to study the structure and dynamics of proteins.* Annual Review of Biophysics and Biomolecular Structure, 1998. **27**: p. 357-406.

15. Vranken, W.F., et al., *The CCPN data model for NMR spectroscopy: development of a software pipeline.* Proteins, 2005. **59**(4): p. 687-96.

16. Reed, M.A., et al., *Effects of domain dissection on the folding and stability of the 43 kDa protein PGK probed by NMR.* Journal of Molecular Biology, 2003. **330**(5): p. 1189-201.

17. Rutherford, K., et al., *Crystal structures of human 108V and 108M catechol O-methyltransferase.* Journal of Molecular Biology, 2008. **380**(1): p. 120-30.

18. Shen, Y., et al., *TALOS+: a hybrid method for predicting protein backbone torsion angles from NMR chemical shifts.* Journal of Biomolecular NMR, 2009. **44**(4): p. 213-23.

3. - Active site compaction and electrostatic reorganisation in catechol-*O*-methyltransferase

Authors: Sylwia Czarnota[a,b], Linus O. Johannissen[a], Nicola J. Baxter[c], Alex L. Wilson,[a,b] Matthew J. Cliff[a], Colin W. Levy[a], Nigel S. Scrutton[a,b], Jonathan P. Waltho[a,b,c], Sam Hay[a,b]*

[a]Manchester Institute of Biotechnology and [b]School of Chemistry, The University of Manchester, 131 Princess Street, Manchester, M1 7DN, United Kingdom

[c]Krebs Institute for Biomolecular Research, Department of Molecular Biology and Biotechnology, The University of Sheffield, Firth Court, Western Bank, Sheffield, S10 2TN, United Kingdom

Abstract

Catechol-*O*-methyltransferase (COMT) is a model S-adenosyl-L-methionine (SAM) dependent methyl transferase, which catalyzes the methylation of catecholamine neurotransmitters such as dopamine in the primary pathway of neurotransmitter deactivation in animals. Despite extensive study, there is no consensus view of the physical basis of catalysis in COMT. Further progress requires new experimental data that directly probes active site geometry, protein dynamics and electrostatics, ideally in a range of positions along the reaction coordinate. Here we establish that sinefungin, a fungal-derived inhibitor of SAM-dependent enzymes that possesses transition state-like charge on the transferring group, can be used as a transition state analog. X-ray crystal structures and NMR backbone assignments of the ternary complexes of the soluble form of human COMT containing dinitrocatechol Mg^{2+} and both SAM and sinefungin were determined. Comparison and further analysis with the aid of density functional theory calculations and molecular dynamics simulations provides evidence for active site "compaction", which is driven by electrostatic stabilization between the transferring methyl group and "equatorial" active site residues that are orthogonal to donor–acceptor (pseudo reaction) coordinate. We propose that upon catecholamine binding the enzyme becomes geometrically preorganized, with little further movement along the donor–acceptor coordinate required for methyl transfer. Catalysis is then facilitated through stabilization of the developing charge on the transferring methyl group *via* equatorial H-bonding and electrostatic interactions, primarily with residues Asp141 and Met40.

Introduction

S-Adenosyl-L-methionine (SAM) dependent methyltransferases (MTases) are ubiquitous bisubstrate Mg^{2+}-dependent enzymes found in plants, animals and microorganisms. Catechol *O*-methyltransferase (COMT) is an archetypal MTase, which catalyzes the methylation of catecholamine neurotransmitters such as dopamine in the primary pathway of neurotransmitter deactivation in animals. Consequently, inhibition of COMT is a key strategy for the treatment of a range of neurological disorders including Parkinson's disease [1-3]. COMT also has potential as a biocatalyst for regiospecific alkylation reactions [4, 5], and has long served as a model MTase enzyme. In this family of enzymes, methyl transfer is proposed to occur by a common S_N2 mechanism with nucleophilic attack on the SAM methyl group from the methyl

accepting substrate (catechol hydroxyl in COMT). The Mg^{2+} is bound between the catechol oxygens, facilitating deprotonation of the catechol in order to render it a more potent nucleophile. The transferring methyl group proceeds with net inversion of configuration, adopting an sp^2-like geometry in the transition state (TS; **Figure 1**). For COMT, the catalytic enhancement has been estimated from experimental data to be on the order of 10^9 to 10^{16} [6, 7].

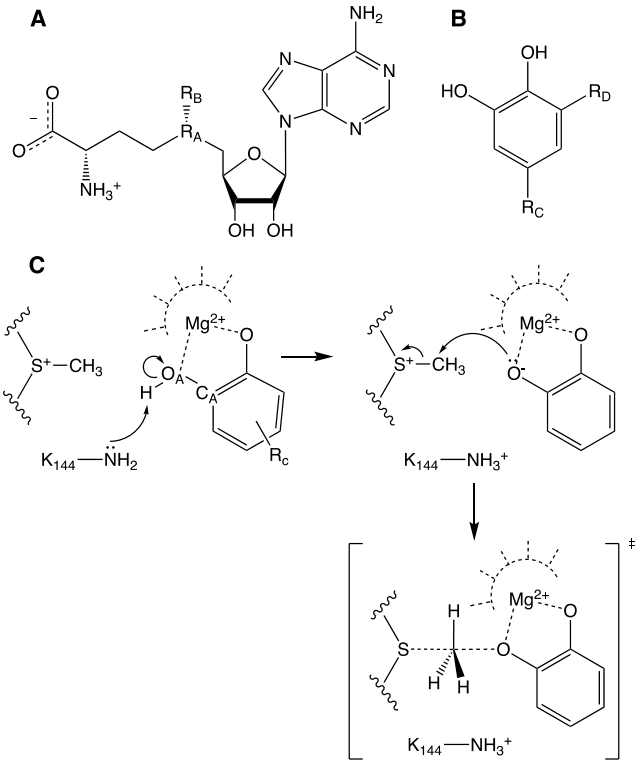

Figure 1. A) The structures of A, S-Adenosyl-L-methionine (SAM, $R_A = S^+$, $R_B = CH_3$) and sinefungin ($R_A = CH$, $R_B = NH_3^+$); B) 3,5-dinitrocatechol (DNC, $R_C = R_D = NO_2$) and dopamine ($R_C = -CH_2CH_2NH_2$, $R_D = H$). C) The proposed mechanism of SAM demethylation catalyzed by COMT. For many catecholamine substrates both oxygens can act as the methyl acceptor, with the stereochemistry determined by the catecholamine binding pose; the oxygen closer to the transferring methyl is the acceptor.

A major feature of the COMT reaction is that the reactant state comprises oppositely charged reactants, which combine to form neutral products; *i.e.* a CH_3^+ group is formerly transferred. This might suggest that electrostatics (pre-/re-organization) should play a major role in the reaction, as has been argued by some [8]. However, kinetic isotope effect (KIE) measurements from the Schowen group in the late 1970s showed an unusually large and inverse CH_3/C^2H_3 KIE of ~0.8 for the COMT reaction [9] with much smaller KIEs observed on uncatalyzed model methyl transfer reactions [7]. These data, alongside more recent KIE measurements from the Klinman group showing a

correlation between k_{cat}/K_m and CH_3/C^3H_3 KIEs on the COMT reaction [10], have been used as evidence for the role of active site compression or 'compaction' during the reaction [7, 11]; essentially the squeezing together of the reacting methyl donor and acceptor moieties, which promotes the reaction. This description is couched within the framework of the 'promoting vibration' hypothesis, which has been used to interpret isotope effects on H-transfer reactions [12-14]. The unusual deuterium KIE on the COMT reaction has also received much attention from the computational community, with a number of proposals put forward to describe catalysis by COMT. Ground state near attack conformers (NACs) have been proposed by Bruice [15, 16], whereas Warshel has recently argued against compaction and NACs in favor of electrostatic preorganization [8]. Williams and colleagues also saw no evidence for compaction [6, 17, 18] and highlighted the role of equatorial H-bonding to the transferring methyl group [19]. Finally, Klinman and Martinez recently observed a trend in donor–acceptor distance in the ground state that they correlate with catalytic efficiency, in favor of the compaction hypothesis [10, 11].

It would appear that there is no consensus view of the physical basis of catalysis in COMT. A major issue is that computational studies are based on relatively few experimental data: X-ray crystal structures of non-reactive inhibitor (e.g. DNC; **Figure 1**) and drug complexes, KIE measurements of COMT and reference reactions and steady state inhibition assays [20]. We suggest that progress towards a consensus description of catalysis by COMT, and by extension the MTase enzyme family, requires new experimental data that directly probes active site geometry, protein dynamics and electrostatics, ideally in a range of poses along the reaction coordinate; at a minimum the reactant state and TS.

Sinefungin (adenosyl-L-ornithine), a fungal-derived inhibitor of SAM-dependent MTases [21], is non-reactive SAM-analogue with an amine group in place of the transferring methyl group (**Figure 1A**). As the amine (R_B) group is likely to be protonated [22], it will have a more TS-like charge distribution than SAM. Sinefungin derivatives are also known to be good TS analogues of the SAM-dependent lysine methyl transferase [23], so ternary complexes of COMT containing sinefungin, Mg^{2+} and an appropriate catecholamine should provide a means to probe COMT in a more TS-like conformation. X-ray crystal structures of sinefungin complexes of MTases have been solved including rat (PDB 4P7K) and "humanized" rat (PDB 4PYL) COMT [24].

Here we have determined the X-ray crystal structures and NMR backbone assignments of the ternary complexes of the soluble form of human COMT (S-COMT) containing DNC, Mg^{2+} and both SAM and sinefungin. These complexes are compared and further analyzed with the aid of density functional theory (DFT) calculations and molecular dynamics (MD) simulations. We find evidence for active site compaction and propose that this is driven by H-bonding between the transferring methyl group and "equatorial" active site residues, rather than by "pushing" along the donor–acceptor axis.

Results and discussion

If the charge distribution of sinefungin is similar to that of SAM in the TS of the COMT reaction, we reasoned that it would be possible to experimentally probe how COMT reorganizes during the reaction by comparing equivalent ternary complexes containing sinefungin and SAM. If sinefungin only contains partial TS character, this doesn't invalidate this approach as the sinefungin complex will represent a reactant pose that is positioned along the reaction coordinate between the ground state and TS (or further) and any conformational change/reorganization that occurs between the two complexes is likely to be relevant to catalysis.

We screened a range of catecholamine substrates and inhibitors and were able to obtain crystals of S-COMT complexes containing Mg^{2+}, DNC and both sinefungin and SAM. These diffracted to 1.3-1.5 Å and the structures were readily solved by molecular replacement (**Figure 2** and **Table S1** in the supporting information (SI)). The sinefungin complex crystallized as a dimer while the SAM complex crystallized as a monomer (see also **Figure S1** in the SI), but the structures are largely superimposable and are similar to existing structures of S-COMT containing SAM and DNC (e.g. PDB 3BWM [25]). The two sinefungin monomers are not identical, but are very similar, with key active site distances differing by <0.03 Å (**Table 1**, **Figure S2** in the SI). S-COMT is known to dimerize [26] and it would appear that the dimer observed here is likely to be functional and/or a crystallographic artefact.

Within the respective ternary complexes, SAM and sinefungin adopt very similar conformations and the only significant difference is the position of the DNC, which is closer to the sinefungin than SAM (**Figure 2**; **Table 1**). This may arise, in part, as the C–NH_3 bond of sinefungin is significantly shorter than the S–CH_3 bond of SAM (**Table 1**). Nevertheless, the distances between the acceptor oxygen and transferring CH_3 or

NH_3 and between the donor (sulfur/CH) and acceptor (oxygen) are shorter by ~0.1 Å and 0.35 Å, respectively, in the sinefungin complex and this movement is consistent with the catecholamine moving towards the SAM in the TS to facilitate O–CH_3 bond formation.

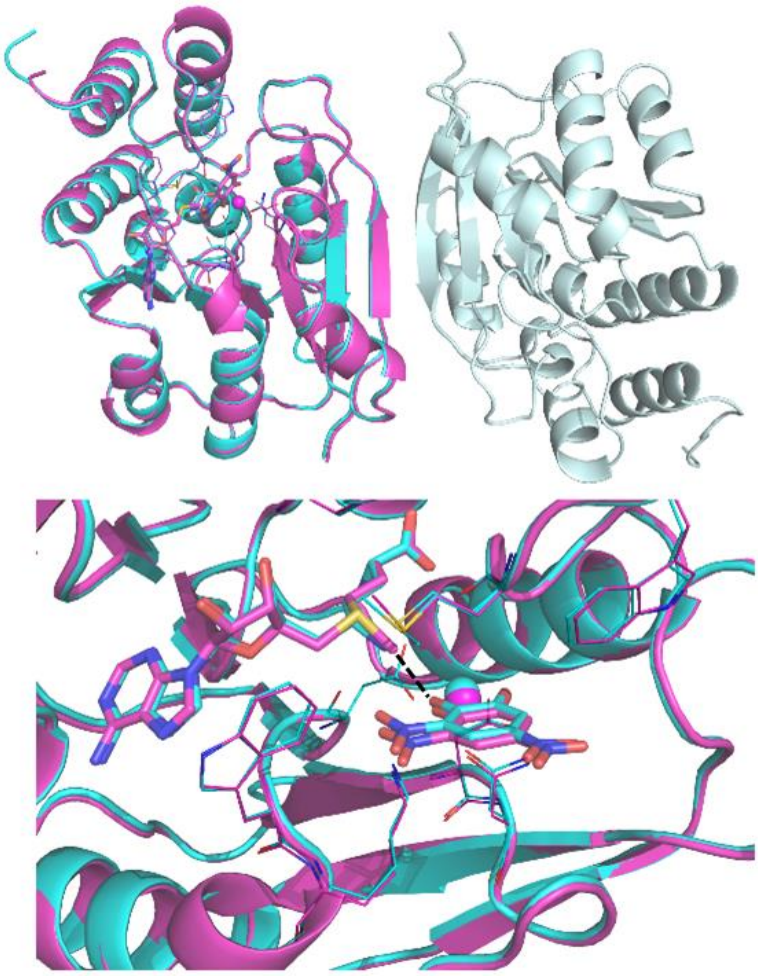

Figure 2. X-ray crystal structures of S-COMT ternary complexes containing DNC, Mg^{2+} and either SAM (magenta; PDB: 6I3C) or sinefungin (cyan, light green; PDB: 6I3D). Structures are aligned over all atoms and the bottom panel shows an overlay of the active site region with selected residues displayed as wireframes, SAM, sinefungin, and DNC shown as sticks and the Mg^{2+} ion indicated as a sphere. The O–CH_3 distance is indicated with a dashed black line.

Table 1. Key reactant distances (*R*) and angles (*A*)[a] observed in the X-ray crystal structures in Figure 2 and Figure S2 in the SI.

	ternary complex	
	SAM	sinefungin[b]
R(D-A), Å	4.57	4.20, 4.22
R(X-A), Å	2.81	2.71, 2.74
R(D-X), Å	1.78	1.51, 1.50
A(D-X-A), ^{o}	168.9	169.7, 169.3
A(X-A-C_A), ^{o}	113.6	115.1, 117.2

[a]D, donor; A, acceptor; X, transferring group (CH_3 or NH_3); C, DNC C_A (Figure 1); [b]measured in chain A and chain B, respectively.

As the reaction apparently occurs via an S_N2 mechanism, the angle between the donor sulfur, transferring methyl carbon and acceptor oxygen should be ~180° in the transition state. This angle is slightly larger in the sinefungin complex than the SAM complex, but the difference is not likely to be significant and as this angle is almost 170°, there is minimal reorganization required to achieve an ideal S_N2 geometry. Similarly, the angle formed between the transferring group, catecholamine acceptor oxygen and catecholamine C_A (**Figure 1**) should ultimately be ~120°. It is ~115° and again is slightly larger in the sinefungin complex. Together, these data show a highly preorganized active site with only minimal rearrangement of substrate (catecholamine) required to reach the anticipated TS geometry. However, X-ray crystallography may not have sufficient resolution to resolve subtle protein reorganization, so we next turned to NMR to further probe these complexes.

We have previously reported the backbone ^{1}H, ^{15}N and ^{13}C NMR chemical shift assignments of the S-COMT:SAM:DNC:Mg^{2+} ternary complex [26]. We used the same approach here to determine the equivalent assignments in the S-COMT:sinefungin:DNC:Mg^{2+} ternary complex. The S-COMT construct contains 233 residues, and excluding the 10 proline residues and 8 residues of the N-terminal His-tag

there are 215 observable residues. 204 of these residues were assigned in the ^{1}H-^{15}N TROSY spectrum of the sinefungin complex (**Figure S3** in the SI). Protein secondary structure prediction using the backbone $^{1}H_N$, ^{15}N, $^{13}C_\alpha$, $^{13}C_\beta$ and $^{13}C'$ chemical shifts and the TALOS+ and TALOS-N algorithms [27, 28] is consistent with the solution conformation being very similar to both our, and previous, X-ray crystal structures (**Figure S4** in the SI) [25], thus providing confidence in the NMR assignment.

Comparison of the differences in NMR chemical shifts between assigned residues in the SAM and sinefungin ternary complexes allows changes in the local environment of the protein backbone to be determined. **Figure 3** shows the residue-by-residue difference in amide nitrogen chemical shift between the two complexes. These can be mapped onto the X-ray crystal structure and most differences are seen to be in the active site. A similar pattern is observed when analyzing the equivalent differences in H, Cα, Cβ, C′ and N-H chemical shifts (**Figure S5** in the SI).

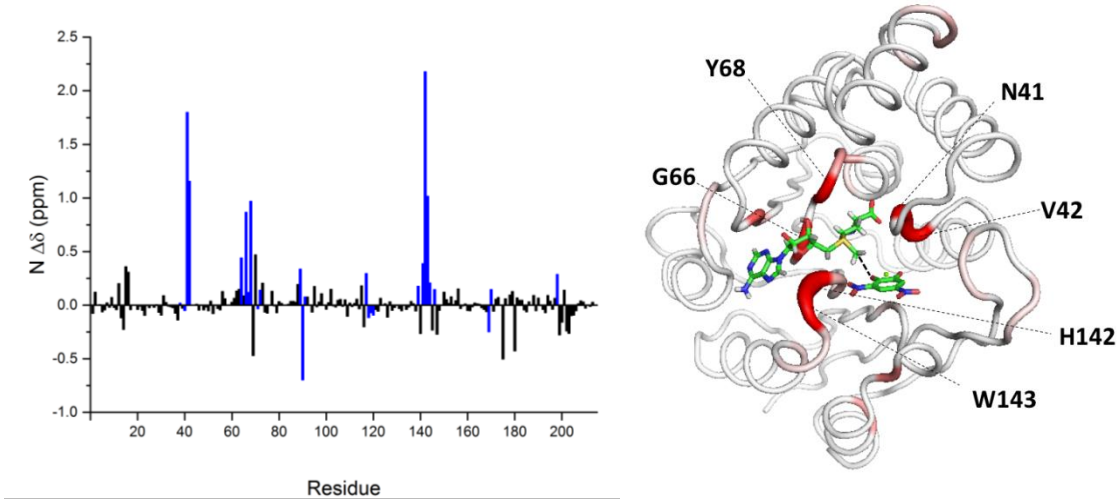

Figure 3. Differences in NMR chemical shift of the backbone amide N atoms between the S-COMT:SAM:DNC:Mg^{2+} and S-COMT:sinefungin:DNC:Mg^{2+} ternary complexes shown as a function of residue number (left) and as a putty diagram rendered on the X-ray crystal structure of the SAM complex (right). Active site residues within 4 Å of the SAM or DNC are shown as blue bars in (A) and the putty diagram is colored from low (white) to high (red) difference in chemical shift. O–CH_3 distance between SAM and DNC indicated with dashed black line. The equivalent differences in H_N, Cα, Cβ, C′ and N-H chemical shifts are shown in **Figure S5** in the SI.

The largest backbone amide N chemical shift differences observed are in the backbone of the following residues: V42, which is hydrogen-bonded to the carboxyl oxygens of

SAM/sinefungin and the neighboring N41 and M40 residues, which are also in close proximity to the transferring methyl group; Y68, which is positioned behind the SAM sulfur (relative to the transferring group) and the neighboring G66 and A67 residues; H142 and W143, which are both in van der Waals contacts with the adenine moiety of SAM; and D141, which is hydrogen-bonded to the amino group of the methionine moiety of SAM and also coordinates the Mg^{2+} ion. These chemical shift differences can all be rationalized in terms of subtle conformational differences in the active sites of the two ternary complexes and may not be expected to be observed in the comparison of ~1.4 Å resolution X-ray crystal structures (as in **Figure 2**). To extend this analysis, we next turned to computational chemistry.

Firstly, an active site "cluster" model was created to allow a comparison of the sinefungin complex to a model of the *bone fide* TS. The model was based on the X-ray crystal structure of the SAM ternary complex (**Figure S6** in the SI) and contained catechol in place of the non-reactive DNC, comprising 586 atoms with SAM and 587 atoms with sinefungin (the DFT models are described further in the SI). An approximate TS was determined for the reaction by performing a partially relaxed scan and the potential energy barrier was found to be 66 kJ mol^{-1}, which is in excellent agreement with the whole-enzyme QM/MM barrier of 67 kJ mol^{-1} recently obtained by Kulik et al [29].

Next, models were built containing DNC, Mg^{2+} and SAM or sinefungin. For methyl transfer from SAM to catechol, the donor-acceptor distance (SAM sulfur–catechol acceptor oxygen) decreases by 0.2 Å between the reactant state and TS. Comparison of the DNC cluster models (**Table 2** and **Figure S6** in the SI) showed that the donor-acceptor distance is also 0.2 Å shorter in the sinefungin complex relative to the SAM complex, suggesting that the sinefungin complex adopts a more TS-like geometry. Additionally, these models support the protonation state of the sinefungin NH_3^+ group, as replacing this with NH_2 causes a significant shift in the position of DNC that is inconsistent with the crystal structure (**Figure S6d** in the SI). Further, the differences in charge distribution between the reactant state and TS of the SAM-catechol model is qualitatively similar to the difference in charge distribution of the SAM and sinefungin DNC models; *i.e.* the positive charge that develops on the transferring SAM methyl group is similar to that observed on the sinefungin NH_3 group (**Table 2**). However, the partial charge on the sinefungin NH_3 is larger than that on the SAM CH_3 in the TS,

suggesting that any resulting protein electrostatic rearrangement upon sinefungin binding may be somewhat greater than for the actual reaction. Nevertheless, these calculations further suggest that the COMT:sinefungin:DNC:Mg^{2+} ternary complex has considerable TS character, both in terms of geometry and electrostatics.

MD simulations were performed on the S-COMT:SAM:DNC:Mg^{2+} and S-COMT:sinefungin:DNC:Mg^{2+} ternary complexes, using the X-ray crystal structures as input structures. DFT cluster models were used to parameterize the substrates and octahedral Mg^{2+} (see SI for details) and the sinefungin complex was treated as a monomer to aid in the comparison with the SAM complex. Simulations were typically run for 50-100 ns using the Amber 14 forcefield. To check the consistency between NMR, crystallography and MD data, phi (Φ) and psi (Ψ) torsion angles values obtained using the 3 approaches were compared (**Figure S7 and S8** in the SI) and show generally good agreement between all methods.

Analysis of MD data to determine differences between the two complexes focused on the distance between the donor atom D (S1 in SAM) and the C_α of the first-shell active site residues that exhibit, or are neighboring residues that exhibit large differences in NMR chemical shifts (**Figure 3**). This reveals a compression or compaction between residues 40-42 and 141-142, which are situated in loops on either side of the catecholamine binding pocket (**Figure 4 and S9** in the SI). Such compaction is consistent with these regions showing large changes in NMR chemical shift. The donor–Y68Cα distance is longer in the sinefungin complex than in the SAM complex, which is also consistent with the NMR shift differences observed in Figs. 3 and S5 in the SI. While it has been proposed that Y68 “pushes” on the SAM sulfur [11], the difference observed here arises in part due to the extra hydrogen atom in sinefungin (as S is replaced by CH) as well as the stronger compaction causing M40 to push against Y68 (**Figure S10** in the SI). We propose that Y68 acts as a rigid “backstop” which helps hold the SAM in place.

Table 2. DFT cluster models: selected distances and charges

	SAM:catechol.:Mg^{2+}, a		DNC:Mg^{2+}, b	
	reactant	TS	SAM	sinefungin
R(D-A)[c], Å	4.65	4.45	4.67	4.37
R(D-X)[c], Å	1.82	2.38	1.82	1.52
R(X-A)[c], Å	2.84	2.08	2.86	2.91
q(D)[c]	0.82	0.44	0.83	0.16
q(XH_3)[c]	0.05	0.32	0.05	0.49

[a)]Reactant state and approximate TS in a model containing catechol in place of DNC; [b)]Reactant state models containing DNC, Mg^{2+} and SAM or sinefungin;[c] d(D-A), donor–acceptor distance; R(D-X), donor–transferring group distance; R(X-A), transferring group–acceptor distance; R(D), the natural charge on the donor; q(XH_3), the natural charge on the transferring group.

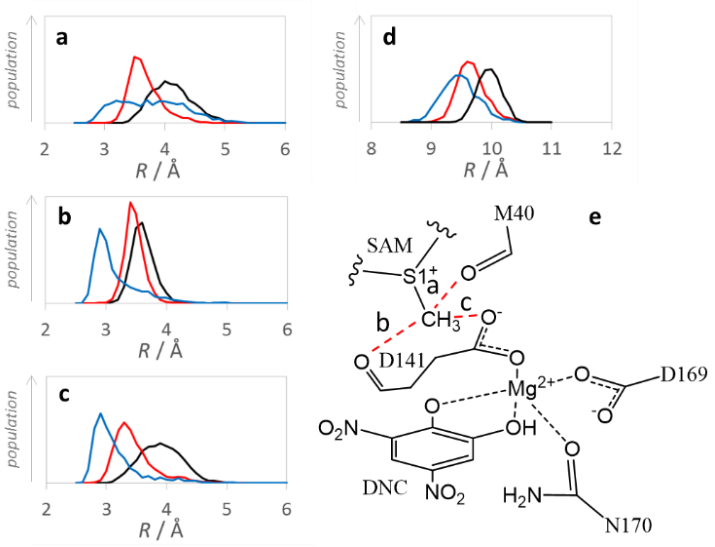

Figure 4. Active site compaction. S1–M40O (a), S1–D141O (b), S1–D141OD2 (c), M40Cα-D141 Cα (d) distance distributions during MD simulations of tertiary complexes containing SAM (black), SAM* (red) and sinefungin (blue); active site illustration with a-c distances (e) Additional distances are plotted in **Figure S9** in the SI.

To determine whether the observed active site compaction is purely driven by electrostatics, MD simulations were also performed with SAM*, a SAM molecule containing sinefungin-like charges on the donor and transferring methyl groups (see the SI for more details of parameters). The degree of compaction was found to be greater

for sinefungin than SAM*, likely reflecting differences in the chemical structure (NH_3 can form stronger H-bonds than CH_3) and geometry between SAM and sinefungin play a role, but confirming that electrostatics clearly plays a key role in this compaction. The increased positive charge on the sinefungin NH_3^+ (and SAM* methyl group) pulls nearby oxygen atoms towards it; these atoms include the backbone oxygen of M40, the backbone oxygen of D141 and the carboxyl group of D141 (**Figure 4**). Notably, there is a compaction of the loops on either side of the DNC, with a 0.5 Å decrease in the average M40Cα–D141Cα distance (**Figure S10** in the SI). This is consistent with role of equatorial CH---O hydrogen bonds proposed by Wilson and Williams [19].

To assess whether our proposed active site compaction is consistent with experimental data we also performed MD simulations with selected backbone dihedrals restrained to values derived from our NMR data. Restraints were applied to the backbone torsion angles of those residues with the largest differences observed between the SAM and sinefungin Φ and Ψ values derived using the TALOS-N algorithm (**Figure S11** in the SI). For all three complexes (SAM, SAM* and sinefungin), constraining Φ and Ψ torsion angles to the values determined from the sinefungin NMR data leads to active site compaction relative to simulations constrained to the SAM NMR values. Again, this confirms that the effects seen in the MD simulations are consistent with the NMR data and shows that compaction is driven, at least in part, by the protein backbone (cf. sidechains).

Finally, the effect of active site compaction on the electrostatic stabilization of sinefungin, and by inference the TS, was analyzed using energy decomposition; the energy of the system during each MD simulation was recalculated with and without charges on selected amino acids, and with either SAM or sinefungin charges applied to the SAM, SAM* or sinefungin molecule. This gives the relative stabilization energy, ΔE, of sinefungin relative to SAM by the amino acid in question. This analysis reveals that D141 dominates the electrostatic stabilization of sinefungin and SAM* (**Figure 5 and S12** in the SI). D141 and M40 both preferentially stabilize sinefungin over SAM during the SAM simulation ($\Delta E < 0$), then as the SAM transferring methyl group acquires positive charge and the oxygen atoms of these two residues move closer in the SAM* and sinefungin simulations, this stabilization effect increases. On the other hand, K144 destabilizes sinefungin ($\Delta E > 0$), as expected for a positively charged residue. However, the change in ΔE for both K144 and M40 between the SAM, SAM* and

sinefungin simulations is much smaller than that for D141, likely due to the net negative charge of D141 and its closer proximity to the developing positive charge on the transferring group.

As Δ*E* is calculated for each MD snapshot, it is possible to observe how this fluctuates throughout the MD simulation. A significant correlation between the M40Cα–D141Cα distance and Δ*E* for D141 was observed, with larger stabilization observed when this distance is shorter and thus the active site is more compact along the "equatorial" plane orthogonal to the donor–acceptor axis.[19] This can be rationalized in terms of the expected distance dependence of the coulombic interaction between D141 and the transferring group (which sits between M40 and D141) and shows a clear link between electrostatic stabilization and active site geometry (**Figure 5b**). Motion along the M40Cα–D141Cα and donor–acceptor coordinates is not correlated (**Figure S13** in the SI) and as there is little correlation between Δ*E* and the donor–acceptor distance, it would appear that this electrostatic stabilization is primarily driven by protein motion orthogonal to the donor–acceptor coordinate.

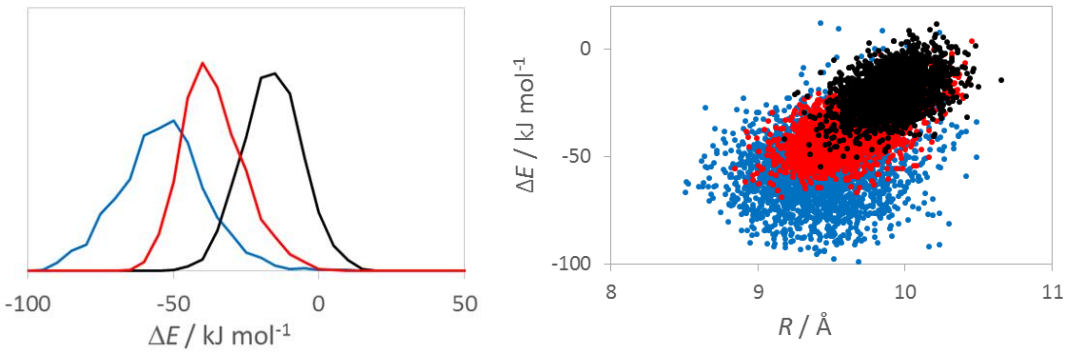

Figure 5. (left) Electrostatic stabilization of sinefungin and SAM* relative to SAM during SAM (black line), SAM* (red line) and sinefungin (blue line) MD simulations. (right) Correlation between active site compaction (M40Cα–D141Cα distance) *vs.* D141 stabilization energy for the SAM (black), SAM* (red) and sinefungin (blue) simulations.

In summary, we suggest that ternary complexes of COMT containing sinefungin, Mg^{2+} and a suitable catecholamine possess some TS-like character; i.e. they can be considered to be a TS analog. By comparison with the equivalent reactant state complex containing SAM, we can experimentally probe the protein reorganization relevant to catalysis. With the aid of DFT calculations and MD simulations, we have shown that active site compaction along the 'equatorial' plane orthogonal to the donor–acceptor axis plays a key role in stabilizing the positive charge that develops on the transferring methyl

group. It is then possible that the unusual deuterium [9] and tritium [10] KIEs observed on the reaction arise through perturbations to the equatorial H-bonding.

Experimental details

Full computational and experimental details are given in the supporting information. X-ray crystal structure models of the S-COMT:SAM:DNC:Mg^{2+} and S-COMT:sinefungin:DNC:Mg^{2+} complexes have been deposited in the protein data bank with the accession codes 6I3C and 6I3D, respectively. The backbone ^{1}H, ^{13}C and ^{15}N chemical shift assignments for S-COMT:SAM:DNC:Mg^{2+} and S-COMT:sinefungin:DNC:Mg^{2+} have been deposited in the BioMagResBank under the BMRB accession codes 26848 and 26851, respectively.

Associated content

Full computational and experimental details as well as additional supporting data are provided in the supporting information.

Corresponding Author

Dr Sam Hay

* sam.hay@manchester.ac.uk

Manchester Institute of Biotechnology and School of Chemistry, The University of Manchester, 131 Princess Street, Manchester M1 7DN, UK

Author Contributions

The manuscript was written through contributions of all authors.

Acknowledgment

This research was supported by a European Commission Marie Curie Fellowship (S.C. Grant number: PITN-GA-2013-ITN 606831), and in part by the UK Biotechnology and Biological Sciences Research Council (BBSRC; reference: BB/H021523/1). We acknowledge Diamond Light Source for time on beamlines i04 & i04-1 under proposal MX12788-32 & MX12788-41. We also acknowledge the assistance given by IT Services and the use of the Computational Shared Facility at The University of Manchester.

Abbreviations

SAM, S-adenosyl-L-methionine; DNC, 3, 5-dinitrocatechol; COMT, catechol O-methyltransferase; NMR, nuclear magnetic resonance; MD, molecular dynamics.

References

1. Fava, M., et al., *Open study of the catechol-O-methyltransferase inhibitor tolcapone in major depressive disorder.* Journal of Clinical Psychopharmacology, 1999. **19**(4): p. 329-35.
2. Kiss, L.E. and P. Soares-da-Silva, *Medicinal chemistry of catechol O-methyltransferase (COMT) inhibitors and their therapeutic utility.* Journal of Medicinal Chemistry, 2014. **57**(21): p. 8692-717.
3. Harrison, S.T., et al., *Synthesis and Evaluation of Heterocyclic Catechol Mimics as Inhibitors of Catechol-O-methyltransferase (COMT).* American Chemical Society Medicinal Chemistry Letters, 2015. **6**(3): p. 318-23.
4. Li, K. and J.W. Frost, *Synthesis of Vanillin from Glucose.* Journal of the American Chemical Society, 1998. **120**(40): p. 10545-10546.
5. Law, B.J., et al., *Effects of Active-Site Modification and Quaternary Structure on the Regioselectivity of Catechol-O-Methyltransferase.* Angewandte Chemie (International ed. in English), 2016. **55**(8): p. 2683-7.
6. Roca, M., et al., *Theoretical modeling of enzyme catalytic power: analysis of "cratic" and electrostatic factors in catechol O-methyltransferase.* Journal of the American Chemical Society, 2003. **125**(25): p. 7726-37.
7. Mihel, I., et al., *.alpha.-Deuterium isotope effects and transition-state structure in an intramolecular model system for methyl-transfer enzymes.* Journal of the American Chemical Society, 1979. **101**(15): p. 4349-4351.
8. Lameira, J., et al., *Methyltransferases do not work by compression, cratic, or desolvation effects, but by electrostatic preorganization.* Proteins, 2015. **83**(2): p. 318-30.
9. Hegazi, M.F., R.T. Borchardt, and R.L. Schowen, *.alpha.-Deuterium and carbon-13 isotope effects for methyl transfer catalyzed by catechol O-methyltransferase. SN2-like transition state.* Journal of the American Chemical Society, 1979. **101**(15): p. 4359-4365.
10. Zhang, J. and J.P. Klinman, *Enzymatic methyl transfer: role of an active site residue in generating active site compaction that correlates with catalytic efficiency.* Journal of the American Chemical Society, 2011. **133**(43): p. 17134-7.
11. Zhang, J., et al., *Mediation of donor-acceptor distance in an enzymatic methyl transfer reaction.* Proceedings of the National Academy of Sciences of the United States of America, 2015. **112**(26): p. 7954-9.
12. Hay, S. and N.S. Scrutton, *Good vibrations in enzyme-catalysed reactions.* Nature chemistry, 2012. **4**(3): p. 161.

13. Schramm, V.L. and S.D. Schwartz, *Promoting Vibrations and the Function of Enzymes. Emerging Theoretical and Experimental Convergence.* Biochemistry, 2018. **57**(24): p. 3299-3308.

14. Klinman, J.P., A.R. Offenbacher, and S. Hu, *Origins of Enzyme Catalysis: Experimental Findings for C-H Activation, New Models, and Their Relevance to Prevailing Theoretical Constructs.* Journal of the American Chemical Society, 2017. **139**(51): p. 18409-18427.

15. Lau, E.Y. and T.C. Bruice, *Importance of Correlated Motions in Forming Highly Reactive Near Attack Conformations in Catechol O-Methyltransferase.* Journal of the American Chemical Society, 1998. **120**(48): p. 12387-12394.

16. Lau, E.Y. and T.C. Bruice, *Comparison of the Dynamics for Ground-State and Transition-State Structures in the Active Site of Catechol O-Methyltransferase.* Journal of the American Chemical Society, 2000. **122**(30): p. 7165-7171.

17. Kanaan, N., J.J. Ruiz Pernia, and I.H. Williams, *QM/MM simulations for methyl transfer in solution and catalysed by COMT: ensemble-averaging of kinetic isotope effects.* Chemical Communications (Cambridge), 2008(46): p. 6114-6.

18. Ruggiero, G.D., et al., *QM/MM Determination of Kinetic Isotope Effects for COMT-Catalyzed Methyl Transfer Does Not Support Compression Hypothesis.* Journal of the American Chemical Society, 2004. **126**(28): p. 8634-8635.

19. Wilson, P.B. and I.H. Williams, *Influence of Equatorial CHO Interactions on Secondary Kinetic Isotope Effects for Methyl Transfer.* Angewandte Chemie (International ed. in English), 2016. **55**(9): p. 3192-5.

20. Tunnicliff, G. and T.T. Ngo, *Kinetics of rat brain soluble catechol-O-methyltransferase and its inhibition by substrate analogues.* The International journal of biochemistry, 1983. **15**(5): p. 733-738.

21. Borchardt, R.T., et al., *Sinefungin, a potent inhibitor of S-adenosylmethionine: Protein O-methyltransferase.* Biochemical and Biophysical Research Communications, 1979. **89**(3): p. 919-924.

22. Stratton, C.F., et al., *Kinetic Isotope Effects and Transition State Structure for Human Phenylethanolamine N-Methyltransferase.* American Chemical Society Chemical Biology, 2017. **12**(2): p. 342-346.

23. Zheng, W., et al., *Sinefungin Derivatives as Inhibitors and Structure Probes of Protein Lysine Methyltransferase SETD2.* Journal of the American Chemical Society, 2012. **134**(43): p. 18004-18014.

24. Ehler, A., et al., *Mapping the conformational space accessible to catechol-O-methyltransferase.* Acta Crystallographica Section D: Biological Crystallography, 2014. **70**(8): p. 2163-2174.

25. Rutherford, K., et al., *Crystal structures of human 108V and 108M catechol O-methyltransferase.* Journal of Molecular Biology, 2008. **380**(1): p. 120-30.

26. Czarnota, S., et al., *1H, 15N, 13C backbone resonance assignments of human soluble catechol O-methyltransferase in complex with S-adenosyl-L-methionine and 3,5-dinitrocatechol.* Biomolecular NMR Assignments, 2017. **11**(1): p. 57-61.

27. Shen, Y., et al., *TALOS+: a hybrid method for predicting protein backbone torsion angles from NMR chemical shifts.* Journal of Biomolecular NMR, 2009. **44**(4): p. 213-23.

28. Shen, Y. and A. Bax, *Protein backbone and sidechain torsion angles predicted from NMR chemical shifts using artificial neural networks.* Journal of biomolecular NMR, 2013. **56**(3): p. 227-241.

29. Kulik, H.J., et al., *How Large Should the QM Region Be in QM/MM Calculations? The Case of Catechol O-Methyltransferase.* The Journal of Physical Chemistry B, 2016. **120**(44): p. 11381-11394.

Supporting information

Experimental Details

Materials

Isotopically-labelled compounds: ^{15}N-labelled ammonium chloride (99%), $^{13}C_6$,$^{2}H_7$-labelled D-Glucose (U-$^{13}C_6$, 99%; 1,2,3,4,5,6,6-d_7 97-98%) and deuterium oxide (99.8%) were purchased from Goss Scientific. 3,5-dinitrocatechol (DNC), S-adenosyl-L-methionine (SAM) and sinefungin (5′-deoxy-5′-(1,4-diamino-4-carboxybutyl)adenosine) were purchased with the highest purity available from Sigma-Aldrich (Poole, UK) and used as received.

Protein expression and purification

Expression and purification of human soluble catechol-O-methyltransferase (S-COMT) for NMR studies was performed as described previously [1]. Protein purification for crystallography involved two more steps after following nickel affinity chromatography. Fractions showing S-COMT content, observed as a peak in UV absorbance at 280 nm after affinity chromatography, were pooled and loaded onto a HiPrep desalting 26/10 column. The column was washed with at least 1.5 column volumes of filtered and degassed water and equilibrated with 2 column volumes of filtered and degassed buffer (50 mM Tris-HCl buffer pH 8 containing 20 mM NaCl). Proteins were then eluted and loaded onto an anion exchange HiTrap Q FF column using 50 mM Tris-HCl pH 8 as a baseline buffer. The fractions column waswere then eluted with 50 mM Tris-HCl, 1 M NaCl, pH 8 and the fractions containing S-COMT were concentrated as described previously [1].

Crystallogenesis

The sitting drop vapour diffusion technique was used to grow crystals of two complexes of human S-COMT with 3,5-dinitrocatechol (DNC), Mg^{2+} and either S-adenosyl-L-methionine (SAM) or its derivative sinefungin. The purified protein was collected, diluted (1 μM) and mixed with SAM/sinefungin (10 μM) and DNC (10 μM) overnight at 4 ˚C through gentle rocking. The S-COMT:SAM:DNC:Mg^{2+} and S-

COMT:sinefungin:DNC:Mg^{2+} protein complexes were then concentrated to a final concentration of 6 mg/mL protein with bound DNC and SAM/sinefungin ligand in a 50 mM Tris buffer (with 100 mM NaCl, 10 mM DTT, 2 mM MgCl2) at pH 7.4. Crystals of the S-COMT:sinefungin:DNC:Mg^{2+} complex were grown by mixing 200 nL of protein the complex with an equal volume of reservoir solution comprising 0.1 M amino acid stock (0.2 M L-Na-glutamate; 0.2 M alanine (racemic); 0.2 M glycine; 0.2 M lysine HCl (racemic); 0.2 M serine (racemic), 0.1 M imidazole; MES monohydrate (acid) pH 6.5, 50% v/v precipitant mix (25% v/v MPD; 25% PEG 1000; 25% PEG 3350) Morpheus condition H4. Crystals of the S-COMT:SAM: DNC:Mg^{2+} SAM complex crystals were grown from a reservoir comprising 0.1 M alcohols mix (0.2 M 1,6-hexanediol; 0.2 M 1-butanol; 0.2 M 1,2-propanediol; 0.2 M 2-propanol; 0.2 M 1,4-butanediol; 0.2 M 1,3-propanediol), 0.1 M imidazole; MES monohydrate (acid) pH 6.5, 50% v/v precipitant mix (25% v/v MPD; 25% PEG 1000; 25% PEG 3350) Morpheus condition D4. All drops were set using a Mosquito (TTP) pipetting robot and incubated at 4 °C. Single crystals suitable for X-ray analysis were flash frozen by plunge freezing in liquid nitrogen.

Crystallography data collection and structure determination

Data were collected from single cryogenically frozen crystals at Diamond Light Source, full details of data and refinement statistics are presented in **Table S1**. Structures were subsequently solved by molecular replacement in Phaser [2]. All models were subsequently completed and refined using iterative cycles of rebuilding and refinement in COOT [3] and Phenix.refine [4]. Validation with Molprobity was integrated into the iterative rebuilding and refinement cycle [5]. Final models with R and R_f of 0.1452 & 0.1798 for the S-COMT:SAM:DNC:Mg^{2+} complex and 0.1169 & 0.1492 for the S-COMT:sinefungin:DNC:Mg^{2+} complex have been deposited with the protein data bank, accession codes 6I3C, 6I3D.

NMR experiments

All NMR measurements were performed at 298 K, using standard pulse sequences on an 800 MHz Bruker Avance III NMR spectrometer with TCI cryoprobe equipped with Z gradients and TopSpin software version 3.2 housed in the Manchester Institute of

Biotechnology. NMR samples containing 0.5 mM human S-COMT, 2.5 mM $MgCl_2$, 5 mM DNC and 5 mM SAM or 5 mM sinefungin in 50 mM Tris-HCl buffer, 50 mM NaCl, 10 mM DTT, 2 mM NaN_3, pH 7.5 were loaded into 5-mm diameter NMR tubes. ^2H_2O was added to the protein samples (10% v/v) to allow a deuterium lock and 0.5% v/v trimethylsilyl propanoic acid (TSP) was added as a reference signal. For the backbone ^1H, ^{13}C and ^{15}N resonance assignment, transverse relaxation-optimised spectroscopy (TROSY)-based 3D HNCACB, HN(CO)CACB, HNCO, HN(CA)CO, HNCA and HN(CO)CA spectra were acquired using a non-uniform sampling strategy (**Table S2**). All NMR spectra were analysed using CCPNMR Analysis version 2.4 [6]. Backbone resonances were assigned using standard triple resonance methodology [7]. Prediction of solution secondary structure from a chemical shift using the TALOS+ webserver [8] was in good agreement with published X-ray crystal structures [9] (**Figure S4**). In total, 97% of all backbone resonances were assigned [1], with 205 and 204 out of a possible 215 residues assigned in ^1H-^{15}N TROSY spectra of the SAM and sinefungin complexes, respectively. Backbone assignments for the two complexes are very similar, the only significant differences are located in the SAM/sinefungin pocket and the DNC loops (**Figure 3** and **Figure S3**).

DFT cluster models

DFT calculations were performed in Gaussian 09 revision D.01 [10].To estimate the charge difference between the reactant and transition states for the SAM:catechol methyl transfer reaction, and compare this to the charges in the SAM:DNC and sinefungin:DNC complexes, cluster models were constructed from the SAM:DNC crystal structure using all amino acids with at least one heavy atom within a radius of 10 Å of the Mg^{2+} ion, as well as the water ligating the Mg^{2+} and one crystallographic water molecule. Any backbone cleavage was capped with a methyl group. This resulted in a model of 586 atoms for the SAM:DNC and 587 atoms for the sinefungin:DNC complex (**Figure S6**). The B3LYP functional [11] was used with the 6-31G(d) basis set for all optimisations, and all protein heavy atoms were kept fixed. To calculate the charges, single-point energy calculations were performed using 6-311G+(d,p) basis set on the SAM, DNC, Mg^{2+} and oxygen atoms ligated to the Mg and the 6-31G(d) basis set for all other atoms. To generate an approximate transition-state structure for the SAM:catechol reaction, a partially relaxed scan (*i.e.* the same atoms were fixed as during the

minimisations) of the C-O distance between the transferring methyl and acceptor catechol oxygen was performed until the maximum potential energy on the adiabatic surface was obtained with a certainty of ±0.02 Å along the C-O distance.

To parametrise the octahedral Mg^{2+} bonding, a DFT model was built from the SAM:DNC crystal structure (Figure S14), which includes the Mg^{2+}, the active site water molecule, dopamine and amino acids D141, D168, N169 and E198 which hydrogen bonds to the hydroxyl of the catecholate. Note that dopamine was used as these parameters were initially prepared for other simulations and consistency of parameters across simulations were desired, but this is expected to have a minor effect on the Mg^{2+} bonding. After energy minimisation at the B3LYP/6-311+G(d,p) level of theory with a PCM continuum model (ε=80), bond force constants were obtained from frequency calculations, while the angle force constants were obtained from fitting harmonic potentials to the energies from relaxed scans of ±10˚.

MD simulations

MD simulations were carried out using the Amber 14 force field in Gromacs 5.1. DNC, SAM & sinefungin GAFF parameters were generated using RESP fitting in Antechamber (**Table S4**). For SAM*, the S1, methyl and surrounding atoms were given the charges of the corresponding sinefungin atoms (highlighted in **Table S4**), with the charge of the extra sinefungin hydrogen distributed between these atoms. Octahedral Mg^{2+} bonding was parametrised using a 6-311+G** DFT model (**Figure S14** and **Table S3**) with a continuum solvation model. Restraints were applied to the 20 residues with the largest difference in Φ and Ψ derived from TALOS-N [12] between the SAM and sinefingin. Energy decomposition. For a given residue X, the energy during the MD simulation can be recalculated with zero partial charges on the atoms of X, as well as swapping the charge of SAM for sinefungin and vice-versa. In this way, the electrostatic stabilisation of sinefungin over SAM by residue X can be calculated:

$$\Delta E(\mathrm{X}) = [E_{\mathrm{Tot}}(q_{\mathrm{X}}=0) - E_{\mathrm{Tot}}]_{\mathrm{SAM}} - [E_{\mathrm{Tot}}(q_{\mathrm{X}}=0) - E_{\mathrm{Tot}}]_{\mathrm{sinefungin}} \qquad (1)$$

where ΔE(X) is the electrostatic stabilisation energy of residue X, ETot is the system energy and q_X =0 indicates that all partial charges of X have been set to 0.

Table S1. X-ray data collection and refinement statistics for both complexes described in this study.

	COMT:SAM:DNC:Mg^{2+}	COMT:Sinefungin:DNC:Mg^{2+}
Wavelength (Å)	0.9282	0.9795
Resolution range (Å)	39.13 - 1.336 (1.384 - 1.336)	37.02 - 1.42 (1.471 - 1.42)
Space group	P 1 21 1	P 1 21 1
Unit cell parameters a (Å) b (Å) c (Å)	 43.694 61.749 46.071	 42.961 75.797 64.345
Total reflections	157981 (12486)	249222 (20113)
Unique reflections	49463 (4891)	76895 (7577)
Multiplicity	3.2 (2.5)	3.2 (2.7)
Completeness (%)	99.50 (99.15)	99.26 (98.25)
Mean I/sigma(I)	8.25 (2.06)	14.80 (4.22)
Wilson B-factor ($Å^2$)	10.33	12.6
R-merge	0.08128 (0.3631)	0.04946 (0.3015)
R-meas	0.09735 (0.4585)	0.05904 (0.3751)
R-pim	0.05295 (0.2766)	0.03189 (0.22)
CC1/2	0.994 (0.824)	0.998 (0.86)
CC*	0.999 (0.95)	1 (0.962)
Reflections used in refinement	49425 (4889)	76889 (7577)
Reflections used for R-free	2468 (212)	3719 (351)

R-work	0.1452 (0.1916)	0.1169 (0.1696)
R-free	0.1798 (0.2439)	0.1492 (0.2320)
CC(work)	0.970 (0.935)	0.979 (0.947)
CC(free)	0.950 (0.921)	0.971 (0.855)
Number of non-hydrogen atoms	1941	4216
macromolecules	1727	3621
ligands	15	84
solvent	199	511
Protein residues	217	434
RMS(bonds)	0.007	0.011
RMS(angles)	0.94	1.16
Ramachandran favored (%)	97.17	96.74
Ramachandran allowed (%)	2.83	3.26
Ramachandran outliers (%)	0	0
Rotamer outliers (%)	0.53	1
Clashscore	0.58	4.84
Average B-factor	15.83	19.88
macromolecules	14.04	17.07
ligands	11.86	13.56
solvent	31.7	40.82

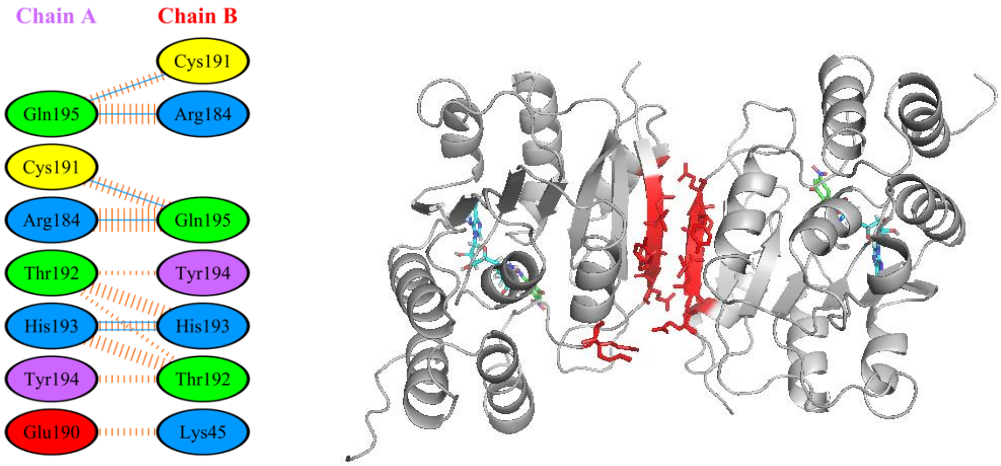

Figure S1. Left, Schematic representation of the anti-parallel β-strand interactions between protein chains in the dimeric S-COMT:sinefungin:DNC:Mg^{2+} X-ray crystal structure. Hydrogen bonds are represented as solid blue lines and non-bonded contacts represented as striped red lines (the width of the striped line is proportional to the number of atomic contacts). Residue colours represents the chemical nature of the amino acid: blue – positive, red – negative, green – neutral, purple – aromatic. Rendered using PDBsum.[13] Right, X-ray crystal structure of the COMT:sinefungin:DNC:Mg^{2+} complex showing in red those residues identified using PDBsum. Interactions are listed below in the accompanying table.

Hydrogen bonds

	<----- A T O M 1 ----->						<----- A T O M 2 ----->					
	Atom no.	Atom name	Res name	Res no.	Chain		Atom no.	Atom name	Res name	Res no.	Chain	Distance
1.	1566	O	ARG	184	A	<-->	3479	NE2	GLN	195	B	2.72
2.	1619	O	CYS	191	A	<-->	3472	N	GLN	195	B	2.92
3.	1629	N	HIS	193	A	<-->	3453	O	HIS	193	B	2.82
4.	1632	O	HIS	193	A	<-->	3450	N	HIS	193	B	2.82
5.	1651	N	GLN	195	A	<-->	3440	O	CYS	191	B	3.03
6.	1658	NE2	GLN	195	A	<-->	3387	O	ARG	184	B	2.95

Non-bonded contacts

	<----- A T O M 1 ----->						<----- A T O M 2 ----->					
	Atom no.	Atom name	Res name	Res no.	Chain		Atom no.	Atom name	Res name	Res no.	Chain	Distance
1.	1564	CA	ARG	184	A	<-->	3480	OE1	GLN	195	B	3.71
2.	1565	C	ARG	184	A	<-->	3479	NE2	GLN	195	B	3.76
3.	1566	O	ARG	184	A	<-->	3478	CD	GLN	195	B	3.59
4.	1566	O	ARG	184	A	<-->	3480	OE1	GLN	195	B	3.62
5.	1566	O	ARG	184	A	<-->	3479	NE2	GLN	195	B	2.72
6.	1567	CB	ARG	184	A	<-->	3480	OE1	GLN	195	B	3.54
7.	1568	CG	ARG	184	A	<-->	3480	OE1	GLN	195	B	3.63
8.	1615	OE2	GLU	190	A	<-->	2278	CE	LYS	45	B	3.65
9.	1615	OE2	GLU	190	A	<-->	2281	NZ	LYS	45	B	3.52
10.	1619	O	CYS	191	A	<-->	3472	N	GLN	195	B	2.92
11.	1619	O	CYS	191	A	<-->	3473	CA	GLN	195	B	3.64
12.	1619	O	CYS	191	A	<-->	3475	O	GLN	195	B	3.86
13.	1619	O	CYS	191	A	<-->	3476	CB	GLN	195	B	3.40
14.	1623	CA	THR	192	A	<-->	3453	O	HIS	193	B	3.14

15.	1624	C	THR	192	A	<-->	3453	O	HIS	193	B	3.46
16.	1626	CB	THR	192	A	<-->	3453	O	HIS	193	B	3.75
17.	1627	CG2	THR	192	A	<-->	3448	CG2	THR	192	B	3.69
18.	1627	CG2	THR	192	A	<-->	3453	O	HIS	193	B	3.38
19.	1627	CG2	THR	192	A	<-->	3466	CD1	TYR	194	B	3.86
20.	1629	N	HIS	193	A	<-->	3453	O	HIS	193	B	2.82
21.	1632	O	HIS	193	A	<-->	3444	CA	THR	192	B	3.18
22.	1632	O	HIS	193	A	<-->	3445	C	THR	192	B	3.48
23.	1632	O	HIS	193	A	<-->	3447	CB	THR	192	B	3.87
24.	1632	O	HIS	193	A	<-->	3448	CG2	THR	192	B	3.53
25.	1632	O	HIS	193	A	<-->	3450	N	HIS	193	B	2.82
26.	1632	O	HIS	193	A	<-->	3453	O	HIS	193	B	3.78
27.	1645	CD1	TYR	194	A	<-->	3448	CG2	THR	192	B	3.73
28.	1647	CE1	TYR	194	A	<-->	3448	CG2	THR	192	B	3.80
29.	1651	N	GLN	195	A	<-->	3440	O	CYS	191	B	3.03
30.	1652	CA	GLN	195	A	<-->	3440	O	CYS	191	B	3.74
31.	1655	CB	GLN	195	A	<-->	3440	O	CYS	191	B	3.45
32.	1657	CD	GLN	195	A	<-->	3387	O	ARG	184	B	3.70
33.	1659	OE1	GLN	195	A	<-->	3385	CA	ARG	184	B	3.76
34.	1659	OE1	GLN	195	A	<-->	3387	O	ARG	184	B	3.60
35.	1659	OE1	GLN	195	A	<-->	3388	CB	ARG	184	B	3.50
36.	1659	OE1	GLN	195	A	<-->	3389	CG	ARG	184	B	3.68
37.	1658	NE2	GLN	195	A	<-->	3387	O	ARG	184	B	2.95

Number of hydrogen bonds: 6

Number of non-bonded contacts: 37

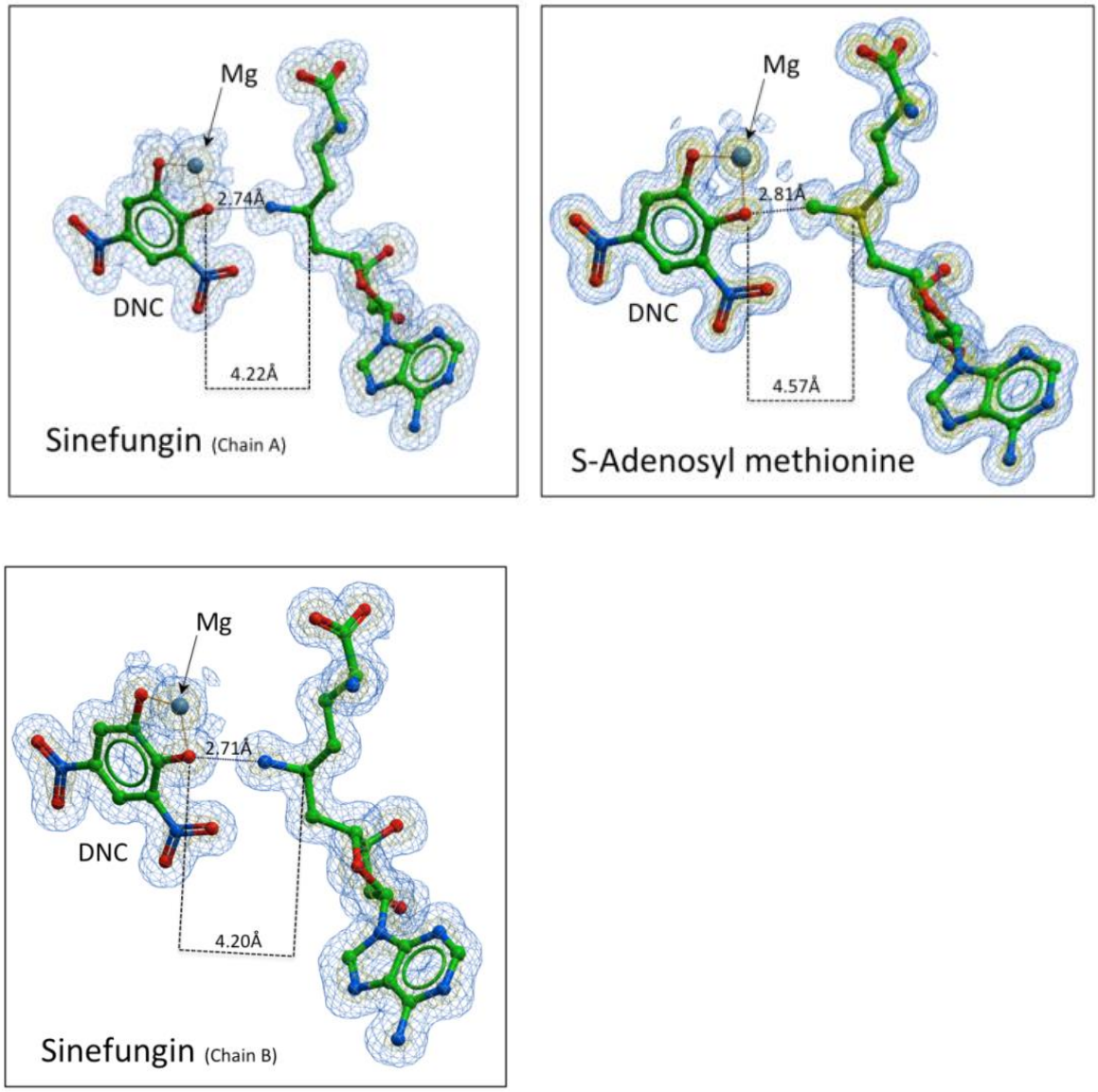

Figure S2. X-ray crystal structure distances between DNC and SAM or sinefungin. The electron density is also shown.

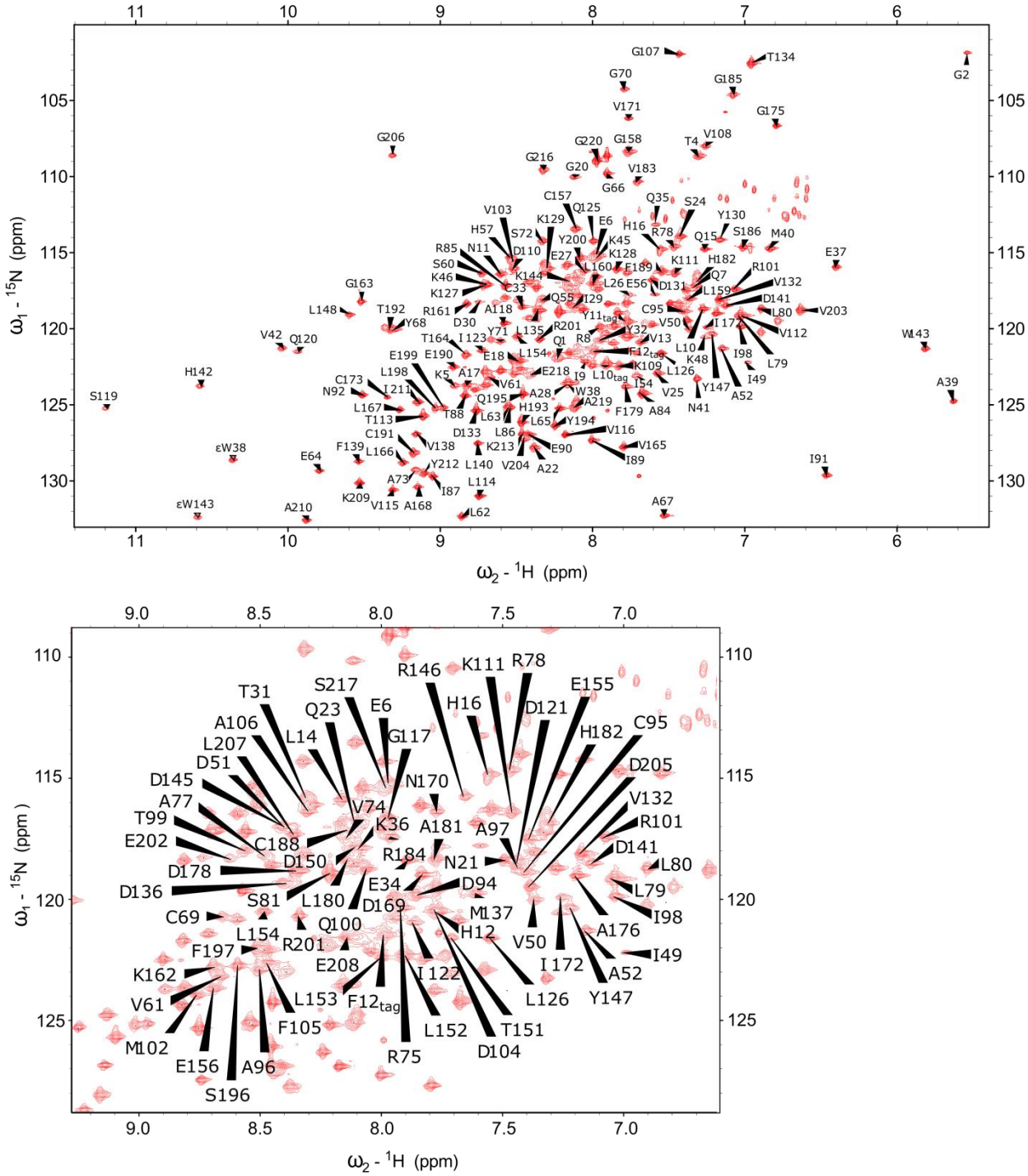

Figure S3. 2D ^{1}H-^{15}N TROSY spectrum of the human S-COMT:Sinefungin:DNC:Mg^{2+} complex recorded at pH 7.5 and 298 K. The assignments of backbone amide resonances are indicated by residue type and sequence number. Acquisition parameters are given in **Table S2**.

Table S2. Selected acquisition parameter settings for the acquisition of NMR spectra of the S-COMT complexes.

Complex 1/ Complex 2[a]	^{1}H-^{15}N TROSY	HNCACB	HN(CO)CACB	HNCO
^{1}H TD[b]	5998/5998	2048/2048	2048/2048	2048/2048
^{1}H AQ (ms)	149.9/149.9	85.2/51.2	85.2/51.2	85.2/51.2
^{15}N TD	256/512	78/78	78/78	88/88
^{15}N AQ (ms)	47.8/90.2	14.6/13.7	14.6/13.7	16.4/15.5
^{13}C TD	-/-	450/450	450/450	106/106
^{13}C AQ (ms)	-/-	16.0/14.0	16.0/14.0	16.4/16.4

Complex 1/ Complex 2*	HN(CA)CO	HNCA	HN(CO)CA
^{1}H TD	2048/2048	2048/2048	-/2048
^{1}H AQ (ms)	85.2/51.2	85.2/51.2	-/51.2
^{15}N TD	88/88	88/88	-/88
^{15}N AQ (ms)	16.4/15.5	16.4/15.5	-/15.5
^{13}C TD	106/106	180/180	-/180
^{13}C AQ (ms)	16.4/16.4	17.2/17.2	-/17.2

[a] Complex 1: S-COMT:SAM:DNC:Mg^{2+}; Complex 2: S-COMT:sinefungin:DNC:Mg^{2+}

[b] TD: the number of time domain data points obtained; AQ: acquisition time.

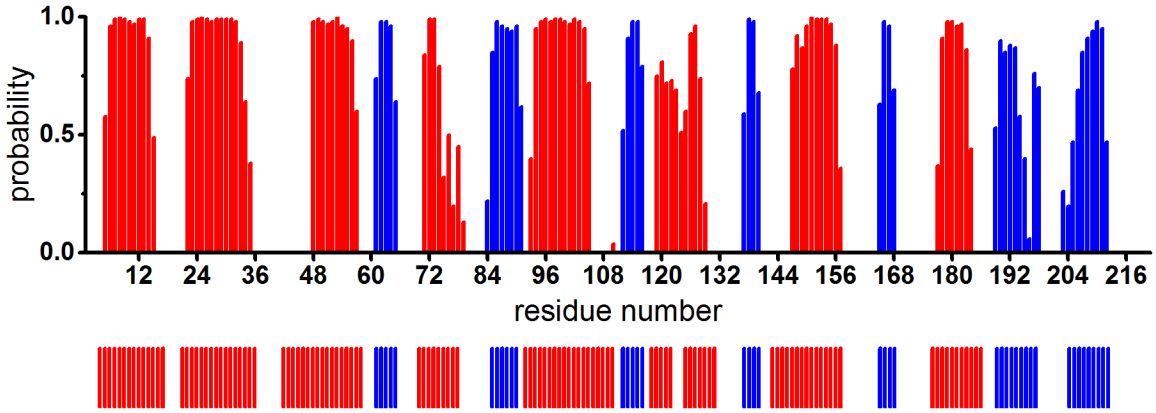

Figure S4. Backbone secondary structure prediction of the S-COMT:sinefungin:DNC:Mg^{2+} complex derived with TALOS+ [8] using the backbone $^{1}H_{N}$, ^{15}N, $^{13}C_{\alpha}$, $^{13}C_{\beta}$ and $^{13}C'$ chemical shifts. The secondary structure prediction is shown as red bars for α-helices and blue bars for β-strands, with the height of the bars representing the probability of the secondary structure assigned by the software. The secondary structure of the human S-COMT:SAM:DNC:Mg^{2+} complex crystal structure PDB: 3BWM [9] is reported below in the same color representation.

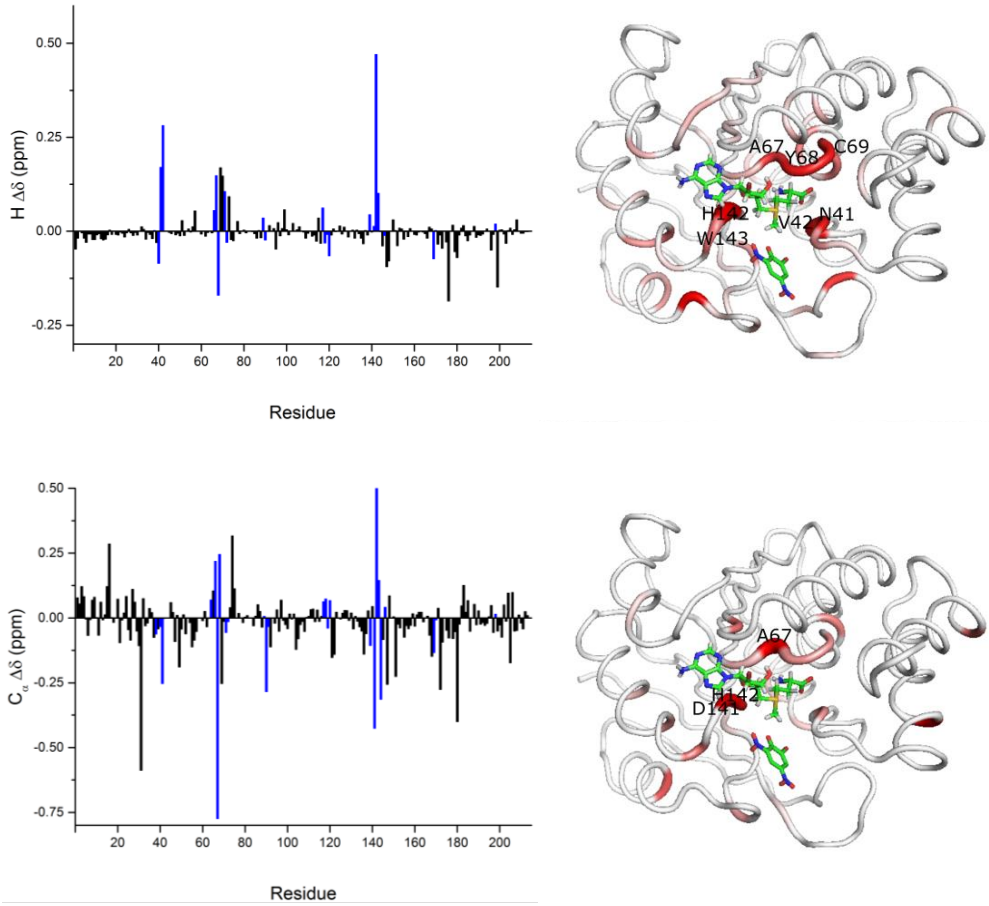

Figure S5. Continued on next page.

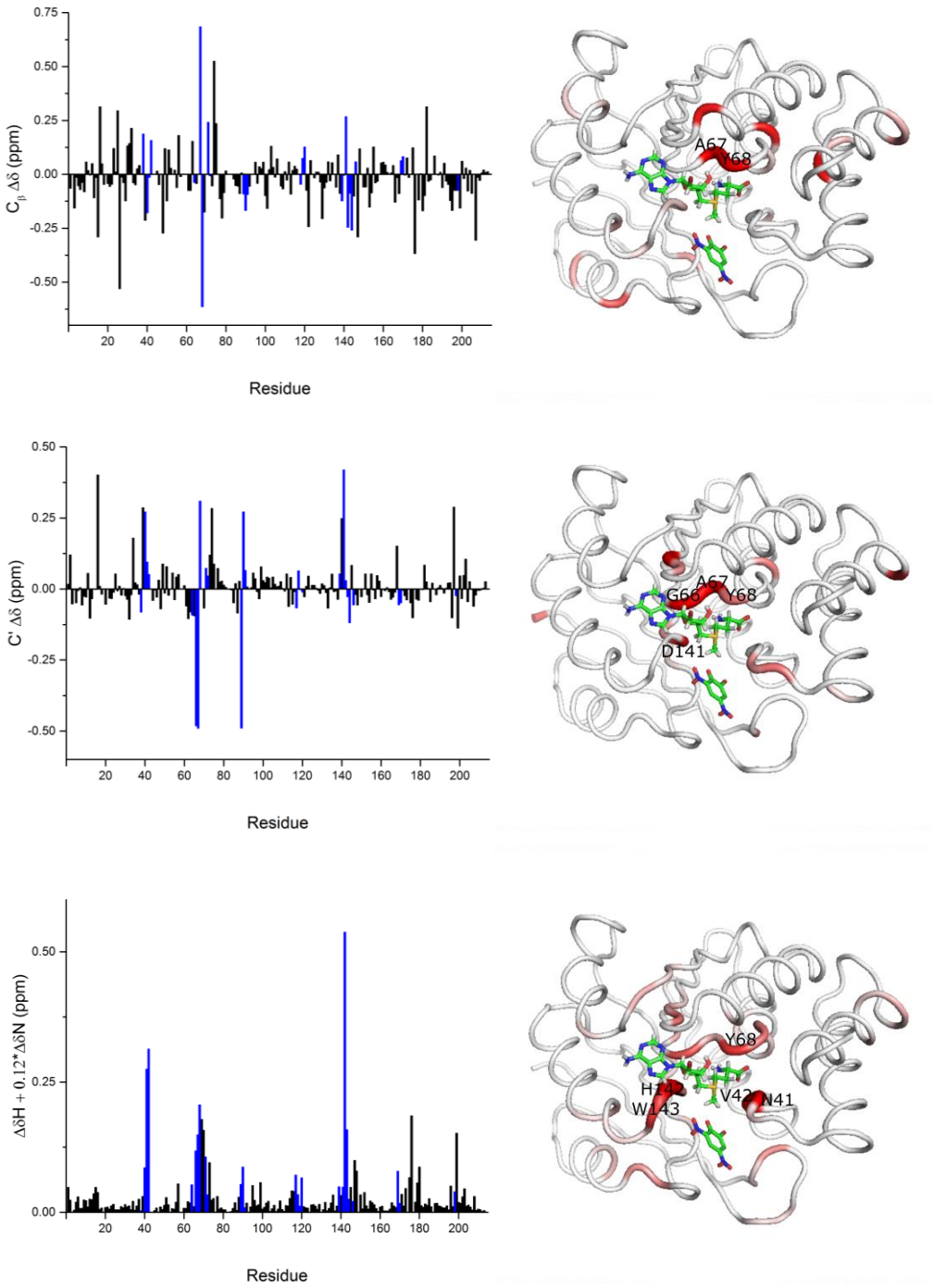

Figure S5. Differences in H, C_α, C_β, C' and rescalled N-H plane hypotenuse NMR shifts (ppm) between human S-COMT:SAM:DNC:Mg^{2+} and human S-COMT:sinefungin: DNC:Mg^{2+} complexes represented as a graph (left) and putty diagram (right). Active site residues (up to 4 Å from ligands position in crystal structure) are shown by blue bars. Putty diagram colored from low to high difference in NMR shift (white to red).

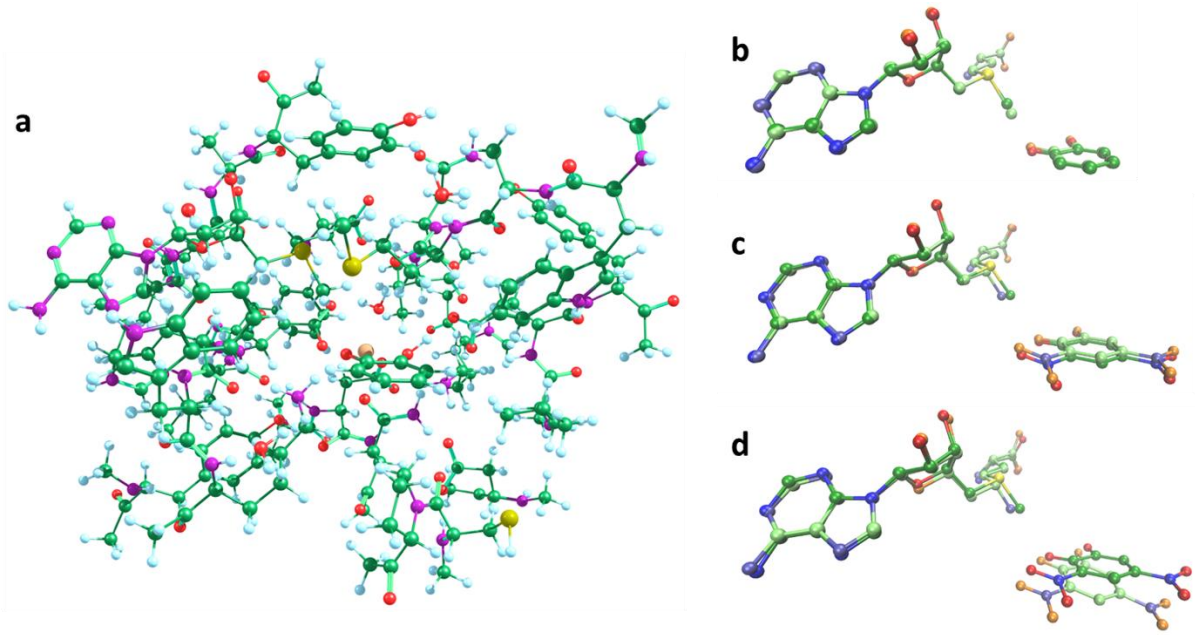

Figure S6. Energy minimized DFT cluster models of COMT. The whole SAM-catechol model (a); close-ups of SAM:catechol for the reactant (dark green cabon atoms) and transition state (light green carbon atoms) (b), SAM:DNC (dark green cabon atoms) and sinefungin:DNC (light green carbon atoms) (c), and SAM:DNC and sinefungin:DNC with NH_2 in place of NH_3^+.

Table S3. Partial atomic charges (*q*) for selected SAM, sinefungin and SAM* atoms used for MD simulations.

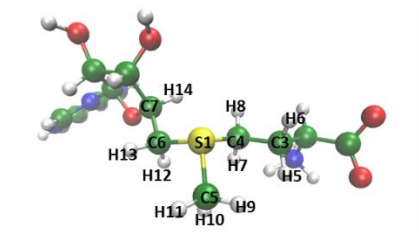

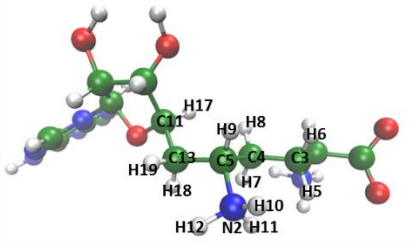

Name	*q*(SAM)	*q*(SAM*)
C3	-0.11873	-0.07224
C4	-0.04721	-0.19952
S1	0.246273	0.396006
C5	-0.15283	-0.71315
H9	0.126886	0.398943

Name	*q*(sinefungin)
C3	-0.07224
C4	-0.19952
C5	0.396006
N2	-0.71315
H10	0.398943

H10	0.126886	0.398943	H11	0.398943
H11	0.126886	0.398943	H12	0.398943
C6	-0.28994	-0.3937	C13	-0.3937
C7	0.04939	0.210796	C11	0.231796
H14	0.120147	0.050759	H17	0.051759
H12	0.19498	0.126416	H18	0.131416
H13	0.19498	0.126416	H19	0.131416
H7	0.09019	0.074431	H9	0.101726
H8	0.09019	0.074431	H7	0.075389
H5	0.106928	0.04724	H8	0.075389
H6	0.106928	0.04724	H5	0.04824
			H6	0.04824

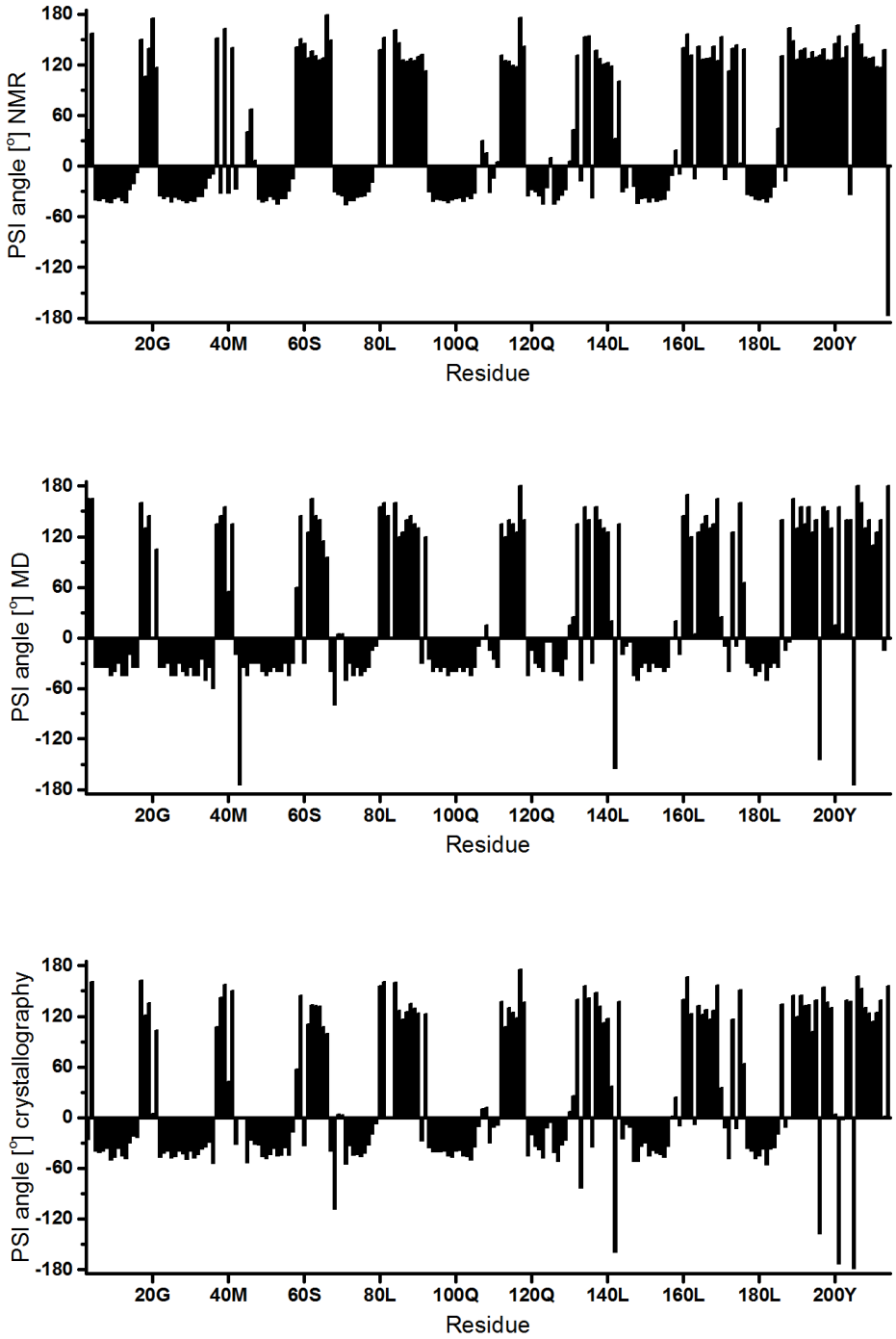

Figure S7. Continued on next page.

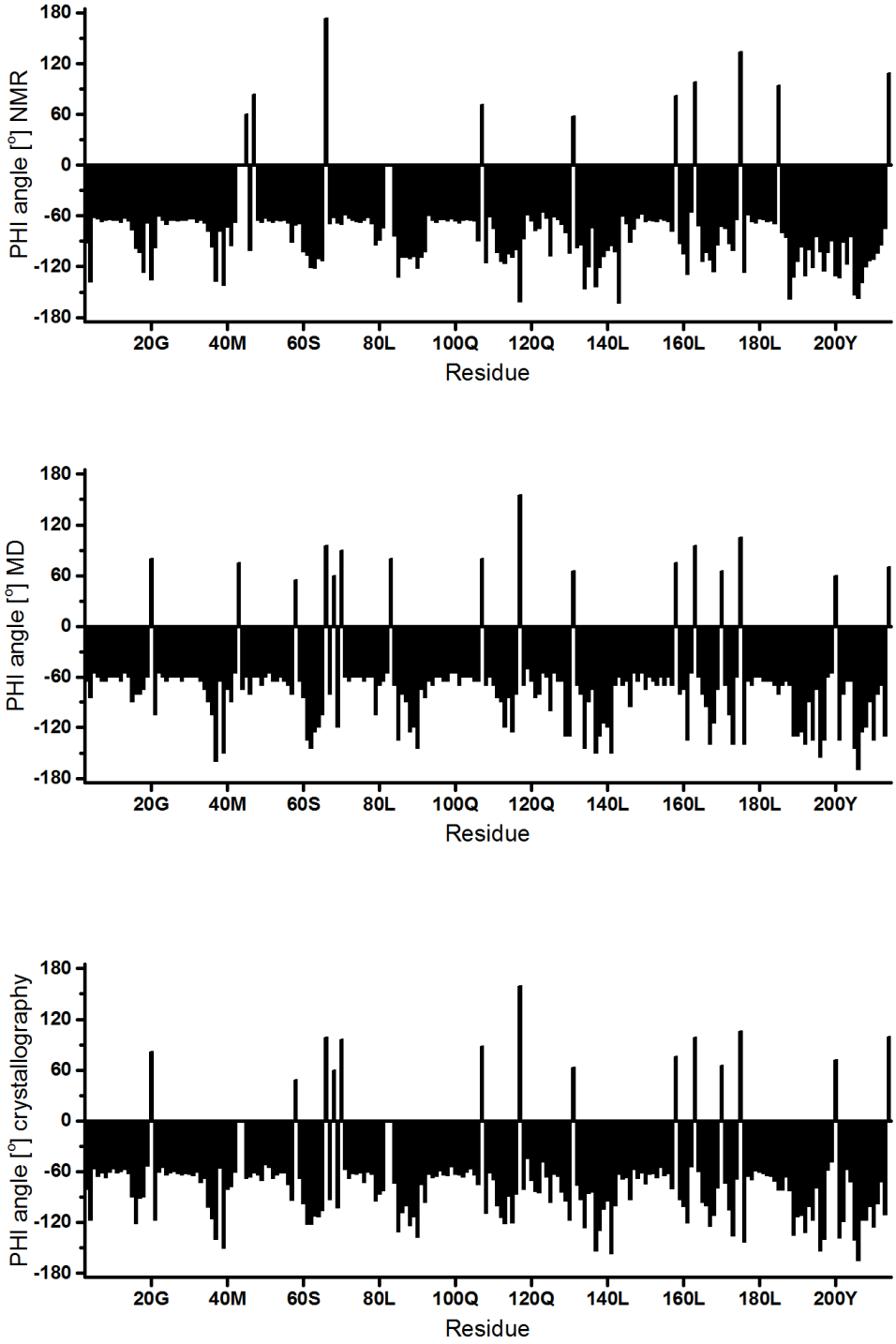

Figure S7. Comparison between torsion angles values Phi (Φ) and Psi (Ψ) [°] for S-COMT:SAM:DNC:Mg^{2+} complex derived from NMR data, MD and crystallography. Phi (Φ) and Psi (Ψ) torsion angles for NMR data were predicted by uploading the backbone $^{1}H_{N}$, ^{15}N, $^{13}C_{\alpha}$, $^{13}C_{\beta}$ and $^{13}C'$ chemical shifts to the TALOS-N webserver [12]. Phi (Φ) and Psi (Ψ) torsion angles for crystallography were extracted from pdb files using the WHAT IF web server [14].

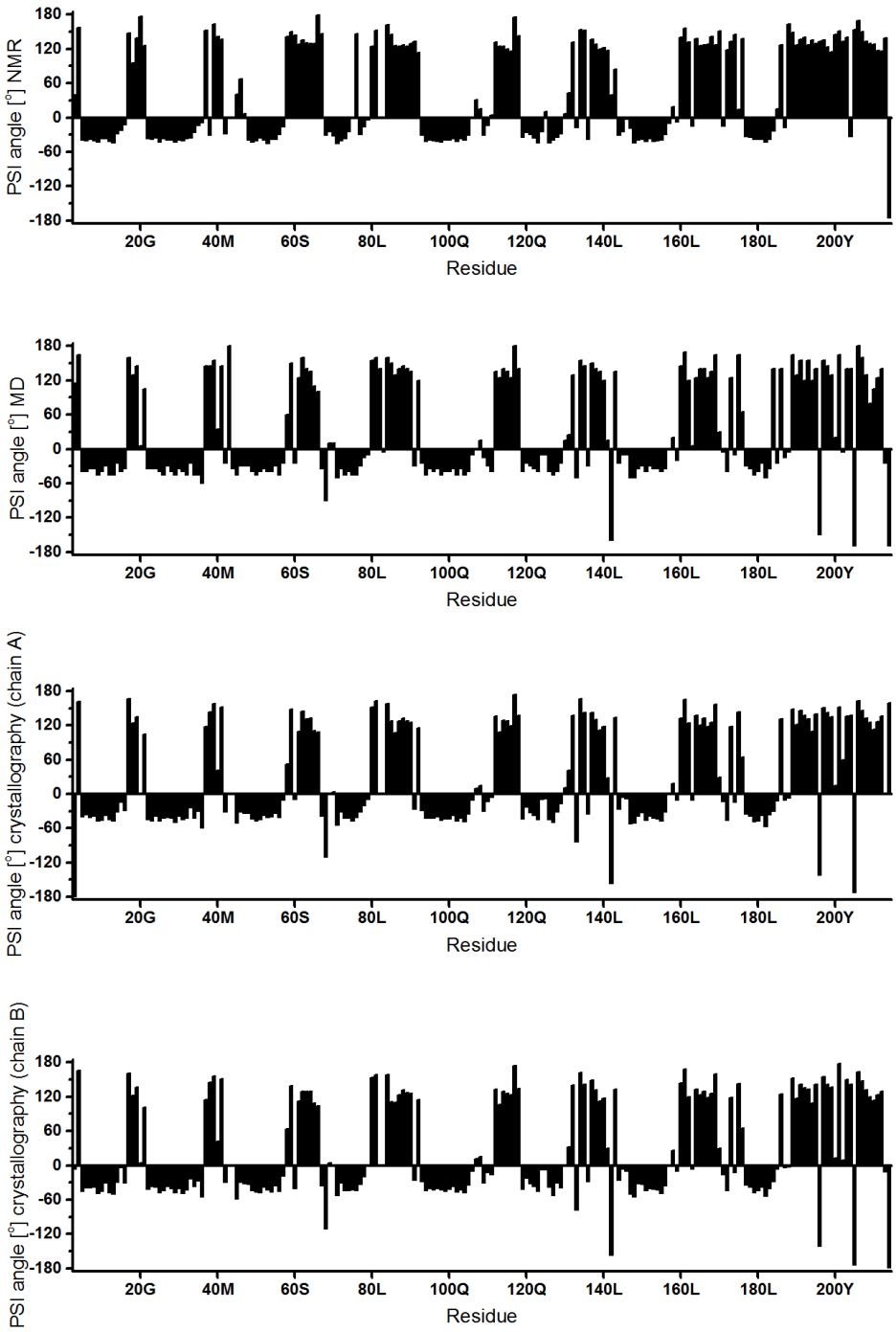

Figure S8. Continued on next page.

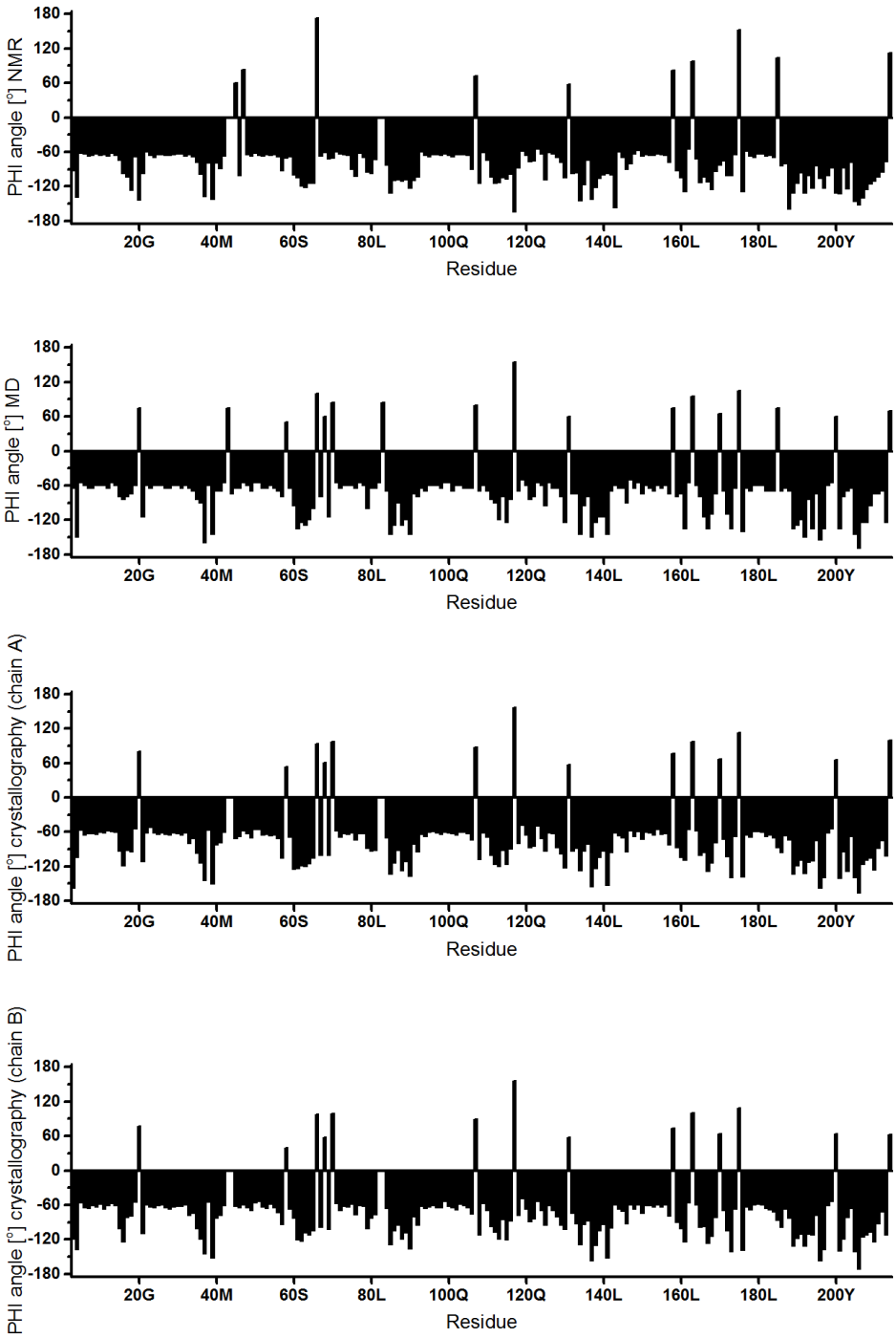

Figure S8. Comparison between torsion angles values Phi (Φ) and Psi (Ψ) [°] for S-COMT:sinefungin:DNC:Mg^{2+} complex derived from NMR data, MD and crystallography (two chains for crystallographic dimer presented). Phi (Φ) and Psi (Ψ) torsion angles for NMR data were predicted by uploading the backbone $^{1}H_{N}$, ^{15}N, $^{13}C_{\alpha}$, $^{13}C_{\beta}$ and $^{13}C'$ chemical shifts to the TALOS-N webserver [12]. Phi (Φ) and Psi (Ψ) torsion angles for crystallography were extracted from pdb files using the WHAT IF web server [14].

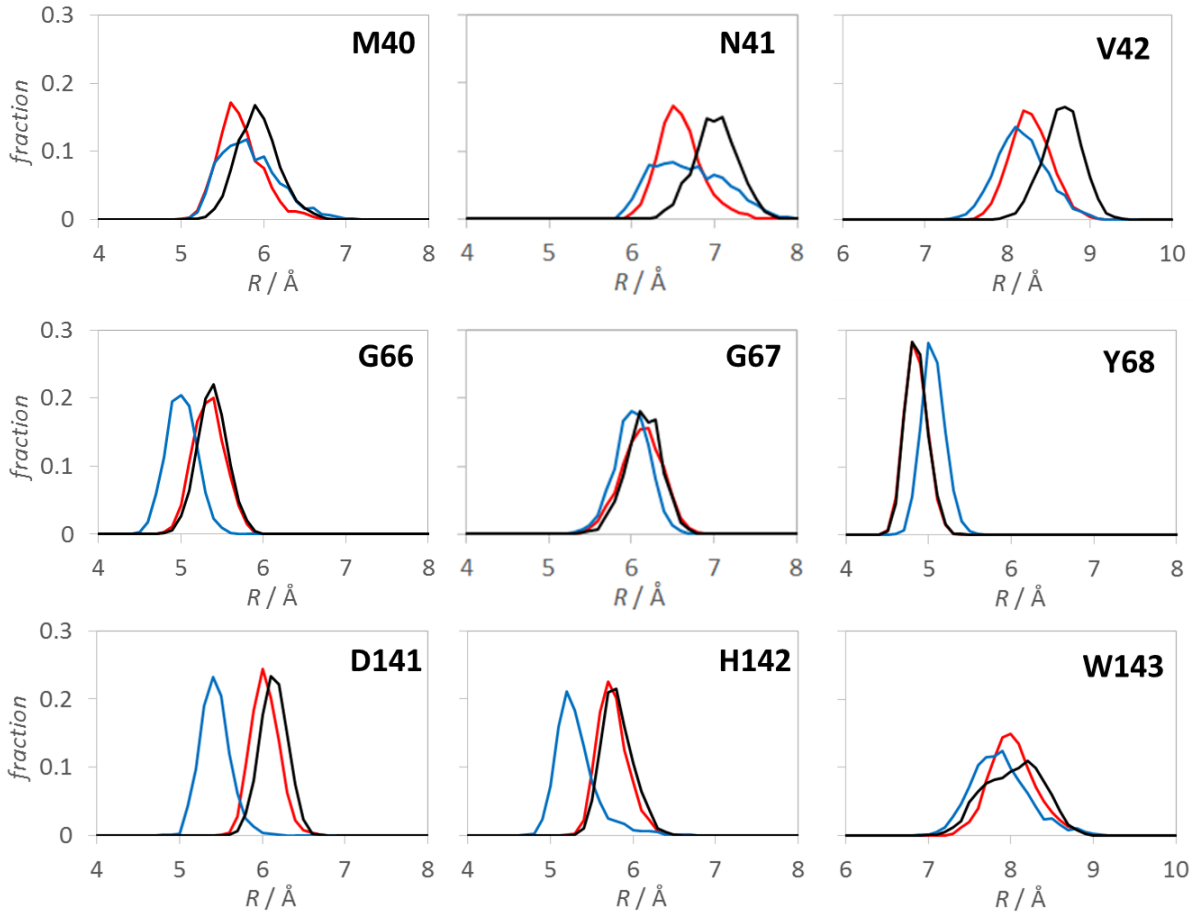

Figure S9. *R*(donor–C_α) from MD simulations for residues with significant changes in chemical shifts for the SAM (black), sinefungin (blue) and SAM* (red) simulations, where D refers to S_1 of SAM and the analogous carbon of sinefungin.

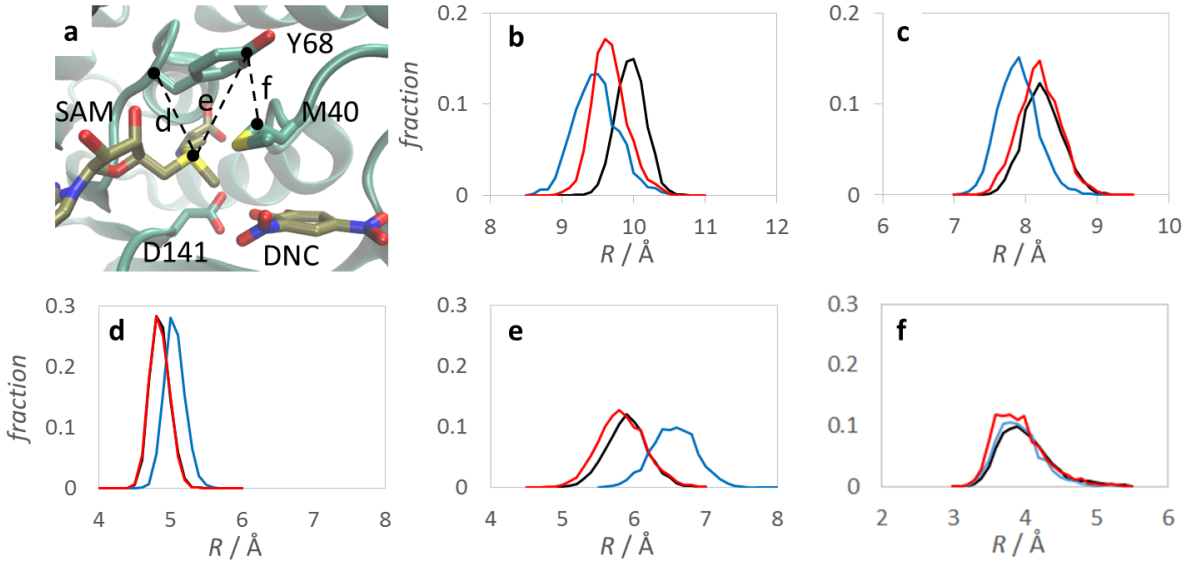

Figure S10. Selected active site distances for the residues shown (a), for the SAM (black), sinefungin (blue) and SAM* (red) MD simulations: M40C_α–D141C_α (b), M40C_α–Y68C_α (c), S_1–Y68C_α (d), S_1–Y68C_Z (e) and M40C_γ–Y68C_Z (f). In sinefungin there is a greater M40–Y68 compaction than in SAM* compared to SAM (c) and as M40 pushes against Y68 the S_1–Y68C_Z distance (e) increases more than the S_1–Y68C_α, Since the M40 sidechain is pushing against the Y68 sidechain, the M40C_γ–Y68C_Z distance does not increase.

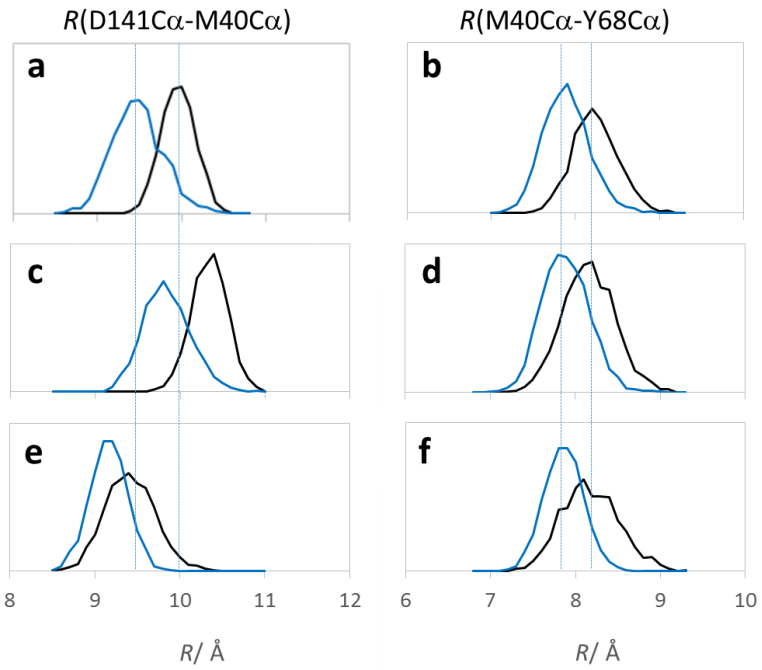

Figure S11. Active site compaction during unconstrained MD simulations (a,b) and SAM (c,d) and sinefungin (e,f) simulations performed with NMR-derived dihedral restraints. For the unconstrained simulation the black and blue lines are for the SAM and sinefungin simulations, respectively; for the restrained simulations the black and blue lines are for the SAM and sinefungin restraints, respectively.

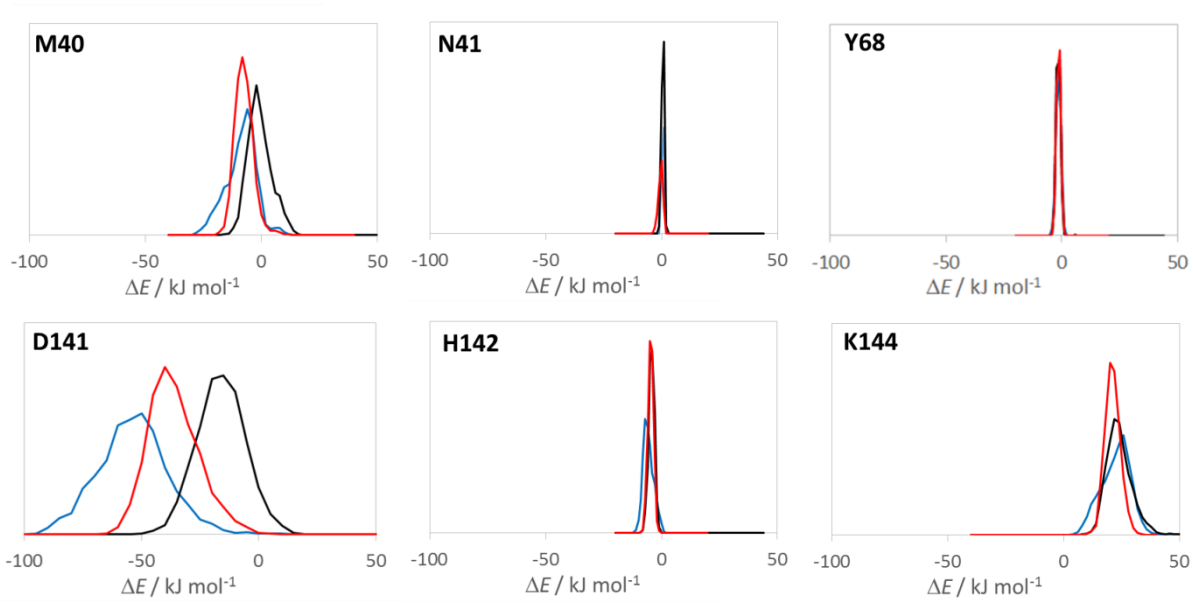

Figure S12. Electrostatic stabilisation energy (ΔE) of sinefungin over SAM by the polar active site residues nearest the SAM methyl or sinefungin NH_3^+ for MD simulations of SAM (black line), SAM* (red line) and sinefungin (blue line).

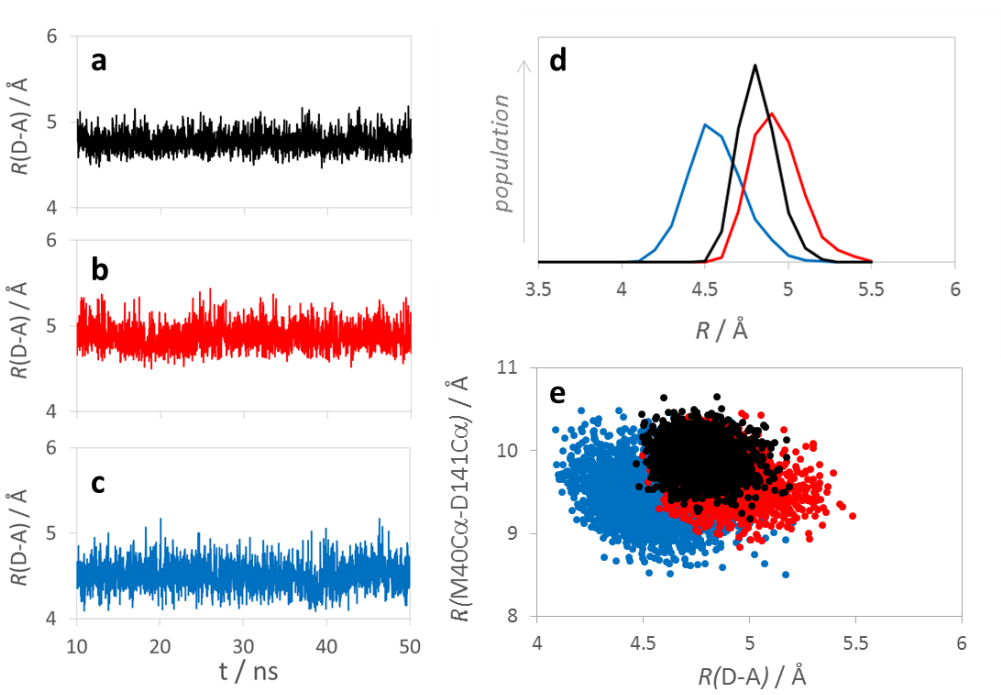

Figure S13. (a-c) Donor-acceptor distances for SAM, SAM* and sinefungin, respectively, for the 50 ns MD simulations used in the analysis; (d) donor-acceptor distance distributions from the same SAM (black line), SAM* (red line) and sinefungin (blue line) MD simulations. (e) D141Cα-M40Cα distance *vs* donor-acceptor distance for the SAM (black), SAM* (red) and sinefungin (blue) simulations.

Note that the donor–acceptor distance distributions in (a) shows the average distance to be longer in the SAM* simulation than the SAM simulation. This is primarily due to a

change in the S_1-C-O_A angle, from an average of 163.5^o in the SAM simulation to 170.3^o in the SAM* simulation. There is little difference (< 0.1Å) between the average C–O_A distances found in each of these simulations as this distance is very close to the van der Waals limit, so the more linear angle forces the donor–acceptor further apart.

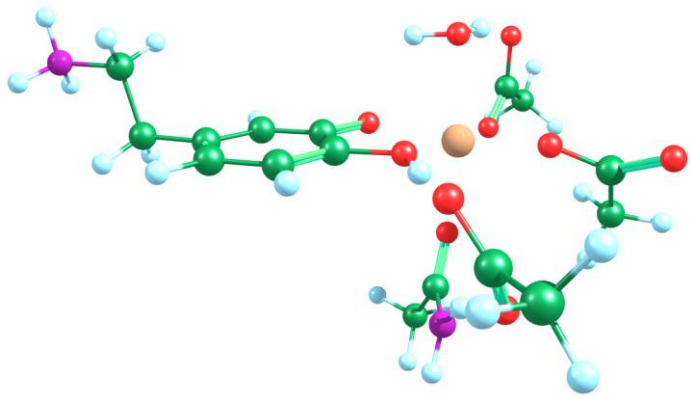

Figure S14. DFT model used for calculating the octahedral Mg^{2+} bonding parameters. Dopamine was used as these parameters were initially prepared for other simulations and consistency of parameters across simulations were desired so the Mg^{2+} bonding parameters will not alter the results.

Table S3. Coordinates for DFT model for calculating the octahedral Mg^{2+} - bonding parameters.

C	3.051529000	-4.814252000	0.308025000
H	3.987902000	-4.411197000	0.703557000
H	3.269242000	-5.665449000	-0.336028000
C	2.308504000	-3.719620000	-0.444807000
O	1.955708000	-2.704804000	0.231242000
O	2.089813000	-3.873594000	-1.677005000
C	4.507028000	-0.252471000	0.520641000
H	5.596881000	-0.230710000	0.501249000
H	4.150470000	-1.265494000	0.713457000
C	3.919334000	0.278480000	-0.786528000
O	4.661137000	0.896264000	-1.578020000
O	2.674481000	0.069408000	-0.986919000
C	0.997532000	0.010650000	4.128652000
H	0.055869000	-0.540508000	4.179165000
H	0.988535000	0.804016000	4.875935000
C	1.185647000	0.522495000	2.718464000
O	1.247746000	-0.287090000	1.776619000
N	1.282045000	1.844674000	2.552012000
H	1.426491000	2.292645000	1.635128000
H	1.231879000	2.449875000	3.356526000
C	1.712843000	5.265377000	-1.298409000
H	0.818939000	5.864262000	-1.490629000
H	2.205712000	5.101896000	-2.260828000
C	1.315970000	3.920460000	-0.695840000

O	1.830532000	3.570347000	0.394592000
O	0.475544000	3.235204000	-1.362112000
Mg	1.040686000	-0.882989000	-0.232039000
O	-0.920277000	-1.537207000	0.058076000
C	-1.856461000	-0.615474000	0.009339000
C	-1.500418000	0.708465000	-0.388716000
O	-0.169650000	0.867201000	-0.681538000
H	0.094109000	1.832740000	-0.909386000
C	-2.441862000	1.722542000	-0.464864000
H	-2.132637000	2.716598000	-0.769008000
C	-3.784377000	1.459891000	-0.146898000
C	-4.171852000	0.179268000	0.247341000
C	-3.210009000	-0.840620000	0.322874000
O	0.597806000	-1.759843000	-2.247142000
H	1.143384000	-2.592502000	-2.169902000
H	-0.292086000	-2.013436000	-1.960181000
H	2.385215000	5.814931000	-0.640069000
H	1.802625000	-0.690479000	4.357958000
H	4.156369000	0.375165000	1.345363000
H	2.455168000	-5.144062000	1.162397000
H	-3.498276000	-1.840368000	0.637100000
C	-5.624059000	-0.121261000	0.565244000
H	-5.690777000	-0.785971000	1.432963000
H	-6.144861000	0.805581000	0.823167000
C	-6.322059000	-0.779376000	-0.624574000
H	-5.866059000	-1.733284000	-0.884122000

H	-6.319818000	-0.134128000	-1.501683000
N	-7.775767000	-1.072355000	-0.314678000
H	-8.237006000	-1.542023000	-1.096993000
H	-8.298828000	-0.214682000	-0.123287000
H	-4.515612000	2.259287000	-0.205320000
H	-7.871474000	-1.677473000	0.504597000

References

1. Czarnota, S., et al., *1H, 15N, 13C backbone resonance assignments of human soluble catechol O-methyltransferase in complex with S-adenosyl-L-methionine and 3,5-dinitrocatechol.* Biomolecular NMR Assignments, 2017. **11**(1): p. 57-61.
2. McCoy, A.J., et al., *Phaser crystallographic software.* Journal of applied crystallography, 2007. **40**(4): p. 658-674.
3. Emsley, P. and K. Cowtan, *Coot: model-building tools for molecular graphics.* Acta Crystallographica Section D: Biological Crystallography, 2004. **60**(12): p. 2126-2132.
4. Afonine, P.V., et al., *phenix. model_vs_data: A high-level tool for the calculation of crystallographic model and data statistics.* Journal of applied crystallography, 2010. **43**(4): p. 669-676.
5. Chen, V.B., et al., *MolProbity: all-atom structure validation for macromolecular crystallography.* Acta Crystallographica Section D: Biological Crystallography, 2010. **66**(1): p. 12-21.
6. Vranken, W.F., et al., *The CCPN data model for NMR spectroscopy: development of a software pipeline.* Proteins, 2005. **59**(4): p. 687-96.
7. Gardner, K.H. and L.E. Kay, *The use of 2H, 13C, 15N multidimensional NMR to study the structure and dynamics of proteins.* Annual Review of Biophysics and Biomolecular Structure, 1998. **27**: p. 357-406.
8. Shen, Y., et al., *TALOS+: a hybrid method for predicting protein backbone torsion angles from NMR chemical shifts.* Journal of Biomolecular NMR, 2009. **44**(4): p. 213-23.
9. Rutherford, K., et al., *Crystal structures of human 108V and 108M catechol O-methyltransferase.* Journal of Molecular Biology, 2008. **380**(1): p. 120-30.
10. Frisch, M., et al., *Gaussian 09 D. 01, Gaussian.* Inc., Wallingford CT, 2016.
11. Becke, A.D., *Density-functional thermochemistry. III. The role of exact exchange.* The Journal of chemical physics, 1993. **98**(7): p. 5648-5652.
12. Shen, Y. and A. Bax, *Protein backbone and sidechain torsion angles predicted from NMR chemical shifts using artificial neural networks.* Journal of biomolecular NMR, 2013. **56**(3): p. 227-241.
13. Laskowski, R.A., et al., *PDBsum: Structural summaries of PDB entries.* Protein Science, 2018. **27**(1): p. 129-134.
14. Hekkelman, M.L., et al., *WIWS: a protein structure bioinformatics Web service collection.* Nucleic acids research, 2010. **38**(suppl_2): p. W719-W723.

4. - Study of S-COMT dynamics by high pressure NMR

Authors: Sylwia Czarnota[a,b], Matthew J. Cliff[a], Nicola J. Baxter[c], Nigel S. Scrutton[a,b], Jonathan P. Waltho[a,b,c], Sam Hay[a,b]*

[a]Manchester Institute of Biotechnology and [b]School of Chemistry, The University of Manchester, 131 Princess Street, Manchester, M1 7DN, United Kingdom

[c]Krebs Institute for Biomolecular Research, Department of Molecular Biology and Biotechnology, The University of Sheffield, Firth Court, Western Bank, Sheffield, S10 2TN, United Kingdom

Abstract

The effect of hydrostatic pressure from 1 bar up to 2500 bar on S-COMT NMR chemical shifts (CS) was studied. The majority of backbone amide resonances shift linearly with pressure in positive nitrogen and positive hydrogen direction (low field ΔHN), indicating that much of the polypeptide backbone structure is sensitive to pressure. A tendency toward low field CS is correlated with a decrease in hydrogen bond distance between the amide nitrogen atom and the oxygen atom of either water or backbone carbonyl groups. On average, CS are larger for helical and coil regions than for strands, but no large structural changes in secondary structure prediction under pressure was observed. Linear CS in the N-H plane are consistent with the protein not undergoing any major conformational change/transition at high pressure, and only exhibiting simple compression within the folded state. Previous Chapter 3 indicated that the ternary complex of COMT is highly organised and experiencing electrostatic stabilization, so we are assuming that it should be quite stable. Incompressibility of the C-terminal loop indicates some additional stabilisation occurring there, possibly via dimerization.

Introduction

High pressure NMR is used to study the structural heterogenity and conformational dynamics of proteins, and protein folding. A protein in solution consists of an ensemble of fluctuating conformers, but the fluctuations are rarely visible in the NMR spectrum, either because they are too rapid or too rare. Application of hydrostatic pressure may perturb the rate of exchange between conformational substates, leading to a fluctuation of conformational equilibrium between different subensembles of conformers characterized with different free-energy levels [1]. Pressure is a fundamental thermodynamic variable for defining conformational state, selecting the population of a conformer according to its relative volume [2, 3]. Protein volume in solution is the sum of three main components: the volume of individual atoms, the volume of internal cavities due to the imperfect atomic packing within the tertiary structure and a contribution due to solvation of peptide bonds and amino acid side chains. Protein compressibility is mostly determined by the compression of the internal cavities and shortening of hydrogen bonds [4]. However, compression is not uniform and can vary across the protein. Some regions can even show a local expansion, caused

by insertion of water molecules into cavities [5]. In rigid proteins, CS typically change linearly with pressure [6]. Such linear dependence of ^{1}H and ^{15}N CS with pressure indicates that no structural transition occurs and the experiment monitors compression within the folded state. It is known that in the presence of ligands and inhibitors, structural changes are typically smaller [5]. Akasaka and others [6] investigated the effect of high hydrostatic pressure (1-2000 bar) on bovine pancreatic trypsin inhibitor (BPTI) by using proton NMR spectroscopy. They reported that all observed CS were linear and reversible. They recognized the strong tendency for low-field proton shifts, which indicated that most of the amide groups form hydrogen bonds either with carbonyls or water molecules and that these hydrogen bonds are shortened by pressure. BPTI was then classified as a practically invariant protein with no structural transition elevated by pressure [2]. Similar behaviour was observed in gurmarin [7], hen lysozyme [8], the immunoglobulin binding domain of streptococcal protein G [9] and simple helical peptides [10, 11]. High pressure NMR methods can also be used to investigate association/dissociation equilibria of oligomeric or aggregated proteins, with pressure shown to dissociate dimers, tetramers and oligomers into monomers. Reported causes for the pressure induced dissociation are: imperfect van der Waals contacts between monomers, solvation of the hydrophobic contacts in the oligomers, a decrease in the size of the internal cavities and an increase in the extent of hydration etc. [12-16]. However, it is also possible that oligomers do not dissociate under pressure. It has been shown that β-amylase tetramer experienced the perturbation of the local conformation in the pressure range up to 4000 bar, but preserved the oligomeric state [17]. Similar results have been reported for dimeric LADH and AP, exposed to 3000 bar [18, 19]. More examples of oligomers which are stable under pressure are available [20-22].

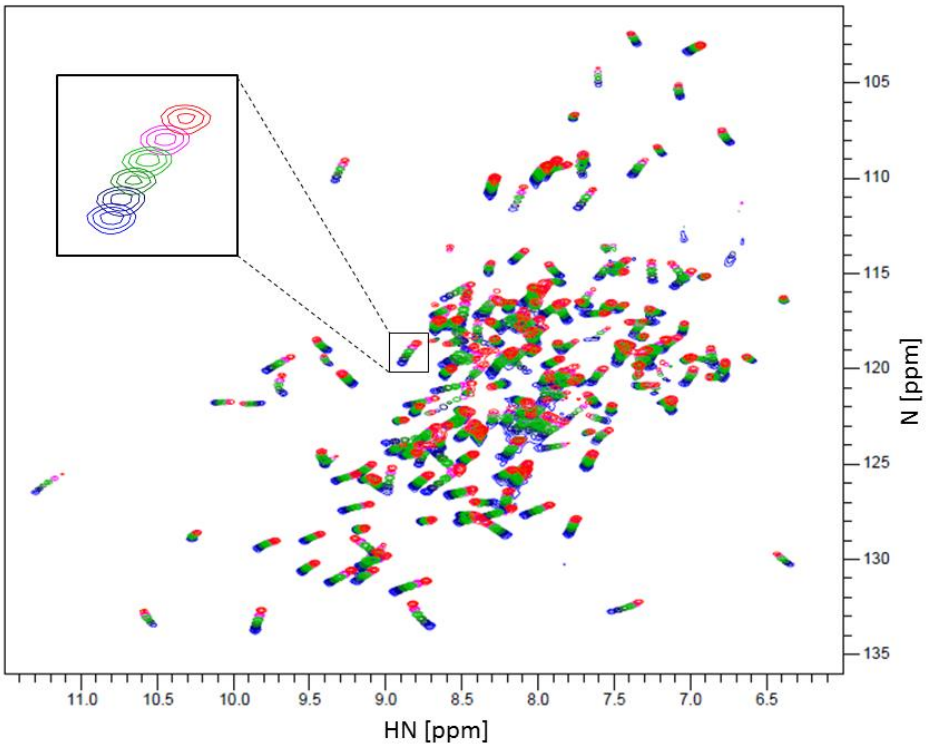

Figure 1. ^{15}N-TROSY spectra of COMT:SAM:DNC:Mg^{2+} complex at pressures from 1 bar (red) to 2.5 kbar (blue) recorded at 600 MHz at 25°C.

Results and discussion

The effect on pressure of two human S-COMT complexes was studied. In this study the COMT:DNC:Mg^{2+}:SAM ternary complex will be called Complex 1 and the COMT:DNC:Mg^{2+}:Sinefungin ternary complex will be called Complex 2. There were 200 residues in the N-H plane assigned in a pressure ^{15}N TROSY set of experiments for both complexes. To obtain information about carbon shifts, perdeuterated ^{13}C-^{15}N HNCO, HN(CA)CB and HN(COCA)CB experiments for 1 bar and 2500 bar were recorded. Among them, 20% and 10% of C_{α} assignments were missing for Complex 1 and Complex 2, respectively. 17% and 7.5% of C_{β} assignment were missing in the same manner. 4% of C' assignment in high pressure was missing for both complexes.

Table 1. Sausage diagrams of Complex 1 and Complex 2 representing chemical shift pressure response up to 2500 bar for the most compressible residues (red); uncompressible residues (white) and unassigned residues (black).

Complex 1: COMT:DNC:Mg^{2+}:SAM	**Complex 2:** COMT:DNC:Mg^{2+}:Sinefungin
ΔδN absolute value shifts (darkest red colour represents ΔN = 2.2ppm)	
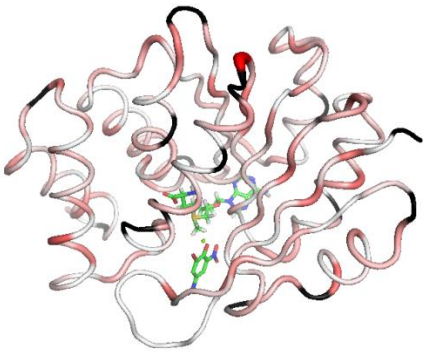	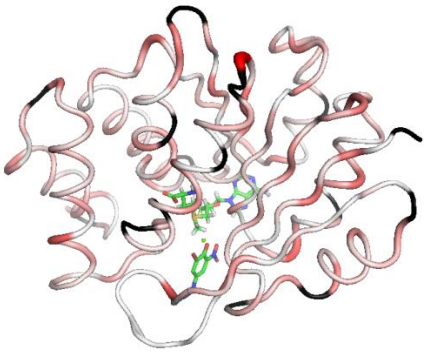
ΔδH absolute value shifts (darkest red colour represents ΔH = 0.3 ppm)	
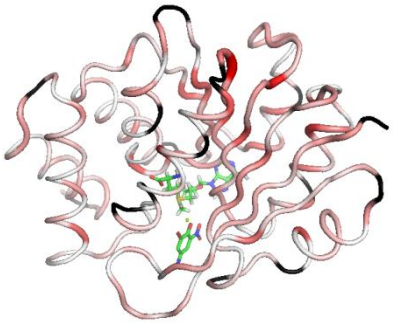	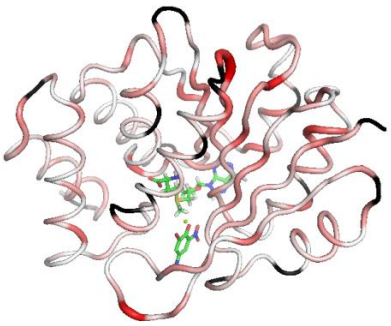

Overall, the patterns of CS between the two complexes are very similar (**SI Figure 1, Table 1**). The correlation between both the H and N CS changes with pressure between the two complexes shows very good agreement with R^2 value of 0.94 for ΔN and 0.93 for ΔH (**SI Figure 2**). The majority of H-N resonances (65% for Complex 1 and 61% for Complex 2) shift linearly to higher resonance frequencies with increasing pressure (**Figure 1; SI Figures 7-10**), which is common [23, 24] and indicates that much of the polypeptide backbone structure is sensitive to pressure. This effect most likely results from a compression of the hydrogen bond distance between the amide nitrogen atom and the oxygen atom of either water or a carbonyl group [25].

In COMT the greatest compression generally occurs for surface exposed hydrogen bonds to water (e.g. S60, K109, D110, D178).

25% of residues for both complexes (50 residues out of assigned 200 in Complex 1 and 58 out of assigned 200 in Complex 2) experience an upfield shift in the H plane (to smaller ppm numbers) and an upfield shift in the N plane, (to higher ppm numbers; N has negative gyromagnetic ratio, so the effect is opposite to H). This opposite effect is likely a reflection of a combination of effects (hydrogen bond geometry changes, backbone and sidechain dihedral angle changes or changes in the dynamic ensemble). 5% of residues are incompressible or independent of pressure (**SI Figure 13**, residues coloured in yellow) and display a negligible response in the N-H dimension to the application of pressure over the 2500 bar range. Compared to amide protons, amide nitrogen pressure shifts in S-COMT are large, as expected (average ΔN=0.52 ppm/2.5 kbar in Complex 1 and average ΔN=0.53 ppm/2.5 kbar in Complex 2; while average proton shift for both complexes is ΔH = 0.08 ppm/ 2.5kbar).

15.5% of residues in Complex 1 and 17.5% of residues in Complex 2 experience non-linear CS (with linear coefficient R^2<0.9) induced by pressure (**Figure 2** and **SI Figure 13**). These residues are located mostly in α-helices and loops, indicating greater stabilisation of β-sheets. A decrease in alpha helicity with the pressure is noticeable.

Significant differences between Complex 1 and Complex 2 were observed mostly in ΔN (**SI Figure 3**). Those shifts are larger in Complex 2, which indicates more compressibility for the complex with sinefungin. The biggest differences were observed for residues R75 ($\Delta N_{Complex1-Complex2}$=-0.297 ppm), D145 ($\Delta N_{Complex1-Complex2}$=-0.698 ppm) and K162 ($\Delta N_{Complex1-Complex2}$=-0.359 ppm). They are all hydrogen bonded to water molecules. Torsion angles of K162 may be perturbed by subtle buffer changes between both complexes.

When looking at the overall pressure induced shifts pattern in COMT structure for both complexes in the N-H plane, two regions of stabilisation are visible, indicated by several incompressible residues (see **SI Figure 10**). Firstly, stabilisation occurs between two N-terminal α-helices. Residues L10, A28, D30 and E34 are almost incompressible, indicating pressure stability. Secondly, the whole C-terminal coil from F197 until D205 appears to be relatively stable, except L198. This is quite unusual behaviour for a coil. E199 is likely to be rigidly held in place by hydrogen bonding to the DNC. D205 is

located on the surface, but appears incompressible. That stabilisation of the C-terminus may be caused by the formation of a dimer through this interface.

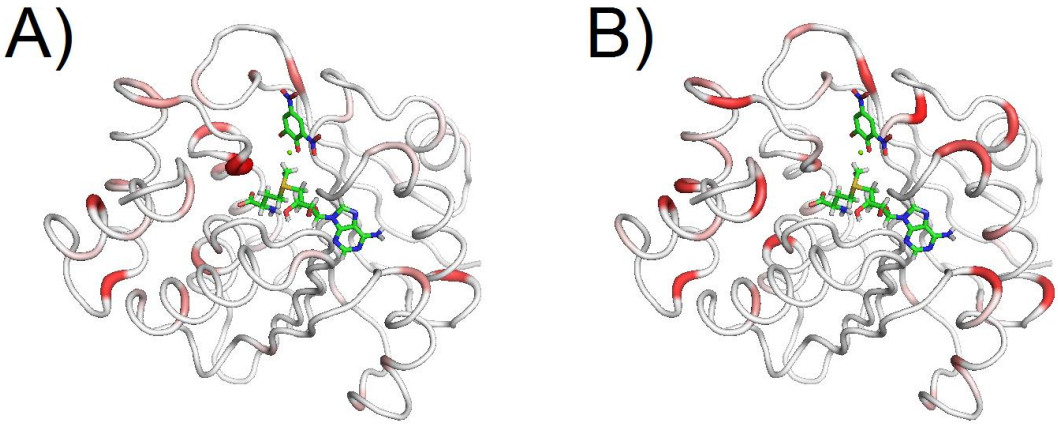

Figure 2. Putty diagrams representing the highest deviations from linear CS induced by pressure. Obtained by examination of R^2 linear coefficient (white colour – highest R^2, red colour – lowest R^2). A - complex 1; B – complex 2.

Secondary Structure

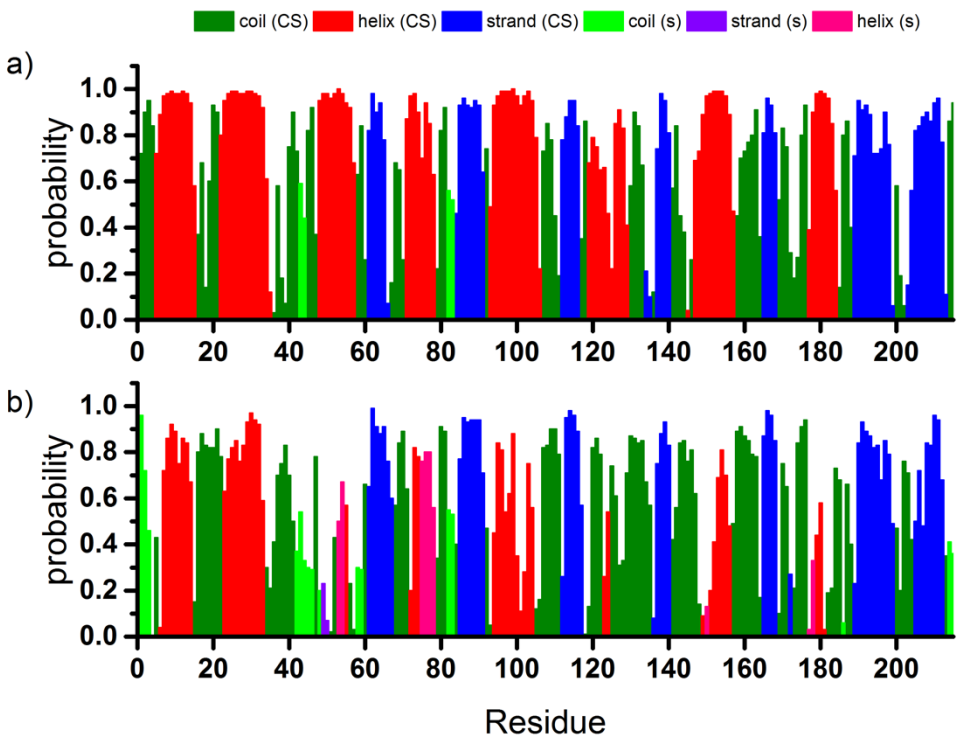

Figure 3. Secondary structure prediction of S-COMT in the S-COMT:SAM:DNC:Mg^{2+} complex obtained with TALOS-N [26] based on CS at ambient pressure (a) and 2500 bar (b). CS –TALOS-N SS prediction based on chemical shift; s – TALOS-N SS prediction based on sequence.

Secondary structure (SS) prediction using the TALOS-N algorithm [26] indicates that both COMT complexes under pressure are less α-helical (**Figure 3** and **SI Figure 4, SI Table 1**). These data are consistent with non-linear CS for α-helices and the upfield direction of C_α shifts (**Figure 4**), which are dominated by dihedral angle changes and can be used to calculate structural changes. The size of the average carbon CS changes with pressure (**Figure 4**) is similar to published pressure shifts for protein G and barnase [27]. Large C_α shifts appear in case of conformational changes, like reported for talin [23]. In both COMT complexes, those residues that experience larger carbon CS are located in the loops (D150, I172, D178). D150 and I172 are related to active site binding residues.

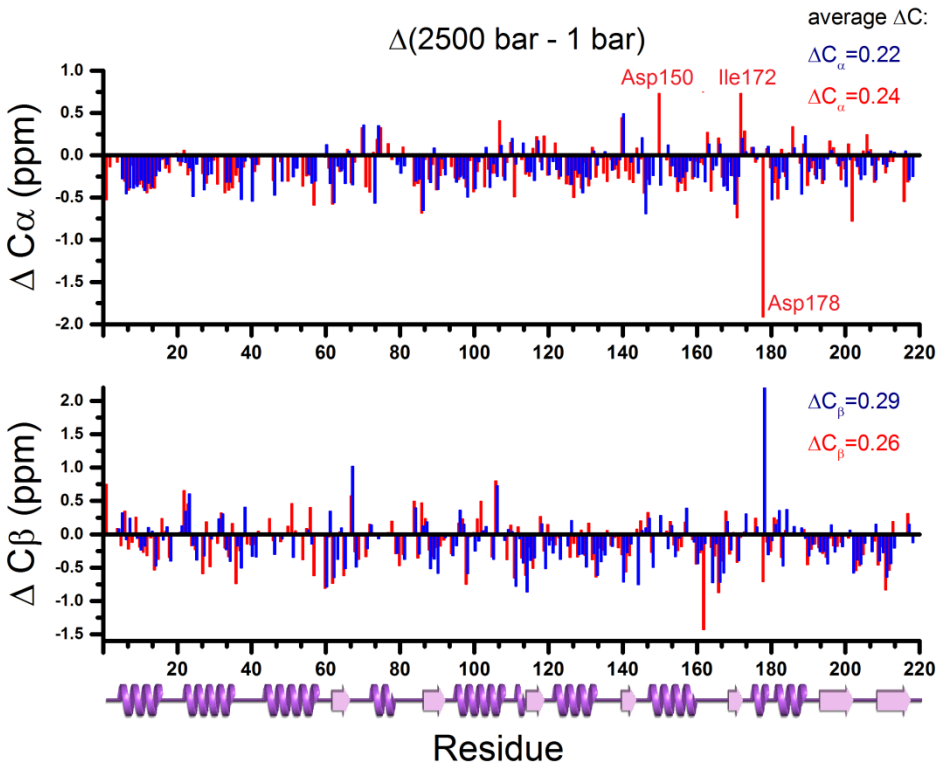

Figure 4. Histograms displaying the chemical shift changes in C_α shift (top) and C_β shift (bottom) as a function of pressure in COMT:DNC:Mg^{2+}:SAM (blue) and COMT:DNC:Mg^{2+}:Sinefungin (red) in ppm. The bar at the bottom indicates the secondary structure elements from the crystal structure of COMT:DNC:Mg^{2+}:SAM complex (PDB: 6I3C, α-helix darker colour, β-sheet lighter colour).

The TALOS-N analysis flagged 23% of residues in both complexes with a 'warning' in the torsion angle calculations, which means that prediction for those residues may contain a significant error. This algorithm is based on CS from the BMRB library and pressure induced shifts are not typical of these data. This may cause errors and high

uncertainty in secondary structure predictions of the complexes at high pressure. What is more, TALOS has an average uncertainty of approximately 13° for φ angle and 12° for ψ angle [28]. However, differences in torsion angles between 2500 bar and 1 bar predicted from TALOS are informatively presented in **SI Figure 14**, excluding residues flagged with a 'warning'. We have also employed CS-ROSETTA [29] for structure calculations to provide an alternative analysis. In the CS-ROSETTA protocol, the query sequence and CS values are compared to the PDB data in three and nine residue fragments. Then, CS-ROSETTA uses a Monte-Carlo simulated annealing process to assemble the fragments. Results obtained show no significant difference between the structures of either complex predicted at 1 bar and 2500 bar structures. The N- and C-termini appear to be disordered, but this is a known limitation of the calculation and these regions can be ignored. Except for these terminal residues, the structure appears to be rigid (little significant change with pressure) and is very similar to known S-COMT crystal structures (**SI Figure 5**).

We have also compared SS changes elevated by pressure to changes calculated for the random-coil model peptide in pressure, using published data for $^{13}C_\alpha$ [30] and ^{15}N [31]. No correlation has been found (see **SI Figure 12**), indicating that high pressure derived shift changes in COMT are not dependent on SS.

Conclusions

The linearity of the majority of pressure induced CS changes suggests that both ternary complexes of S-COMT studied are relatively rigid and the structure largely invariant with pressure range between 1 and 2500 bar. These data are consistent with the protein not undergoing any major conformational change/transition at high pressure, and only exhibiting simple compression within the folded state. The upfield direction of C_α CS indicates a decrease in alpha helicity with the pressure, but these CS changes are not large when compared to protein experienced conformational changes [23]. Incompressibility of the C-terminal loop indicates some additional stabilisation in that region, which is likely derived from DNC binding and possibly as it plays a role in a transient dimer interface.

However, dihedrals calculations by TALOS or CS-ROSETTA may not provide the accuracy of the sub-Å structural changes. For the future studies, we propose to use the measured Cα and Cβ chemical shift changes to derive optimum target values for the

backbone dihedrals, and then use the molecular dynamics procedure to calculate a structure based on these angles.

Experimental details

Isotopically-labelled compounds: ^{15}N-labelled ammonium chloride (99%), $^{13}C_6$,$^{2}H_7$-labelled D-Glucose (U-$^{13}C_6$, 99%; 1,2,3,4,5,6,6-d_7 97-98%) and deuterium oxide (99.8%) were purchased from Goss Scientific. 3,5-dinitrocatechol (DNC), S-adenosyl-L-methionine (SAM) and sinefungin (5′-deoxy-5′-(1,4-diamino-4-carboxybutyl)adenosine) were purchased with the highest purity available from Sigma-Aldrich (Poole, UK) and used as received.

Expression and purification of human soluble catechol-O-methyltransferase NMR studies was performed as described previously [32]. NMR samples containing 0.5 mM human S-COMT, 2.5 mM $MgCl_2$, 5 mM DNC and 5 mM SAM or 5 mM sinefungin in 50 mM Tris-HCl buffer, 50 mM NaCl, 10 mM DTT, 2 mM NaN_3, pH 7.5 were loaded into high pressure NMR tubes. $^{2}H_2O$ was added to the protein samples (10% v/v) to allow a deuterium lock and 0.5% v/v trimethylsilyl propanoic acid (TSP) was added as a reference signal.

All NMR measurements were performed at 298 K. Preliminary perdeuterated ^{15}N-TROSY spectra for COMT:DNC:Mg^{2+}:Sinefungin complex were collected on a Bruker Avance 600 MHz magnet equipped with a 5 mm ^{1}H–^{13}C/^{15}N/^{2}H CPTXI cyroprobe at the University of Sheffield, in the range of 1 bar to 2500 bar pressure at 250 bar increments. All following spectra were recorded at the University of Manchester, Manchester Institute of Biotechnology. Perdeuterated ^{15}N-TROSY data for COMT:DNC:Mg^{2+}:SAM were collected on a 600 MHz Bruker four-channel liquid-state spectrometer equipped with a high sensitivity TXI cryoprobe with cooled proton channel from 1 bar to 2500 bar pressure at 500 bar increments. Perdeuterated ^{13}C-^{15}N HNCO, HN(CA)CB and HN(COCA)CB data sets for 1 bar and 2500 bar were recorded on an 800 MHz Bruker Avance III NMR spectrometer fitted with a TCI cryoprobe equipped with Z gradients and TopSpin software version 3.2. High pressure was applied to the sample via a remote Xtreme-60 Syringe pump from Deadalus Innovations LLC. 200 µl of sample were placed in a 2.5 kbar high pressure NMR tube (3 mm I.D. x 5 mm O.D.). The sample surface was covered in a thin layer of paraffin oil and the application of pressure was transferred to the sample from the syringe pump.

Assignments of pressure spectra were based on assignments published before under BMRB accession codes: 26848 (COMT:DNC:Mg^{2+}:SAM) and 26851 (COMT:DNC:Mg^{2+}:Sinefungin) [32]. Pressure induced shifts were monitored using CCPNMR Analysis [33] and fitted to linear equations using in-house Python scripts. Backbone dihedral angles were calculated for 1 bar pressure and 2500 bar pressure using TALOS-N [26] by uploading the backbone $^{1}H_{N}$, ^{15}N, $^{13}C_{\alpha}$, $^{13}C_{\beta}$ and $^{13}C'$ chemical shifts to the TALOS-N webserver. Data for residues flagged with 'warning' were not taken for further investigations, due to high uncertainty in chemical shift prediction.

References

1. Akasaka, K., *Probing Conformational Fluctuation of Proteins by Pressure Perturbation.* Chemical Reviews, 2006. **106**(5): p. 1814-1835.
2. Kremer, W., *High-pressure NMR studies in proteins*, in *Annual Reports on NMR Spectroscopy*. 2006, Elsevier. p. 177-203.
3. Li, H. and K. Akasaka, *Conformational fluctuations of proteins revealed by variable pressure NMR.* Biochimica et Biophysica Acta (BBA)-Proteins and Proteomics, 2006. **1764**(3): p. 331-345.
4. Mozhaev, V.V., et al., *High pressure effects on protein structure and function.* Proteins-Structure Function and Genetics, 1996. **24**(1): p. 81-91.
5. Williamson, M.P., *Pressure-dependent conformation and fluctuation in folded protein molecules*, in *High Pressure Bioscience*. 2015, Springer. p. 109-127.
6. Li, H., H. Yamada, and K. Akasaka, *Effect of pressure on individual hydrogen bonds in proteins. Basic pancreatic trypsin inhibitor.* Biochemistry, 1998. **37**(5): p. 1167-1173.
7. Inoue, K., et al., *High pressure NMR study of a small protein, gurmarin.* Journal of biomolecular NMR, 1998. **12**(4): p. 535-541.
8. Refaee, M., et al., *Pressure-dependent changes in the solution structure of hen egg-white lysozyme.* Journal of molecular biology, 2003. **327**(4): p. 857-865.
9. Li, H., et al., *Pressure alters electronic orbital overlap in hydrogen bonds.* Journal of biomolecular NMR, 2000. **18**(3): p. 207-216.
10. Iwadate, M., et al., *Pressure-dependent changes in the structure of the melittin α-helix determined by NMR.* Journal of biomolecular NMR, 2001. **19**(2): p. 115-124.
11. Orekhov, V.Y., et al., *Pressure effect on the dynamics of an isolated α-helix studied by 15N-1H NMR relaxation.* Journal of biomolecular NMR, 2000. **17**(3): p. 257-263.
12. Silva, J.L., D. Foguel, and C.A. Royer, *Pressure provides new insights into protein folding, dynamics and structure.* Trends in biochemical sciences, 2001. **26**(10): p. 612-618.
13. Foguel, D. and J.L. Silva, *New insights into the mechanisms of protein misfolding and aggregation in amyloidogenic diseases derived from pressure studies.* Biochemistry, 2004. **43**(36): p. 11361-11370.
14. Foguel, D., et al., *Dissociation of amyloid fibrils of α-synuclein and transthyretin by pressure reveals their reversible nature and the formation of water-excluded cavities.* Proceedings of the National Academy of Sciences, USA, 2003. **100**(17): p. 9831-9836.
15. Peng, X., J. Jonas, and J.L. Silva, *Molten-globule conformation of Arc repressor monomers determined by high-pressure 1H NMR spectroscopy.* Proceedings of the National Academy of Sciences, USA, 1993. **90**(5): p. 1776-1780.

16. Niraula, T.N., et al., *Decreased thermodynamic stability as a crucial factor for familial amyloidotic polyneuropathy.* Journal of molecular biology, 2002. **320**(2): p. 333-342.

17. Tanaka, N., D. Mitani, and S. Kunugi, *Pressure-induced perturbation on the active site of β-amylase monitored from the sulfhydryl reaction.* Biochemistry, 2001. **40**(20): p. 5914-5920.

18. Cioni, P. and G.B. Strambini, *Pressure/temperature effects on protein flexibilty from acrylamide quenching of protein phosphorescence.* Journal of molecular biology, 1999. **291**(4): p. 955-964.

19. Cioni, P. and G.B. Strambini, *Pressure effects on the structure of oligomeric proteins prior to subunit dissociation.* Journal of molecular biology, 1996. **263**(5): p. 789-799.

20. Balny, C., *High Pressure and Protein Oligomeric Dissociation.* High Pressure Research, 2002. **22**(3-4): p. 737-741.

21. Suarez, M.C., S.S. Lehrer, and J.L. Silva, *Local heterogeneity in the pressure denaturation of the coiled-coil tropomyosin because of subdomain folding units.* Biochemistry, 2001. **40**(5): p. 1300-1307.

22. Dallet, S. and M.-D. Legoy, *Hydrostatic pressure induces conformational and catalytic changes on two alcohol dehydrogenases but no oligomeric dissociation.* Biochimica et Biophysica Acta (BBA) - Protein Structure and Molecular Enzymology, 1996. **1294**(1): p. 15-24.

23. Baxter, N.J., et al., *Pressure-Dependent Chemical Shifts in the R3 Domain of Talin Show that It Is Thermodynamically Poised for Binding to Either Vinculin or RIAM.* Structure, 2017. **25**(12): p. 1856-1866. e2.

24. Kitahara, R., et al., *Pressure-induced chemical shifts as probes for conformational fluctuations in proteins.* Progress in nuclear magnetic resonance spectroscopy, 2013. **71**: p. 35-58.

25. Akasaka, K., et al., *Pressure response of protein backbone structure. Pressure-induced amide 15 N chemical shifts in BPTI.* Protein Science, 1999. **8**(10): p. 1946-1953.

26. Shen, Y. and A. Bax, *Protein backbone and sidechain torsion angles predicted from NMR chemical shifts using artificial neural networks.* Journal of biomolecular NMR, 2013. **56**(3): p. 227-241.

27. Wilton, D.J., et al., *Pressure-dependent 13C chemical shifts in proteins: origins and applications.* Journal of Biomolecular NMR, 2009. **44**(1): p. 25-33.

28. Cornilescu, G., F. Delaglio, and A. Bax, *Protein backbone angle restraints from searching a database for chemical shift and sequence homology.* Journal of biomolecular NMR, 1999. **13**(3): p. 289-302.

29. Lange, O.F., et al., *Determination of solution structures of proteins up to 40 kDa using CS-Rosetta with sparse NMR data from deuterated samples.* Proceedings of the National Academy of Sciences, USA, 2012. **109**(27): p. 10873-10878.

30. Erlach, M.B., et al., *Pressure dependence of backbone chemical shifts in the model peptides Ac-Gly-Gly-Xxx-Ala-NH2.* Journal of biomolecular NMR, 2016. **65**(2): p. 65-77.

31. Koehler, J., et al., *Pressure dependence of 15N chemical shifts in model peptides Ac-Gly-Gly-X-Ala-NH2.* Materials, 2012. **5**(10): p. 1774-1786.

32. Czarnota, S., et al., *1H, 15N, 13C backbone resonance assignments of human soluble catechol O-methyltransferase in complex with S-adenosyl-L-methionine and 3,5-dinitrocatechol.* Biomolecular NMR Assignments, 2017. **11**(1): p. 57-61.

33. Vranken, W.F., et al., *The CCPN data model for NMR spectroscopy: development of a software pipeline.* Proteins, 2005. **59**(4): p. 687-96.

Supporting information

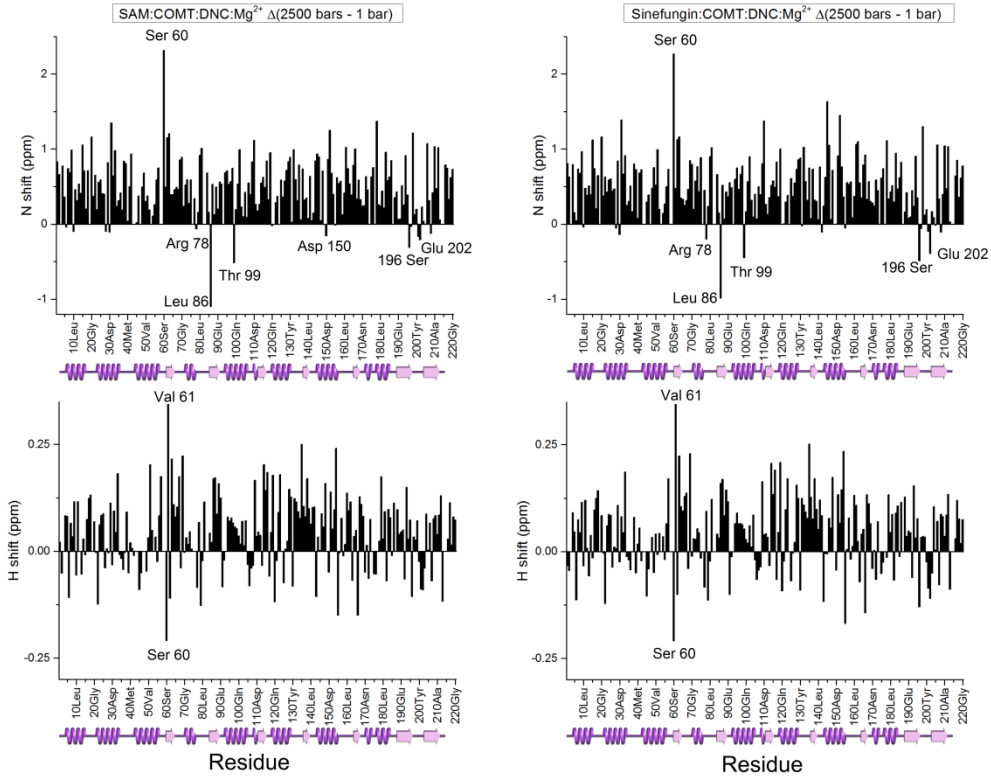

SI Figure 1. Histograms displaying the chemical shift changes in H shift (ppm) and N shift (ppm) as a function of pressure in COMT:DNC:Mg^{2+}:SAM (right) and COMT:DNC:Mg^{2+}:Sinefungin (left). The bar below graphs represents protein secondary structure (PDB: 6I3C, α-helix darker colour, β-sheet lighter colour).

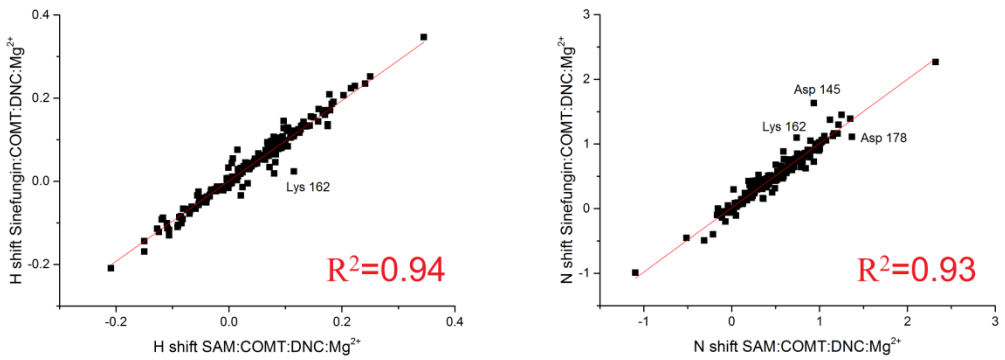

SI Figure 2. Correlations between the difference in shifts (in ppm) for two COMT complexes, elevated by exposure to 2500 bar. Data presented for ΔH (left) and ΔN (right) shifts, obtained by subtraction of 1 bar shifts from 2500 bar shifts (Δ(2500 bar shifts – 1 bar shifts)).

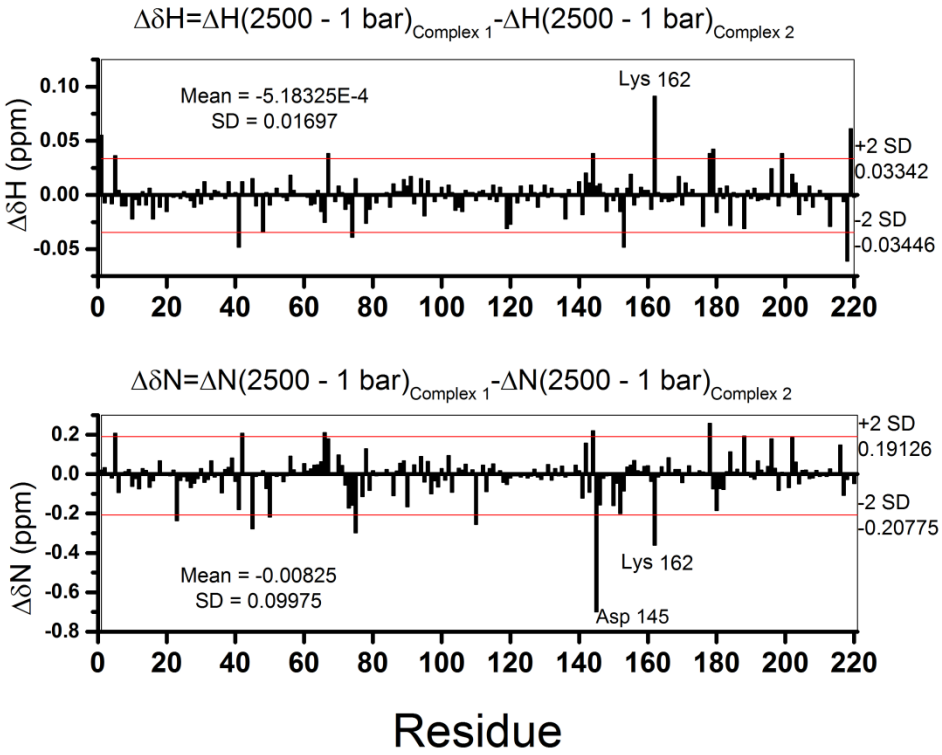

SI Figure 3. Histograms displaying the H and N chemical shift changes difference between COMT:DNC:Mg^{2+}:SAM and COMT:DNC:Mg^{2+}:Sinefungin. 2 x SD (standard deviation) is presented as a solid red line.

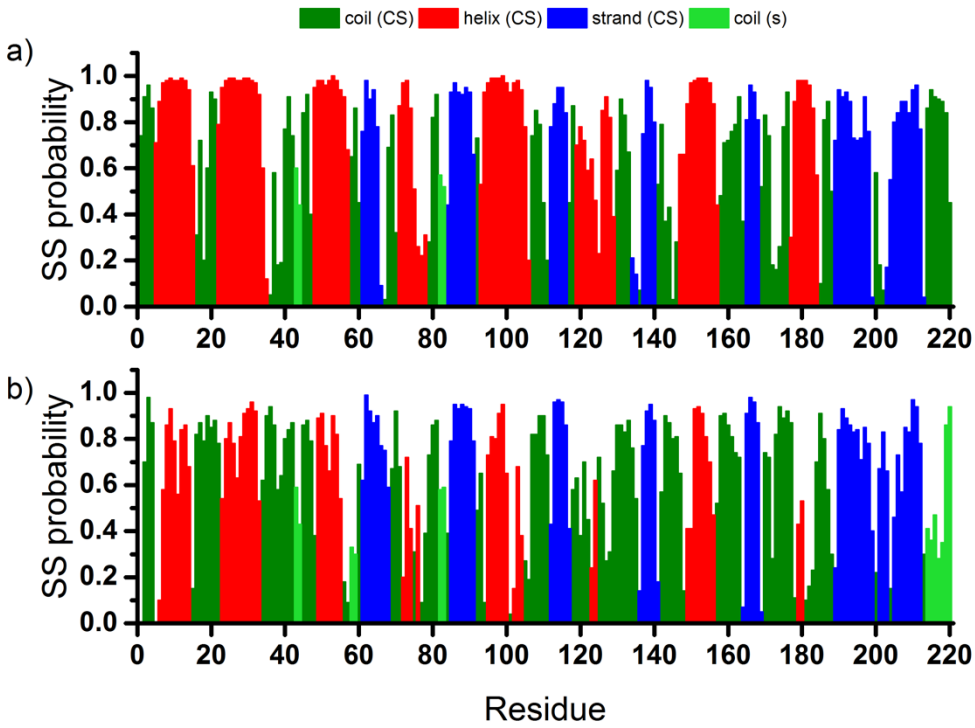

SI Figure 4. Secondary structure prediction of S-COMT in the S-COMT:Sinefungin:DNC:Mg^{2+} complex obtained with TALOS-N based on chemical shifts in ambient pressure (a) and 2500 bar (b). CS – prediction based on chemical shift; s – sequence based prediction.

	COMT:DNC:Mg^{2+}:SAM		COMT:DNC:Mg^{2+}:Sinefungin	
	1 bar	2500 bar	1 bar	2500 bar
secondary structure	number of residues	number of residues	number of residues	number of residues
coil	82	113	81	113
helix	87	52	88	56
strand	51	55	51	51

SI Table 1. Differences in secondary structure elevated by pressure rendered using TALOS-N.

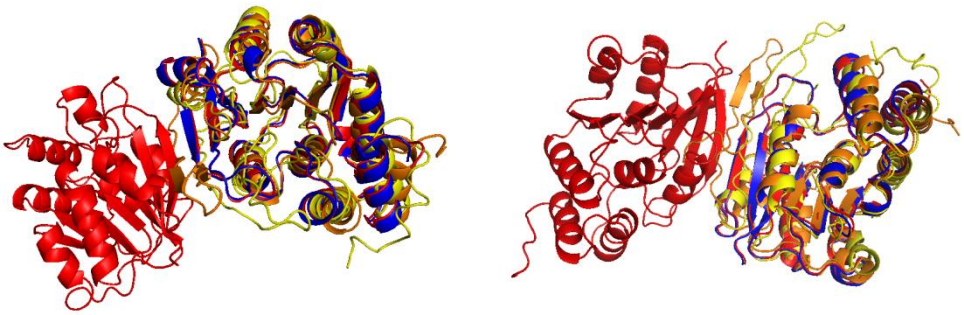

SI Figure 5. Two orthogonal structure representations of S-COMT alignments. Red: S-COMT:Sinefungin:DNC:Mg^{2+} complex (PDB:6I3D); blue: S-COMT:SAM:DNC:Mg^{2+} complex (PDB:6I3C); yellow: CS-ROSETTA calculated structure for S-COMT:Sinefungin:DNC:Mg^{2+} CS in 1 bar; orange: CS-ROSETTA calculated structure for S-COMT:Sinefungin:DNC:Mg^{2+} CS in 2500 bar.

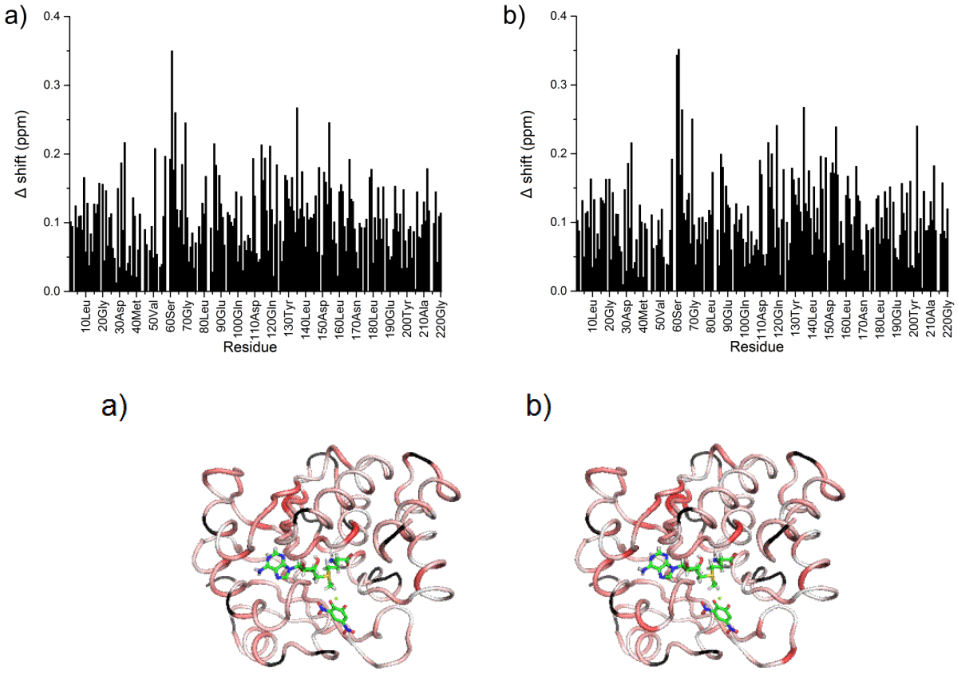

SI Figure 6. Hypotenuse shift in the N-H plane (ppm), rescaled for N by scaling factor c=0.12 ($\Delta = \sqrt{(\delta H)^2 + [c(\delta N)]^2}$) per residue for a) COMT:DNC:Mg^{2+}:SAM complex; b) COMT:DNC:Mg^{2+}:Sinefungin complex. Below are sausage diagrams of both complexes representing most labile residues (red); most stabile residues (white) and unassigned residues (black).

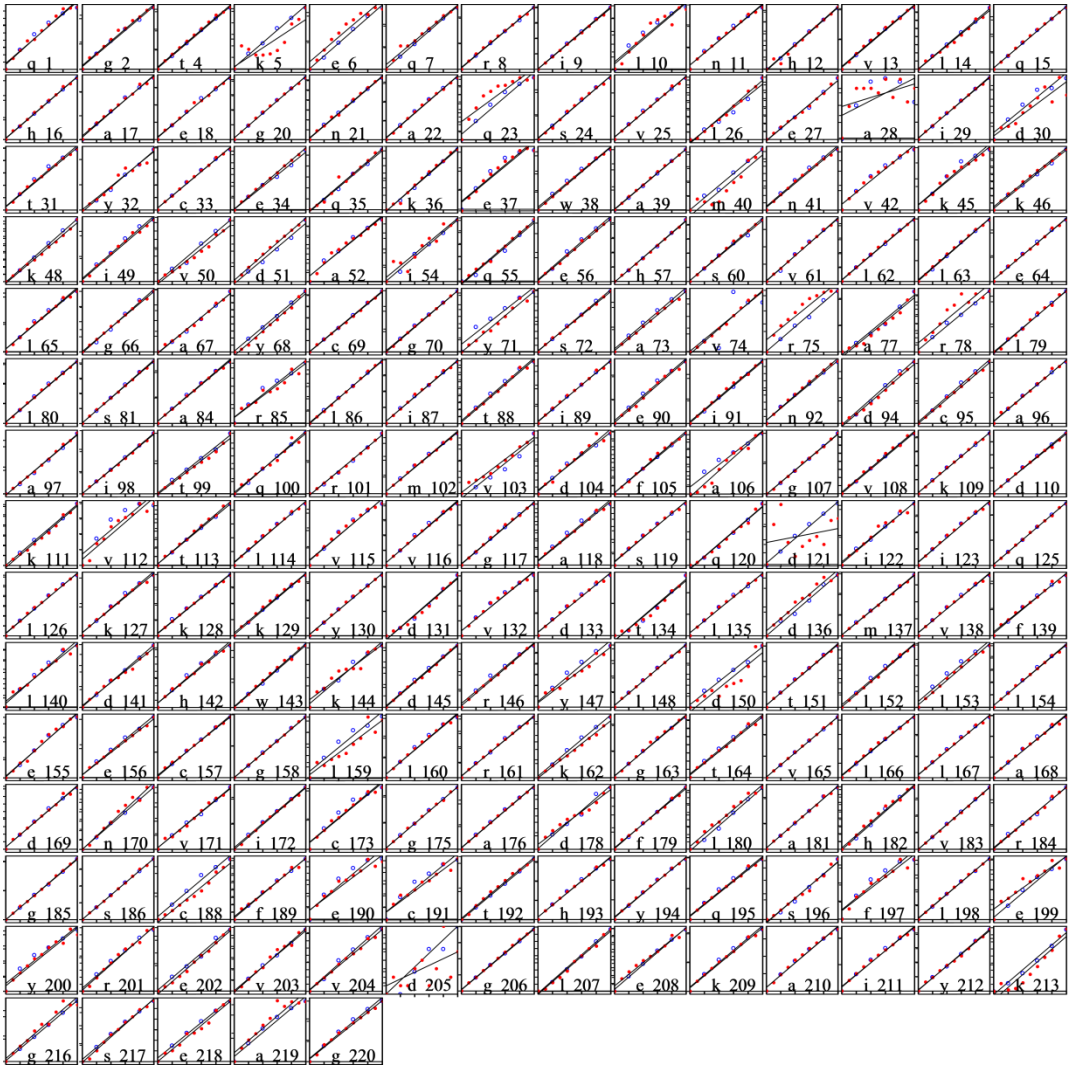

SI Figure 7. Hypotenuse shift in the N-H plane (ppm), rescaled for N by scaling factor c=0.12 ($\Delta = \sqrt{(\delta H)^2 + [c(\delta N)]^2}$) per assigned residue for COMT:DNC:Mg^{2+}:SAM complex (blue) and COMT:DNC:Mg^{2+}:Sinefungin complex (red) fitted to linear equation.

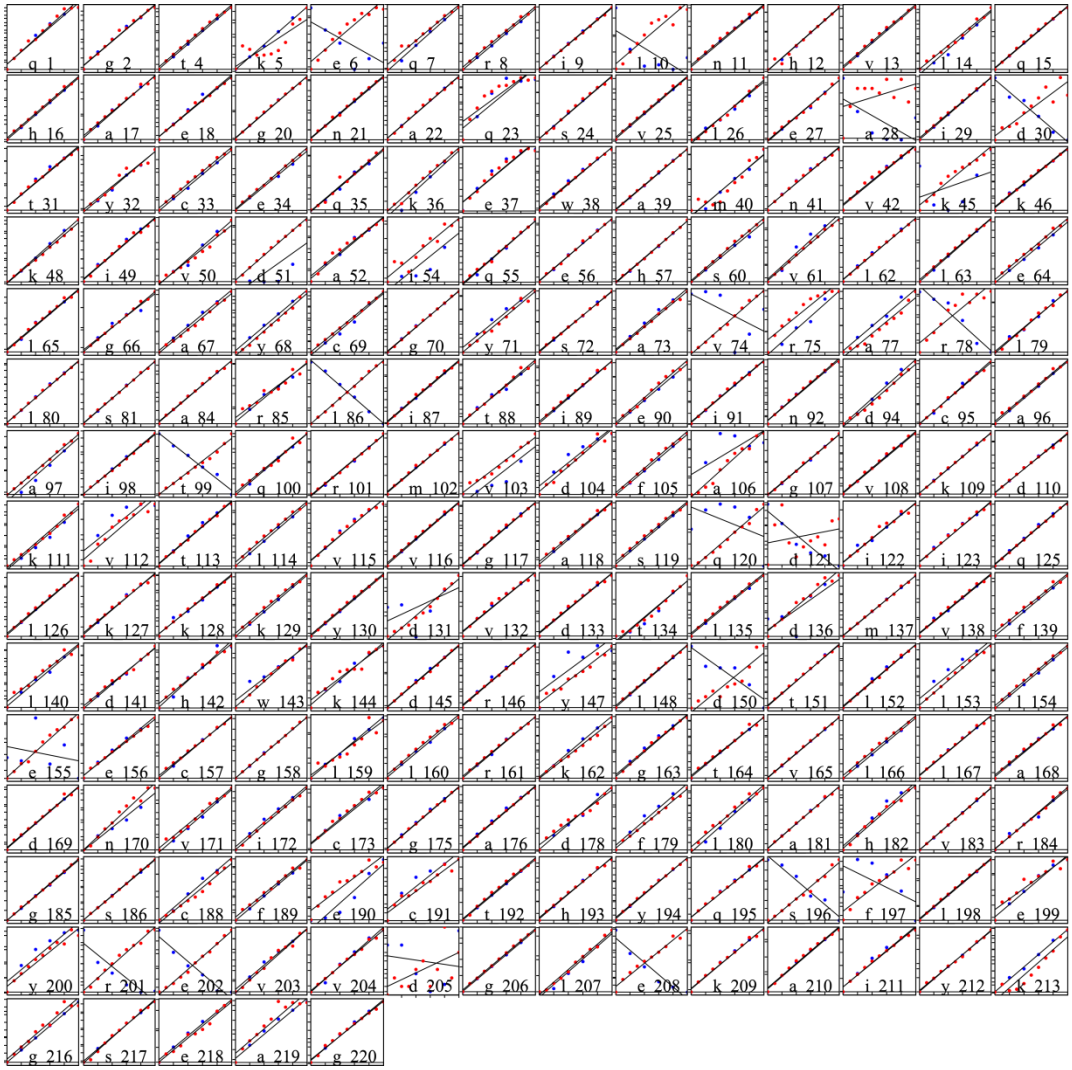

SI Figure 8. N shifts (ppm) per assigned residue for COMT:DNC:Mg^{2+}:SAM complex (blue) and COMT:DNC:Mg^{2+}:Sinefungin complex (red) fitted to linear equation.

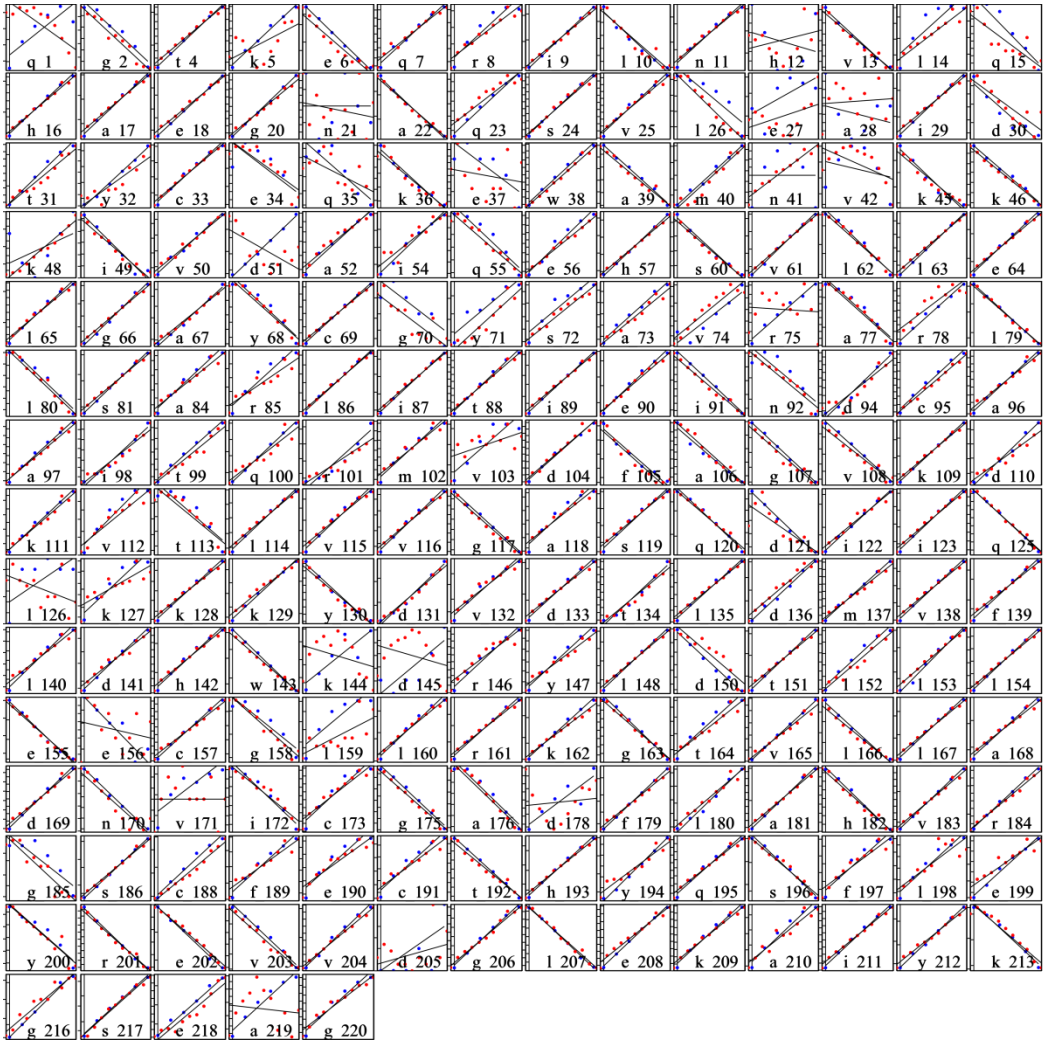

SI Figure 9. H shifts (ppm) per assigned residue for COMT:DNC:Mg^{2+}:SAM complex (blue) and COMT:DNC:Mg^{2+}:Sinefungin complex (red) fitted to linear equation.

SI Figure 10. Graphs representing pressure responses from an overlay of ^{1}H-^{15}N TROSY spectra of COMT:DNC:Mg^{2+}:Sinefungin (red) and COMT:DNC:Mg^{2+}:SAM (blue) per assigned residue from 1 bar to 2500 bar in 800 MHz (COMT:DNC:Mg^{2+}:SAM) and 600 Mz (COMT:DNC:Mg^{2+}:Sinefungin). Residue D51 was deleted for further analysis, due to overlapping with another peak and assignment uncertainty.

	COMT:DNC:Mg2+:SAM complex							COMT:DNC:Mg2+:Sinefungin complex						
Residue No.	$_{H}R^2$	$\lvert_{H}R^2\rvert$	$_{N}R^2$	$\lvert_{N}R^2\rvert$	*hyp*	$_{N\text{-}H}R^2$	$\lvert_{N\text{-}H}R^2\rvert$	$_{H}R^2$	$\lvert_{H}R^2\rvert$	$_{N}R^2$	$\lvert_{N}R^2\rvert$	*hyp*	$_{N\text{-}H}R^2$	$\lvert_{N\text{-}H}R^2\rvert$
1	0.8416	0.8416	0.9838	0.9838	0.9813	0.9204	0.9204	-0.8447	0.8447	0.9755	0.9755	0.9864	-0.7302	0.7302
2	-0.9755	0.9755	0.9926	0.9926	0.9967	-0.9453	0.9453	-0.9809	0.9809	0.9895	0.9895	0.9932	-0.9604	0.9604
4	0.9977	0.9977	0.9995	0.9995	0.9991	0.9992	0.9992	0.9927	0.9927	0.9983	0.9983	0.9972	0.9968	0.9968
5	0.9944	0.9944	0.9990	0.9990	0.9971	0.9947	0.9947	0.6437	0.6437	0.9432	0.9432	0.8552	0.7996	0.7996
6	-0.9983	0.9983	-0.7131	0.7131	0.9979	0.7437	0.7437	-0.9666	0.9666	0.5483	0.5483	0.9663	-0.3262	0.3262
7	0.9882	0.9882	0.9982	0.9982	0.9994	0.9815	0.9815	0.9826	0.9826	0.9889	0.9889	0.9897	0.9885	0.9885
8	0.9278	0.9278	0.9997	0.9997	0.9995	0.9194	0.9194	0.9633	0.9633	0.9991	0.9991	0.9981	0.9665	0.9665
9	0.9997	0.9997	0.9996	0.9996	0.9998	0.9994	0.9994	0.9979	0.9979	0.9992	0.9992	0.9997	0.9959	0.9959
10	-0.9848	0.9848	-0.7150	0.7150	0.9698	0.8225	0.8225	-0.9610	0.9610	-0.5656	0.5656	0.9510	0.6883	0.6883
11	0.9886	0.9886	0.9963	0.9963	0.9913	0.9977	0.9977	0.9919	0.9919	0.9984	0.9984	0.9946	0.9962	0.9962
12	-0.2413	0.2413	0.9992	0.9992	0.9994	-0.2313	0.2313	0.3211	0.3211	0.9918	0.9918	0.9919	0.3282	0.3282
13	-0.9956	0.9956	0.9983	0.9983	0.9977	-0.9991	0.9991	-0.9861	0.9861	0.9975	0.9975	0.9958	-0.9909	0.9909
14	0.8697	0.8697	0.9873	0.9873	0.9995	0.7824	0.7824	0.9661	0.9661	0.9946	0.9946	0.9959	0.9516	0.9516
15	-0.9614	0.9614	0.9993	0.9993	0.9993	-0.9515	0.9515	-0.8598	0.8598	0.9988	0.9988	0.9987	-0.8742	0.8742
16	0.9969	0.9969	0.9999	0.9999	0.9995	0.9974	0.9974	0.9957	0.9957	0.9990	0.9990	0.9985	0.9967	0.9967
17	0.9957	0.9957	0.9955	0.9955	0.9958	0.9986	0.9986	0.9944	0.9944	0.9939	0.9939	0.9949	0.9912	0.9912
18	0.9999	0.9999	0.9899	0.9899	0.9973	0.9912	0.9912	0.9962	0.9962	0.9941	0.9941	0.9963	0.9958	0.9958
20	0.9996	0.9996	0.9983	0.9983	0.9987	0.9972	0.9972	0.9957	0.9957	0.9975	0.9975	0.9986	0.9893	0.9893
21	-0.1915	0.1915	0.9992	0.9992	0.9991	-0.2027	0.2027	-0.2182	0.2182	0.9979	0.9979	0.9977	-0.2178	0.2178
22	-0.9966	0.9966	0.9984	0.9984	0.9974	-0.9996	0.9996	-0.9955	0.9955	0.9984	0.9984	0.9979	-0.9954	0.9954
23	0.9943	0.9943	0.9032	0.9032	0.9824	0.9379	0.9379	0.9461	0.9461	0.8640	0.8640	0.8985	0.9532	0.9532
24	0.9971	0.9971	0.9986	0.9986	0.9980	0.9995	0.9995	0.9909	0.9909	0.9989	0.9989	0.9969	0.9941	0.9941
25	0.9911	0.9911	0.9994	0.9994	0.9968	0.9949	0.9949	0.9921	0.9921	0.9988	0.9988	0.9976	0.9936	0.9936

26	-0.9007	0.9007	0.9922	0.9922	0.9823	-0.9460	0.9460	-0.9821	0.9821	0.9926	0.9926	0.9954	-0.9727	0.9727
27	0.6729	0.6729	0.9970	0.9970	0.9973	0.6431	0.6431	0.4811	0.4811	0.9966	0.9966	0.9964	0.5335	0.5335
28	-0.3047	0.3047	-0.6589	0.6589	0.6172	0.8155	0.8155	0.0979	0.0979	-0.7770	0.7770	0.5392	-0.2373	0.2373
29	0.9974	0.9974	0.9999	0.9999	0.9993	0.9983	0.9983	0.9951	0.9951	0.9994	0.9994	0.9990	0.9947	0.9947
30	-0.9507	0.9507	-0.9897	0.9897	0.9693	0.9364	0.9364	-0.8840	0.8840	-0.8995	0.8995	0.9238	0.7377	0.7377
31	0.9910	0.9910	0.9902	0.9902	0.9906	0.9975	0.9975	0.9785	0.9785	0.9942	0.9942	0.9961	0.9593	0.9593
32	0.9976	0.9976	0.9973	0.9973	0.9974	0.9993	0.9993	0.9057	0.9057	0.9758	0.9758	0.9833	0.8490	0.8490
33	0.9908	0.9908	0.9992	0.9992	0.9974	0.9869	0.9869	0.9949	0.9949	0.9997	0.9997	0.9978	0.9955	0.9955
34	-0.7183	0.7183	0.9984	0.9984	0.9980	-0.7284	0.7284	-0.8761	0.8761	0.9980	0.9980	0.9991	-0.8512	0.8512
35	-0.8723	0.8723	0.9969	0.9969	0.9976	-0.8852	0.8852	-0.7046	0.7046	0.9801	0.9801	0.9877	-0.6606	0.6606
36	-0.9903	0.9903	0.9839	0.9839	0.9990	-0.9549	0.9549	-0.9638	0.9638	0.9968	0.9968	0.9959	-0.9777	0.9777
37	-0.8145	0.8145	0.9576	0.9576	0.9586	-0.6282	0.6282	-0.2484	0.2484	0.9734	0.9734	0.9729	-0.3206	0.3206
38	0.9956	0.9956	0.9948	0.9948	0.9951	0.9997	0.9997	0.9946	0.9946	0.9975	0.9975	0.9985	0.9910	0.9910
39	-0.9962	0.9962	0.9997	0.9997	0.9999	-0.9944	0.9944	-0.9866	0.9866	0.9993	0.9993	0.9993	-0.9845	0.9845
40	0.9949	0.9949	0.9842	0.9842	0.9957	0.9745	0.9745	0.9633	0.9633	0.8446	0.8446	0.9545	0.8759	0.8759
41	0.0153	0.0153	0.9943	0.9943	0.9933	0.1215	0.1215	0.9793	0.9793	0.9974	0.9974	0.9966	0.9826	0.9826
42	-0.2633	0.2633	0.9869	0.9869	0.9830	-0.1062	0.1062	-0.5881	0.5881	0.9895	0.9895	0.9889	-0.4736	0.4736
45	-0.9797	0.9797	0.3907	0.3907	0.9780	-0.2248	0.2248	-0.9799	0.9799	0.9702	0.9702	0.9837	-0.9653	0.9653
46	-0.9945	0.9945	0.9961	0.9961	0.9980	-0.9889	0.9889	-0.9970	0.9970	0.9942	0.9942	0.9973	-0.9920	0.9920
48	0.4912	0.4912	0.9990	0.9990	0.9992	0.4990	0.4990	0.9852	0.9852	0.9981	0.9981	0.9976	0.9878	0.9878
49	-0.9746	0.9746	0.9946	0.9946	0.9937	-0.9814	0.9814	-0.9822	0.9822	0.9947	0.9947	0.9942	-0.9888	0.9888
50	0.9932	0.9932	0.9908	0.9908	0.9938	0.9892	0.9892	0.9913	0.9913	0.9832	0.9832	0.9889	0.9737	0.9737
51	0.9981	0.9981	0.7770	0.7770	0.9938	0.8076	0.8076	-0.6635	0.6635	0.9988	0.9988	0.9986	-0.6958	0.6958
52	0.9853	0.9853	0.9920	0.9920	0.9874	0.9958	0.9958	0.9763	0.9763	0.9931	0.9931	0.9873	0.9819	0.9819
54	0.9899	0.9899	0.9062	0.9062	0.9969	0.8443	0.8443	0.9443	0.9443	0.9409	0.9409	0.9577	0.9308	0.9308
55	-0.9554	0.9554	0.9965	0.9965	0.9938	-0.9671	0.9671	-0.9801	0.9801	0.9977	0.9977	0.9975	-0.9790	0.9790
56	0.9833	0.9833	0.9986	0.9986	0.9940	0.9911	0.9911	0.9967	0.9967	0.9965	0.9965	0.9984	0.9918	0.9918

57	0.9995	0.9995	0.9995	0.9995	0.9995	0.9999	0.9999	0.9991	0.9991	0.9991	0.9991	0.9996	0.9979	0.9979
60	-0.9909	0.9909	0.9975	0.9975	0.9978	-0.9898	0.9898	-0.9913	0.9913	0.9995	0.9995	0.9988	-0.9926	0.9926
61	0.9980	0.9980	0.9775	0.9775	0.9974	0.9881	0.9881	0.9991	0.9991	0.9931	0.9931	0.9990	0.9963	0.9963
62	-0.9890	0.9890	0.9965	0.9965	0.9991	-0.9746	0.9746	-0.9928	0.9928	0.9961	0.9961	0.9986	-0.9809	0.9809
63	0.9996	0.9996	0.9986	0.9986	0.9992	0.9995	0.9995	0.9982	0.9982	0.9976	0.9976	0.9984	0.9983	0.9983
64	0.9958	0.9958	0.9985	0.9985	0.9983	0.9898	0.9898	0.9968	0.9968	0.9996	0.9996	0.9980	0.9970	0.9970
65	0.9910	0.9910	0.9953	0.9953	0.9932	0.9976	0.9976	0.9923	0.9923	0.9970	0.9970	0.9947	0.9936	0.9936
66	0.9962	0.9962	0.9864	0.9864	0.9972	0.9709	0.9709	0.9987	0.9987	0.9988	0.9988	0.9989	0.9968	0.9968
67	0.9944	0.9944	0.9979	0.9979	0.9975	0.9856	0.9856	0.9949	0.9949	0.9956	0.9956	0.9969	0.9851	0.9851
68	-0.9619	0.9619	0.9983	0.9983	0.9997	-0.9454	0.9454	-0.9766	0.9766	0.9975	0.9975	0.9955	-0.9876	0.9876
69	0.9988	0.9988	0.9920	0.9920	0.9999	0.9854	0.9854	0.9989	0.9989	0.9895	0.9895	0.9994	0.9846	0.9846
70	-0.8608	0.8608	0.9992	0.9992	0.9992	-0.8458	0.8458	-0.8723	0.8723	0.9996	0.9996	0.9995	-0.8804	0.8804
71	0.9441	0.9441	0.9869	0.9869	0.9747	0.9705	0.9705	0.9570	0.9570	0.9912	0.9912	0.9923	0.9348	0.9348
72	0.9380	0.9380	0.9995	0.9995	0.9992	0.9436	0.9436	0.9890	0.9890	0.9994	0.9994	0.9993	0.9899	0.9899
73	0.9916	0.9916	0.9934	0.9934	0.9940	0.9928	0.9928	0.9849	0.9849	0.9988	0.9988	0.9986	0.9855	0.9855
74	0.9297	0.9297	-0.5569	0.5569	0.8236	-0.5028	0.5028	0.9533	0.9533	0.9924	0.9924	0.9978	0.9224	0.9224
75	0.9902	0.9902	0.9892	0.9892	0.9975	0.9651	0.9651	-0.0959	0.0959	0.9545	0.9545	0.9522	0.1197	0.1197
77	-0.9736	0.9736	0.9934	0.9934	0.9885	-0.9596	0.9596	-0.9802	0.9802	0.9676	0.9676	0.9822	-0.9651	0.9651
78	0.9940	0.9940	-0.9723	0.9723	0.9957	-0.9437	0.9437	0.8959	0.8959	-0.9457	0.9457	0.9347	-0.8679	0.8679
79	-0.9998	0.9998	0.9957	0.9957	0.9997	-0.9958	0.9958	-0.9945	0.9945	0.9924	0.9924	0.9963	-0.9819	0.9819
80	-0.9799	0.9799	0.9986	0.9986	0.9989	-0.9680	0.9680	-0.9844	0.9844	0.9990	0.9990	0.9992	-0.9788	0.9788
81	0.9989	0.9989	0.9994	0.9994	0.9993	0.9998	0.9998	0.9970	0.9970	1.0000	1.0000	0.9995	0.9975	0.9975
84	0.9839	0.9839	0.9982	0.9982	0.9971	0.9926	0.9926	0.9815	0.9815	0.9990	0.9990	0.9986	0.9840	0.9840
85	0.9534	0.9534	0.9950	0.9950	0.9815	0.9682	0.9682	0.9471	0.9471	0.9980	0.9980	0.9773	0.9551	0.9551
86	0.9957	0.9957	-0.9982	0.9982	0.9996	-0.9894	0.9894	0.9959	0.9959	-0.9964	0.9964	0.9990	-0.9890	0.9890
87	0.9982	0.9982	0.9986	0.9986	0.9985	0.9990	0.9990	0.9965	0.9965	0.9982	0.9982	0.9973	0.9969	0.9969
88	0.9940	0.9940	0.9938	0.9938	0.9944	0.9900	0.9900	0.9957	0.9957	0.9889	0.9889	0.9958	0.9873	0.9873

89	0.9988	0.9988	0.9993	0.9993	0.9989	0.9996	0.9996	0.9974	0.9974	0.9971	0.9971	0.9977	0.9978	0.9978
90	0.9929	0.9929	0.9989	0.9989	0.9943	0.9874	0.9874	0.9961	0.9961	0.9898	0.9898	0.9957	0.9937	0.9937
91	-0.9990	0.9990	0.9983	0.9983	0.9998	-0.9953	0.9953	-0.9931	0.9931	0.9996	0.9996	0.9976	-0.9935	0.9935
92	-0.8692	0.8692	0.9948	0.9948	0.9964	-0.8147	0.8147	-0.9751	0.9751	0.9959	0.9959	0.9968	-0.9600	0.9600
94	0.9899	0.9899	0.9953	0.9953	0.9967	0.9865	0.9865	0.9295	0.9295	0.9990	0.9990	0.9948	0.9404	0.9404
95	0.9912	0.9912	0.9977	0.9977	0.9976	0.9917	0.9917	0.9962	0.9962	0.9993	0.9993	0.9991	0.9964	0.9964
96	0.9959	0.9959	0.9995	0.9995	0.9984	0.9980	0.9980	0.9877	0.9877	0.9979	0.9979	0.9965	0.9879	0.9879
97	0.9945	0.9945	0.9823	0.9823	0.9981	0.9578	0.9578	0.9927	0.9927	0.9991	0.9991	0.9990	0.9917	0.9917
98	0.9875	0.9875	0.9997	0.9997	1.0000	0.9833	0.9833	0.9746	0.9746	0.9997	0.9997	0.9993	0.9728	0.9728
99	0.9953	0.9953	-0.9917	0.9917	0.9970	-0.9826	0.9826	0.9815	0.9815	-0.9928	0.9928	0.9937	-0.9803	0.9803
100	0.9990	0.9990	0.9992	0.9992	0.9994	0.9988	0.9988	0.9494	0.9494	0.9959	0.9959	0.9885	0.9391	0.9391
101	0.9612	0.9612	0.9982	0.9982	0.9978	0.9747	0.9747	0.9373	0.9373	0.9992	0.9992	0.9990	0.9444	0.9444
102	0.9804	0.9804	0.9984	0.9984	0.9968	0.9898	0.9898	0.9751	0.9751	0.9988	0.9988	0.9976	0.9812	0.9812
103	0.9016	0.9016	0.9157	0.9157	0.9737	0.6541	0.6541	0.6270	0.6270	0.9909	0.9909	0.9912	0.5675	0.5675
104	0.9948	0.9948	0.9612	0.9612	0.9939	0.9821	0.9821	0.9849	0.9849	0.8806	0.8806	0.9844	0.9012	0.9012
105	-0.9819	0.9819	0.9997	0.9997	0.9997	-0.9777	0.9777	-0.9606	0.9606	0.9978	0.9978	0.9969	-0.9670	0.9670
106	-0.9853	0.9853	0.7126	0.7126	0.9800	-0.7941	0.7941	-0.9877	0.9877	0.9681	0.9681	0.9885	-0.9635	0.9635
107	-0.9992	0.9992	0.9994	0.9994	0.9996	-0.9981	0.9981	-0.9844	0.9844	0.9985	0.9985	0.9994	-0.9767	0.9767
108	-0.9981	0.9981	0.9991	0.9991	0.9997	-0.9950	0.9950	-0.9829	0.9829	0.9986	0.9986	0.9970	-0.9873	0.9873
109	0.9991	0.9991	0.9993	0.9993	0.9992	0.9997	0.9997	0.9979	0.9979	0.9990	0.9990	0.9990	0.9976	0.9976
110	0.9940	0.9940	0.9990	0.9990	0.9992	0.9896	0.9896	0.9731	0.9731	0.9986	0.9986	0.9986	0.9731	0.9731
111	0.9954	0.9954	0.9887	0.9887	0.9988	0.9733	0.9733	0.9884	0.9884	0.9910	0.9910	0.9947	0.9786	0.9786
112	0.9476	0.9476	0.8865	0.8865	0.9233	0.9856	0.9856	0.9625	0.9625	0.9349	0.9349	0.9585	0.9739	0.9739
113	-0.9077	0.9077	0.9937	0.9937	0.9997	-0.8562	0.8562	-0.9302	0.9302	0.9929	0.9929	0.9981	-0.8916	0.8916
114	0.9947	0.9947	0.9996	0.9996	0.9961	0.9957	0.9957	0.9946	0.9946	0.9996	0.9996	0.9958	0.9961	0.9961
115	0.9876	0.9876	0.9822	0.9822	0.9858	0.9994	0.9994	0.9907	0.9907	0.9806	0.9806	0.9879	0.9967	0.9967
116	0.9936	0.9936	0.9985	0.9985	0.9947	0.9979	0.9979	0.9965	0.9965	0.9987	0.9987	0.9970	0.9988	0.9988

117	-0.9991	0.9991	0.9986	0.9986	0.9991	-0.9959	0.9959	-0.9908	0.9908	0.9983	0.9983	0.9979	-0.9935	0.9935
118	0.9625	0.9625	0.9982	0.9982	0.9883	0.9764	0.9764	0.9758	0.9758	0.9995	0.9995	0.9950	0.9806	0.9806
119	0.9903	0.9903	0.9987	0.9987	0.9949	0.9957	0.9957	0.9919	0.9919	0.9987	0.9987	0.9952	0.9968	0.9968
120	-0.9943	0.9943	-0.4819	0.4819	0.9943	0.5662	0.5662	-0.9926	0.9926	-0.1934	0.1934	0.9926	0.2861	0.2861
121	-0.9978	0.9978	-0.9611	0.9611	0.9965	0.9763	0.9763	-0.8285	0.8285	0.6433	0.6433	0.2551	-0.7800	0.7800
122	0.9981	0.9981	0.9907	0.9907	0.9971	0.9959	0.9959	0.9856	0.9856	0.9938	0.9938	0.9888	0.9906	0.9906
123	0.9959	0.9959	0.9914	0.9914	0.9955	0.9983	0.9983	0.9952	0.9952	0.9929	0.9929	0.9951	0.9984	0.9984
125	-0.9983	0.9983	0.9971	0.9971	0.9995	-0.9912	0.9912	-0.9935	0.9935	0.9980	0.9980	0.9993	-0.9878	0.9878
126	0.6431	0.6431	0.9983	0.9983	0.9977	0.6782	0.6782	-0.5510	0.5510	0.9975	0.9975	0.9975	-0.5429	0.5429
127	0.9506	0.9506	0.9955	0.9955	0.9929	0.9750	0.9750	0.8405	0.8405	0.9974	0.9974	0.9954	0.8605	0.8605
128	0.9961	0.9961	0.9938	0.9938	0.9969	0.9921	0.9921	0.9964	0.9964	0.9997	0.9997	0.9982	0.9976	0.9976
129	0.9974	0.9974	0.9998	0.9998	0.9994	0.9974	0.9974	0.9895	0.9895	0.9976	0.9976	0.9960	0.9920	0.9920
130	-0.9922	0.9922	0.9996	0.9996	0.9988	-0.9945	0.9945	-0.9856	0.9856	0.9998	0.9998	0.9983	-0.9867	0.9867
131	0.9924	0.9924	0.5925	0.5925	0.9925	0.6754	0.6754	0.9908	0.9908	-0.7484	0.7484	0.9908	-0.7338	0.7338
132	0.9808	0.9808	0.9899	0.9899	0.9872	0.9981	0.9981	0.9749	0.9749	0.9931	0.9931	0.9898	0.9903	0.9903
133	0.9926	0.9926	0.9956	0.9956	0.9943	0.9996	0.9996	0.9925	0.9925	0.9952	0.9952	0.9947	0.9966	0.9966
134	0.9877	0.9877	0.9770	0.9770	0.9850	0.9980	0.9980	0.9815	0.9815	0.9839	0.9839	0.9841	0.9917	0.9917
135	0.9948	0.9948	0.9965	0.9965	0.9955	0.9975	0.9975	0.9962	0.9962	0.9980	0.9980	0.9970	0.9975	0.9975
136	0.9957	0.9957	0.8154	0.8154	0.9958	0.8426	0.8426	0.9829	0.9829	0.7702	0.7702	0.9834	0.7079	0.7079
137	0.9983	0.9983	0.9999	0.9999	0.9996	0.9988	0.9988	0.9941	0.9941	0.9997	0.9997	0.9994	0.9937	0.9937
138	0.9957	0.9957	0.9953	0.9953	0.9960	0.9957	0.9957	0.9961	0.9961	0.9968	0.9968	0.9963	0.9983	0.9983
139	0.9947	0.9947	0.9997	0.9997	0.9966	0.9963	0.9963	0.9922	0.9922	0.9979	0.9979	0.9940	0.9958	0.9958
140	0.9880	0.9880	0.9964	0.9964	0.9886	0.9903	0.9903	0.9834	0.9834	0.9836	0.9836	0.9841	0.9800	0.9800
141	0.9974	0.9974	0.9987	0.9987	0.9995	0.9940	0.9940	0.9883	0.9883	0.9955	0.9955	0.9948	0.9877	0.9877
142	0.9902	0.9902	0.9806	0.9806	0.9902	0.9836	0.9836	0.9918	0.9918	-0.9819	0.9819	0.9928	-0.9612	0.9612
143	-0.9996	0.9996	0.9721	0.9721	0.9996	-0.9701	0.9701	-0.9957	0.9957	0.9959	0.9959	0.9967	-0.9890	0.9890
144	0.8624	0.8624	0.9899	0.9899	0.9893	0.8731	0.8731	-0.3669	0.3669	0.9772	0.9772	0.9705	-0.3512	0.3512

145	0.8450	0.8450	0.9987	0.9987	0.9987	0.8188	0.8188	-0.3171	0.3171	0.9987	0.9987	0.9987	-0.3391	0.3391
146	0.9892	0.9892	0.9942	0.9942	0.9931	0.9991	0.9991	0.9550	0.9550	0.9972	0.9972	0.9985	0.9387	0.9387
147	0.9866	0.9866	0.8445	0.8445	0.9851	0.9167	0.9167	0.9860	0.9860	0.9855	0.9855	0.9870	0.9769	0.9769
148	0.9981	0.9981	0.9995	0.9995	0.9987	0.9994	0.9994	0.9981	0.9981	0.9994	0.9994	0.9988	0.9986	0.9986
150	-0.9941	0.9941	-0.9333	0.9333	0.9947	0.9189	0.9189	-0.9403	0.9403	-0.4600	0.4600	0.9411	0.6359	0.6359
151	0.9980	0.9980	0.9976	0.9976	0.9978	0.9999	0.9999	0.9975	0.9975	0.9980	0.9980	0.9984	0.9975	0.9975
152	0.9866	0.9866	0.9964	0.9964	0.9961	0.9942	0.9942	0.9772	0.9772	0.9989	0.9989	0.9988	0.9789	0.9789
153	0.9918	0.9918	0.9595	0.9595	0.9821	0.9547	0.9547	0.9953	0.9953	0.9968	0.9968	0.9964	0.9984	0.9984
154	0.9979	0.9979	0.9993	0.9993	0.9983	0.9951	0.9951	0.9982	0.9982	0.9991	0.9991	0.9984	0.9976	0.9976
155	-0.9941	0.9941	-0.2632	0.2632	0.9941	0.2179	0.2179	-0.9926	0.9926	-0.8813	0.8813	0.9926	0.8948	0.8948
156	-0.9187	0.9187	0.9959	0.9959	0.9959	-0.9087	0.9087	-0.1484	0.1484	0.9984	0.9984	0.9978	-0.1163	0.1163
157	0.9981	0.9981	0.9987	0.9987	0.9987	0.9988	0.9988	0.9940	0.9940	0.9980	0.9980	0.9981	0.9923	0.9923
158	-0.9262	0.9262	0.9996	0.9996	0.9996	-0.9200	0.9200	-0.9793	0.9793	0.9998	0.9998	0.9997	-0.9814	0.9814
159	0.8972	0.8972	0.9979	0.9979	0.9748	0.9089	0.9089	0.7532	0.7532	0.9908	0.9908	0.9537	0.7667	0.7667
160	0.9884	0.9884	0.9985	0.9985	0.9916	0.9909	0.9909	0.9933	0.9933	0.9964	0.9964	0.9944	0.9964	0.9964
161	0.9931	0.9931	0.9986	0.9986	0.9982	0.9948	0.9948	0.9934	0.9934	0.9996	0.9996	0.9988	0.9956	0.9956
162	0.9967	0.9967	0.9975	0.9975	0.9973	0.9993	0.9993	0.9958	0.9958	0.9940	0.9940	0.9963	0.9934	0.9934
163	-0.9958	0.9958	0.9920	0.9920	0.9984	-0.9769	0.9769	-0.9947	0.9947	0.9925	0.9925	0.9968	-0.9861	0.9861
164	0.9681	0.9681	0.9991	0.9991	0.9955	0.9763	0.9763	0.9772	0.9772	0.9982	0.9982	0.9949	0.9836	0.9836
165	0.9996	0.9996	0.9998	0.9998	0.9998	0.9994	0.9994	0.9889	0.9889	0.9992	0.9992	0.9995	0.9857	0.9857
166	-0.9941	0.9941	0.9999	0.9999	0.9987	-0.9934	0.9934	-0.9865	0.9865	0.9998	0.9998	0.9969	-0.9845	0.9845
167	0.9961	0.9961	0.9959	0.9959	0.9961	0.9999	0.9999	0.9964	0.9964	0.9955	0.9955	0.9964	0.9992	0.9992
168	0.9932	0.9932	0.9978	0.9978	0.9956	0.9982	0.9982	0.9913	0.9913	0.9983	0.9983	0.9956	0.9944	0.9944
169	0.9972	0.9972	0.9989	0.9989	0.9979	0.9992	0.9992	0.9910	0.9910	0.9985	0.9985	0.9959	0.9909	0.9909
170	-0.9979	0.9979	0.9878	0.9878	0.9996	-0.9776	0.9776	-0.9305	0.9305	0.9538	0.9538	0.9875	-0.7920	0.7920
171	0.8693	0.8693	0.9973	0.9973	0.9981	0.8384	0.8384	-0.0322	0.0322	0.9952	0.9952	0.9962	-0.0582	0.0582
172	-0.9804	0.9804	0.9944	0.9944	0.9990	-0.9543	0.9543	-0.9678	0.9678	0.9930	0.9930	0.9988	-0.9350	0.9350

173	0.9544	0.9544	0.9826	0.9826	0.9702	0.9862	0.9862	0.9683	0.9683	0.9954	0.9954	0.9860	0.9848	0.9848
175	-0.9942	0.9942	0.9977	0.9977	0.9993	-0.9853	0.9853	-0.9887	0.9887	0.9989	0.9989	0.9987	-0.9883	0.9883
176	-0.9738	0.9738	0.9957	0.9957	0.9985	-0.9499	0.9499	-0.9805	0.9805	0.9989	0.9989	0.9991	-0.9734	0.9734
178	0.8668	0.8668	0.9929	0.9929	0.9934	0.8104	0.8104	0.1306	0.1306	0.9898	0.9898	0.9871	0.2539	0.2539
179	0.9999	0.9999	0.9860	0.9860	0.9997	0.9874	0.9874	0.9969	0.9969	0.9850	0.9850	0.9982	0.9770	0.9770
180	0.9919	0.9919	0.9967	0.9967	0.9967	0.9920	0.9920	0.9838	0.9838	0.9919	0.9919	0.9928	0.9836	0.9836
181	0.9985	0.9985	0.9985	0.9985	0.9986	0.9994	0.9994	0.9950	0.9950	0.9992	0.9992	0.9984	0.9945	0.9945
182	-0.9971	0.9971	0.9816	0.9816	0.9973	-0.9797	0.9797	-0.9919	0.9919	0.9917	0.9917	0.9938	-0.9929	0.9929
183	0.9994	0.9994	1.0000	1.0000	0.9999	0.9995	0.9995	0.9951	0.9951	0.9998	0.9998	0.9997	0.9945	0.9945
184	0.9980	0.9980	0.9940	0.9940	0.9972	0.9938	0.9938	0.9962	0.9962	0.9967	0.9967	0.9983	0.9925	0.9925
185	-0.8698	0.8698	0.9998	0.9998	0.9997	-0.8706	0.8706	-0.9450	0.9450	0.9997	0.9997	0.9996	-0.9466	0.9466
186	0.9995	0.9995	0.9998	0.9998	0.9999	0.9991	0.9991	0.9970	0.9970	0.9999	0.9999	0.9995	0.9967	0.9967
188	0.9886	0.9886	0.9936	0.9936	0.9910	0.9942	0.9942	0.9912	0.9912	0.9194	0.9194	0.9906	0.9454	0.9454
189	0.9795	0.9795	0.9998	0.9998	0.9982	0.9802	0.9802	0.9600	0.9600	0.9990	0.9990	0.9957	0.9692	0.9692
190	0.9431	0.9431	0.9604	0.9604	0.9499	0.8219	0.8219	0.9514	0.9514	0.9720	0.9720	0.9577	0.8946	0.8946
191	0.9705	0.9705	0.9390	0.9390	0.9691	0.9934	0.9934	0.9687	0.9687	0.9340	0.9340	0.9696	0.9459	0.9459
192	-0.9987	0.9987	0.9998	0.9998	0.9999	-0.9977	0.9977	-0.9867	0.9867	0.9953	0.9953	0.9973	-0.9787	0.9787
193	0.9965	0.9965	0.9969	0.9969	0.9966	0.9996	0.9996	0.9973	0.9973	0.9963	0.9963	0.9974	0.9979	0.9979
194	0.9984	0.9984	0.9974	0.9974	0.9976	0.9928	0.9928	0.9672	0.9672	0.9979	0.9979	0.9979	0.9653	0.9653
195	0.9906	0.9906	0.9954	0.9954	0.9929	0.9989	0.9989	0.9908	0.9908	0.9993	0.9993	0.9955	0.9929	0.9929
196	-0.9944	0.9944	-0.9834	0.9834	0.9941	0.9883	0.9883	-0.9883	0.9883	-0.9940	0.9940	0.9925	0.9882	0.9882
197	0.9642	0.9642	-0.5892	0.5892	0.9604	-0.3668	0.3668	0.9568	0.9568	-0.8855	0.8855	0.9641	-0.7340	0.7340
198	0.9717	0.9717	0.9994	0.9994	0.9993	0.9787	0.9787	0.8675	0.8675	0.9992	0.9992	0.9990	0.8685	0.8685
199	0.9939	0.9939	0.9892	0.9892	0.9939	0.9943	0.9943	0.9391	0.9391	0.9786	0.9786	0.9558	0.9625	0.9625
200	-0.9650	0.9650	0.9456	0.9456	0.9781	-0.8478	0.8478	-0.9568	0.9568	0.9615	0.9615	0.9787	-0.9124	0.9124
201	-0.9980	0.9980	-0.9194	0.9194	0.9951	0.9388	0.9388	-0.9932	0.9932	-0.9488	0.9488	0.9927	0.9649	0.9649
202	-0.9959	0.9959	-0.9753	0.9753	0.9961	0.9759	0.9759	-0.9950	0.9950	-0.6560	0.6560	0.9967	0.6036	0.6036

203	-0.9938	0.9938	0.9957	0.9957	0.9994	-0.9812	0.9812	-0.9905	0.9905	0.9963	0.9963	0.9945	-0.9826	0.9826
204	0.9931	0.9931	0.9946	0.9946	0.9932	0.9983	0.9983	0.9973	0.9973	0.9496	0.9496	0.9974	0.9419	0.9419
205	0.7063	0.7063	-0.1390	0.1390	0.9335	0.4217	0.4217	0.3561	0.3561	-0.5611	0.5611	0.6085	0.1768	0.1768
206	0.9955	0.9955	0.9998	0.9998	0.9997	0.9964	0.9964	0.9901	0.9901	0.9991	0.9991	0.9991	0.9893	0.9893
207	-0.9988	0.9988	0.9890	0.9890	0.9982	-0.9895	0.9895	-0.9924	0.9924	0.9925	0.9925	0.9958	-0.9854	0.9854
208	0.9988	0.9988	-0.9652	0.9652	0.9978	-0.9765	0.9765	0.9875	0.9875	-0.9895	0.9895	0.9883	-0.9829	0.9829
209	0.9900	0.9900	0.9955	0.9955	0.9925	0.9988	0.9988	0.9922	0.9922	0.9980	0.9980	0.9958	0.9941	0.9941
210	0.9775	0.9775	0.9945	0.9945	0.9939	0.9940	0.9940	0.9581	0.9581	0.9944	0.9944	0.9944	0.9613	0.9613
211	0.9963	0.9963	0.9862	0.9862	0.9923	0.9966	0.9966	0.9955	0.9955	0.9873	0.9873	0.9938	0.9906	0.9906
212	0.9988	0.9988	0.9997	0.9997	0.9996	0.9988	0.9988	0.9943	0.9943	0.9991	0.9991	0.9982	0.9954	0.9954
213	-0.9918	0.9918	0.9981	0.9981	0.9919	-0.9902	0.9902	-0.9689	0.9689	0.8132	0.8132	0.9521	-0.7813	0.7813
216	0.9962	0.9962	1.0000	1.0000	0.9999	0.9965	0.9965	0.9681	0.9681	0.9778	0.9778	0.9789	0.9680	0.9680
217	0.9960	0.9960	0.9985	0.9985	0.9975	0.9992	0.9992	0.9914	0.9914	0.9982	0.9982	0.9965	0.9964	0.9964
218	0.9958	0.9958	0.9952	0.9952	0.9957	0.9917	0.9917	0.9587	0.9587	0.9664	0.9664	0.9920	0.8818	0.8818
219	0.9788	0.9788	0.9897	0.9897	0.9860	0.9978	0.9978	-0.1571	0.1571	0.9553	0.9553	0.9451	-0.1150	0.1150
220	0.9788	0.9788	0.9968	0.9968	0.9933	0.9918	0.9918	0.9810	0.9810	0.9980	0.9980	0.9957	0.9883	0.9883

SI Table 2. R^2 coefficient of linearity determination for H ($_{H}R^2$), N ($_{N}R^2$), rescaled hypotenuse (hyp) and the N-H plane ($_{N\text{-}H}R^2$) linear fits of pressure induced shifts from 1 bar to 2500 bars per assigned residue. Hypotenuse shifts in the N-H plane (ppm), rescaled for N by scaling factor c=0.12 ($\Delta = \sqrt{(\delta H)^2 + [c(\delta N)]^2}$). Poorest fits (smallest R^2) indicated by gradient of red colour. Shifts in to lower resonance frequencies (high field ΔH or ΔN) indicated by yellow colour.

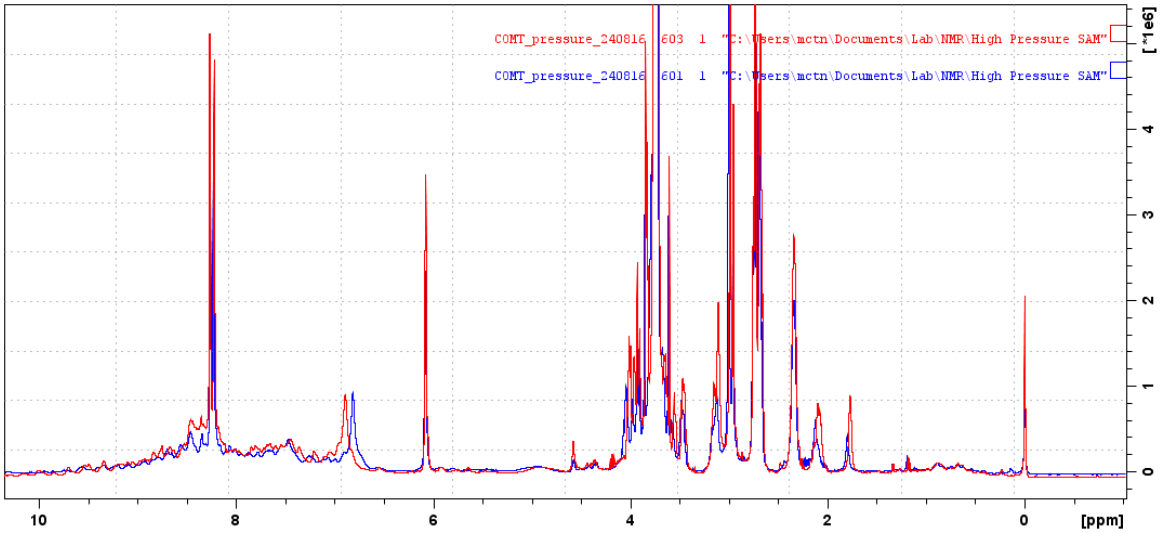

SI Figure 11. 1D proton spectra of human S-COMT:SAM:DNC:Mg^{2+} complex at 1 bar (blue) and 2500 bar (red) recorded at 600 MHz. Spectra were referenced to TSP (0 ppm).

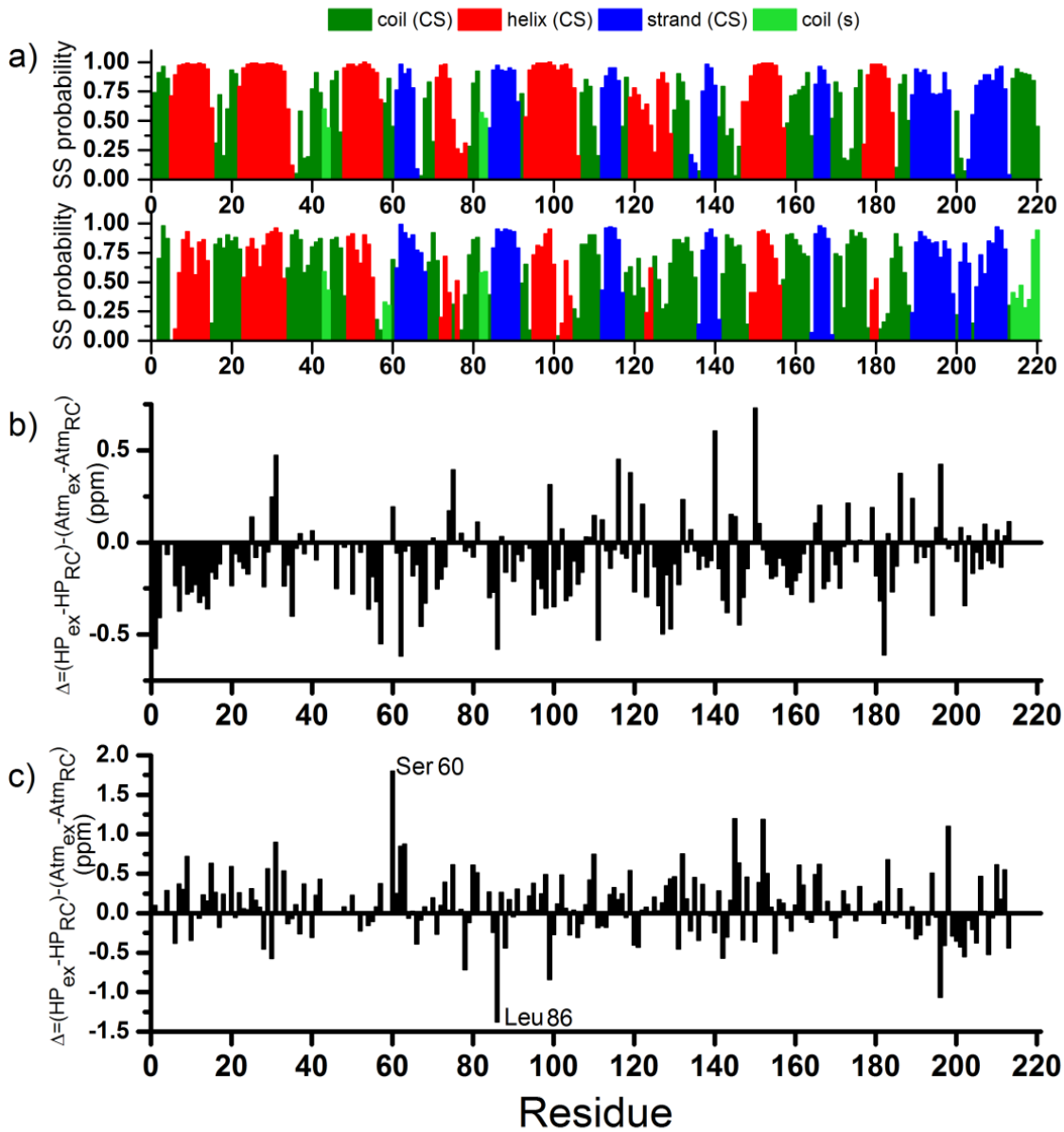

SI Figure 12. a) Secondary structure prediction of S-COMT in the S-COMT:Sinefungin:DNC:Mg^{2+} complex obtained with TALOS-N based on chemical shifts in ambient pressure (top a) and 2500 bar (bottom a). CS – prediction based on chemical shift; s – sequence based prediction. b) $^{13}C_{\alpha}$ difference between experimental derived chemical shifts (ex) versus calculated from random coil (RC) for 2500 bar (HP) and 1 bar (Atm). c) ^{15}N difference between experimental derived chemical shifts (ex) versus calculated from random coil (RC) for 2500 bar (HP) and 1 bar (Atm) No correlation has been found between changes from graph b) and c) versus secondary structure pressure derived change (a).

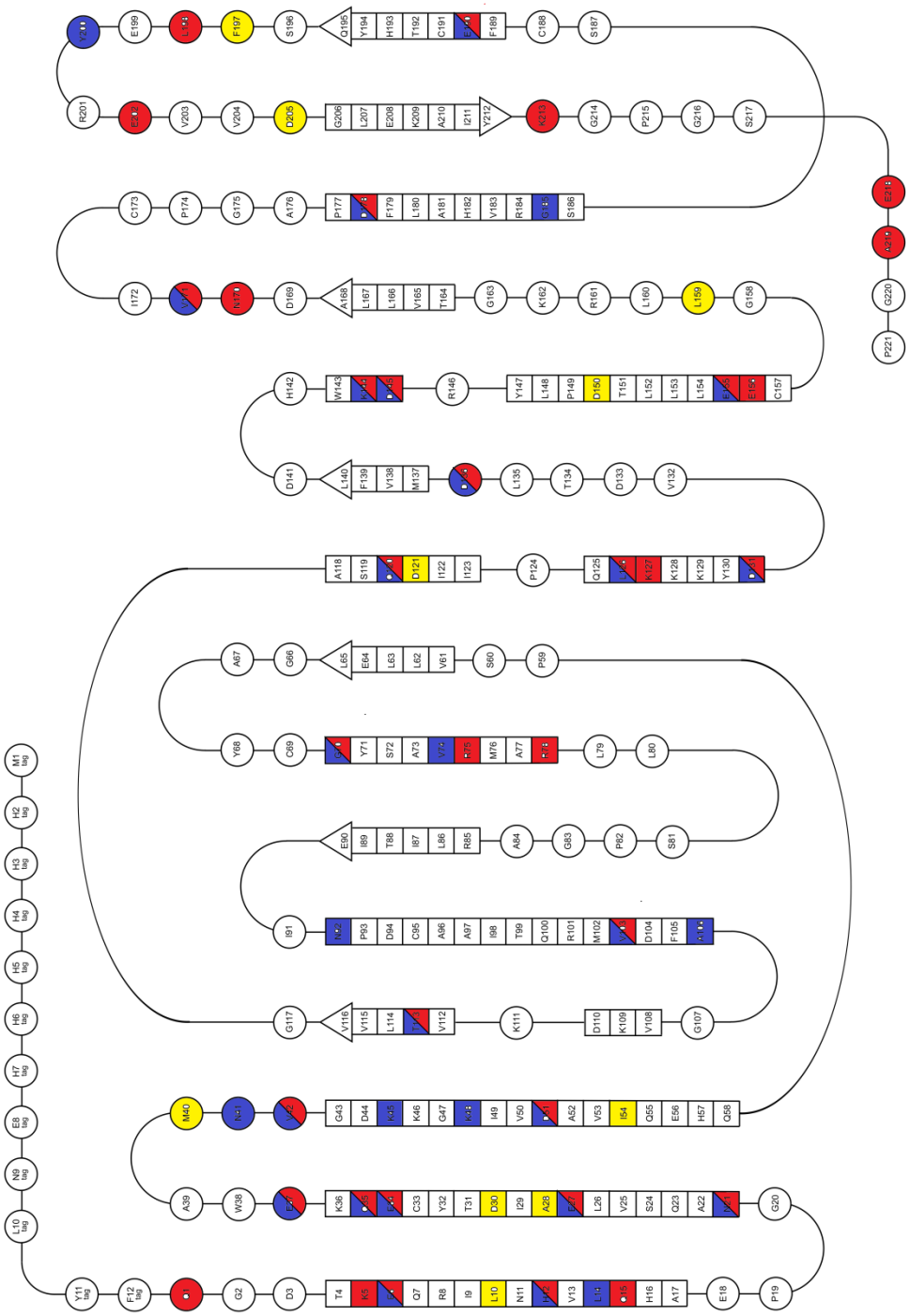

SI Figure 13. Canonical bead diagram of COMT structure. Incompressible residues coloured in yellow; residues that experienced pressure induced shifts in the N-H plane with linear coefficient lower than 0.9 ($R^2 < 0.9$) coloured in blue for Complex 1 and red for Complex 2.

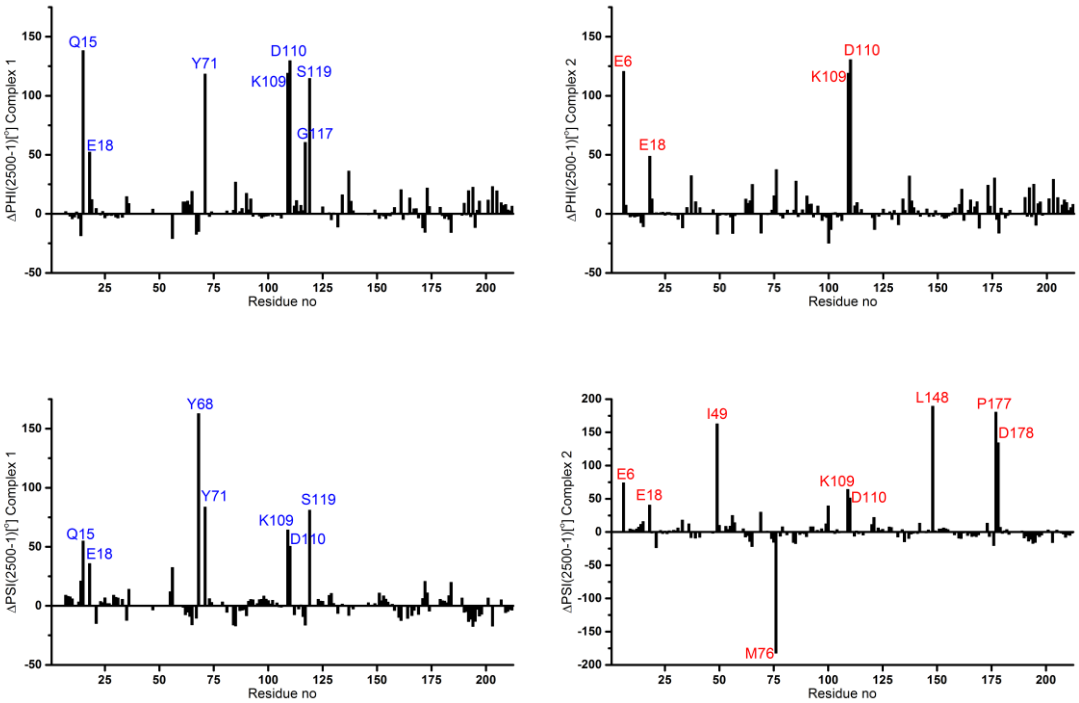

SI Figure 14. Differences in torsion angles values Phi (Φ) and Psi (Ψ) [°] between 2500 bar and 1 bar for S-COMT:SAM:DNC:Mg^{2+} (Complex 1) and S-COMT:Sinefungin:DNC:Mg^{2+} (Complex 2) derived from NMR data. Torsion angles were predicted by uploading the backbone $^{1}H_{N}$, ^{15}N, $^{13}C_{\alpha}$, $^{13}C_{\beta}$ and $^{13}C'$ chemical shifts to the TALOS-N webserver.

5. Preliminary results of protein backbone dynamics of S-COMT determined by NMR: evidence for dimerization

Authors: Sylwia Czarnota[a,b], Matthew J. Cliff[a], Nigel S. Scrutton[a,b], Jonathan P. Waltho[a,b,c], Sam Hay[a,b]*

[a]Manchester Institute of Biotechnology and [b]School of Chemistry, The University of Manchester, 131 Princess Street, Manchester, M1 7DN, United Kingdom

[c]Krebs Institute for Biomolecular Research, Department of Molecular Biology and Biotechnology, The University of Sheffield, Firth Court, Western Bank, Sheffield, S10 2TN, United Kingdom

Abstract

Backbone dynamics of human S-COMT were studied by ^{15}N NMR relaxation at 600 MHz and 800 MHz magnetic field strengths. The model-free formalism was used to determine internal motions parameters, identifying high rigidity of the protein and high contribution of slower dynamics (R_{ex} parameter appears for 25% of residues). Diffusion tensor analysis by Relax and HYDRONMR softwares strongly pictured dimerization, which is influencing relaxation rates. COMT is known to dimerize and a crystallographic dimer of COMT:DNC:Mg^{2+}:Sinefungin was obtained by our group in the past (PDB:6I3D, Chapter 3).

Introduction

Protein motions are essential for their functionality, and knowledge of protein dynamics is a key to understand the reaction mechanism and absolutely essential background for potential drug design and development. ^{15}N relaxation measurement is a well-known method to study the backbone dynamics of proteins in solution [1-3]. The analysis of the relaxation data in conjunction with the model-free (MF) approach of Lipari and Szabo [4, 5] reveals atomic level of nanosecond to picosecond timescale motions and probes the chemical exchange relaxation parameter R_{ex}, which is an indicator of slower dynamics (µs-ms) [6]. The MF formalism defines a spectral density in terms of molecular correlation time (τ_m), typically a few nanoseconds; effective internal correlation time (τ_e), which is in the picoseconds to nanoseconds time scale; and order parameter (S^2), which is a degree of restrictions of these fast internal motions [7].

The data presented in the preceding Chapters show S-COMT to have a relatively stable structure (see Chapters 3&4), but little data describing protein dynamics have been published for COMT to date. MD simulations of COMT by Lau and Bruice show that the physical properties of the active site do not change significantly between the catecholate or the transition state-bound states. In their simulations, most of the calculated fluctuations were smaller than those estimated from crystallographic B-factors. The only region that fluctuates was the C-terminal residues [8]. In MD simulations of apo-COMT, flexibility was reported for the Trp38 loop, while the Trp143 loop was classified as more constrained, because of side-chain interactions with other residues in catalytic site [9]. There were no conformational changes reported from

experimental studies, neither any significant flexibility of any part of the COMT structure.

NMR relaxation data analysis

Relaxation rates at field strengths of 600 MHz and 800 MHz for COMT:DNC:Mg^{2+}:Sinefungin and COMT:DNC:Mg^{2+}:SAM complexes are presented in **SI Table 2**. The ^{15}N R_1 and R_2 relaxation rates (**Figure 1**) were extracted from the decaying exponential function fit of the peak intensity versus relaxation delay time per assigned residue. Exponential function fits of the data are presented in **SI Figures 1-8**. It is noticeable that the data for the COMT:DNC:Mg^{2+}:SAM complex are noisy and do not fit well to the exponential function . In addition, the {^{1}H}-^{15}N hetNOE data for the COMT:DNC:Mg^{2+}:SAM complex exhibits poor signal to noise ratio (**SI Figure 9**). The quality of the spectra changes over time and the order that experiments were recorded in is significant. In case of T_1 and $T_{1\rho}$ experiments, better signal to noise (s/n) ratio appears for whichever was recorded first. For experiments at 600 MHz, $T_{1\rho}$ was recorded first and that shows better s/n ratio than T_1; while for experiments at 800 MHz the order was opposite and consequently $T_{1\rho}$ exhibits a worse s/n ratio. Moreover, the general trend for R_1 recorded at multiple magnetic field for proteins is known to be decrease with increasing magnetic field, while for R_2 it is increase with increasing magnetic field [10]. These trends are visible for the complex with sinefungin, but not for the complex with SAM (**SI Figure 10**). SAM is also known as a compound that degrades over time [11], therefore the COMT:DNC:Mg^{2+}:SAM complex has poor stability, and it is not appropriate for the data to be analysed further. However, model-free calculations for this are informatively presented in SI.

The data for the COMT:DNC:Mg^{2+}:Sinefungin complex are considerably better. By examining NMR relaxation rates, three loops of flexibility can be indicated: around residue Lys45, Ser81 and the third nearby residue Val132. These residues and neighbouring ones show a decrease in a trend of quite high hetNOE values and it is consistent with R_2 values. The protein is also dynamic at the beginning of the sequence, as well as at the end; as expected. However, correlation time estimated from T_1/T_2 ratio is higher than expected, with the average value of 54 ns for 600 MHz and 83 ns for 800 MHz. This is an indication of oligomeric states presented in the sample and influencing the rates.

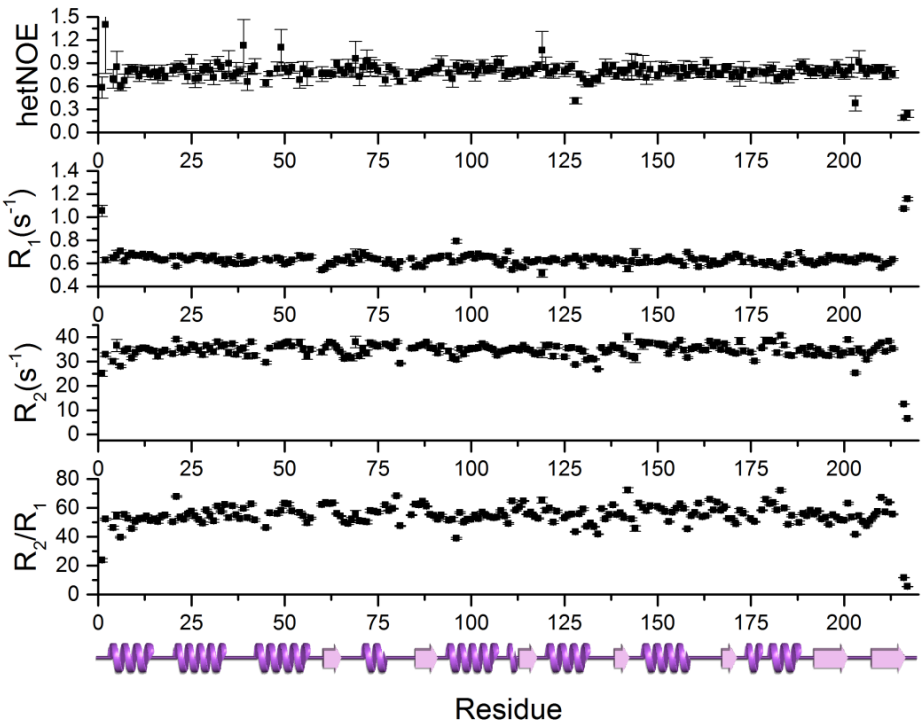

Figure 1. ^{15}N spin relaxation data for the COMT:DNC:Mg^{2+}:Sinefungin complex. Shown are: the steady-state heteronuclear NOE, the longitudinal (R_1) and transversal (R_2) relaxation rates as well as the R_2/R_1 ratio and at 600 MHz field strength. The bar at the bottom indicates the secondary structure elements from the crystal structure of COMT:DNC:Mg^{2+}:Sinefungin complex (PDB: 6I3D, chain A, α-helix darker colour, β-sheet lighter colour). Measurements were performed at 25°C.

Model-free analysis

MF model and parameters	Residues Fit
$\boldsymbol{m0}$: $\boldsymbol{none}$	53
$\boldsymbol{m1}$: $\{\boldsymbol{S^2}\}$	22
$\boldsymbol{m2}$: $\{\boldsymbol{S^2}, \boldsymbol{\tau_e}\}$	11
$\boldsymbol{m3}$: $\{\boldsymbol{S^2}, \boldsymbol{R_{ex}}\}$	2
$\boldsymbol{m4}$: $\{\boldsymbol{S^2}, \boldsymbol{\tau_e}, \boldsymbol{R_{ex}}\}$	3
$\boldsymbol{m5}$: $\{\boldsymbol{S_s^2}, \boldsymbol{S_f^2}, \boldsymbol{\tau_s}\}$	44
$\boldsymbol{m6}$: $\{\boldsymbol{S_s^2}, \boldsymbol{\tau_f}, \boldsymbol{S_f^2}, \boldsymbol{\tau_s}\}$	0

$\boldsymbol{m7 : \{S_s^2, S_f^2, \tau_s, R_{ex}\}}$	0
$\boldsymbol{m8 : \{S_s^2, \tau_f, S_f^2, \tau_s, R_{ex}\}}$	0
$\boldsymbol{m9 : \{R_{ex}\}}$	60
$\boldsymbol{no\ model}$	20

Table 1. Parameters fit in each Model-free (MF) model in Relax, and the number of residues fitted to each model in the analysis of COMT:DNC:Mg^{2+}:Sinefungin complex.

Initially, Relax software was used for relaxation rates fitting, using PDB: 6I3D (chain A) file as a structural model. Parameters fit in each Model-free model and the numbers of residues fitted are presented in **Table 1**. The resulting best fit value for the correlation time was 25 ns and the ratio between the long and short axes of the rotational diffusion tensor (D_z/D_x) fitted as 1.5. The correlation time is not consistent with a protein of the size of S-COMT, and estimation of the value using HYDRONMR gave 12 ns. The D_z/D_x value from this calculation was more consistent with the experimental values (**Table 2**). Previous data had indicated that S-COMT is monomeric, except that it crystallises as a dimer. The Relax software and HYDRONMR calculations were repeated using the dimer as a structural model (PDB: 6I3D, both chains). This gives the correlation time values of 25 ns and 31 ns, respectively, and that is also inconsistent. The fitting procedure can be compromised by a poor structural model, and lead to over estimates of S^2 and R_{ex} contributions (**Figure 2**). With this in mind, we used in-house Python scripts for model-free analysis that are not dependent on a PDB coordination frame. This gives τ_c of 24 ns and D_z/D_x of 1.41, similarly to Relax. Individual NH vectors in our calculations have angle theta fitted, and plotting these on the structure shows those with a small angle theta point across the beta sheet. A diffusion tensor was calculated on this basis and points along the dimerization interface. Results suggest transient dimerization. Using this fitting procedure we obtained S^2 average of 0.97 ± 0.03 and fewer, smaller R_{ex} terms than with Relax software (**Figure 3**).

S^2 order parameters are relatively high, suggesting that protein is very rigid. Relax software indicates two dynamic loops in the COMT:DNC:Mg^{2+}:Sinefungin

complex: around residue Arg75 and around residue Asp136. The second loop is consistent with the hetNOE/R_2 indicated loop. The average S^2 value calculated by Relax is 0.925 ± 0.020 T_1/T_2 ratios from experimental data are much higher than predicted by HYDRONMR, which is further evidence of a dimer contribution. An R_{ex} conformational exchange constant exists for 25% of residues (predicted by Relax) and it indicates intramolecular exchange between monomeric and dimeric states. It is clear that the diffusion tensor direction does not reflect the obtained crystallographic species (PDB: 6I3C – monomer; 6I3D – dimer).

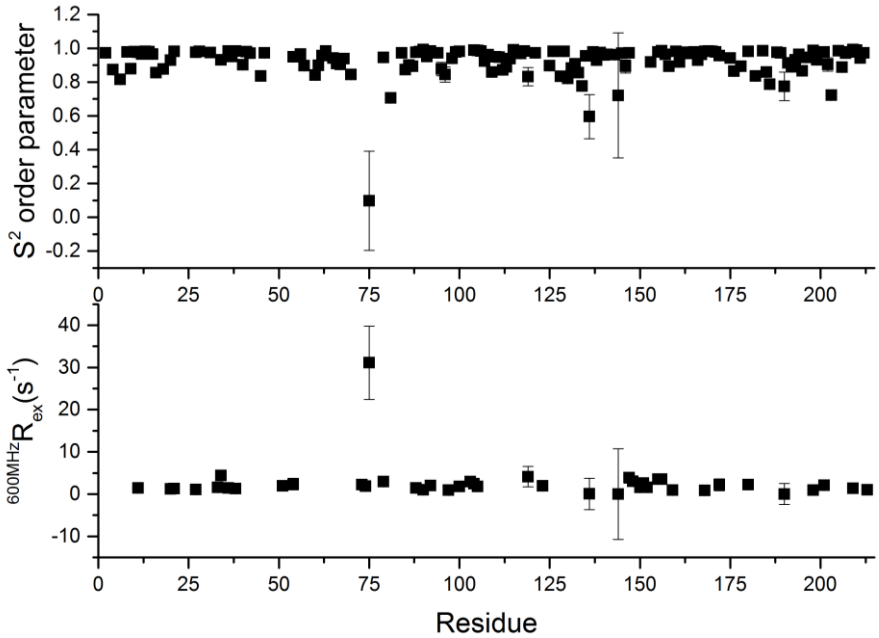

Figure 2. S^2 order parameter values and R_{ex} parameters for 600 MHz field strength for the COMT:DNC:Mg^{2+}:Sinefungin complex obtained using Relax software.

	COMT:DNC:Mg^{2+}: Sinefungin (monomer)	COMT:DNC:Mg^{2+}: Sinefungin (dimer)
diffusion type	prolate spheroid	ellipsoid
Average τ_c (ns)	Relax: 25 HYDRONMR: 12	Relax: 25 HYDRONMR: 31
S^2	Relax: 0.93 ± 0.02	Relax: 0.89 ± 0.02
D_z/D_x	Relax: 1.49 HYDRONMR: 1.24	Relax: 1.45 HYDRONMR: 1.70
Mean T_1/T_2	NMR experimental: 54.15 (600 MHz) 83.07 (800 MHz) HYDRONMR: 15.94 (600 MHz) 27.51 (800 MHz)	HYDRONMR: 95.69 (600 MHz) 169.7 (800 MHz)
diffusion tensor	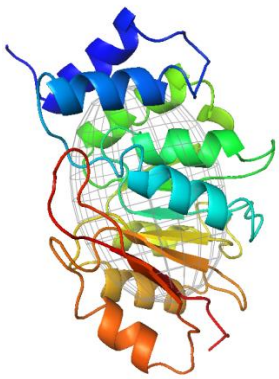	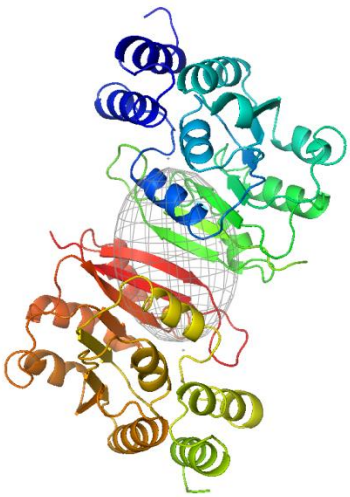

Table 2. Summary of selected data obtained by Relax and HYDRONMR softwares.

In the Relax software the diffusion tensor parameters strongly influence the optimisation of, and model selection between, the various model-free models. Herein, it is easily recognizable that model selection was wrong and diffusion tensor was wrongly fitted to the coordination frame.

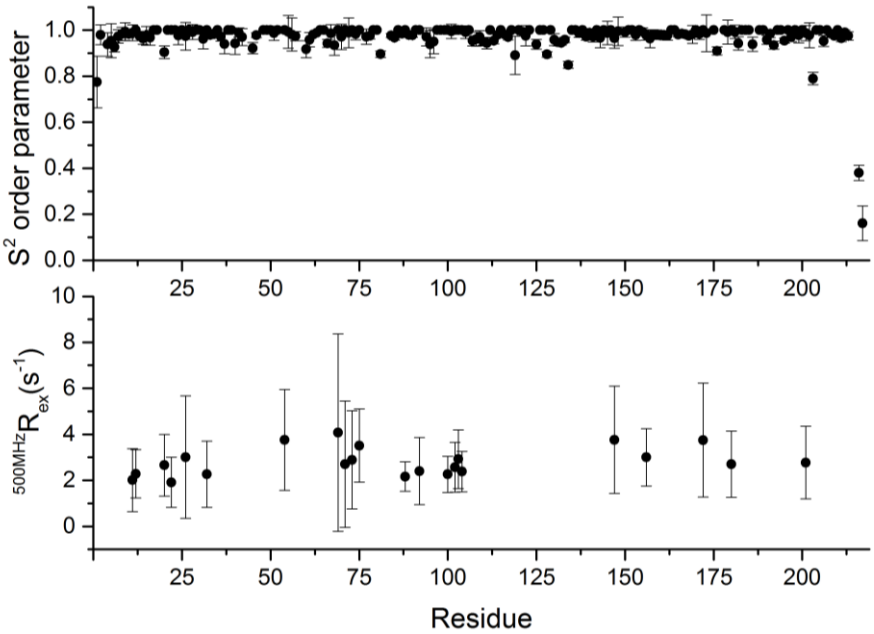

Figure 3. S^2 order parameter values and R_{ex} parameters for 500 MHz field strength for the COMT:DNC:Mg^{2+}:Sinefungin complex obtained using in-house Python scripts.

In the case of using in-house Python scripts for model-free analysis that are not dependent on the PDB coordination frame, S^2 parameters are still very high (average of 0.97 ± 0.03), likely contaminated by dimer contribution (**Figure 3**).An R_{ex} term exists now for 22 residues (11% of assigned residues, **Figure 3**) and the rotational correlation time τ_c is equal to 23 ns, which confirms the fast exchange between dimer and monomer. The D_z/D_x ratio is similar to that obtained from Relax, equal to 1.41. However, the theta angles of the calculated diffusion tensor differ from the Relax obtained diffusion tensor by 54° across the β-sheet (**Figure 4**), which clearly indicates a dimer contribution along the β-sheet. This is evidence consistent with our COMT:DNC:Mg^{2+}:Sinefungin crystallographic dimer, obtained previously (PDB:6I3D, Chapter 3). S^2 decreases in three regions, consistent with a decrease in hetNOE and R_2, around residues: Lys45, Ser81 and Val132. All of these residues are located in the loops, which are usually dynamic parts of a protein. Flexibility is also observed at the N-terminus and C-terminus, which is expected. Overall, S-COMT is very rigid and

highly ordered protein, which is consistent with the data presented in Chapter 3 and Chapter 4.

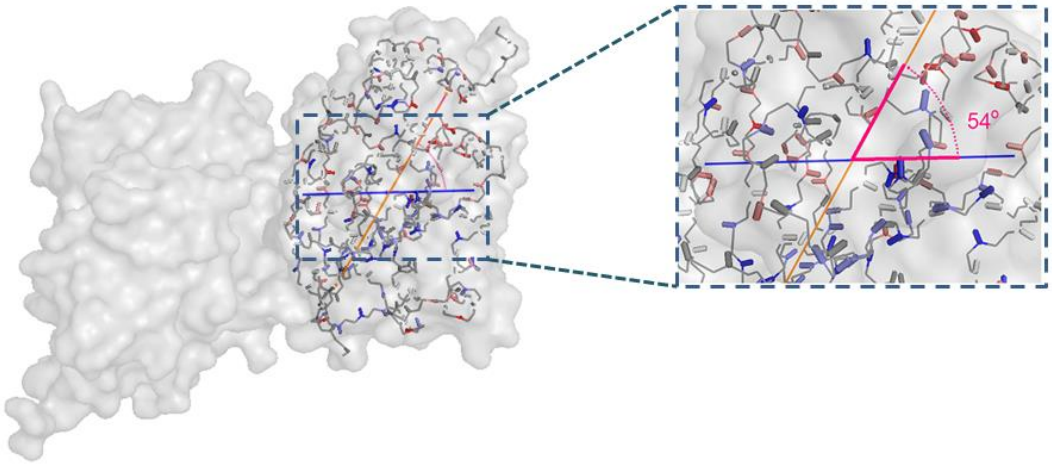

Figure 4. Surface representation of the COMT:DNC:Mg^{2+}:Sinefungin crystallographic dimer (PDB: 6I3D) with highlighted long axis diffusion tensor obtained by Relax software (orange) and calculated with in-house scripts (blue). The angle between them is coloured in magenta and equal to 54°. NH vectors are shown as sticks and coloured according to the angle theta with long axis of rotational diffusion tensor.

Conclusion and future work

The main conclusions from preliminary relaxation data are that further investigation is needed and that a dimer contribution is clear. The measured relaxation rates and NOEs reflect a combination of monomer and dimer states. To obtain the relaxation dynamic profile, ideally the monomer : dimer ratio has to be estimated or the monomer form has to be separated from the dimer, which will allow examination of the differential dynamics of the two forms. T_1, T_2 and NOE measurements do not provide enough data to permit determination of separate model-free dynamics parameters for the monomeric and dimeric states, but reflect a combination of the two states. Much effort has been made to separate these two forms, including different buffer additives supplementation, his-tag cleavage, longer purification with more steps and other minor differences in sample preparation, but it did not prevent absolutely the dimer formation. Ehler et al. obtained a few domain swapped COMT crystal structures and they claimed that the structural plasticity of COMT is not limited to loops, but entire sub-domains can be swapped to form COMT dimers [12]. This indicates an intrinsic structural plasticity of COMT.

Care should be taken, therefore, when considering relaxation parameters for a sample with dimer contribution, as it was reported that even small contributions from dimerization cause overestimates of the S^2 order parameter and errors in calculations of the internal correlation time [13]. The S^2 values were found to be high, but the nature of the proposed dimer interface (PDB: 6I3D) was quite unremarkable. However, to the best knowledge of the authors, we established evidences to confirm that S-COMT is a highly ordered and very rigid protein. Flexibility was observed in terminal regions and loops. For the future investigations, the proposed approach is to get relaxation rates from experiments performed at different sample concentrations, so the effect of dimer formation on intramolecular conformational exchange can be monitored as the concentration dependence of the difference between auto- and cross-correlated transverse relaxation rates. This approach includes determination of the dissociation constant, K_d, of a monomer-dimer equilibrium and can be obtained from a series of HSQC spectra at different protein concentrations, by following the approach published by Akke's group [14]. They have identified the dimer interaction surface by observation of chemical shift changes in the protein dilution series. These experiments have been tried and relaxation rates were recorded at 100 µM of protein concentration, but we have approached a very high s/n ratio. Furthermore, the monomer-dimer equilibrium studies were not seen to be relevant for the overall project and were beyond the scope of this PhD programme. A different approach is to perform mutagenesis to avoid dimerization. As the sample contained 10 mM DTT, we believe that dimerization is not caused by cysteine bridges, but instead a dimer interface occurs through the β-sheet, as in crystallographic species (Chapter 3, **SI Figure S1**), which is confirmed by theta angles calculation. We suggest mutagenesis of Arg184, as it is in strong polar contact with Gln195 from the second chain.

Another aspect that may be worth considering is a constant time Carr-Purcell-Meiboom-Gill (CPMG) relaxation dispersion experiment, which may help to understand conformational exchange in the µs-ms timescale and investigate protein equilibrium conformations.

Experimental details

Isotopically-labelled compounds: ^{15}N-labelled ammonium chloride (99%), $^{13}C_6$,$^{2}H_7$-labelled D-Glucose (U-$^{13}C_6$, 99%; 1,2,3,4,5,6,6-d_7 97-98%) and deuterium

oxide (99.8%) were purchased from Goss Scientific. 3,5-dinitrocatechol (DNC), S-adenosyl-L-methionine (SAM) and sinefungin (5′-deoxy-5′-(1,4-diamino-4-carboxybutyl)adenosine) were purchased with the highest purity available from Sigma-Aldrich (Poole, UK) and used as received.

Expression and purification of human soluble catechol-O-methyltransferase NMR studies was performed as described previously [15]. NMR samples containing 1 mM human S-COMT, 5 mM $MgCl_2$, 10 mM DNC and 10 mM sinefungin or 10 mM SAM in 50 mM Tris-HCl buffer, 50 mM NaCl, 10 mM DTT, 2 mM NaN_3, pH 7.5 were loaded into 5-mm diameter NMR tubes. ^2H_2O was added to the protein samples (10% v/v) to allow a deuterium lock and 0.5% v/v trimethylsilyl propanoic acid (TSP) was added as a reference signal.

NMR data were collected at a range of field strengths on a range of instruments. ^{15}N relaxation data for COMT:DNC:Mg^{2+}:Sinefungin complex were collected on a Bruker Avance 600 MHz magnet equipped with a 5 mm ^1H–^{13}C/^{15}N/^2H CPTXI cyroprobe at the University of Sheffield. ^{15}N relaxation data for the COMT:DNC:Mg^{2+}:SAM complex were collected on a 600 MHz Bruker four-channel liquid-state spectrometer equipped with a high sensitivity TXI cryoprobe with cooled proton channel. All high-field ^{15}N relaxation data sets were recorded on an 800 MHz Bruker Avance III NMR spectrometer fitted with a TCI cryoprobe equipped with Z gradients and TopSpin software version 3.2 housed in the Manchester Institute of Biotechnology.

All the experimental parameters and calculated relaxation rates obtained from the Relax software calculations and in-house Python scripts are presented in the SI for access by interested readers (**SI Table 2-5**).

Methods

The ^{15}N longitudinal relaxation rate (R_1), the ^{15}N spin-lock relaxation rate ($R_{1\rho}$) and the heteronuclear Overhauser effect ({^1H}-^{15}N NOE) were all recorded at two magnetic field strengths (600 MHz and 800 MHz) using the TROSY-readout pulse programs described in Ref. [16]. Experiments were performed at 25^oC on perdeuterated ^{15}N-labelled human S-COMT for two complexes (COMT:DNC:Mg^{2+}:Sinefungin and COMT:DNC:Mg^{2+}:SAM). $R_{1\rho}$ experiments were collected instead of R_2 experiments to prevent off-resonance artefacts from the ^{15}N pulses. $R_{1\rho}$ values were later converted to R_2 using the relation:

$$R_2 = \frac{R_{1\rho}}{sin^2\theta} - \frac{R_1}{tan^2\theta} \quad (5.1)$$

$$\theta = arctan\left(\frac{\gamma B_1}{\Delta\omega}\right) \quad (5.2)$$

where γB_1 is the ^{15}N spin-lock frequency, and $\Delta\omega$ is the difference in chemical shift (in Hz) between the peak and the carrier frequency.

Twelve relaxation delay time points were recorded randomly with some recorded twice or three times for a systematic error estimation (***R_1***: 0.05 s, 1.2 s, 6 s, 1.2 s, 2.7 s, 0.3 s, 0.8 s, 0.8 s, 4 s, 0.2 s, 0.5 s, 1.8 s; ***$R_{1\rho}$***: 1 ms, 200 ms, 20 ms, 110 ms, 20 ms, 60 ms, 90 ms, 10 ms, 40 ms, 20 ms, 140 ms, 10 ms). The sets of pseudo-3-dimensional spectra were analysed using CCPNMR Analysis [17]. T_1 and $T_{1\rho}$ decays were fit to single exponentials using in-house Python scripts (SI Figures 1-8) and recalculated to R_1 and R_2. Errors in fits were estimated by calculating the standard error among the measured duplicate/triplicate points. The $\{^1H\}$-^{15}N hetNOE values were calculated by taking the ratio of the peak volume of the presaturated spectrum to the reference spectrum, I_{sat}/I_{ref} (*(1.17)*. Errors in hetNOE were estimated on the basis of the noise in the spectrum.

The model-free (MF) formalism was applied to characterise fast timescale motions from collected NMR relaxation data using the program Relax (Ver. 4.0.2) [18, 19]. For the fitting, a ^{15}N CSA value of −172 ppm was fixed and the N–H bond length was fixed at 1.02 Å. Ten model-free models (with 0 to 5 adjustable parameters) with local τ_m model as a starting point, were used to describe the internal dynamics.

$$m0 : \{\} \quad (5.3)$$

$$m1 : \{S^2\} \quad (5.4)$$

$$m2 : \{S^2, \tau_e\} \quad (5.5)$$

$$m3 : \{S^2, R_{ex}\} \quad (5.6)$$

$$m4 : \{S^2, \tau_e, R_{ex}\} \quad (5.7)$$

$$m5 : \{S_s^2, S_f^2, \tau_s\} \quad (5.8)$$

$$m6 : \{S_s^2, \tau_f, S_f^2, \tau_s\} \quad (5.9)$$

$$m7 : \{S_s^2, S_f^2, \tau_s, R_{ex}\} \quad (5.10)$$

$$m8 : \{S_s^2, \tau_f, S_f^2, \tau_s, R_{ex}\} \quad (5.11)$$

$$m9 : \{R_{ex}\} \quad (5.12)$$

where S^2 is the generalized order parameter of a bond-vector, τ is the correlation time, R_{ex} is the chemical exchange relaxation rate (contribution to R_2 accounting for slow processes in the µs-ms timescale), subscript *e* refers to the local motion, subscript *s* and *f* refer to the slow and the fast motions.

Five different diffusion tensors were tested (no global diffusion tensor with a local τ_m parameter for each residue, sphere, prolate spheroid, oblate spheroid and ellipsoid). Selection of local model-free models during iterations for diffusion tensor optimization was done using Akaike information criterion (AIC) [20]. The best fitted model for each residue was selected on the basis of the small sample size-corrected Akaike information criterion (AIC_c). Finally, error estimates on the extracted local parameters were obtained by performing 500 Monte Carlo simulations to the fitted Lipari-Szabo parameters. Diffusion tensor representation obtained with Relax Python script connected with PyMol was plotted onto each complex's crystal structure. The D_z/D_x ratio was calculated as a measure of anisotropy. Results were compared with the calculated prediction from pdb structures obtained with HYDRONMR software version 7.C [21].

References

1. Peng, J.W. and G. Wagner, *Mapping of spectral density functions using heteronuclear NMR relaxation measurements.* Journal of Magnetic Resonance (1969), 1992. **98**(2): p. 308-332.
2. Kay, L.E., D.A. Torchia, and A. Bax, *Backbone dynamics of proteins as studied by nitrogen-15 inverse detected heteronuclear NMR spectroscopy: application to staphylococcal nuclease.* Biochemistry, 1989. **28**(23): p. 8972-8979.
3. Clore, G.M., et al., *Analysis of the backbone dynamics of interleukin-1. beta. using two-dimensional inverse detected heteronuclear nitrogen-15-proton NMR spectroscopy.* Biochemistry, 1990. **29**(32): p. 7387-7401.
4. Lipari, G. and A. Szabo, *Model-free approach to the interpretation of nuclear magnetic resonance relaxation in macromolecules. 1. Theory and range of validity.* Journal of the American Chemical Society, 1982. **104**(17): p. 4546-4559.
5. Lipari, G. and A. Szabo, *Model-free approach to the interpretation of nuclear magnetic resonance relaxation in macromolecules. 2. Analysis of experimental results.* Journal of the American Chemical Society, 1982. **104**(17): p. 4559-4570.
6. Bloom, M., L. Reeves, and E. Wells, *Spin echoes and chemical exchange.* The Journal of Chemical Physics, 1965. **42**(5): p. 1615-1624.
7. Stone, M.J., *NMR Relaxation Studies of the Role of Conformational Entropy in Protein Stability and Ligand Binding.* Accounts of Chemical Research, 2001. **34**(5): p. 379-388.
8. Lau, E.Y. and T.C. Bruice, *Comparison of the Dynamics for Ground-State and Transition-State Structures in the Active Site of Catechol O-Methyltransferase.* Journal of the American Chemical Society, 2000. **122**(30): p. 7165-7171.
9. Rutherford, K., et al., *The 108M polymorph of human catechol O-methyltransferase is prone to deformation at physiological temperatures.* Biochemistry, 2006. **45**(7): p. 2178-2188.
10. Morin, S., *A practical guide to protein dynamics from 15N spin relaxation in solution.* Progress in Nuclear Magnetic Resonance Spectroscopy, 2011. **59**(3): p. 245-262.
11. Lankau, T., T.N. Kuo, and C.H. Yu, *Computational Study of the Degradation of S-Adenosyl Methionine in Water.* The Journal of Physical Chemistry A, 2017. **121**(2): p. 505-514.
12. Ehler, A., et al., *Mapping the conformational space accessible to catechol-O-methyltransferase.* Acta Crystallographica Section D: Biological Crystallography, 2014. **70**(8): p. 2163-2174.
13. Schurr, J.M., H.P. Babcock, and B.S. Fujimoto, *A test of the model-free formulas. Effects of anisotropic rotational diffusion and dimerization.* Journal of Magnetic Resonance, Series B, 1994. **105**(3): p. 211-224.
14. Åkerud, T., et al., *Intramolecular dynamics of low molecular weight protein tyrosine phosphatase in monomer–dimer equilibrium studied by NMR: a model*

for changes in dynamics upon target binding. Journal of molecular biology, 2002. **322**(1): p. 137-152.

15. Czarnota, S., et al., *1H, 15N, 13C backbone resonance assignments of human soluble catechol O-methyltransferase in complex with S-adenosyl-L-methionine and 3,5-dinitrocatechol.* Biomolecular NMR Assignments, 2017. **11**(1): p. 57-61.

16. Lakomek, N.-A., J. Ying, and A. Bax, *Measurement of 15 N relaxation rates in perdeuterated proteins by TROSY-based methods.* Journal of biomolecular NMR, 2012. **53**(3): p. 209-221.

17. Vranken, W.F., et al., *The CCPN data model for NMR spectroscopy: development of a software pipeline.* Proteins, 2005. **59**(4): p. 687-96.

18. d'Auvergne, E.J. and P.R. Gooley, *Optimisation of NMR dynamic models I. Minimisation algorithms and their performance within the model-free and Brownian rotational diffusion spaces.* Journal of Biomolecular NMR, 2008. **40**(2): p. 107-19.

19. d'Auvergne, E.J. and P.R. Gooley, *Optimisation of NMR dynamic models II. A new methodology for the dual optimisation of the model-free parameters and the Brownian rotational diffusion tensor.* Journal of Biomolecular NMR, 2008. **40**(2): p. 121-33.

20. Hurvich, C.M. and C.-L. Tsai, *Regression and time series model selection in small samples.* Biometrika, 1989. **76**(2): p. 297-307.

21. De la Torre, J.G., M. Huertas, and B. Carrasco, *HYDRONMR: prediction of NMR relaxation of globular proteins from atomic-level structures and hydrodynamic calculations*. 2000, Elsevier.

Supporting Information

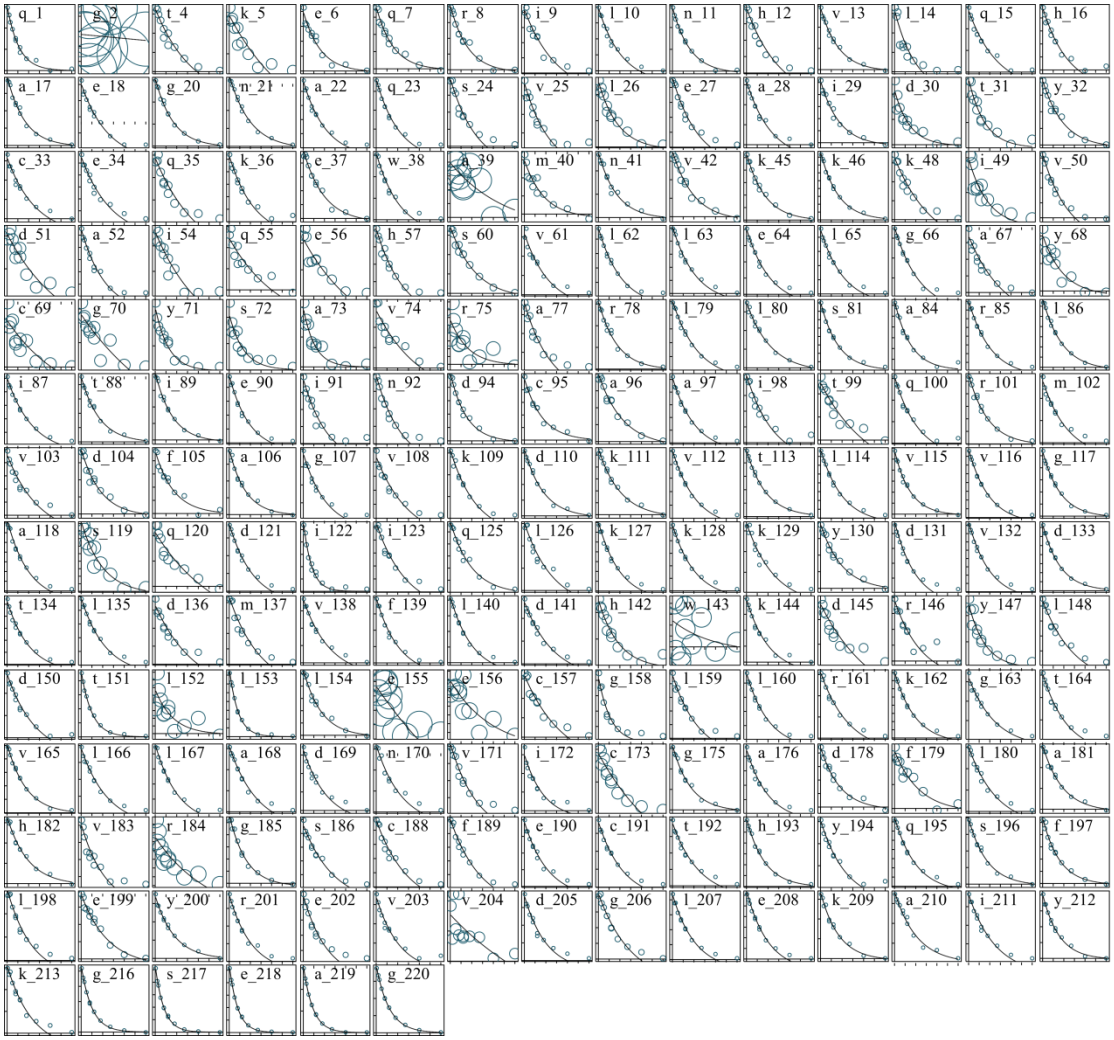

SI Figure 1. R_1 single exponential fit of peak height versus the relaxation delay time in 600 MHz for the COMT:DNC:Mg^{2+}:SAM complex. Rendered using in-house Python scripts.

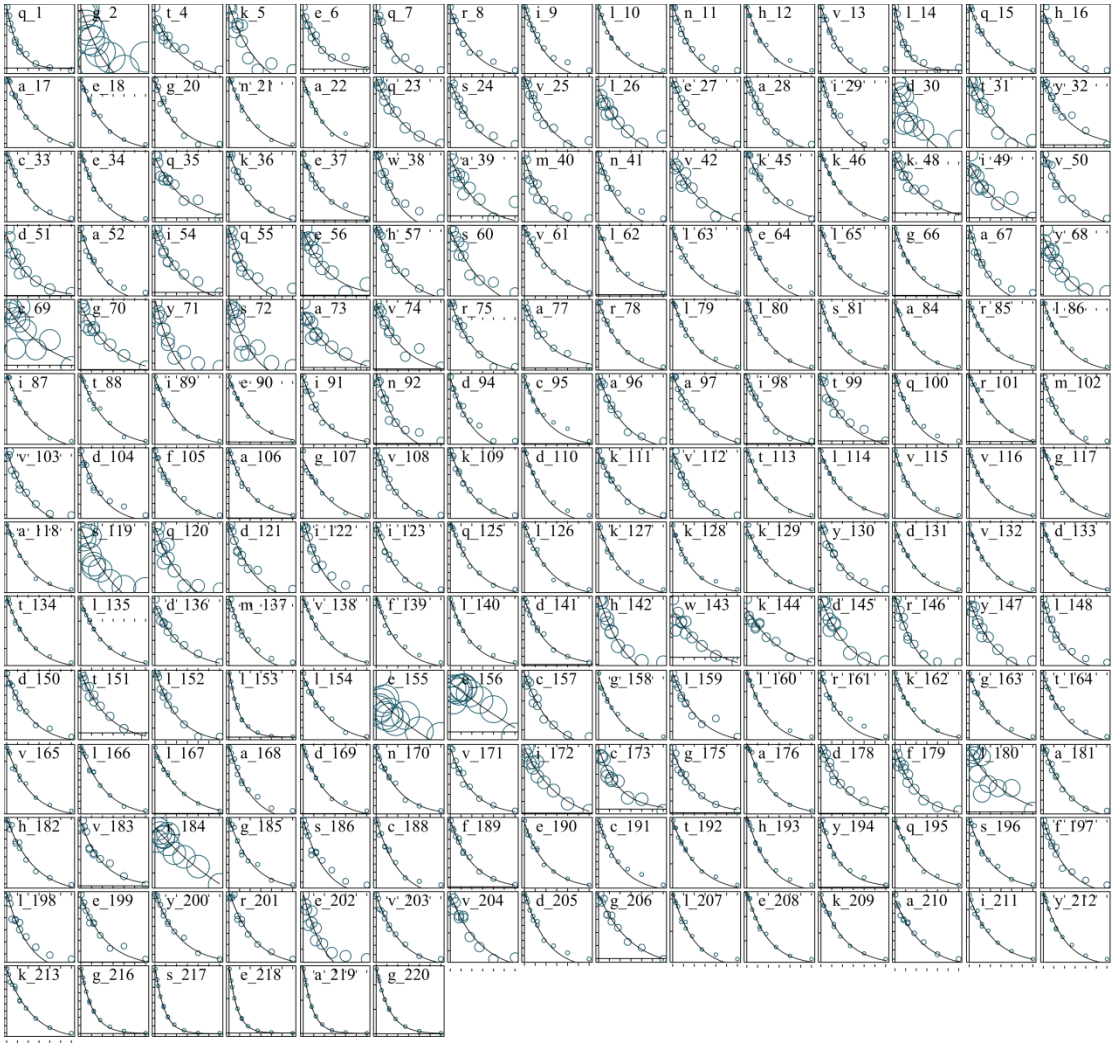

SI Figure 2. R_1 single exponential fit of peak height versus the relaxation delay time in 800 MHz for the COMT:DNC:Mg^{2+}:SAM complex. Rendered using in-house Python scripts.

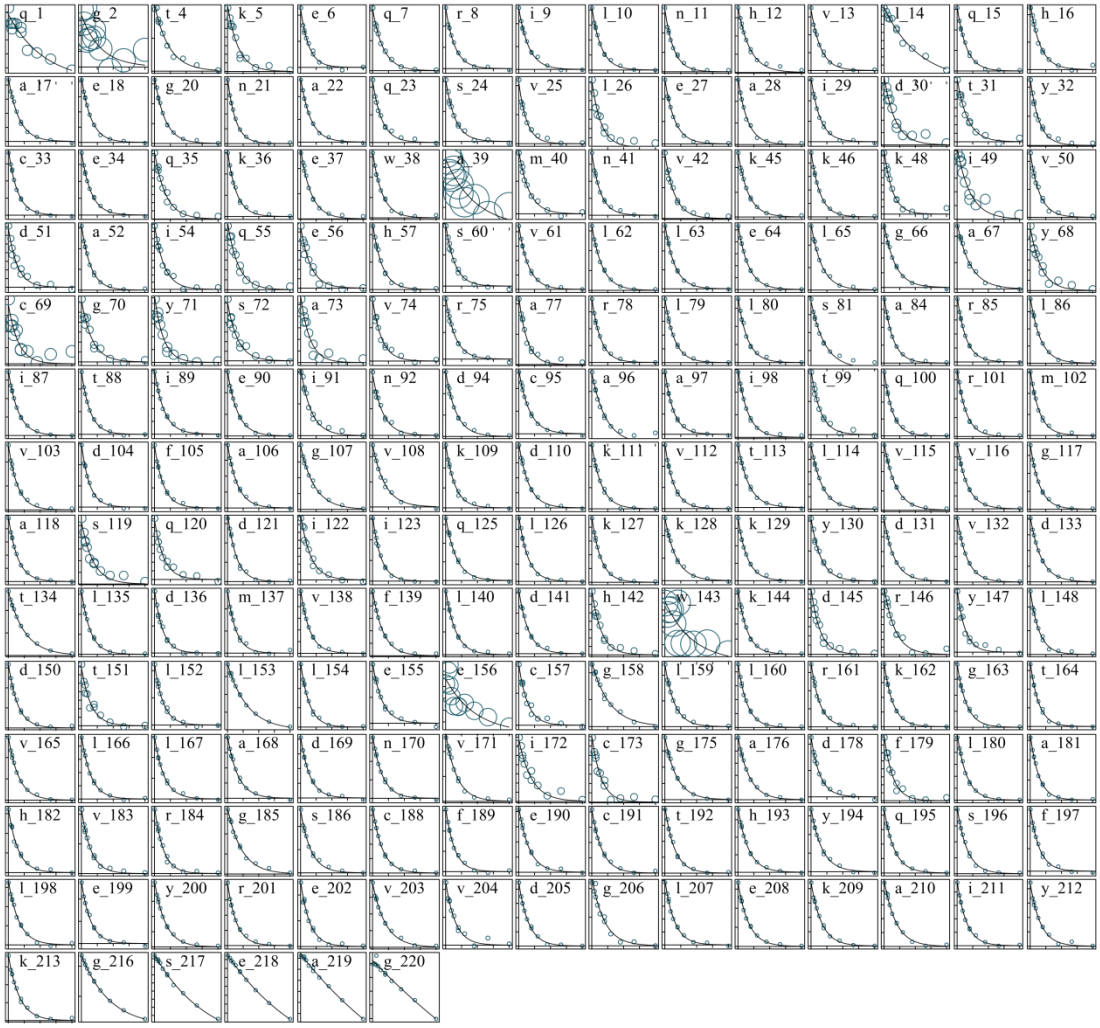

SI Figure 3. $R_{1\rho}$ single exponential fit of peak height versus the relaxation delay time in 600 MHz for the COMT:DNC:Mg^{2+}:SAM complex. Rendered using in-house Python scripts.

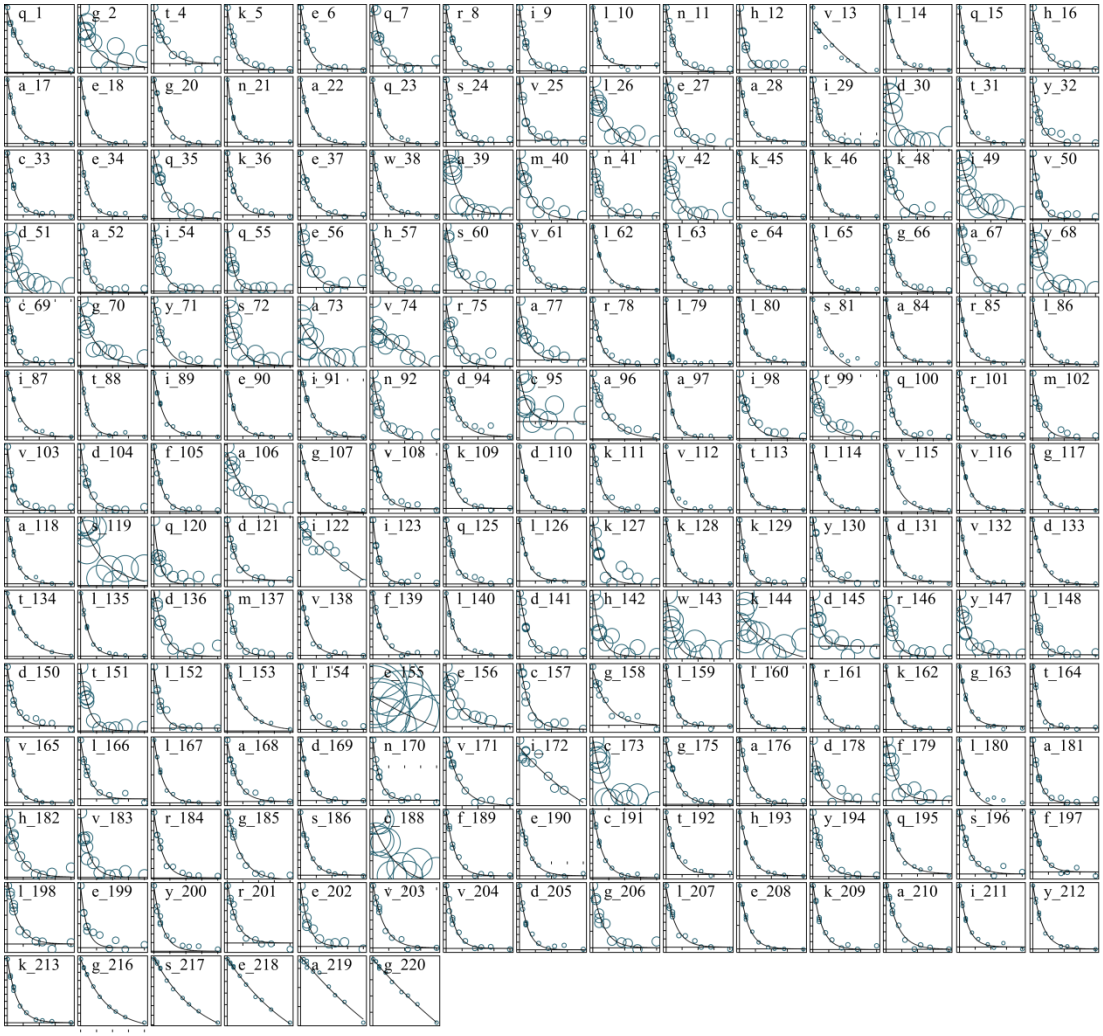

SI Figure 4. $R_{1\rho}$ single exponential fit of peak height versus the relaxation delay time in 800 MHz for the COMT:DNC:Mg^{2+}:SAM complex. Rendered using in-house Python scripts.

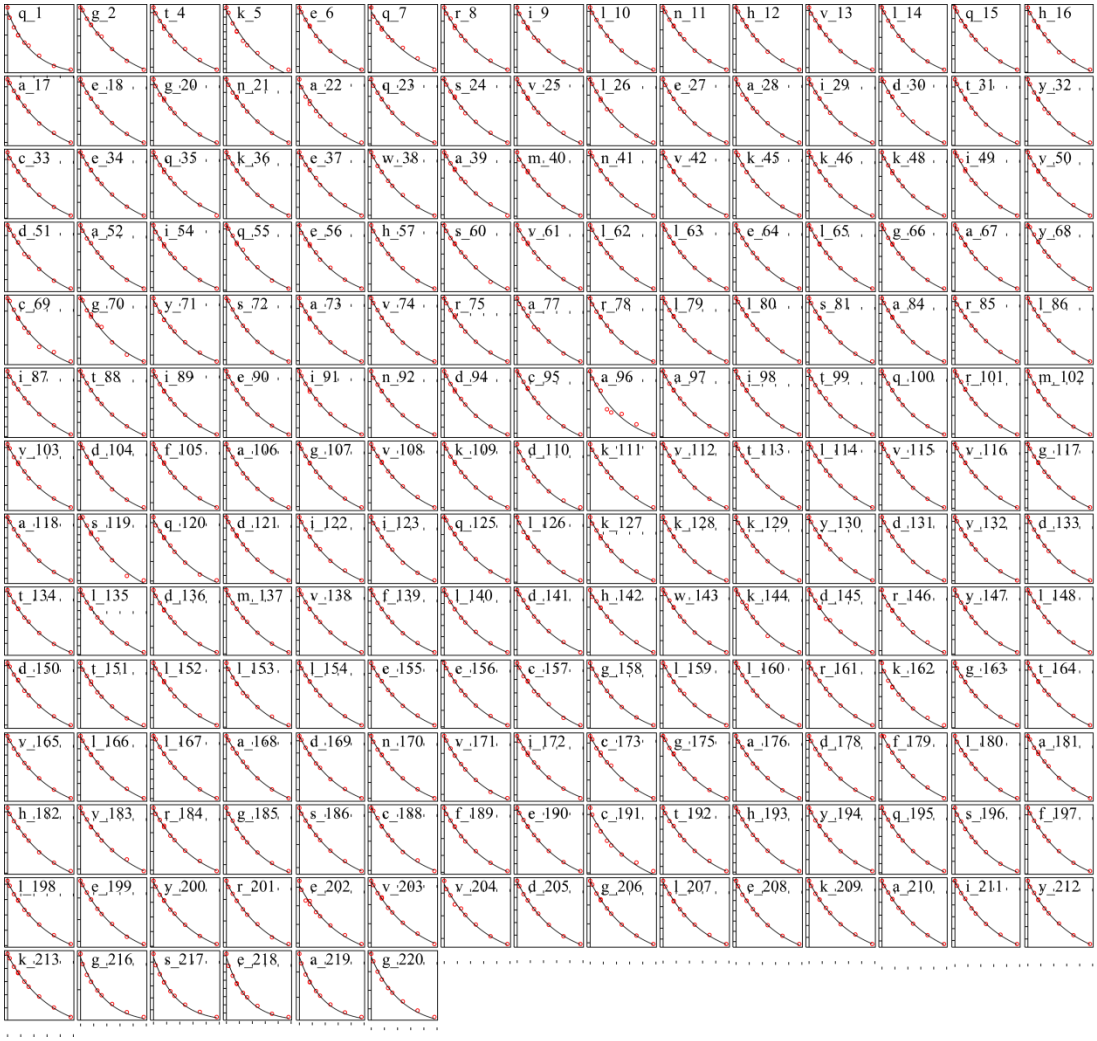

SI Figure 5. R_1 single exponential fit of peak height versus the relaxation delay time in 600 MHz for the COMT:DNC:Mg^{2+}:Sinefungin complex. Rendered using in-house Python scripts.

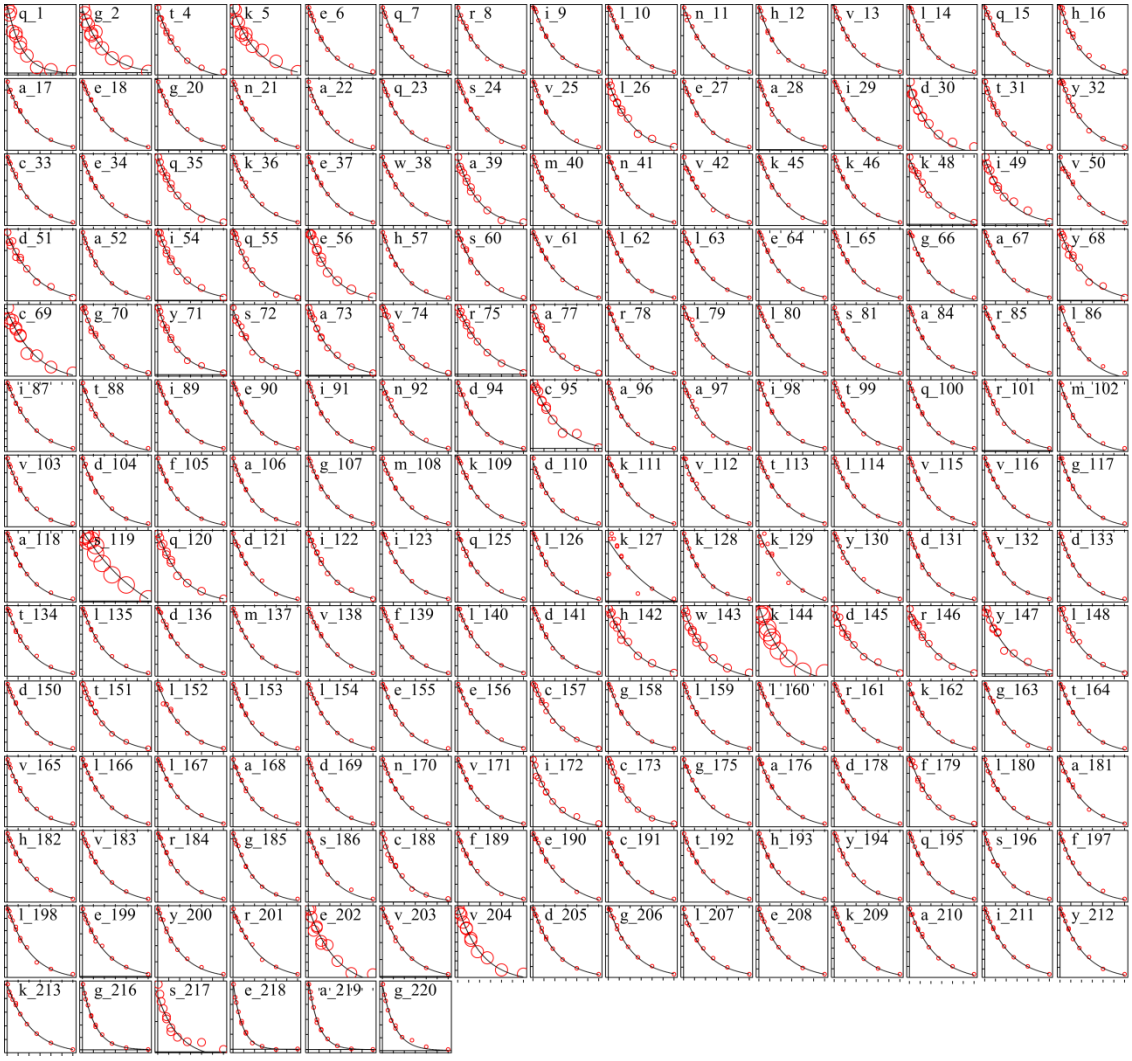

SI Figure 6. R_1 single exponential fit of peak height versus the relaxation delay time in 800 MHz for the COMT:DNC:Mg^{2+}:Sinefungin complex. Rendered using in-house Python scripts.

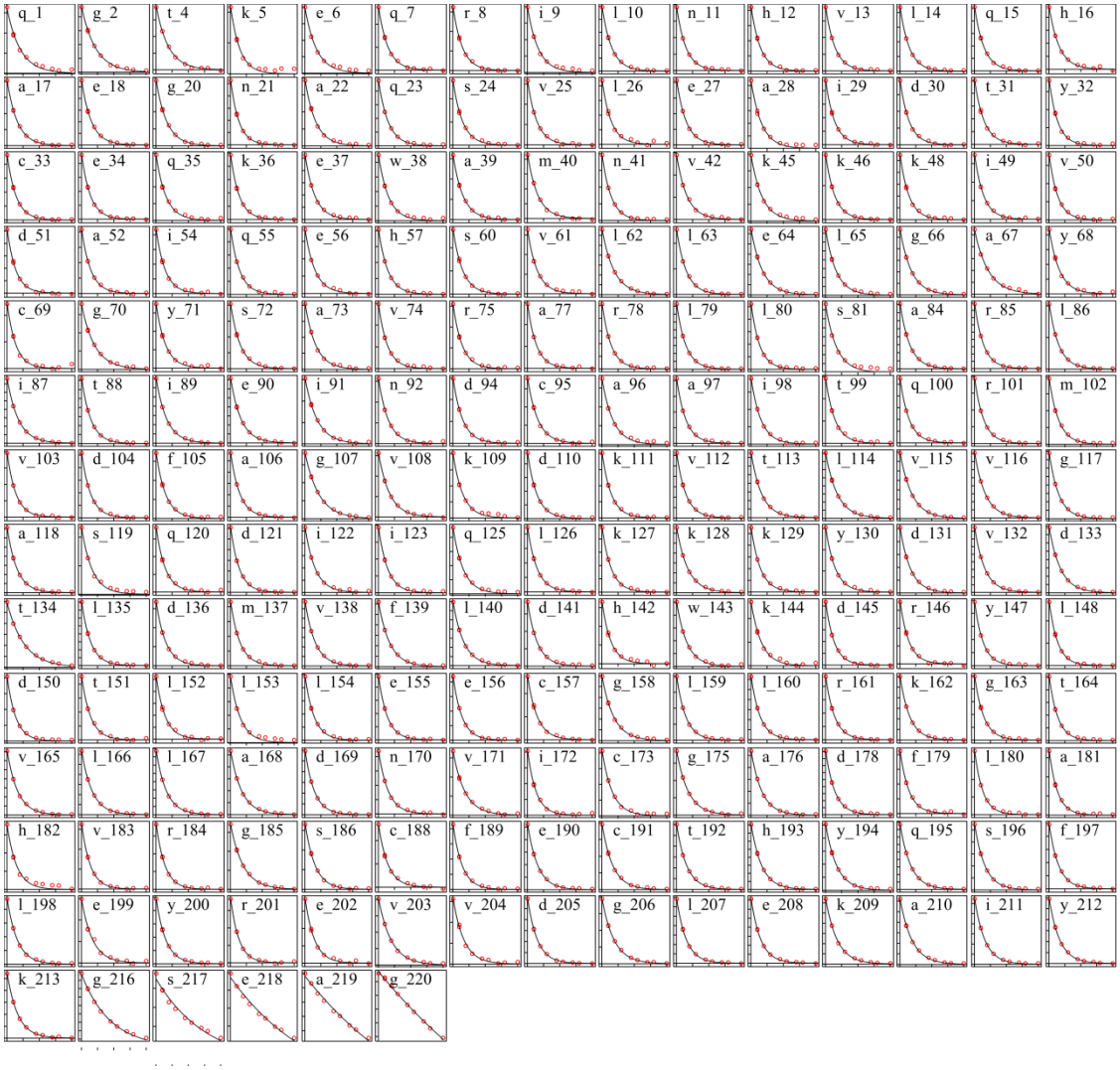

SI Figure 7. $R_{1\rho}$ single exponential fit of peak height versus the relaxation delay time in 600 MHz for the COMT:DNC:Mg^{2+}:Sinefungin complex. Rendered using in-house Python scripts.

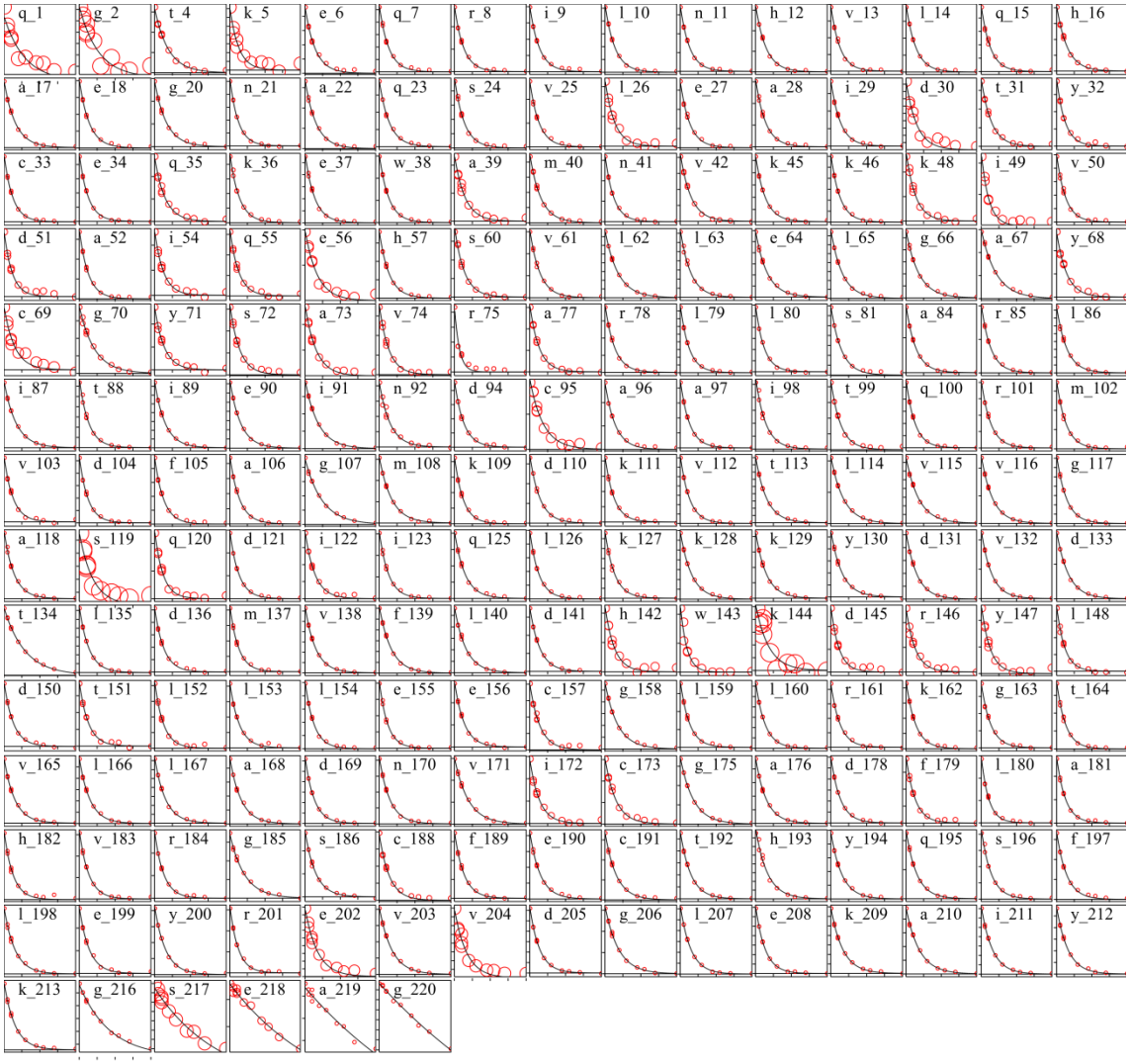

SI Figure 8. $R_{1\rho}$ single exponential fit of peak height versus the relaxation delay time in 800 MHz for the COMT:DNC:Mg^{2+}:Sinefungin complex. Rendered using in-house Python scripts.

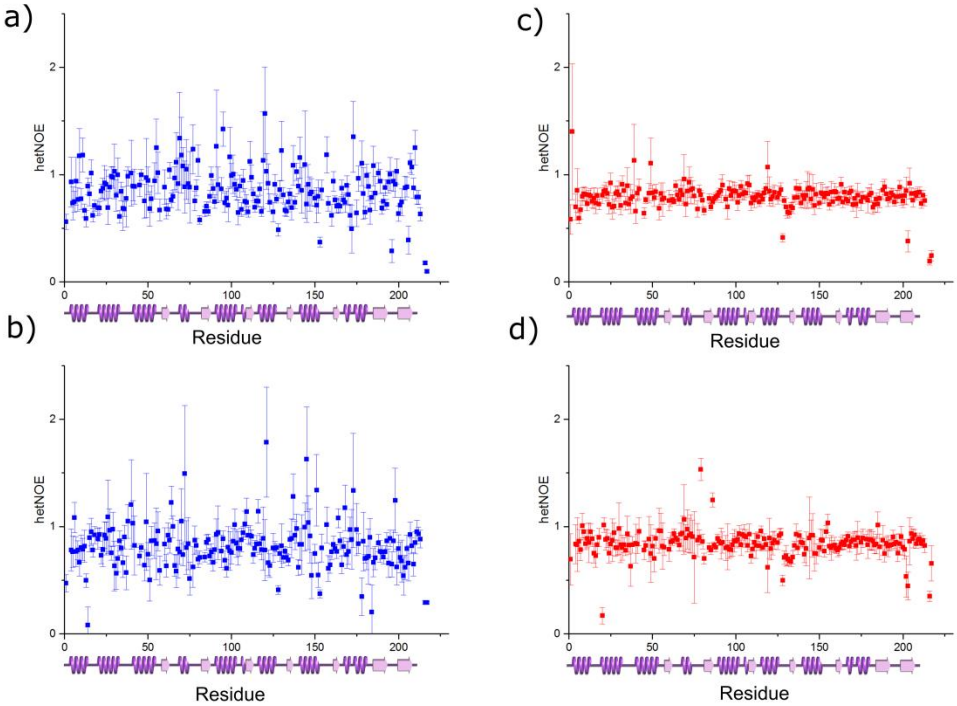

SI Figure 9. {^{1}H}-^{15}N hetNOE values of human S-COMT complexes recorded in different magnetic fields: a) COMT:DNC:Mg^{2+}:SAM at 600 MHz; b) COMT:DNC:Mg^{2+}:SAM at 800 MHz; c) COMT:DNC:Mg^{2+}:Sinefungin at 600 MHz; d) COMT:DNC:Mg^{2+}:Sinefungin at 800 MHz. The bar at the bottom of each graph indicates the secondary structure elements from the crystal structure of the COMT:DNC:Mg^{2+}:SAM complex (PDB: 6I3C , α-helix darker colour, β-sheet lighter colour). Measurements were performed at 25°C.

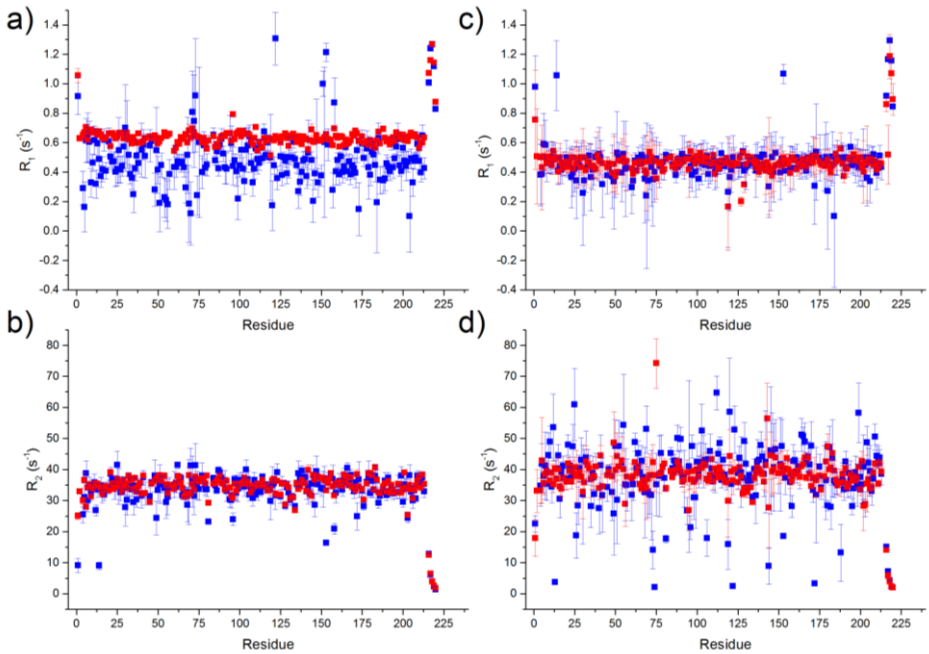

SI Figure 10. R_1 and R_2 values of human S-COMT complexes. a) and b) – data at 600 MHz; c) and d) – data at 800 MHz. Red colour - COMT:DNC:Mg^{2+}:Sinefungin, blue colour - COMT:DNC:Mg^{2+}:SAM. Measurements were performed at 25°C.

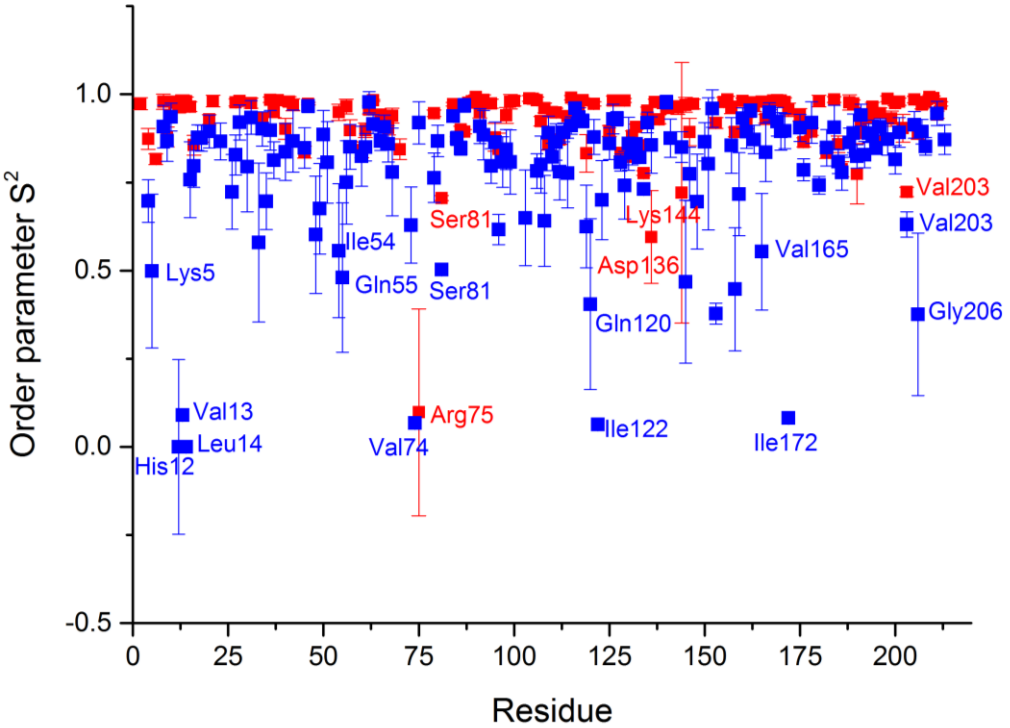

SI Figure 11. S^2 values of human S-COMT complexes. Red colour – COMT:DNC:Mg^{2+}: Sinefungin, blue colour - COMT:DNC:Mg^{2+}:SAM.

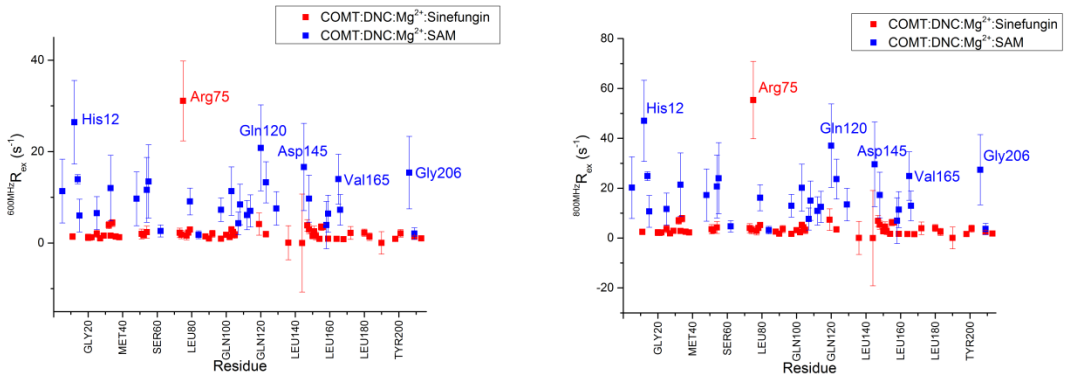

SI Figure 12. R_{ex} parameters of human S-COMT complexes for 600 MHz (left) and 800 MHz (right). Red colour – COMT:DNC:Mg^{2+}:Sinefungin, blue colour - COMT:DNC:Mg^{2+}:SAM.

	COMT:DNC:Mg^{2+}: SAM (monomer)	COMT:DNC:Mg^{2+}: Sinefungin (monomer)	COMT:DNC:Mg^{2+}: Sinefungin (dimer)
diffusion type	prolate spheroid	prolate spheroid	ellipsoid
average τ_m (ns)	Relax: 26 HYDRONMR: 13	Relax: 25 HYDRONMR: 12	Relax: 25 HYDRONMR: 31
S^2	Relax: 0.78 ± 0.06	Relax: 0.93 ± 0.02	Relax: 0.89 ± 0.02
D_z/D_x	Relax: 1.21 HYDRONMR: 1.25	Relax: 1.49 HYDRONMR: 1.24	Relax: 1.45 HYDRONMR: 1.70
Mean T_1/T_2	NMR experimental: 107.63 (600 MHz) 88.95 (800 MHz) HYDRONMR: 17.78 (600 MHz) 30.80 (800 MHz)	NMR experimental: 54.15 (600 MHz) 83.07 (800 MHz) HYDRONMR: 15.94 (600 MHz) 27.51 (800 MHz)	HYDRONMR: 95.69 (600 MHz) 169.70 (800 MHz)
diffusion tensor	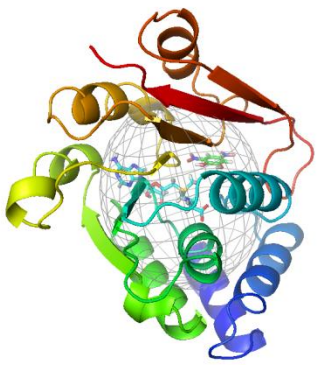	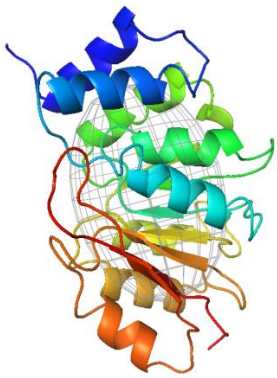	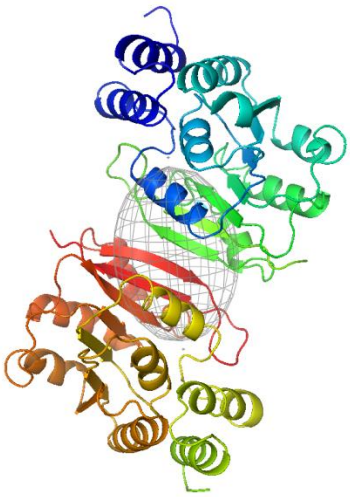

SI Table 1. Summary of selected data obtained by Relax and HYDRONMR softwares for the COMT:DNC:Mg^{2+}:Sinefungin (monomer and dimer) and the COMT:DNC:Mg^{2+}:SAM (monomer) complexes.

Residue	R_1 600 SAM (s^{-1})	R_1 600 Sin (s^{-1})	R_1 800 SAM (s^{-1})	R_1 800 Sin (s^{-1})	R_2 600 SAM (s^{-1})	R_2 600 Sin (s^{-1})	$R_2$800 SAM (s^{-1})	R_2 800 Sin (s^{-1})	hNOE 600 SAM	hNOE 600 Sin	hNOE 800 SAM	hNOE 800 Sin
GLN1	0.91446±0.12397	1.0552±0.04791	0.97863±0.20958	0.7548±0.3378	9.13768±2.24111	25.05208±1.1424	22.49133±2.71531	17.91942±5.95911	0.56158±0.07039	0.58333±0.13782	0.47286±0.08002	0.69378±0.23882
GLY2	-	0.62886±0.02047	-	0.50568±0.3221	-	32.87284±0.72479	-	33.13494±6.95335	-	1.4±0.63386	-	-
THR4	0.29028±0.11581	0.64905±0.02368	0.3801±0.20839	0.49916±0.12046	25.39959±2.55577	30.02226±1.0569	34.73848±6.58599	33.20366±4.02271	0.93161±0.23162	0.69701±0.12137	0.78174±0.19447	0.8356±0.18234
LYS5	0.16243±0.16833	0.66892±0.04638	0.38574±0.20191	0.43164±0.28626	31.05427±4.53153	36.58635±2.4839	41.75976±6.50192	42.88295±13.82703	0.73315±0.15515	0.85275±0.20219	0.76473±0.14439	0.83125±0.24927
GLU6	0.61403±0.14843	0.70555±0.01213	0.59136±0.20808	0.50555±0.0923	38.71347±4.07101	27.96286±0.54219	37.88864±5.30919	35.60921±3.70279	0.74835±0.09756	0.59437±0.05089	1.08408±0.14006	0.86111±0.11215
GLN7	0.634±0.16645	0.61717±0.01669	0.58254±0.1714	0.49939±0.07285	29.93749±3.44451	34.22609±0.97913	41.22232±10.72097	38.40921±3.51041	0.93897±0.22262	0.67355±0.08719	0.76666±0.1399	0.78298±0.09897
ARG8	0.60504±0.14019	0.66709±0.01409	0.45724±0.12214	0.46559±0.07003	34.67942±2.8837	35.17763±0.84249	35.23665±5.24249	39.51787±3.33392	0.76853±0.11182	0.79727±0.08139	0.78063±0.08676	1.00825±0.11586
ILE9	0.32759±0.09542	0.68661±0.01204	0.4977±0.10382	0.49284±0.04959	32.7219±2.81271	31.32375±0.59311	44.5655±7.2846	38.95237±2.2984	1.17558±0.25195	0.82014±0.06513	0.66609±0.12626	0.95028±0.07505
LEU10	0.46233±0.0581	0.66646±0.00973	0.47034±0.08009	0.50485±0.03711	33.86941±1.9219	33.72232±0.53315	48.84949±5.18769	36.38967±1.7062	0.77322±0.09886	0.8169±0.06365	0.80251±0.11789	0.84096±0.05543
ASN11	0.61487±0.0993	0.66778±0.01203	0.49926±0.11018	0.44359±0.05896	35.85427±2.6671	35.19768±0.71678	34.41717±5.15618	38.94352±2.7315	1.18209±0.15668	0.72901±0.06613	0.78806±0.10314	0.88741±0.08552
HIS12	0.31817±0.09593	0.67824±0.01024	0.50007±0.08114	0.54194±0.06163	26.88489±1.7709	35.53385±0.65064	53.51985±10.715	35.14422±2.6447	0.66563±0.06139	0.81095±0.04484	0.81586±0.14906	0.84961±0.18587
VAL13	0.59361±0.09914	0.651±0.01215	0.49903±0.09836	0.48412±0.05173	33.41881±2.2791	35.38324±0.70996	3.74125±0.23771	40.35443±2.497	0.59003±0.07823	0.79919±0.07285	0.49749±0.0628	0.95095±0.07327
LEU14	0.4889±0.12812	0.67564±0.01057	1.0564±0.23648	0.49533±0.0496	9.03186±1.20549	34.58093±0.62048	40.3632±2.84841	37.0465±2.26619	0.89062±0.07925	0.75±0.06076	0.08102±0.16882	0.88682±0.07341
GLN15	0.37211±0.07363	0.6535±0.01725	0.40748±0.09225	0.40149±0.0771	34.84538±2.5573	34.21413±1.0414	44.44272±3.6532	40.01212±3.9517	0.81946±0.10841	0.77983±0.09628	0.89544±0.12893	0.75236±0.09276
HIS16	0.41821±0.08659	0.63588±0.01904	0.4406±0.11854	0.49775±0.09842	32.33225±3.1022	32.10835±1.036	30.52281±6.11139	34.54015±4.01351	1.01477±0.12184	0.7337±0.09437	0.95211±0.12578	0.72739±0.1052
ALA17	0.61685±0.0747	0.62433±0.01091	0.41494±0.09311	0.46038±0.06051	31.76287±1.58161	33.89662±0.60751	39.21471±3.09331	33.80935±2.4503	0.62046±0.0623	0.80469±0.07019	0.77931±0.06233	0.83037±0.08595
GLU18	0.40823±0.05697	0.63142±0.00792	0.45495±0.08074	0.42571±0.04819	33.97706±1.8439	34.63742±0.47116	41.10394±3.26292	37.23429±2.20259	0.7103±0.05067	0.72316±0.04881	0.92053±0.07931	0.89759±0.08372
GLY20	0.60541±0.09617	0.66046±0.01202	0.4991±0.11853	0.46897±0.06994	34.20331±2.16422	33.20805±0.61311	37.04862±3.48696	35.99183±2.57753	0.69112±0.07254	0.80672±0.07558	0.88581±0.09821	0.17062±0.07782
ASN21	0.5042±0.06927	0.57514±0.00771	0.43215±0.06622	0.43354±0.03716	38.66123±2.11801	39.04766±0.58582	47.89004±3.28	41.91455±1.96889	0.69022±0.05966	0.84431±0.05486	0.92547±0.06221	1.01271±0.0678

ALA22	0.47006±0.05136	0.66362±0.01248	0.49974±0.06347	0.46507±0.06321	36.8095±1.32383	35.59445±0.5997	41.26557±2.81755	39.58781±2.34605	0.8459±0.06434	0.85366±0.07483	0.73244±0.07723	0.87864±0.09685
GLN23	0.47247±0.06449	0.64677±0.00991	0.36467±0.20833	0.49823±0.05205	34.05362±3.63222	33.62091±0.55292	37.18465±3.49858	36.04434±2.2988	0.87115±0.09405	0.82353±0.06668	0.78529±0.15632	0.88761±0.08249
SER24	0.40107±0.10136	0.62675±0.01612	0.39439±0.16058	0.42195±0.08084	34.30361±3.8589	34.79063±0.95989	47.36761±7.1312	39.02525±3.72741	0.9212±0.16299	0.72079±0.08543	0.91927±0.12534	0.75234±0.09119
VAL25	0.42009±0.11365	0.63932±0.01371	0.41906±0.15354	0.49764±0.07105	41.45336±4.5025	36.87805±0.86763	60.91214±11.55799	40.64887±3.43052	0.90855±0.13626	0.92059±0.09328	0.88937±0.15197	0.8367±0.10259
LEU26	0.54757±0.22135	0.66416±0.02047	0.34196±0.25949	0.45354±0.16318	34.53187±5.81249	35.9976±1.30339	18.75815±7.27072	37.78661±8.40229	0.69201±0.1551	0.69537±0.10959	1.08979±0.3414	0.87164±0.19924
GLU27	0.41457±0.09063	0.66668±0.0113	0.43191±0.13996	0.48211±0.05914	32.58353±2.6754	34.4947±0.65188	28.32749±6.11329	38.52267±2.72431	0.88258±0.10456	0.70606±0.06492	0.96458±0.20032	0.94098±0.09121
ALA28	0.44001±0.06925	0.66302±0.01399	0.445±0.13167	0.49076±0.0614	35.13683±2.5789	32.76426±0.89435	40.48745±4.14962	38.95123±2.8747	0.98308±0.0882	0.82171±0.07023	0.75283±0.06572	0.8024±0.07834
ILE29	0.5718±0.1086	0.62632±0.00911	0.49812±0.0998	0.43125±0.05344	34.68579±2.65711	36.62501±0.60434	43.10179±7.13489	37.60076±2.49701	0.97458±0.10073	0.83951±0.05642	0.97491±0.15944	0.80103±0.06871
ASP30	0.69983±0.29242	0.64597±0.02374	0.25788±0.35668	0.49999±0.19587	27.80888±6.00639	35.33508±1.447	31.934±15.93099	32.81877±8.68803	1.02938±0.25463	0.8087±0.13047	0.63326±0.2315	0.97987±0.24096
THR31	0.65586±0.22922	0.66583±0.01839	0.34286±0.23505	0.49802±0.10627	30.20706±4.7922	33.97031±1.0588	42.90373±3.44481	35.85023±4.88719	0.80604±0.14825	0.71295±0.08909	0.56265±0.1493	0.83103±0.16676
TYR32	0.51631±0.14042	0.62085±0.01235	0.42129±0.15725	0.41282±0.09899	35.35821±3.67709	38.0133±0.80992	43.76502±8.59288	42.51259±5.28752	0.99811±0.15909	0.90984±0.07757	0.7008±0.12427	0.80253±0.11673
CYS33	0.38501±0.0678	0.63122±0.00898	0.45794±0.09833	0.46591±0.04374	35.08983±2.1826	36.31325±0.61175	41.40263±5.1296	41.29633±2.1984	0.60844±0.06024	0.85093±0.05709	0.8673±0.09236	0.82951±0.06889
GLU34	0.36074±0.07927	0.59292±0.00924	0.51175±0.0843	0.46832±0.04071	33.5002±2.13471	36.90044±0.62965	40.22397±4.28189	40.32837±2.1107	0.84264±0.0881	0.73381±0.06246	0.80112±0.06921	0.77675±0.04825
GLN35	0.24832±0.12345	0.63354±0.02334	0.36392±0.22634	0.44272±0.14997	29.4818±4.09211	33.68141±1.3228	28.09088±6.76552	36.79557±5.90179	0.6844±0.20367	0.8955±0.16931	0.66387±0.13753	0.93223±0.16647
LYS36	0.42421±0.08349	0.60613±0.00857	0.41423±0.13004	0.44123±0.08181	34.89016±2.7136	37.18316±0.60564	38.87136±5.39871	37.46642±3.91051	0.67862±0.06849	0.72626±0.04833	0.90218±0.10917	0.82595±0.08395
GLU37	0.51098±0.10858	0.59636±0.01535	0.42955±0.1189	0.43125±0.06845	30.32065±2.57001	32.88637±0.97483	32.00997±4.5078	37.78724±3.21679	0.77687±0.26298	0.77385±0.13617	0.56986±0.15784	0.6307±0.18552
TRP38	0.46161±0.07262	0.66194±0.0104	0.49824±0.13809	0.41904±0.0648	34.67075±2.42321	34.80245±0.56725	40.92481±4.21171	40.90478±3.05329	0.98308±0.0882	0.79286±0.06381	1.04812±0.15844	0.83096±0.07701
ALA39	-	0.59768±0.0211	-	0.51196±0.16284	-	35.56253±0.79646	-	-	-	1.13057±0.33648	-	-
MET40	0.5493±0.18104	0.60492±0.021	0.52153±0.18232	0.47758±0.08772	31.48866±3.8069	32.22648±1.1466	27.5107±8.21964	33.99935±3.5864	1.01362±0.30768	0.66069±0.11572	1.20512±0.41721	0.84144±0.18077
ASN41	0.58569±0.10405	0.60658±0.01132	0.49811±0.11578	0.4704±0.06019	37.41603±2.3924	37.99137±0.71919	41.2929±9.84962	44.48923±3.13481	0.89305±0.13569	0.82677±0.07152	1.02875±0.21165	0.83757±0.08921

VAL42	0.50827±0.1503	0.62867±0.01581	0.31662±0.224	0.45831±0.09183	32.23032±3.647	32.40097±0.85113	31.72726±11.93498	34.51326±3.95511	0.88846±0.16177	0.8643±0.09658	0.82353±0.2742	0.95291±0.13265
LYS45	0.57912±0.10972	0.63963±0.01063	0.37604±0.12402	0.43121±0.07204	31.41191±2.8152	29.55369±0.58139	34.2702±4.54702	38.0333±3.38661	0.90214±0.10691	0.64072±0.04978	0.72536±0.08343	0.77988±0.08505
LYS46	0.60818±0.03454	0.62595±0.00462	0.43488±0.03139	0.45736±0.03199	35.7964±0.87965	35.40169±0.29249	40.07528±1.5505	39.04449±1.55959	0.99768±0.05043	0.76254±0.02944	0.80258±0.03534	0.82351±0.04546
LYS48	0.27965±0.11321	0.64862±0.01764	0.36952±0.21583	0.39479±0.13444	38.01968±5.132	36.33241±1.0316	32.62845±9.04539	37.76662±6.55841	0.75323±0.15767	0.82673±0.08993	0.63965±0.14691	0.88343±0.20919
ILE49	0.54811±0.29287	0.63077±0.02651	0.33534±0.32158	0.45474±0.18632	24.39924±5.402	36.75924±1.60481	25.74429±13.24104	48.57497±9.95077	0.9696±0.3666	1.10407±0.23591	1.04296±0.45113	0.74899±0.26906
VAL50	0.41381±0.09246	0.59236±0.01193	0.36887±0.14226	0.37143±0.07405	33.27569±3.4164	37.43946±0.82065	47.47145±8.484	39.84228±3.90709	0.94335±0.12871	0.83065±0.07339	0.74012±0.11198	0.81794±0.10127
ASP51	0.18982±0.19438	0.60636±0.01643	0.53051±0.2808	0.39832±0.14926	35.28685±6.18102	37.98526±1.1664	30.2313±13.992	44.25289±7.60861	0.68077±0.1603	0.78426±0.08237	0.50081±0.19613	0.70069±0.1234
ALA52	0.44791±0.07986	0.62885±0.01087	0.49875±0.10531	0.4775±0.05596	35.15864±2.62149	36.30985±0.67009	47.51353±8.32988	40.93681±2.8364	0.77305±0.12516	0.84091±0.06929	0.86681±0.13636	0.88826±0.09036
ILE54	0.22697±0.13421	0.66814±0.021	0.39412±0.19402	0.47434±0.1506	33.98904±4.36731	37.8501±1.2912	42.08405±9.7928	42.83965±7.72022	0.9417±0.16931	0.68638±0.10913	0.86976±0.16514	0.96097±0.20974
GLN55	0.20948±0.14475	0.64393±0.01861	0.52181±0.2218	0.49276±0.11465	29.41782±5.14262	35.12692±1.1185	54.31814±16.28594	39.98902±6.05838	1.24868±0.26944	0.82398±0.09978	0.83862±0.33264	0.95656±0.16633
GLU56	0.18054±0.16326	0.65184±0.02543	0.42215±0.32284	0.46469±0.19261	31.17741±5.6692	32.3195±1.3805	35.12949±11.50302	28.86221±7.193	1.01658±0.19331	0.76678±0.15585	0.95668±0.18	0.81715±0.21669
HIS57	0.38562±0.10202	0.65875±0.01321	0.42747±0.14966	0.47406±0.05496	34.09557±3.3169	34.94132±0.67	34.97018±8.4465	37.63085±2.47771	0.66994±0.10266	0.78146±0.05883	0.58985±0.1367	0.80589±0.07587
SER60	0.43212±0.14794	0.54256±0.01477	0.2972±0.18031	0.42394±0.09262	35.10295±4.20969	33.75839±0.94242	31.83837±8.23651	37.11166±4.80871	0.88372±0.16065	0.75787±0.09537	0.83482±0.15353	0.78696±0.11104
VAL61	0.43311±0.07048	0.56225±0.01195	0.33857±0.09673	0.38418±0.06231	34.29631±1.7538	35.75913±0.81224	35.18115±5.18061	37.76655±2.84161	0.67989±0.09284	0.75796±0.05595	0.63422±0.1057	0.85661±0.08573
LEU62	0.47115±0.05073	0.60143±0.00632	0.47601±0.05713	0.46037±0.02593	41.3797±1.09931	37.85938±0.31346	48.76114±2.85901	42.34118±0.87544	0.67627±0.05737	0.76847±0.04349	0.91699±0.11809	0.86704±0.042
LEU63	0.46824±0.04699	0.58999±0.00334	0.45936±0.05634	0.4084±0.02403	35.43113±1.13211	37.45773±0.20966	40.2587±3.9905	38.70397±1.1553	1.04195±0.07312	0.75253±0.02212	0.8711±0.11895	0.93455±0.04468
GLU64	0.45755±0.0578	0.63566±0.00738	0.49786±0.07269	0.46677±0.03395	37.26215±1.33235	35.63528±0.34039	45.20834±3.98674	40.84417±1.27304	0.76264±0.06753	0.89503±0.0519	1.22392±0.15232	0.89168±0.04581
LEU65	0.46828±0.05231	0.62473±0.0059	0.45524±0.05445	0.46192±0.02546	31.64385±1.17511	33.93937±0.32193	38.89575±2.6363	35.25261±1.01311	0.79579±0.0559	0.81159±0.04355	0.99949±0.10241	0.87525±0.03889
GLY66	0.42981±0.06452	0.6229±0.0075	0.51525±0.06862	0.45583±0.03838	32.70082±1.56103	31.20529±0.38408	42.75723±4.89372	33.77942±1.23283	0.9671±0.10761	0.76879±0.05104	0.6377±0.10265	0.82694±0.05342
ALA67	0.29421±0.10517	0.65642±0.01775	0.49943±0.13291	0.46518±0.0682	32.22399±2.25614	32.27477±0.64237	37.57271±5.4091	36.48641±1.93063	1.11547±0.27755	0.85149±0.10114	0.5824±0.153	0.92723±0.10874

TYR68	0.51498±0.2583	0.59954±0.01776	0.35232±0.29644	0.41131±0.14639	28.61086±5.46201	31.38783±1.1031	32.60747±14.53102	35.46105±6.27638	0.91395±0.24277	0.8089±0.09104	0.78888±0.26935	0.93718±0.16501
CYS69	0.18458±0.26064	0.68156±0.0433	0.23929±0.49475	0.39209±0.25492	32.73211±10.46402	38.03829±2.421	52.93946±7.518	34.01563±10.07304	1.33711±0.4302	0.95775±0.22753	0.76052±0.11236	1.06615±0.32478
GLY70	0.11794±0.21285	0.63432±0.02527	0.33907±0.26564	0.47037±0.1021	41.20903±5.72512	32.28108±1.05072	32.75191±8.24318	36.93528±2.98707	1.18066±0.35302	0.7252±0.11591	1.05103±0.3024	0.89137±0.12728
TYR71	0.80812±0.27526	0.6929±0.02828	0.49825±0.21971	0.5358±0.13943	36.11132±8.2771	35.20003±1.5617	31.9378±6.29212	38.10494±6.73342	1.07961±0.1724	0.84576±0.11784	0.73824±0.10318	0.97487±0.1813
SER72	0.74631±0.31494	0.66732±0.02237	0.43267±0.26539	0.49855±0.12427	31.51607±6.00769	33.51387±1.2658	31.74839±14.38899	38.15434±5.60359	0.8845±0.24311	0.92793±0.14338	1.49237±0.63521	0.91588±0.16128
ALA73	0.92003±0.3854	0.64744±0.02213	0.34841±0.3155	0.47612±0.1402	41.33631±7.06809	37.58671±1.13461	14.09189±6.15225	42.28127±5.75286	1.04829±0.27994	0.85471±0.12053	0.80458±0.24933	0.93252±0.17916
VAL74	0.24122±0.13304	0.63988±0.0144	0.40229±0.20607	0.4721±0.11173	34.92004±4.5262	36.87305±0.98646	2.11809±0.73802	38.10613±5.23602	0.91432±0.18091	0.86777±0.0766	0.84066±0.24295	0.90653±0.1542
ARG75	0.6018±0.51128	0.63529±0.01404	0.48909±0.14745	0.35507±0.14022	33.61974±3.44691	36.16792±0.91006	35.19954±9.98949	74.1319±8.03104	0.88309±0.33243	0.80083±0.07473	0.51475±0.15171	0.71356±0.42708
ALA77	0.39893±0.10999	0.59889±0.0152	0.44761±0.15546	0.45286±0.12718	38.0242±4.06369	37.10966±0.99565	37.81895±12.93103	38.46789±6.08319	1.23645±0.22822	0.67965±0.0749	0.62353±0.18904	0.87376±0.15422
ARG78	0.5819±0.09306	0.63057±0.00823	0.43765±0.08827	0.4648±0.05002	36.74773±2.25741	36.60774±0.553	45.18375±5.91092	38.90592±2.33831	0.75571±0.09288	0.84848±0.05564	0.87189±0.13396	0.90004±0.07031
LEU79	0.42751±0.04764	0.59634±0.00574	0.46641±0.05971	0.40753±0.02398	33.50544±1.7142	35.52759±0.33488	--±14.24498	40.73736±1.1496	0.87621±0.07557	0.81277±0.03838	0.82194±0.06999	1.53275±0.10412
LEU80	0.44963±0.07421	0.55638±0.00826	0.41607±0.07172	0.41953±0.0339	33.56661±2.21289	38.02789±0.57464	37.17082±4.10401	41.85725±1.7313	1.13282±0.14565	0.75954±0.0671	0.69471±0.07691	0.86037±0.0698
SER81	0.61271±0.03703	0.61375±0.00571	0.51615±0.03654	0.48417±0.02844	23.19617±0.72913	29.18001±0.29937	17.7075±1.2349	33.90655±1.2072	0.57802±0.03852	0.66509±0.03965	0.71278±0.05872	0.70194±0.05173
ALA84	0.65229±0.04819	0.64228±0.00573	0.5036±0.0448	0.49812±0.0211	37.16174±1.1208	35.37762±0.31588	45.22519±1.90511	39.47657±0.93076	0.65602±0.04808	0.7783±0.04184	0.7156±0.04457	0.80484±0.04224
ARG85	0.47925±0.03212	0.5705±0.00439	0.44881±0.03895	0.43723±0.01871	34.95265±0.89768	35.59378±0.31559	40.32875±2.383	37.58926±0.92179	0.70502±0.04087	0.6996±0.03377	0.85125±0.07216	0.78196±0.03941
LEU86	0.54115±0.04102	0.58777±0.0034	0.45138±0.05267	0.45592±0.06953	33.19203±0.93867	36.44442±0.24886	42.88524±1.97782	38.97813±1.02094	0.65693±0.03854	0.74924±0.02643	0.87915±0.05226	1.24808±0.06689
ILE87	0.425±0.04898	0.56914±0.00524	0.37901±0.04974	0.42391±0.02144	39.72822±1.08525	36.73831±0.29149	40.97512±2.72744	39.86916±0.80523	0.79843±0.05544	0.77778±0.03649	0.72422±0.07396	0.82387±0.03322
THR88	0.58603±0.06448	0.62126±0.00606	0.43423±0.05792	0.48349±0.02867	39.04971±1.5776	37.97171±0.37924	50.09633±4.21273	42.4428±1.4219	0.98937±0.08223	0.79186±0.0404	0.76256±0.08019	0.80763±0.04102
ILE89	0.62404±0.07203	0.64107±0.00668	0.49333±0.06361	0.45179±0.02735	37.35278±1.56664	35.5522±0.33512	42.54513±3.56351	40.98414±1.09831	0.87058±0.08047	0.80383±0.04297	0.66527±0.08104	0.88903±0.04163
GLU90	0.52348±0.05174	0.64703±0.00634	0.45728±0.06761	0.47308±0.02658	36.0331±1.22633	35.36712±0.32996	49.70903±3.98083	39.19685±1.09311	0.74892±0.06155	0.83173±0.04377	0.78483±0.1212	0.86346±0.0401

ILE91	0.4308±0.10799	0.64275±0.01459	0.52294±0.12423	0.48047±0.04947	36.48221±3.30487	33.39408±0.65552	37.76774±3.29713	36.05534±1.66767	1.26228±0.52368	0.84838±0.11047	0.92975±0.14248	0.84184±0.1445
ASN92	0.42276±0.10454	0.66282±0.01486	0.49984±0.14724	0.46979±0.09078	32.96602±3.21241	36.36104±0.83861	37.07035±9.1837	36.60837±3.88292	0.90639±0.16388	0.90041±0.09771	0.94443±0.24947	0.85125±0.09905
ASP94	0.66139±0.12088	0.66451±0.01524	0.49789±0.10594	0.48723±0.08458	30.33716±2.36281	34.20474±0.8944	26.68639±4.3369	38.97597±4.0877	0.86431±0.10725	0.77002±0.09071	0.76967±0.15065	0.80016±0.11664
CYS95	0.59482±0.12045	0.61072±0.02469	0.49801±0.07531	0.41792±0.19143	30.12051±2.52779	31.75098±1.378	41.00142±27.59197	26.88763±6.56289	1.42457±0.1597	0.69792±0.11115	0.88708±0.07176	0.81131±0.21373
ALA96	0.43993±0.12814	0.79104±0.01477	0.43749±0.14402	0.53983±0.06838	23.8783±2.00021	30.77189±0.65277	21.37821±3.82831	36.75985±3.033	0.73786±0.09019	0.86777±0.0766	0.68482±0.08681	0.78641±0.0831
ALA97	0.47909±0.0472	0.62242±0.00964	0.38131±0.11142	0.48665±0.04658	36.77828±1.4006	35.24723±0.67097	47.45386±3.67469	39.34626±2.15539	0.78203±0.06573	0.80476±0.04279	0.61043±0.08017	0.78472±0.06763
ILE98	0.40236±0.09744	0.65805±0.01285	0.47829±0.11818	0.49654±0.05856	32.49771±2.562	32.99324±0.67482	30.90653±6.87538	35.91542±3.20579	0.71376±0.1529	0.8451±0.08985	0.807±0.19131	0.83128±0.10604
THR99	0.21957±0.14435	0.67063±0.01623	0.40227±0.1742	0.45682±0.08799	33.81284±4.17379	34.93285±0.94582	30.90359±9.75029	36.57537±4.13241	1.16605±0.27749	0.84874±0.07715	0.77265±0.18119	0.86858±0.10535
GLN100	0.44391±0.07288	0.67976±0.0082	0.49852±0.08344	0.50908±0.03595	36.59901±2.2714	35.3866±0.50768	42.39867±5.78098	40.07078±1.77411	0.98904±0.11484	0.84277±0.05757	0.75846±0.10899	0.86166±0.04702
ARG101	0.5494±0.10311	0.64162±0.01112	0.35225±0.07266	0.47087±0.04399	35.61838±2.38369	35.20708±0.71596	39.19007±5.08902	37.60352±2.28249	1.00389±0.17877	0.74153±0.07385	0.86323±0.11972	0.8794±0.07697
MET102	0.42147±0.07804	0.68048±0.01148	0.49915±0.0871	0.52994±0.05982	36.4211±2.64001	35.70328±0.66758	42.24652±6.52758	40.65685±2.62502	0.9072±0.10966	0.80405±0.06069	1.01722±0.14685	0.93309±0.07706
VAL103	0.33688±0.08796	0.65557±0.01205	0.45571±0.14099	0.47±0.08088	34.44023±2.99391	37.28573±0.74576	52.49126±8.60034	40.46036±4.07051	0.86131±0.09499	0.8875±0.0585	0.843±0.12928	0.82855±0.09938
ASP104	0.54841±0.14733	0.66196±0.00935	0.49994±0.11379	0.49981±0.03985	39.86613±3.17221	36.2565±0.54417	42.52989±8.44248	41.63198±1.9074	0.64721±0.11587	0.81538±0.04632	0.79551±0.15574	0.92398±0.05141
PHE105	0.58012±0.1238	0.66027±0.01323	0.44695±0.10554	0.46949±0.08139	36.79305±2.7208	35.53551±0.77619	43.08697±5.2743	41.35459±4.03242	0.89175±0.10296	0.83333±0.06903	0.79478±0.07167	0.91297±0.10421
ALA106	0.64375±0.0785	0.65264±0.00825	0.5094±0.08894	0.49136±0.04513	31.82616±1.88219	34.73226±0.47785	17.87416±5.89318	36.92017±2.0179	0.6759±0.06355	0.82667±0.04037	0.87674±0.10954	0.90591±0.06715
GLY107	0.46116±0.06447	0.60637±0.01177	0.3851±0.09025	0.46727±0.04321	33.13399±1.32535	32.51482±0.46457	43.29178±1.90591	36.34915±1.0633	0.94352±0.10351	0.91406±0.07409	0.94021±0.06139	0.82409±0.05899
MET108	0.32881±0.09152	0.58516±0.01371	0.4398±0.11924	0.46394±0.06616	30.72727±2.45965	33.92062±0.72263	45.84993±5.47129	38.17335±2.30826	0.74965±0.12064	0.90294±0.09246	1.02383±0.11958	0.92897±0.09489
LYS109	0.42265±0.06981	0.63263±0.01055	0.44679±0.10933	0.455±0.0502	36.52213±2.6276	34.36166±0.64164	40.25589±5.05538	43.27169±2.3592	0.74053±0.07318	0.73333±0.06576	1.13851±0.12735	0.7256±0.06596
ASP110	0.5579±0.06675	0.70343±0.01068	0.49809±0.07629	0.51544±0.06054	31.86149±1.74569	34.66334±0.56778	36.16787±2.94529	36.10534±2.5568	0.65405±0.04831	0.78261±0.05521	0.91915±0.07626	0.78998±0.08477
LYS111	0.48676±0.09733	0.54572±0.00967	0.39728±0.11777	0.38422±0.04647	32.73634±2.54671	35.3773±0.69026	37.58961±4.9115	40.23358±2.28201	1.12317±0.18862	0.7594±0.06609	0.91899±0.09082	0.85322±0.08097

VAL112	0.46099±0.04828	0.60341±0.00587	0.42987±0.13394	0.46443±0.0249	35.07892±1.36789	35.1626±0.44101	64.61343±5.50271	38.98066±1.3326	0.97383±0.11692	0.78924±0.03999	0.90911±0.05981	0.82213±0.1175
THR113	0.56199±0.05862	0.56924±0.00548	0.43706±0.05369	0.42295±0.02157	32.70358±1.24291	34.58545±0.31739	44.95431±2.94792	37.35716±0.88066	0.81932±0.06296	0.81448±0.04085	0.73706±0.08017	0.9069±0.04224
LEU114	0.49306±0.03329	0.56465±0.00515	0.42228±0.03532	0.43159±0.01828	37.67934±0.65986	36.59854±0.26219	48.45219±1.99134	40.66924±0.6469	0.69454±0.04487	0.74419±0.04058	0.79715±0.07246	0.81842±0.03789
VAL115	0.67497±0.05355	0.62972±0.00615	0.52624±0.07323	0.47709±0.02593	34.54067±0.92189	35.02858±0.29616	36.55903±2.54183	38.95472±0.89501	0.75423±0.05476	0.80288±0.04316	0.83652±0.08009	0.95779±0.04776
VAL116	0.51476±0.03349	0.60826±0.0053	0.45568±0.03217	0.45721±0.01658	35.17634±0.72828	34.5841±0.28459	43.01906±1.82332	37.45275±0.63525	0.75086±0.04902	0.76856±0.03855	1.14171±0.1114	0.80483±0.03075
GLY117	0.59863±0.05475	0.61374±0.00536	0.4402±0.04774	0.46763±0.02649	33.60515±1.0996	33.0601±0.33213	38.27561±3.2186	36.26419±1.2228	0.86577±0.0581	0.83058±0.0376	0.83885±0.09764	0.88672±0.04628
ALA118	0.49958±0.03328	0.63015±0.00605	0.46614±0.04726	0.48993±0.02872	34.3183±0.83056	33.22933±0.36046	36.37656±2.8709	35.84472±1.2854	0.65636±0.04472	0.86842±0.0488	0.7846±0.09428	0.82879±0.05179
SER119	0.5±0.2926	0.51398±0.0331	0.26381±0.37697	0.16381±0.29528	29.91509±6.10507	33.61815±2.02241	15.95268±8.06926	29.90599±11.63909	1.13286±0.45207	1.06888±0.24338	0.8881±0.29483	0.62065±0.23475
GLN120	0.17243±0.16848	0.6238±0.02305	0.36404±0.22902	0.46274±0.16862	34.8954±5.99449	36.39971±1.5311	58.52291±17.27506	44.28352±8.53878	1.56959±0.43225	0.84457±0.13435	0.77946±0.28425	0.89057±0.18785
ASP121	0.44443±0.06072	0.61424±0.00691	0.41389±0.15204	0.44453±0.07013	35.45796±2.41909	36.7809±0.47797	35.27343±6.2444	39.25098±3.30319	1.02884±0.16599	0.76923±0.03996	1.78647±0.5123	0.79315±0.1045
ILE122	1.3061±0.17939	0.64293±0.01742	0.49909±0.14869	0.4446±0.10573	31.56413±4.4893	32.16819±0.93057	2.46058±0.41208	36.49574±4.531	0.91684±0.1853	0.794±0.08938	0.66096±0.11968	0.843±0.10528
ILE123	0.35812±0.07959	0.62805±0.01142	0.45846±0.10852	0.45839±0.06616	39.0168±2.91951	36.23632±0.71849	52.79262±7.68001	40.02762±3.08511	0.73963±0.08206	0.83333±0.06903	0.63604±0.11155	0.87204±0.08379
GLN125	0.50627±0.09419	0.6006±0.00914	0.44118±0.08774	0.45276±0.04602	31.32041±2.11249	31.80285±0.52021	38.83997±5.27362	35.77607±2.06159	0.65104±0.09226	0.78767±0.06103	0.80044±0.13452	0.85102±0.06639
LEU126	0.37753±0.07079	0.64139±0.01012	0.44477±0.0781	0.49791±0.04044	35.59851±2.1774	35.41535±0.60571	43.70321±3.8192	40.71457±1.97351	0.90899±0.09209	0.82443±0.06925	0.79501±0.06476	0.91504±0.06416
LYS127	0.49973±0.03505	0.64115±0.01096	0.44674±0.07855	0.19976±0.03124	35.409±0.88804	35.61481±0.57703	39.10152±11.30002	37.76501±1.3861	0.77154±0.03548	0.86093±0.06117	0.80258±0.03534	0.93306±0.05135
LYS128	0.47642±0.04698	0.6608±0.00697	0.54031±0.0586	0.52979±0.03063	28.27024±1.1905	28.70453±0.33636	37.25394±2.17591	32.14754±1.1462	0.48496±0.05814	0.4125±0.03944	0.41076±0.04091	0.4986±0.04749
LYS129	0.38885±0.06848	0.62955±0.00784	0.40851±0.08343	0.31448±0.05031	34.14154±2.2493	35.12391±0.50029	49.13585±6.00152	33.91425±1.9208	0.86025±0.08258	0.75771±0.03869	0.7483±0.06998	0.71064±0.06375
TYR130	0.49945±0.14139	0.57603±0.01482	0.42983±0.14855	0.45208±0.06985	32.5995±3.62811	34.09214±0.86083	41.77368±6.72869	33.90782±2.90491	1.22262±0.27558	0.6981±0.0813	0.82099±0.20253	0.72888±0.09705
ASP131	0.49953±0.04989	0.64845±0.00885	0.44719±0.06621	0.50716±0.03991	30.21652±1.6944	30.59204±0.46591	36.21496±2.59709	32.65972±1.5531	0.80862±0.07122	0.6487±0.05418	0.71231±0.05038	0.69378±0.05534
VAL132	0.49961±0.02999	0.63307±0.00514	0.46076±0.02929	0.49063±0.01769	31.33303±0.74249	31.24919±0.28631	38.07042±1.4148	34.24144±0.7412	0.66903±0.05588	0.64103±0.03553	0.7696±0.04223	0.67901±0.03362

ASP133	0.60446±0.04068	0.65838±0.00583	0.46334±0.03518	0.49971±0.02147	31.02159±0.80976	30.94039±0.27208	36.31429±1.28321	34.16056±0.76564	0.65822±0.0454	0.70192±0.04112	0.71044±0.03985	0.67389±0.04603
THR134	0.48821±0.04693	0.64087±0.00807	0.47303±0.04807	0.48669±0.0311	28.09611±0.80822	26.86923±0.2343	31.12607±0.88041	29.4441±0.65261	0.74475±0.09052	0.68862±0.05089	0.68689±0.05381	0.71464±0.05946
LEU135	0.44447±0.04912	0.60109±0.00505	0.45676±0.05793	0.46816±0.02498	35.31493±1.33169	35.63258±0.34817	40.17666±3.25059	37.10169±1.2395	0.81874±0.05165	0.78309±0.03269	0.87944±0.07535	0.82329±0.03943
ASP136	0.26938±0.1147	0.6421±0.01362	0.40804±0.1806	0.42603±0.07785	38.69858±3.99929	33.62846±0.78242	31.5539±8.84521	38.80375±3.68571	0.69144±0.11155	0.87193±0.08147	0.89005±0.17974	0.92798±0.09869
MET137	0.33358±0.0899	0.62122±0.00991	0.50009±0.09999	0.46839±0.04762	37.4763±3.16491	34.4452±0.62033	42.53952±7.13502	40.61329±2.3415	1.086±0.18604	0.78621±0.06141	1.27978±0.21213	0.80085±0.06192
VAL138	0.39917±0.0611	0.58852±0.0061	0.43424±0.06603	0.39954±0.03025	39.61976±1.52083	36.52325±0.36482	43.04441±4.08032	39.89422±1.28121	0.74135±0.05677	0.86869±0.04683	0.9169±0.13029	0.91555±0.04282
PHE139	0.47762±0.05844	0.64099±0.00711	0.49933±0.07005	0.45217±0.03312	36.64404±1.38424	35.55219±0.36155	47.7609±4.46963	39.32449±1.20444	1.02724±0.07996	0.735±0.04344	0.98202±0.13499	0.85437±0.04213
LEU140	0.48685±0.05606	0.62772±0.00676	0.51741±0.06128	0.42465±0.03163	37.57999±1.33834	35.44536±0.33392	44.1771±3.26274	38.41058±1.34751	0.891±0.07082	0.80645±0.04144	0.62039±0.0738	0.84513±0.04181
ASP141	0.37176±0.08039	0.62115±0.01188	0.51453±0.10618	0.45568±0.05427	32.93342±2.4897	33.09141±0.70508	38.51785±7.30109	36.02526±2.5152	1.15796±0.1919	0.77345±0.07831	0.83335±0.14989	0.74248±0.07742
HIS142	0.53149±0.22125	0.5522±0.02371	0.41766±0.2226	0.40913±0.161	34.12239±5.21871	39.85488±1.7834	42.4248±16.43402	41.27751±8.46953	0.85371±0.21314	0.80824±0.12785	0.83195±0.27774	0.79219±0.15836
TRP143	-	0.6156±0.01761	-	0.46468±0.17237	-	32.1273±0.97178	-	56.39499±11.36697	-	0.86101±0.16674	-	-
LYS144	0.48±0.05967	0.68865±0.03932	0.30014±0.21045	0.4396±0.3298	35.51738±1.9513	31.48953±1.8284	8.91401±5.85202	27.69747±13.00102	1.09221±0.49965	0.87445±0.13735	0.99548±0.2221	0.89364±0.38179
ASP145	0.20267±0.14448	0.6034±0.01638	0.4006±0.26296	0.40532±0.14819	35.4085±5.96422	38.04991±1.1268	46.0853±20.4831	44.42147±7.53578	0.72444±0.16922	0.7717±0.08341	1.62791±0.48671	0.9184±0.14326
ARG146	0.38902±0.10788	0.60901±0.02415	0.49893±0.14526	0.37561±0.14661	28.584±3.73159	36.72178±1.6565	44.71584±13.53103	39.28376±7.40172	0.90697±0.18859	0.86124±0.13934	1.03654±0.25078	0.91812±0.2027
TYR147	0.64332±0.25082	0.65047±0.01846	0.3998±0.20411	0.42673±0.15677	39.37995±4.9773	37.73111±1.2135	40.69707±14.15901	40.18015±7.69832	0.82091±0.15988	0.713±0.08597	0.91307±0.25223	0.7465±0.16026
LEU148	0.32811±0.09646	0.61372±0.01547	0.52975±0.14554	0.44556±0.10179	35.19443±3.1301	37.63096±1.0392	46.54736±9.42258	43.80078±5.53639	0.83664±0.1266	0.81724±0.10391	0.54475±0.21549	0.7485±0.09402
ASP150	0.37629±0.07247	0.61138±0.01143	0.44352±0.11058	0.45423±0.06909	33.98303±2.5454	37.22024±0.72092	38.78008±6.51902	38.70254±3.39719	0.78066±0.07362	0.7362±0.05333	0.74689±0.08921	0.80204±0.07631
THR151	0.99927±0.08675	0.62348±0.0185	0.39646±0.18342	0.46482±0.1062	33.68759±5.77561	37.07797±1.2507	41.65073±15.03006	40.75255±5.14272	0.7152±0.16129	0.82863±0.0986	1.33835±0.33275	0.87593±0.10406
LEU152	0.6018±0.51128	0.63595±0.01518	0.48909±0.14745	0.44114±0.08741	37.13643±3.91449	36.44555±1.083	47.51445±8.65858	41.11636±4.65972	0.79551±0.15475	0.81992±0.09107	0.54831±0.11407	0.87026±0.09414
LEU153	1.2138±0.06133	0.65692±0.00966	1.0669±0.06476	0.49651±0.04632	16.31429±0.5039	33.19622±0.5205	18.52231±0.64989	39.09428±2.206	0.37153±0.04532	0.78916±0.05372	0.37391±0.03734	0.76933±0.05353

LEU154	0.58601±0.10856	0.62499±0.00883	0.40715±0.09575	0.45418±0.04002	36.44609±2.5917	35.60335±0.56908	37.36454±5.3857	40.29538±1.9393	0.85542±0.09269	0.82738±0.05408	0.79955±0.1294	0.95152±0.05742
GLU155	-	0.61872±0.00839	-	0.47629±0.04615	-	36.87014±0.60315	-	43.56075±2.5532	-	0.82143±0.06471	-	1.03214±0.08424
GLU156	-	0.61774±0.00988	-	0.45658±0.06357	-	38.7213±0.64924	-	39.88205±3.10011	-	0.72±0.04929	-	0.8171±0.07535
CYS157	0.27721±0.11924	0.58039±0.01479	0.41928±0.15371	0.39122±0.09971	36.93342±4.47009	34.62388±0.95857	35.86874±6.60423	38.25543±4.37791	1.18389±0.17007	0.83516±0.10022	1.01534±0.16627	0.80135±0.11548
GLY158	0.87128±0.16964	0.69482±0.00822	0.49971±0.07497	0.49989±0.03619	20.93726±1.76843	31.55928±0.35612	28.14145±3.51014	36.2097±1.23524	0.72967±0.06919	0.74747±0.04414	0.60972±0.11908	0.81876±0.0516
LEU159	0.4041±0.08927	0.64434±0.01145	0.4257±0.14635	0.48151±0.05407	32.4719±3.1966	35.11116±0.69314	42.67219±5.28428	39.19924±2.6326	-	0.84407±0.07763	0.64384±0.07696	0.82792±0.07329
LEU160	0.48116±0.05209	0.63209±0.00705	0.49799±0.05931	0.47846±0.03034	34.9949±1.79849	35.86461±0.44881	42.92199±2.84698	38.44419±1.4657	0.62041±0.10109	0.83684±0.04804	0.76296±0.07021	0.79491±0.04426
ARG161	0.38275±0.07129	0.57152±0.00849	0.49828±0.0911	0.41805±0.04275	36.23704±2.44621	36.09434±0.59866	39.36135±3.81049	39.33335±2.2057	0.93651±0.0927	0.77397±0.06063	0.83442±0.07629	0.78037±0.06181
LYS162	0.50719±0.03247	0.64316±0.00763	0.47304±0.03566	0.4528±0.04727	36.14014±0.95479	34.67464±0.42881	40.97397±1.7244	39.67041±2.10301	0.76288±0.03844	0.77907±0.05159	0.79391±0.03605	0.80333±0.07145
GLY163	0.39999±0.07527	0.63632±0.0094	0.43428±0.0831	0.44±0.05198	33.47611±2.0232	34.65904±0.54768	37.60308±3.73781	37.5454±2.50311	0.70589±0.06459	0.90714±0.06751	0.76684±0.06207	0.83822±0.06093
THR164	0.43668±0.07702	0.58241±0.00845	0.44569±0.09452	0.44212±0.05094	37.81832±2.5706	38.32967±0.58128	51.13051±5.32029	40.97825±2.616	0.71422±0.06752	0.74419±0.05073	1.0781±0.08848	0.85557±0.06687
VAL165	0.56866±0.0566	0.6208±0.00614	0.46037±0.06524	0.48742±0.03092	35.61415±1.22263	36.34857±0.33408	50.72445±2.86384	41.62383±1.37022	0.70613±0.06031	0.83575±0.04407	0.8665±0.07978	0.82904±0.04449
LEU166	0.40455±0.05898	0.59116±0.00656	0.45016±0.08276	0.44194±0.03433	40.41885±1.66854	37.76157±0.37506	48.85803±6.15273	43.79629±1.44823	0.87214±0.076	0.76699±0.04282	0.64281±0.08005	0.87234±0.04744
LEU167	0.47274±0.05241	0.59886±0.00553	0.40881±0.05754	0.43659±0.02637	36.13062±1.3106	34.84774±0.31567	42.46317±3.12812	37.36782±1.10491	0.76341±0.05067	0.75±0.03646	0.813±0.08498	0.9085±0.03968
ALA168	0.38363±0.06897	0.61364±0.00849	0.49875±0.09669	0.47444±0.04356	38.20217±1.74628	37.2952±0.41555	44.02213±4.88751	43.71037±1.63187	0.74034±0.09145	0.8303±0.05514	1.17439±0.21252	0.81592±0.0531
ASP169	0.44414±0.06915	0.6577±0.00784	0.46152±0.08055	0.4899±0.03055	34.2558±1.95411	34.53093±0.4554	41.59327±5.15641	38.58726±1.5054	0.89897±0.09098	0.84483±0.05266	0.73743±0.12648	0.86062±0.04828
ASN170	0.42376±0.071	0.64552±0.01018	0.47365±0.10444	0.48508±0.04504	32.9301±2.28419	33.84287±0.60189	47.61677±7.74024	34.57567±2.0023	0.81181±0.09949	0.72222±0.05996	0.76877±0.12211	0.87575±0.06441
VAL171	0.39493±0.09918	0.67857±0.01341	0.51116±0.12913	0.462±0.06248	35.85929±2.4676	33.26418±0.62233	33.37744±4.02076	37.10878±2.11012	0.61981±0.104	0.77876±0.07852	0.97203±0.11511	0.87696±0.07718
ILE172	0.54785±0.08328	0.66043±0.02324	0.30454±0.26049	0.50053±0.1322	24.8878±4.3363	38.45018±1.4828	3.32432±0.50833	37.40135±6.40829	0.49372±0.22298	0.7234±0.12255	0.88064±0.27873	0.82188±0.13332
CYS173	0.14857±0.18064	0.61119±0.02161	0.53604±0.32661	0.50527±0.12197	36.80804±5.78932	34.39385±1.1913	31.7912±15.4	36.4778±5.37023	1.35258±0.32992	0.80686±0.11429	1.33637±0.53145	0.89526±0.15234

GLY175	0.59282±0.09185	0.64138±0.01225	0.497±0.1596	0.46876±0.05826	33.06232±1.66111	33.64458±0.57651	40.86236±4.0044	38.00892±1.9421	0.64193±0.12416	0.75146±0.08501	0.97209±0.24353	0.8526±0.10358
ALA176	0.4937±0.05571	0.59837±0.00811	0.4738±0.07793	0.44959±0.04184	28.15386±1.2851	30.15452±0.43198	34.19496±3.774	33.46047±1.7229	0.96359±0.11864	0.7871±0.05747	0.84112±0.09269	0.89123±0.08464
ASP178	0.55755±0.12549	0.6078±0.00501	0.46353±0.19218	0.43914±0.03227	35.9007±3.77341	35.51212±0.30732	37.79379±9.81003	37.79499±1.5611	1.10443±0.20865	0.78388±0.03258	0.34772±0.17508	0.8824±0.04496
PHE179	0.43034±0.21485	0.5866±0.0203	0.50058±0.23623	0.45394±0.10294	37.54774±5.184	38.61498±1.339	36.4605±12.47204	42.54812±4.9727	0.82433±0.24039	0.7619±0.11641	0.8612±0.27119	0.82895±0.12588
LEU180	0.38171±0.07332	0.61568±0.01259	0.2704±0.39225	0.47989±0.06896	32.35804±1.39231	38.75043±0.85172	28.40954±1.6674	47.40554±3.9753	0.64886±0.05291	0.80986±0.06343	0.70033±0.03989	0.87829±0.09125
ALA181	0.53497±0.09041	0.60209±0.01317	0.45136±0.10852	0.43857±0.06741	36.23099±2.63299	38.24567±0.90353	47.16024±6.74288	39.88501±3.50292	0.98963±0.10899	0.82621±0.08816	0.70831±0.10863	0.87628±0.09624
HIS182	0.51671±0.08479	0.57298±0.01097	0.4055±0.09831	0.39729±0.05661	33.34037±2.4237	33.56841±0.75034	27.95141±7.20042	40.57435±3.00139	0.88893±0.13037	0.6942±0.06175	0.7219±0.25742	0.86713±0.08612
VAL183	0.44566±0.11213	0.56362±0.01239	0.50279±0.17355	0.44303±0.06136	37.85501±3.72791	40.6297±0.90435	43.63133±12.36202	45.21783±2.96582	0.66893±0.12833	0.72213±0.07077	0.89896±0.17637	0.82609±0.07782
ARG184	0.19314±0.34051	0.61311±0.0111	0.10054±0.48275	0.4562±0.06969	36.44974±3.45931	36.71609±0.79107	36.20004±5.18832	39.61037±3.3095	0.78691±0.05631	0.76974±0.05812	0.20128±0.25564	0.83773±0.09118
GLY185	0.62892±0.10305	0.67306±0.01497	0.4723±0.09567	0.52112±0.06263	29.18149±1.58888	32.64934±0.56106	35.59055±3.40186	36.60699±1.67663	1.08143±0.1846	0.72321±0.07713	0.66426±0.13265	1.01289±0.12249
SER186	0.34691±0.09433	0.59278±0.01304	0.4984±0.1185	0.47924±0.06826	31.54268±2.7157	32.40108±0.75019	35.88047±4.1562	34.80328±2.92451	0.82678±0.15841	0.77647±0.08689	0.70778±0.10818	0.8094±0.12036
CYS188	0.34099±0.08773	0.69316±0.01958	0.49791±0.08625	0.55919±0.10685	32.59806±1.6997	34.54308±1.015	13.18341±9.2243	35.74863±4.5367	1.01404±0.09512	0.85487±0.0815	0.84536±0.08002	0.87181±0.14055
PHE189	0.35585±0.08338	0.6324±0.01019	0.48202±0.11736	0.45631±0.05241	36.34721±2.75449	35.44172±0.65126	37.34324±4.74042	38.51362±2.67439	0.93819±0.1147	0.88462±0.07189	0.76797±0.10157	0.74612±0.07625
GLU190	0.45837±0.06054	0.60537±0.00767	0.48923±0.08595	0.37255±0.04483	31.74213±1.6959	32.92549±0.47001	33.68613±3.56089	35.82989±2.0028	0.68862±0.05851	0.82±0.06035	0.76007±0.06314	0.84223±0.06133
CYS191	0.43634±0.06334	0.62067±0.01158	0.49845±0.08677	0.43089±0.06473	37.33917±1.80054	36.10242±0.59478	42.49899±3.37676	40.34228±2.33525	0.74984±0.08315	0.77109±0.06906	0.71624±0.0643	0.81806±0.09869
THR192	0.40339±0.05938	0.58554±0.0069	0.43203±0.06722	0.42166±0.03487	33.04127±1.8779	32.56259±0.41993	33.83504±2.9797	34.28915±1.5105	0.87764±0.0738	0.78125±0.04627	0.76317±0.05848	0.82381±0.05183
HIS193	0.59782±0.04719	0.60324±0.00528	0.49781±0.0543	0.48766±0.02484	33.92636±0.98686	34.89992±0.29478	38.88568±2.71411	35.22038±0.92453	0.72152±0.04593	0.83105±0.04156	0.86701±0.07461	0.83137±0.04728
TYR194	0.43039±0.07355	0.6334±0.00876	0.57044±0.09661	0.49643±0.04209	32.26027±2.02981	33.15845±0.44312	36.96218±5.65792	38.17103±1.65621	0.93064±0.10157	0.80667±0.05996	0.6587±0.13327	0.90139±0.06402
GLN195	0.49201±0.03457	0.60844±0.00518	0.44369±0.05359	0.47892±0.0171	32.44264±0.81513	32.44877±0.26654	28.117±2.62441	36.48877±0.70308	1.00508±0.15303	0.74439±0.03913	0.88875±0.07785	0.83487±0.03814
SER196	0.57129±0.07269	0.66822±0.00856	0.47386±0.09596	0.51877±0.04287	32.52395±1.7918	32.41049±0.43874	33.82522±4.77901	37.62866±2.07701	0.28859±0.10672	0.79375±0.05586	0.64816±0.11818	0.85413±0.07447

PHE197	0.62315±0.11073	0.63852±0.00905	0.45751±0.12733	0.49717±0.05706	35.30508±2.9266	35.25791±0.54415	39.08632±5.34043	36.50838±2.6011	0.93751±0.09277	0.7947±0.05921	0.8657±0.10011	0.7508±0.07669
LEU198	0.44414±0.07298	0.65344±0.00966	0.49773±0.12465	0.48545±0.06769	32.71912±2.12941	35.05434±0.5159	34.90131±6.78802	37.12661±3.06341	0.90754±0.12032	0.88194±0.06482	1.24324±0.29951	0.83835±0.09403
GLU199	0.40629±0.13133	0.63029±0.01279	0.43101±0.12782	0.47095±0.06297	37.93±2.96962	32.5077±0.7742	58.19648±9.58656	40.7544±3.079	1.03055±0.11625	0.8±0.08703	0.62368±0.16627	0.90383±0.09801
TYR200	0.56312±0.08436	0.65275±0.00926	0.44651±0.10794	0.49879±0.04632	29.54063±1.6116	33.59564±0.53546	37.58675±4.85202	33.39211±1.8931	0.6372±0.0708	0.75524±0.06134	0.79388±0.12913	0.80566±0.07401
ARG201	0.4763±0.06335	0.61601±0.01253	0.42939±0.12211	0.43193±0.06232	35.18159±2.02089	38.95097±0.82242	35.15812±6.05109	42.63971±3.24741	0.7164±0.07329	0.80252±0.07542	0.71171±0.14433	0.78866±0.09314
GLU202	0.43998±0.09914	0.63392±0.02372	0.49838±0.1964	0.4005±0.21184	33.71754±3.20279	34.05191±1.4424	40.78732±10.33402	28.23801±7.92961	0.74295±0.12484	0.84789±0.12926	0.67909±0.19586	0.53465±0.19233
VAL203	0.47006±0.07063	0.60841±0.01112	0.44746±0.10634	0.46453±0.04838	24.37782±1.4972	25.27955±0.47148	28.83957±4.05479	28.69011±1.7033	-0.12768±-0.15081	0.37913±0.09889	0.54083±0.17969	0.44577±0.12918
VAL204	0.10053±0.24634	0.64267±0.02894	0.36077±0.18868	0.45912±0.25234	38.0444±3.44021	34.99833±1.46571	48.62129±5.33066	35.37877±9.11783	0.87501±0.11114	0.91892±0.14274	0.62075±0.11344	0.86331±0.21867
ASP205	0.49245±0.06582	0.6654±0.00808	0.49823±0.08179	0.48382±0.03367	32.81077±1.738	33.53508±0.44139	42.04894±4.8125	36.82819±1.43531	0.88613±0.09373	0.82456±0.05306	0.79508±0.12606	0.9335±0.06613
GLY206	0.32813±0.09444	0.64446±0.01155	0.33768±0.1457	0.46834±0.06081	29.95949±2.54385	30.73335±0.53272	39.49161±8.10536	33.73212±2.03936	0.39001±0.12934	0.76087±0.06374	0.65747±0.16508	0.89035±0.08996
LEU207	0.47362±0.05441	0.65501±0.00688	0.49889±0.0716	0.4822±0.03223	33.20461±1.5796	33.48809±0.38313	33.03877±4.4733	34.3339±1.3505	1.10925±0.0896	0.82297±0.04338	0.92543±0.11759	0.92109±0.05056
GLU208	0.49983±0.03706	0.64064±0.00629	0.52056±0.05656	0.4501±0.02755	30.61868±1.0651	34.70397±0.3687	37.04953±2.58482	38.9319±1.3139	1.07078±0.06802	0.80556±0.04161	0.82137±0.07373	0.83952±0.03989
LYS209	0.58982±0.0863	0.63297±0.00726	0.45545±0.07585	0.47091±0.02941	37.93064±1.61563	36.29848±0.33725	50.45624±4.25158	41.8445±1.07715	0.87703±0.09352	0.83333±0.04899	0.64842±0.10943	0.87683±0.04434
ALA210	0.47334±0.07754	0.56093±0.00671	0.39357±0.11003	0.4159±0.04009	36.55291±1.31035	37.67929±0.3286	44.38826±3.58695	41.8736±1.37082	1.25139±0.1595	0.83673±0.04657	0.8502±0.10281	0.88408±0.05485
ILE211	0.39713±0.06297	0.59621±0.00664	0.42615±0.06679	0.43895±0.02737	36.17782±1.66781	34.1111±0.37318	43.84021±3.6424	35.37085±1.10081	0.79079±0.06335	0.73232±0.04382	0.94962±0.10849	0.84184±0.04108
TYR212	0.64677±0.07517	0.59975±0.00702	0.51039±0.07081	0.45998±0.03443	37.46173±1.65548	38.34696±0.39952	43.84229±2.47599	42.01674±1.34674	0.7891±0.06672	0.80829±0.04664	0.92992±0.06519	0.86922±0.04874
LYS213	0.42616±0.07092	0.63388±0.00803	0.43357±0.08521	0.45501±0.03984	32.93343±1.88572	35.2958±0.43427	38.46865±3.46744	39.2644±1.60831	0.63216±0.06277	0.75824±0.04827	0.88356±0.08207	0.82208±0.06207
GLY216	1.0078±0.01872	1.0726±0.00793	0.91654±0.01395	0.85968±0.04867	12.81761±0.11456	12.50283±0.08415	15.01708±0.12389	14.15039±0.44723	0.17667±0.01618	0.19136±0.0324	0.2911±0.01361	0.35037±0.04646
SER217	1.2406±0.01838	1.1583±0.01545	1.166±0.0159	0.51754±0.19998	6.05351±0.06893	6.44531±0.0979	7.22892±0.06922	5.78379±1.27681	0.09862±0.01375	0.24392±0.04868	0.29253±0.01456	0.65729±0.16427

SI Table 2. NMR relaxation experimental data for two complexes: **SAM:** COMT:DNC:Mg^{2+}:SAM; **Sin:** COMT:DNC:Mg^{2+}:Sinefungin.

Residue	S^2	δS^2	S^2_f	δS^2_f	S^2_s	δS^2_f	τ_e (ps)	$\delta \tau_e$ (ps)	τ_f (ps)	$\delta \tau_f$ (ps)	τ_s (ps)	$\delta \tau_s$ (ps)	$^{800MHz}R_{ex}$ (s^{-1})	$\delta^{800MHz}R_{ex}$ (s^{-1})
GLN1	-	-	-	-	-	-	-	-	-	-	-	-	-	-
GLY2	0.973373	0.017121	-	-	-	-	-	-	-	-	-	-	-	-
ASP3	-	-	-	-	-	-	-	-	-	-	-	-	-	-
THR4	0.873887	0.029734	0.91833	0.027456	0.951604	0.015345	-	-	-	-	1079.144	1379.2	-	-
LYS5	-	-	-	-	-	-	-	-	-	-	-	-	-	-
GLU6	0.816253	0.01536	0.903455	0.014405	0.90348	0.008835	-	-	-	-	1076.147	182.9605	-	-
GLN7	-	-	-	-	-	-	-	-	-	-	-	-	-	-
ARG8	0.978852	0.021458	-	-	-	-	3364.309	7782.861	-	-	-	-	-	-
ILE9	0.878927	0.028361	0.943519	0.020422	0.931542	0.037216	-	-	-	-	6403.99	7458.168	-	-
LEU10	0.979453	0.009985	-	-	-	-	1397.463	4335.143	-	-	-	-	-	-
ASN11	0.97628	0.009165	-	-	-	-	1042.497	2807.566	-	-	-	-	2.515985	1.163508
HIS12	0.965153	0.01746	-	-	-	-	2408.064	4426.491	-	-	-	-	-	-
VAL13	0.98137	0.016704	-	-	-	-	3096.799	6632.731	-	-	-	-	-	-
LEU14	0.979856	0.012823	-	-	-	-	1832.463	5248.411	-	-	-	-	-	-

GLN15	0.965148	0.013578	-	-	-	-	979.2251	3246.978	-	-	-	-	-	-
HIS16	0.855711	0.028163	0.915234	0.024125	0.934963	0.01583	-	-	-	-	1289.249	2381.122	-	-
ALA17	-	-	-	-	-	-	-	-	-	-	-	-	-	-
GLU18	0.876817	0.012615	0.933003	0.010933	0.939779	0.008093	-	-	-	-	1753.591	1343.839	-	-
PRO19	-	-	-	-	-	-	-	-	-	-	-	-	-	-
GLY20	0.92855	0.013847	-	-	-	-	160.6814	52.42659	-	-	-	-	2.202797	1.263196
ASN21	-	-	-	-	-	-	-	-	-	-	-	-	2.078938	0.916397
ALA22	0.981344	0.016241	-	-	-	-	4144.545	6065.784	-	-	-	-	2.256056	1.083873
GLN23	-	-	-	-	-	-	-	-	-	-	-	-	-	-
SER24	-	-	-	-	-	-	-	-	-	-	-	-	-	-
VAL25	-	-	-	-	-	-	-	-	-	-	-	-	3.573142	1.415282
LEU26	-	-	-	-	-	-	-	-	-	-	-	-	-	-
GLU27	0.977074	0.010157	-	-	-	-	929.4485	3444.01	-	-	-	-	1.883768	1.124386
ALA28	0.981037	0.009004	-	-	-	-	1057.305	3183.208	-	-	-	-	-	-
ILE29	-	-	-	-	-	-	-	-	-	-	-	-	2.882494	1.001055
ASP30	-	-	-	-	-	-	-	-	-	-	-	-	-	-

THR31	0.975088	0.014503	-	-	-	-	752.9569	3757.957	-	-	-	-	-	-
TYR32	-	-	-	-	-	-	-	-	-	-	-	-	6.980367	1.417498
CYS33	-	-	-	-	-	-	-	-	-	-	-	-	2.838473	0.933181
GLU34	0.930896	0.015104	-	-	-	-	24.10623	16.48851	-	-	-	-	7.779377	1.342029
GLN35	-	-	-	-	-	-	-	-	-	-	-	-	-	-
LYS36	0.984261	0.007572	-	-	-	-	421.1325	515.8867	-	-	-	-	2.565633	1.124023
GLU37	0.951661	0.01762	-	-	-	-	-	-	-	-	-	-	-	-
TRP38	0.982919	0.008324	-	-	-	-	1166.901	3801.582	-	-	-	-	2.260429	0.967475
ALA39	-	-	-	-	-	-	-	-	-	-	-	-	-	-
MET40	0.902265	0.029744	0.934431	0.031969	0.965577	0.019357	-	-	-	-	691.6248	1883.461	-	-
ASN41	0.979414	0.014119	-	-	-	-	2357.476	5332.982	-	-	-	-	-	-
VAL42	0.970198	0.016538	-	-	-	-	-	-	-	-	-	-	-	-
GLY43	-	-	-	-	-	-	-	-	-	-	-	-	-	-
ASP44	-	-	-	-	-	-	-	-	-	-	-	-	-	-
LYS45	0.835811	0.016912	0.898011	0.015029	0.930736	0.008003	-	-	-	-	1012.117	211.1473	-	-
LYS46	0.9733	0.003547	-	-	-	-	988.5239	705.0012	-	-	-	-	-	-

GLY47	-	-	-	-	-	-	-	-	-	-	-	-	-	-
LYS48	-	-	-	-	-	-	-	-	-	-	-	-	-	-
ILE49	-	-	-	-	-	-	-	-	-	-	-	-	-	-
VAL50	-	-	-	-	-	-	-	-	-	-	-	-	-	-
ASP51	-	-	-	-	-	-	-	-	-	-	-	-	3.520186	1.880969
ALA52	-	-	-	-	-	-	-	-	-	-	-	-	3.002099	1.070333
VAL53	-	-	-	-	-	-	-	-	-	-	-	-	-	-
ILE54	0.949154	0.023013	-	-	-	-	1262.433	4045.466	-	-	-	-	4.238256	2.396858
GLN55	-	-	-	-	-	-	-	-	-	-	-	-	-	-
GLU56	0.965325	0.020969	-	-	-	-	723.7901	3238.044	-	-	-	-	-	-
HIS57	0.897871	0.03027	0.953584	0.01919	0.941575	0.037255	-	-	-	-	2111.682	6666.662	-	-
GLN58	-	-	-	-	-	-	-	-	-	-	-	-	-	-
PRO59	-	-	-	-	-	-	-	-	-	-	-	-	-	-
SER60	0.841879	0.021993	0.87961	0.019116	0.957105	0.010909	-	-	-	-	1373.568	1393.869	-	-
VAL61	0.898191	0.020327	0.927703	0.017437	0.968188	0.009812	-	-	-	-	1421.137	2297.595	-	-
LEU62	0.956306	0.011774	0.986867	0.007559	0.969032	0.012015	-	-	-	-	1651.212	4287.581	-	-

LEU63	0.982982	0.002605	-	-	-	-	936.2796	518.4029	-	-	-	-	-	-
GLU64	0.981153	0.012492	-	-	-	-	4326.459	6107.336	-	-	-	-	-	-
LEU65	0.941844	0.009987	0.961073	0.007378	0.979992	0.007741	-	-	-	-	2103.439	3867.724	-	-
GLY66	0.909265	0.010384	0.930585	0.009889	0.977089	0.00573	-	-	-	-	1034.205	663.8241	-	-
ALA67	0.904313	0.019323	0.976114	0.017585	0.926607	0.015908	-	-	-	-	24789.98	5690.515	-	-
TYR68	0.939191	0.021033	-	-	-	-	-	-	-	-	-	-	-	-
CYS69	-	-	-	-	-	-	-	-	-	-	-	-	-	-
GLY70	0.844189	0.029303	0.900329	0.026364	0.937645	0.023393	-	-	-	-	1955.625	3561.185	-	-
TYR71	-	-	-	-	-	-	-	-	-	-	-	-	-	-
SER72	-	-	-	-	-	-	-	-	-	-	-	-	-	-
ALA73	-	-	-	-	-	-	-	-	-	-	-	-	3.965899	1.853428
VAL74	-	-	-	-	-	-	-	-	-	-	-	-	3.325037	1.643717
ARG75	0.097745	0.293227	0.342953	0.206373	-0.0001	0.37605	-	-	-	-	6516.507	7354.035	55.32665	15.52251
MET76	-	-	-	-	-	-	-	-	-	-	-	-	-	-
ALA77	-	-	-	-	-	-	-	-	-	-	-	-	2.861954	1.615571
ARG78	-	-	-	-	-	-	-	-	-	-	-	-	4.029252	0.885245

LEU79	0.945913	0.009081	-	-	-	-	-	-	-	-	-	-	5.219939	0.726102
LEU80	-	-	-	-	-	-	-	-	-	-	-	-	-	-
SER81	0.705372	0.00712	0.802249	0.007864	0.879244	0.005462	-	-	-	-	1483.925	176.7161	-	-
PRO82	-	-	-	-	-	-	-	-	-	-	-	-	-	-
GLY83	-	-	-	-	-	-	-	-	-	-	-	-	-	-
ALA84	0.971798	0.004882	-	-	-	-	1181.902	1608.066	-	-	-	-	-	-
ARG85	0.873262	0.007545	0.919935	0.006996	0.949265	0.003738	-	-	-	-	1144.1	198.4808	-	-
LEU86	0.900328	0.009108	0.938437	0.006407	0.959391	0.010029	-	-	-	-	2141.378	2464.882	-	-
ILE87	0.893899	0.006407	0.930582	0.006152	0.960581	0.003575	-	-	-	-	1693.269	691.6062	-	-
THR88	0.975451	0.007547	-	-	-	-	1263.784	2695.594	-	-	-	-	2.569556	0.690311
ILE89	0.979781	0.008367	-	-	-	-	2724.384	3644.907	-	-	-	-	-	-
GLU90	0.992142	0.006275	-	-	-	-	2102.59	4890.672	-	-	-	-	1.749509	0.54698
ILE91	0.951095	0.018233	0.969414	0.014702	0.981103	0.014525	-	-	-	-	1907.316	6033.53	-	-
ASN92	0.983772	0.014599	-	-	-	-	4647.266	5501.889	-	-	-	-	3.608183	1.397538
PRO93	-	-	-	-	-	-	-	-	-	-	-	-	-	-
ASP94	0.973466	0.012646	-	-	-	-	1204.437	4455.607	-	-	-	-	-	-

CYS95	0.877755	0.039324	0.916946	0.036198	0.957259	0.01925	-	-	-	-	943.7613	1492.312	-	-
ALA96	0.844407	0.045047	1.000006	0.018457	0.844418	0.051773	-	-	-	-	12440.31	6368.158	-	-
ALA97	-	-	-	-	-	-	-	-	-	-	-	-	1.659121	1.013211
ILE98	0.940362	0.022604	0.967794	0.017042	0.971655	0.020982	-	-	-	-	2312.664	7287.646	-	-
THR99	0.978945	0.020491	-	-	-	-	3724.964	6750.587	-	-	-	-	-	-
GLN100	0.980878	0.014312	-	-	-	-	2460.828	5659.535	-	-	-	-	3.15259	0.905367
ARG101	-	-	-	-	-	-	-	-	-	-	-	-	-	-
MET102	0.970556	0.022968	-	-	-	-	2683.189	5620.555	-	-	-	-	2.416418	1.16949
VAL103	-	-	-	-	-	-	-	-	-	-	-	-	5.219052	1.231441
ASP104	0.988611	0.008174	-	-	-	-	2666.965	4434.497	-	-	-	-	4.31648	0.898121
PHE105	0.986894	0.013828	-	-	-	-	4267.052	6148.337	-	-	-	-	3.170053	1.397053
ALA106	0.983325	0.009446	-	-	-	-	2760.397	4822.447	-	-	-	-	-	-
GLY107	0.923427	0.013434	0.935916	0.011752	0.986656	0.008137	-	-	-	-	2526.498	3144.201	-	-
VAL108	0.960969	0.01386	-	-	-	-	-	-	-	-	-	-	-	-
LYS109	0.858651	0.017059	0.928008	0.015705	0.925263	0.011926	-	-	-	-	1445.085	1633.869	-	-
ASP110	0.949075	0.012499	-	-	-	-	1839.641	2460.399	-	-	-	-	-	-

LYS111	0.948227	0.01203	-	-	-	-	-	-	-	-	-	-	-	-
VAL112	0.871314	0.013188	0.920009	0.010115	0.947071	0.013156	-	-	-	-	2034.583	2535.741	-	-
THR113	0.890679	0.008858	0.915081	0.00742	0.973333	0.008922	-	-	-	-	2723.081	3461.513	-	-
LEU114	0.937975	0.006152	0.960501	0.005814	0.976547	0.003643	-	-	-	-	931.8551	488.966	-	-
VAL115	0.989992	0.006281	-	-	-	-	1898.558	4850.906	-	-	-	-	-	-
VAL116	0.97604	0.005708	-	-	-	-	48.61767	22.76491	-	-	-	-	-	-
GLY117	0.968904	0.006155	-	-	-	-	-	-	-	-	-	-	-	-
ALA118	0.983457	0.006787	-	-	-	-	-	-	-	-	-	-	-	-
SER119	0.832375	0.053347	-	-	-	-	-	-	-	-	-	-	7.360688	4.32717
GLN120	-	-	-	-	-	-	-	-	-	-	-	-	-	-
ASP121	0.972904	0.006481	-	-	-	-	1171.731	2601.949	-	-	-	-	-	-
ILE122	-	-	-	-	-	-	-	-	-	-	-	-	-	-
ILE123	-	-	-	-	-	-	-	-	-	-	-	-	3.454507	1.165349
PRO124	-	-	-	-	-	-	-	-	-	-	-	-	-	-
GLN125	0.896448	0.015431	0.918513	0.014015	0.975977	0.007219	-	-	-	-	1471.144	1816.362	-	-
LEU126	0.982465	0.013351	-	-	-	-	2563.636	6205.921	-	-	-	-	-	-

LYS127	-	-	-	-	-	-	-	-	-	-	-	-	-	-
LYS128	0.834069	0.008941	0.92348	0.007826	0.90318	0.005413	-	-	-	-	526.1471	45.15856	-	-
LYS129	0.98243	0.005421	-	-	-	-	383.4106	194.2419	-	-	-	-	-	-
TYR130	0.821848	0.02192	0.883196	0.01909	0.930539	0.013684	-	-	-	-	1252.944	1795.212	-	-
ASP131	0.882186	0.013487	0.934402	0.011576	0.944119	0.006677	-	-	-	-	747.2057	134.4283	-	-
VAL132	0.907591	0.007921	0.947072	0.006756	0.958313	0.003805	-	-	-	-	501.3071	77.20533	-	-
ASP133	0.855367	0.013323	0.900249	0.011701	0.950145	0.017348	-	-	28.52626	14.70179	2067.858	4008.211	-	-
THR134	0.776662	0.006763	0.842318	0.008024	0.922054	0.006541	-	-	-	-	1152.585	235.3416	-	-
LEU135	0.953886	0.009346	0.975195	0.008067	0.978149	0.004664	-	-	-	-	1144.42	1791.599	-	-
ASP136	0.595581	0.131232	0.982105	0.076642	0.750915	0.121169	-	-	-	-	47016.28	6738.933	0.082854	6.628878
MET137	0.978102	0.008015	-	-	-	-	788.9362	3052.702	-	-	-	-	-	-
VAL138	0.929227	0.012503	0.991479	0.009135	0.968035	0.012976	-	-	-3.8E-07	72.48708	39088.8	9666.88	-	-
PHE139	0.974911	0.00515	-	-	-	-	1226.059	1827.014	-	-	-	-	-	-
LEU140	0.960135	0.015182	0.983024	0.008688	0.976716	0.017385	-	-	-	-	2156.059	7433.22	-	-
ASP141	0.964334	0.013223	-	-	-	-	56.14034	189.4593	-	-	-	-	-	-
HIS142	-	-	-	-	-	-	-	-	-	-	-	-	-	-

TRP143	0.962727	0.019499	-	-	-	-	-	-	-	-	-	-	-	-
LYS144	0.721312	0.369663	0.972754	0.243361	0.839826	0.388171	-	-	-	-	30474.93	9345.109	-7.4E-06	19.11051
ASP145	0.970146	0.020775	-	-	-	-	1645.053	5850.988	-	-	-	-	-	-
ARG146	0.892788	0.039208	-	-	-	-	28357.07	9766.946	-	-	-	-	-	-
TYR147	0.972541	0.013719	-	-	-	-	589.5972	1910.607	-	-	-	-	6.874101	2.223448
LEU148	-	-	-	-	-	-	-	-	-	-	-	-	5.325108	1.757099
PRO149	-	-	-	-	-	-	-	-	-	-	-	-	-	-
ASP150	-	-	-	-	-	-	-	-	-	-	-	-	2.779105	1.199794
THR151	-	-	-	-	-	-	-	-	-	-	-	-	4.553153	1.970575
LEU152	-	-	-	-	-	-	-	-	-	-	-	-	2.815539	1.557226
LEU153	0.918957	0.015365	0.962692	0.013716	0.954571	0.010895	-	-	-	-	1454.063	2953.276	-	-
LEU154	-	-	-	-	-	-	-	-	-	-	-	-	1.640787	0.805855
GLU155	0.977905	0.012874	-	-	-	-	-	-	-	-	-	-	6.227786	1.284005
GLU156	0.984995	0.009021	-	-	-	-	336.9476	803.873	-	-	-	-	6.289625	1.153014
CYS157	0.963119	0.017424	-	-	-	-	-	-	-	-	-	-	-	-
GLY158	0.893354	0.013452	0.948535	0.010271	0.941825	0.013198	-	-	-	-	1663.397	2552.969	-	-

LEU159	-	-	-	-	-	-	-	-	-	-	-	-	1.69121	1.039788
LEU160	0.981215	0.008125	-	-	-	-	1406.858	4576.162	-	-	-	-	-	-
ARG161	0.91816	0.015561	0.94818	0.013392	0.968339	0.007181	-	-	-	-	1167.17	1514.974	-	-
LYS162	0.976507	0.006012	-	-	-	-	1076.075	2172.559	-	-	-	-	-	-
GLY163	0.968444	0.017352	-	-	-	-	16764.8	9593.873	-	-	-	-	-	-
THR164	-	-	-	-	-	-	-	-	-	-	-	-	1.621676	0.912286
VAL165	0.978598	0.006097	-	-	-	-	1689.489	2923.812	-	-	-	-	-	-
LEU166	0.930324	0.013239	0.966824	0.01078	0.962248	0.01515	-	-	-	-	1890.758	4454.968	-	-
LEU167	0.964163	0.008172	0.974712	0.007709	0.989177	0.004502	-	-	-	-	938.6129	2412.654	-	-
ALA168	0.982039	0.009173	-	-	-	-	1508.655	4300.053	-	-	-	-	1.513222	0.710623
ASP169	0.983333	0.010066	-	-	-	-	2446.573	5054.262	-	-	-	-	-	-
ASN170	0.982527	0.00659	-	-	-	-	685.5255	1851.921	-	-	-	-	-	-
VAL171	0.97773	0.012643	-	-	-	-	1517.358	5163.124	-	-	-	-	-	-
ILE172	0.95607	0.018736	-	-	-	-	1326.241	3534.64	-	-	-	-	3.922587	2.525894
CYS173	-	-	-	-	-	-	-	-	-	-	-	-	-	-
PRO174	-	-	-	-	-	-	-	-	-	-	-	-	-	-

GLY175	0.941716	0.01744	0.971951	0.014203	0.968892	0.014274	-	-	-	-	1276.225	4824.057	-	-
ALA176	0.863829	0.013073	0.887504	0.010672	0.973325	0.007797	-	-	-	-	1699.537	2259.67	-	-
PRO177	-	-	-	-	-	-	-	-	-	-	-	-	-	-
ASP178	0.894307	0.01035	0.936663	0.008096	0.95478	0.011685	-	-	-	-	2433.877	2789.501	-	-
PHE179	0.973588	0.01627	-	-	-	-	1183.491	5311.863	-	-	-	-	-	-
LEU180	0.981121	0.01675	-	-	-	-	1878.048	6156.318	-	-	-	-	4.010232	1.389075
ALA181	-	-	-	-	-	-	-	-	-	-	-	-	-	-
HIS182	0.836496	0.017951	0.887182	0.016428	0.942869	0.008155	-	-	-	-	1428.031	947.5627	-	-
VAL183	0.980375	0.007664	-	-	-	-	733.9392	1825.999	-	-	-	-	2.475251	1.463541
ARG184	0.984789	0.008262	-	-	-	-	985.8293	3966.604	-	-	-	-	-	-
GLY185	0.858333	0.023884	0.923273	0.016516	0.929663	0.029748	-	-	-	-	2084.62	4653.876	-	-
SER186	0.78718	0.021626	0.850756	0.017636	0.925271	0.019178	-	-	-	-	2091.51	2532.914	-	-
SER187	-	-	-	-	-	-	-	-	-	-	-	-	-	-
CYS188	0.976988	0.021442	-	-	-	-	3265.564	6255.645	-	-	-	-	-	-
PHE189	0.973479	0.010553	-	-	-	-	1414.491	4085.392	-	-	-	-	-	-
GLU190	0.774566	0.085508	0.948349	0.055761	0.872762	0.060674	-	-	7.431143	6.000747	49439.23	8229.902	0.062259	4.388701

CYS191	0.912747	0.024939	0.957588	0.017015	0.953174	0.030334	-	-	-	-	1856.968	6940.372	-	-
THR192	0.889989	0.011216	0.913973	0.009916	0.973758	0.00521	-	-	-	-	1304.717	1219.782	-	-
HIS193	0.93182	0.009632	0.9547	0.007218	0.976035	0.008621	-	-	-	-	1680.607	3570.563	-	-
TYR194	0.964311	0.013073	0.97546	0.010846	0.98857	0.006353	-	-	-	-	1683.823	2762.635	-	-
GLN195	0.86604	0.006539	0.909364	0.006695	0.952358	0.003993	-	-	-	-	1451.104	456.4687	-	-
SER196	0.945765	0.01535	0.973976	0.012101	0.971035	0.013806	-	-	-	-	1594.626	5166.947	-	-
PHE197	-	-	-	-	-	-	-	-	-	-	-	-	-	-
LEU198	0.987635	0.008158	-	-	-	-	4307.072	4630.246	-	-	-	-	1.617684	0.842013
GLU199	0.93122	0.021631	0.952209	0.018811	0.977957	0.009936	-	-	-	-	2156.632	3397.283	-	-
TYR200	0.974553	0.006702	-	-	-	-	731.5957	1134.29	-	-	-	-	-	-
ARG201	0.978943	0.010249	-	-	-	-	1285.138	3686.93	-	-	-	-	3.766219	1.473274
GLU202	0.90377	0.039812	0.947302	0.032343	0.954047	0.025466	-	-	-	-	1517.105	5242.205	-	-
VAL203	0.723143	0.013649	0.822231	0.01433	0.879489	0.010777	-	-	-	-	596.5409	94.01089	-	-
VAL204	-	-	-	-	-	-	-	-	-	-	-	-	-	-
ASP205	0.985221	0.009418	-	-	-	-	2236.613	4984.342	-	-	-	-	-	-
GLY206	0.887734	0.015188	0.920926	0.013824	0.963957	0.00816	-	-	-	-	1643.224	2018.384	-	-

LEU207	0.970378	0.011662	0.984319	0.008928	0.985837	0.009188	-	-	-	-	2918.022	6201.555	-	-
GLU208	0.977679	0.006699	-	-	-	-	1276.369	2973.88	-	-	-	-	-	-
LYS209	0.992165	0.005972	-	-	-	-	2230.374	5092.541	-	-	-	-	2.435422	0.555814
ALA210	0.989	0.006646	-	-	-	-	-	-	-	-	-	-	-	-
ILE211	0.942426	0.010061	0.958291	0.010018	0.983445	0.005468	-	-	-	-	709.4683	395.4268	-	-
TYR212	0.972546	0.005942	-	-	-	-	1743.452	2341.944	-	-	-	-	-	-
LYS213	-	-	-	-	-	-	-	-	-	-	-	-	1.822844	0.710263

SI Table 3. Model-free analysis results for COMT:DNC:Mg^{2+}:Sinefungin complex obtained by Relax software. R_{ex} parameter calculated for a magnetic field of 800 MHz.

	S^2	δS^2	S^2_f	δS^2_f	S^2_s	δS^2_f	τ_e (ps)	$\delta \tau_e$ (ps)	τ_f (ps)	$\delta \tau_f$ (ps)	τ_s (ps)	$\delta \tau_s$ (ps)	${}^{800MHz}R_{ex}$ (s^{-1})	$\delta^{800MHz}R_{ex}$ (s^{-1})
GLN1	-	-	-	-	-	-	-	-	-	-	-	-	-	-
GLY2	-	-	-	-	-	-	-	-	-	-	-	-	-	-
ASP3	-	-	-	-	-	-	-	-	-	-	-	-	-	-
THR4	0.697155	0.060245	-	-	-	-	-	-	-	-	-	-	-	-
LYS5	0.498692	0.218307	-	-	-	-	-	-	-	-	-	-	20.22912	12.40656
GLU6	-	-	-	-	-	-	-	-	-	-	-	-	-	-

GLN7	-	-	-	-	-	-	-	-	-	-	-	-	-	-
ARG8	0.908772	0.060406	-	-	-	-	-	-	-	-	-	-	-	-
ILE9	0.868619	0.058489	-	-	-	-	-	-	-	-	-	-	-	-
LEU10	0.935651	0.03925	-	-	-	-	-	-	-	-	-	-	-	-
ASN11	-	-	-	-	-	-	-	-	-	-	-	-	-	-
HIS12	2.02E-08	0.24789	0.15388	0.215256	-0.00024	0.387781	-	-	-	-	2541.925	1012.654	47.02482	16.26653
VAL13	0.089612	0.005557	-	-	-	-	0.618324	0.108372	-	-	-	-	-	-
LEU14	2.14E-07	0.011623	-	-	-	-	6.96E-07	0.05322	-	-	-	-	24.86636	1.758669
GLN15	0.757762	0.107332	-	-	-	-	-	-	-	-	-	-	10.68912	6.381101
HIS16	0.796928	0.060861	-	-	-	-	-	-	-	-	-	-	-	-
ALA17	0.877236	0.035957	0.926528	0.037747	0.946734	0.022781	-	-	-	-	865.767	416.1683	-	-
GLU18	0.875792	0.037014	-	-	-	-	-	-	-	-	-	-	-	-
PRO19	-	-	-	-	-	-	-	-	-	-	-	-	-	-
GLY20	0.894612	0.046548	0.942462	0.043792	0.949226	0.035224	-	-	-	-	1292.455	2685.187	-	-
ASN21	-	-	-	-	-	-	-	-	-	-	-	-	-	-
ALA22	-	-	-	-	-	-	-	-	-	-	-	-	-	-

GLN23	0.866555	0.051895	-	-	-	-	-	-	-	-	-	-	-	-
SER24	-	-	-	-	-	-	-	-	-	-	-	-	-	-
VAL25	-	-	-	-	-	-	-	-	-	-	-	-	11.63872	6.414729
LEU26	0.723565	0.106372	-	-	-	-	-	-	-	-	-	-	-	-
GLU27	0.828188	0.056694	-	-	-	-	-	-	-	-	-	-	-	-
ALA28	0.920476	0.049715	-	-	-	-	-	-	-	-	-	-	-	-
ILE29	-	-	-	-	-	-	-	-	-	-	-	-	-	-
ASP30	0.794279	0.127982	-	-	-	-	-	-	-	-	-	-	-	-
THR31	0.934371	0.047682	-	-	-	-	54.47456	389.6987	-	-	-	-	-	-
TYR32	-	-	-	-	-	-	-	-	-	-	-	-	-	-
CYS33	0.579714	0.225358	0.630486	0.204529	0.919481	0.209632	-	-	-	-	1129.985	1746.262	21.39992	12.76606
GLU34	0.901747	0.048182	-	-	-	-	-	-	-	-	-	-	-	-
GLN35	0.69657	0.080489	-	-	-	-	7.560551	7.773269	-	-	-	-	-	-
LYS36	0.898138	0.056278	-	-	-	-	15.3495	222.6862	-	-	-	-	-	-
GLU37	0.813336	0.052265	-	-	-	-	21.16039	30.61384	-	-	-	-	-	-
TRP38	-	-	-	-	-	-	-	-	-	-	-	-	-	-

ALA39	0.488758	0.165777	-	-	-	-	-	-	-	-	-	-	-	-
MET40	0.836657	0.08064	-	-	-	-	-	-	-	-	-	-	-	-
ASN41	-	-	-	-	-	-	-	-	-	-	-	-	-	-
VAL42	0.867773	0.088026	-	-	-	-	-	-	-	-	-	-	-	-
GLY43	-	-	-	-	-	-	-	-	-	-	-	-	-	-
ASP44	-	-	-	-	-	-	-	-	-	-	-	-	-	-
LYS45	0.847998	0.05776	-	-	-	-	-	-	-	-	-	-	-	-
LYS46	0.966264	0.018009	-	-	-	-	-	-	-	-	-	-	-	-
GLY47	-	-	-	-	-	-	-	-	-	-	-	-	-	-
LYS48	0.602119	0.166431	-	-	-	-	4.917	48.11054	-	-	-	-	17.25243	10.4899
ILE49	0.675731	0.128624	-	-	-	-	-	-	-	-	-	-	-	-
VAL50	0.886299	0.068282	-	-	-	-	-	-	-	-	-	-	-	-
ASP51	0.807018	0.115281	-	-	-	-	21.10828	206.9964	-	-	-	-	-	-
ALA52	-	-	-	-	-	-	-	-	-	-	-	-	-	-
VAL53	-	-	-	-	-	-	-	-	-	-	-	-	-	-
ILE54	0.556635	0.190196	-	-	-	-	-	-	-	-	-	-	20.69437	12.62896

GLN55	0.480437	0.211972	-	-	-	-	-	-	-	-	-	-	23.98844	14.29475
GLU56	0.750617	0.11818	-	-	-	-	-	-	-	-	-	-	-	-
HIS57	0.850862	0.06366	-	-	-	-	24.37282	153.3148	-	-	-	-	-	-
GLN58	-	-	-	-	-	-	-	-	-	-	-	-	-	-
PRO59	-	-	-	-	-	-	-	-	-	-	-	-	-	-
SER60	0.824315	0.08518	-	-	-	-	-	-	-	-	-	-	-	-
VAL61	0.850176	0.038588	-	-	-	-	20.4651	41.2606	-	-	-	-	-	-
LEU62	0.977591	0.029958	-	-	-	-	553.0202	1493.461	-	-	-	-	4.704208	2.326856
LEU63	0.915827	0.026557	-	-	-	-	-	-	-	-	-	-	-	-
GLU64	-	-	-	-	-	-	-	-	-	-	-	-	-	-
LEU65	0.86786	0.026757	-	-	-	-	-	-	-	-	-	-	-	-
GLY66	0.906853	0.034612	-	-	-	-	-	-	-	-	-	-	-	-
ALA67	0.859321	0.051666	-	-	-	-	-	-	-	-	-	-	-	-
TYR68	0.779709	0.124161	-	-	-	-	-	-	-	-	-	-	-	-
CYS69	-	-	-	-	-	-	-	-	-	-	-	-	-	-
GLY70	-	-	-	-	-	-	-	-	-	-	-	-	-	-

TYR71	-	-	-	-	-	-	-	-	-	-	-	-	-	-
SER72	-	-	-	-	-	-	-	-	-	-	-	-	-	-
ALA73	0.629058	0.108046	-	-	-	-	-	-	-	-	-	-	-	-
VAL74	0.067057	0.016002	-	-	-	-	-	-	-	-	-	-	-	-
ARG75	0.919336	0.059784	-	-	-	-	69.29124	1700.713	-	-	-	-	-	-
MET76	-	-	-	-	-	-	-	-	-	-	-	-	-	-
ALA77	-	-	-	-	-	-	-	-	-	-	-	-	-	-
ARG78	-	-	-	-	-	-	-	-	-	-	-	-	-	-
LEU79	0.763407	0.070251	-	-	-	-	-	-	-	-	-	-	16.16636	5.219306
LEU80	0.867671	0.044635	-	-	-	-	10.91578	46.0338	-	-	-	-	-	-
SER81	0.502697	0.015143	0.636006	0.01584	0.790814	0.014505	-	-	-	-	1499.062	133.5204	-	-
PRO82	-	-	-	-	-	-	-	-	-	-	-	-	-	-
GLY83	-	-	-	-	-	-	-	-	-	-	-	-	-	-
ALA84	0.938102	0.014435	-	-	-	-	933.4982	215.1699	-	-	-	-	3.179723	1.526607
ARG85	0.874816	0.020022	0.903941	0.025913	0.968047	0.016561	-	-	-	-	917.3687	411.1171	-	-
LEU86	0.847348	0.0196	0.896449	0.020635	0.94555	0.013761	-	-	-	-	1188.176	340.4897	-	-

ILE87	0.968617	0.019452	-	-	-	-	45.10577	493.3554	-	-	-	-	-	-
THR88	-	-	-	-	-	-	-	-	-	-	-	-	-	-
ILE89	-	-	-	-	-	-	-	-	-	-	-	-	-	-
GLU90	-	-	-	-	-	-	-	-	-	-	-	-	-	-
ILE91	0.909622	0.049476	-	-	-	-	-	-	-	-	-	-	-	-
ASN92	0.88429	0.070342	-	-	-	-	-	-	-	-	-	-	-	-
PRO93	-	-	-	-	-	-	-	-	-	-	-	-	-	-
ASP94	0.79674	0.048845	-	-	-	-	-	-	-	-	-	-	-	-
CYS95	0.864284	0.057809	-	-	-	-	-	-	-	-	-	-	-	-
ALA96	0.616318	0.043095	-	-	-	-	4.68836	2.265458	-	-	-	-	-	-
ALA97	0.807955	0.071395	-	-	-	-	13.0393	49.04658	-	-	-	-	12.95406	4.610245
ILE98	0.843493	0.056548	-	-	-	-	-	-	-	-	-	-	-	-
THR99	0.807936	0.091531	-	-	-	-	-	-	-	-	-	-	-	-
GLN100	-	-	-	-	-	-	-	-	-	-	-	-	-	-
ARG101	-	-	-	-	-	-	-	-	-	-	-	-	-	-
MET102	-	-	-	-	-	-	-	-	-	-	-	-	-	-

VAL103	0.649695	0.135669	-	-	-	-	-	-	-	-	-	-	20.19451	9.435292
ASP104	-	-	-	-	-	-	-	-	-	-	-	-	-	-
PHE105	-	-	-	-	-	-	-	-	-	-	-	-	-	-
ALA106	0.782558	0.049047	0.862435	0.046209	0.907525	0.028266	-	-	-	-	1555.218	936.3025	-	-
GLY107	0.800703	0.080725	-	-	-	-	-	-	-	-	-	-	7.65243	4.418528
VAL108	0.640962	0.129096	-	-	-	-	-	-	-	-	-	-	14.99831	7.891847
LYS109	0.890914	0.046802	-	-	-	-	-	-	-	-	-	-	-	-
ASP110	0.822182	0.038834	0.880172	0.037796	0.934251	0.02288	-	-	-	-	1273.15	433.1788	-	-
LYS111	0.864738	0.051771	-	-	-	-	-	-	-	-	-	-	-	-
VAL112	0.780763	0.080171	-	-	-	-	-	-	-	-	-	-	10.85543	5.691858
THR113	0.891624	0.026703	-	-	-	-	12.98455	10.62715	-	-	-	-	-	-
LEU114	0.77655	0.098854	0.820923	0.088596	0.946143	0.027421	-	-	-	-	1160.95	537.4351	12.50459	6.24714
VAL115	0.911557	0.024886	0.969836	0.022045	0.939882	0.024301	-	-	-	-	1798.076	3365.987	-	-
VAL116	0.96104	0.01682	-	-	-	-	-	-	-	-	-	-	-	-
GLY117	0.935329	0.026585	-	-	-	-	-	-	-	-	-	-	-	-
ALA118	0.924998	0.019391	-	-	-	-	43.54499	57.61622	-	-	-	-	-	-

SER119	0.625027	0.117178	-	-	-	-	-	-	-	-	-	-	-	-
GLN120	0.405121	0.242453	-	-	-	-	-	-	-	-	-	-	37.05898	16.74204
ASP121	0.878883	0.049732	-	-	-	-	-	-	-	-	-	-	-	-
ILE122	0.063675	0.009352	-	-	-	-	0.178763	0.120867	-	-	-	-	-	-
ILE123	0.700114	0.1122	-	-	-	-	7.582307	48.61885	-	-	-	-	23.64741	8.011293
PRO124	-	-	-	-	-	-	-	-	-	-	-	-	-	-
GLN125	0.860269	0.045356	-	-	-	-	18.38805	43.4139	-	-	-	-	-	-
LEU126	0.929723	0.0416	-	-	-	-	-	-	-	-	-	-	-	-
LYS127	0.930941	0.020752	-	-	-	-	15.83329	37.37846	-	-	-	-	-	-
LYS128	0.80656	0.02423	-	-	-	-	36.46659	7.306699	-	-	-	-	-	-
LYS129	0.741833	0.095953	-	-	-	-	-	-	-	-	-	-	13.45491	6.553305
TYR130	0.859901	0.07503	-	-	-	-	-	-	-	-	-	-	-	-
ASP131	0.833688	0.033786	-	-	-	-	11.3762	5.842277	-	-	-	-	-	-
VAL132	0.85952	0.017614	0.892243	0.019664	0.95777	0.01382	-	-	-	-	766.3073	287.906	-	-
ASP133	0.821621	0.01738	0.885521	0.017347	0.927936	0.011562	-	-	-	-	1020.725	158.8489	-	-
THR134	0.730863	0.014643	0.786107	0.017261	0.929706	0.016177	-	-	-	-	1006.839	296.3327	-	-

LEU135	0.920098	0.029016	-	-	-	-	-	-	-	-	-	-	-	-
ASP136	0.856207	0.079554	-	-	-	-	-	-	-	-	-	-	-	-
MET137	-	-	-	-	-	-	-	-	-	-	-	-	-	-
VAL138	-	-	-	-	-	-	-	-	-	-	-	-	-	-
PHE139	-	-	-	-	-	-	-	-	-	-	-	-	-	-
LEU140	0.977742	0.019719	-	-	-	-	99.25411	387.0434	-	-	-	-	-	-
ASP141	0.875583	0.054665	-	-	-	-	-	-	-	-	-	-	-	-
HIS142	-	-	-	-	-	-	-	-	-	-	-	-	-	-
TRP143	0.437321	0.189066	-	-	-	-	-	-	-	-	-	-	-	-
LYS144	0.850286	0.043359	-	-	-	-	-	-	-	-	-	-	-	-
ASP145	0.468346	0.23097	-	-	-	-	-	-	-	-	-	-	29.60988	16.98032
ARG146	0.774081	0.075648	-	-	-	-	-	-	-	-	-	-	-	-
TYR147	-	-	-	-	-	-	-	-	-	-	-	-	-	-
LEU148	0.695752	0.134807	-	-	-	-	-	-	-	-	-	-	17.28627	9.153135
PRO149	-	-	-	-	-	-	-	-	-	-	-	-	-	-
ASP150	0.865394	0.053864	-	-	-	-	10.33768	104.4089	-	-	-	-	-	-

THR151	0.802854	0.187793	-	-	-	-	6161.931	8378.711	-	-	-	-	-	-
LEU152	0.959928	0.053286	-	-	-	-	132.0211	443.1426	-	-	-	-	-	-
LEU153	0.378031	0.029519	0.691358	0.02856	0.54689	0.05213	-	-	63.60202	25.33501	2984.842	1669.526	-	-
LEU154	-	-	-	-	-	-	-	-	-	-	-	-	-	-
GLU155	0.637553	0.077915	-	-	-	-	-	-	-	-	-	-	-	-
GLU156	0.408042	0.116271	-	-	-	-	-	-	-	-	-	-	-	-
CYS157	0.855325	0.079068	-	-	-	-	-	-	-	-	-	-	-	-
GLY158	0.447485	0.174377	0.589758	0.142844	0.75879	0.207798	-	-	-	-	2373.364	3174.537	6.976079	9.183029
LEU159	0.716919	0.117696	-	-	-	-	9.691291	42.68856	-	-	-	-	11.40289	7.226331
LEU160	0.931599	0.0299	-	-	-	-	33.70191	1591.296	-	-	-	-	-	-
ARG161	0.893772	0.047286	-	-	-	-	-	-	-	-	-	-	-	-
LYS162	0.953924	0.018583	-	-	-	-	29.33738	110.584	-	-	-	-	-	-
GLY163	0.871903	0.040648	-	-	-	-	14.13865	46.32962	-	-	-	-	-	-
THR164	-	-	-	-	-	-	-	-	-	-	-	-	-	-
VAL165	0.553848	0.165487	0.647228	0.135905	0.855922	0.108228	-	-	-	-	2192.439	2198.03	24.86898	9.731992
LEU166	0.835763	0.082866	-	-	-	-	10.26698	145.2304	-	-	-	-	12.91125	5.986578

LEU167	0.949293	0.026504	-	-	-	-	24.57851	307.6176	-	-	-	-	-	-
ALA168	-	-	-	-	-	-	-	-	-	-	-	-	-	-
ASP169	0.922419	0.040681	-	-	-	-	-	-	-	-	-	-	-	-
ASN170	0.895056	0.053649	-	-	-	-	-	-	-	-	-	-	-	-
VAL171	0.895822	0.049515	-	-	-	-	-	-	-	-	-	-	-	-
ILE172	0.081499	0.010288	-	-	-	-	-	-	-	-	-	-	-	-
CYS173	-	-	-	-	-	-	-	-	-	-	-	-	-	-
PRO174	-	-	-	-	-	-	-	-	-	-	-	-	-	-
GLY175	0.904787	0.038579	-	-	-	-	-	-	-	-	-	-	-	-
ALA176	0.785708	0.031311	-	-	-	-	-	-	-	-	-	-	-	-
PRO177	-	-	-	-	-	-	-	-	-	-	-	-	-	-
ASP178	0.919901	0.059121	-	-	-	-	55.7296	977.9208	-	-	-	-	-	-
PHE179	-	-	-	-	-	-	-	-	-	-	-	-	-	-
LEU180	0.7422	0.025128	-	-	-	-	8.921815	2.124581	-	-	-	-	-	-
ALA181	-	-	-	-	-	-	-	-	-	-	-	-	-	-
HIS182	0.848834	0.051607	-	-	-	-	-	-	-	-	-	-	-	-

VAL183	-	-	-	-	-	-	-	-	-	-	-	-	-	-
ARG184	0.906551	0.061841	-	-	-	-	20.26343	431.9493	-	-	-	-	-	-
GLY185	0.808806	0.033785	-	-	-	-	-	-	-	-	-	-	-	-
SER186	0.778029	0.049842	-	-	-	-	7.346329	6.665346	-	-	-	-	-	-
SER187	-	-	-	-	-	-	-	-	-	-	-	-	-	-
CYS188	0.863015	0.041418	-	-	-	-	-	-	-	-	-	-	-	-
PHE189	0.889616	0.05496	-	-	-	-	-	-	-	-	-	-	-	-
GLU190	0.82401	0.033021	-	-	-	-	11.33381	5.171871	-	-	-	-	-	-
CYS191	0.940671	0.030757	-	-	-	-	36.70653	227.2087	-	-	-	-	-	-
THR192	0.82893	0.037001	-	-	-	-	-	-	-	-	-	-	-	-
HIS193	0.889757	0.026712	0.938564	0.025229	0.948041	0.016687	-	-	-	-	1417.893	1332.025	-	-
TYR194	0.881098	0.045397	-	-	-	-	-	-	-	-	-	-	-	-
GLN195	0.848124	0.018556	-	-	-	-	-	-	-	-	-	-	-	-
SER196	0.907245	0.023346	-	-	-	-	510.7859	186.4918	-	-	-	-	-	-
PHE197	-	-	-	-	-	-	-	-	-	-	-	-	-	-
LEU198	0.872977	0.045408	-	-	-	-	-	-	-	-	-	-	-	-

GLU199	-	-	-	-	-	-	-	-	-	-	-	-	-	-
TYR200	0.814801	0.040416	0.865932	0.052055	0.940861	0.035865	-	-	-	-	912.402	758.0784	-	-
ARG201	0.891725	0.041846	-	-	-	-	22.21541	137.2548	-	-	-	-	-	-
GLU202	-	-	-	-	-	-	-	-	-	-	-	-	-	-
VAL203	0.630989	0.035575	0.714327	0.049748	0.883473	0.045112	-	-	-	-	707.5151	486.7067	-	-
VAL204	-	-	-	-	-	-	-	-	-	-	-	-	-	-
ASP205	0.913625	0.03804	-	-	-	-	-	-	-	-	-	-	-	-
GLY206	0.375701	0.230243	0.444828	0.229791	0.844628	0.332603	-	-	-	-	891.7752	605.047	27.41773	14.11715
LEU207	0.893758	0.034562	-	-	-	-	-	-	-	-	-	-	-	-
GLU208	0.852168	0.024962	-	-	-	-	-	-	-	-	-	-	-	-
LYS209	-	-	-	-	-	-	-	-	-	-	-	-	3.663383	2.248928
ALA210	-	-	-	-	-	-	-	-	-	-	-	-	-	-
ILE211	0.945619	0.034334	-	-	-	-	-	-	-	-	-	-	-	-
TYR212	-	-	-	-	-	-	-	-	-	-	-	-	-	-
LYS213	0.871489	0.042188	0.893511	0.054257	0.975348	0.037345	-	-	-	-	551.6088	853.5034	-	-

SI Table 4. Model-free analysis results for COMT:DNC:Mg^{2+}:SAM complex obtained by Relax software. R_{ex} parameter calculated for a magnetic field of 800 MHz.

	$^{500MHz}R_{ex}(s^{-1})$	$^{500MHz}R_{ex\_min}(s^{-1})$	$^{500MHz}R_{ex\_max}(s^{-1})$	S^2	S^2min	S^2max	T_e < 100 or T_f (ps)	T_e >-100 or T_s (ps)	T min	T max
GLN1	-	-	-	0.775	0.826	0.714	-	1310	1060	1610
GLY2	-	-	-	0.98	0.992	0.949	-	-	-	-
ASP3	-	-	-	-	-	-	-	-	-	-
THR4	-	-	-	0.938	0.959	0.908	42	-	17.3	103
LYS5	-	-	-	0.954	0.979	0.905	-	2000	-	-
GLU6	-	-	-	0.927	0.938	0.916	100	-	-	-
GLN7	-	-	-	0.973	0.984	0.955	100	-	-	-
ARG8	-	-	-	0.984	0.993	0.964	-	2370	197	28600
ILE9	-	-	-	0.994	0.999	0.961	-	2000	-	-
LEU10	-	-	-	0.983	0.989	0.972	-	2000	-	-
ASN11	2.01	1.44	2.81	0.989	0.997	0.963	100	-	-	-
HIS12	2.28	1.81	2.86	1	-	-	-	-	-	-
VAL13	-	-	-	0.975	0.983	0.963	-	2000	-	-
LEU14	-	-	-	0.964	0.975	0.949	-	1540	1010	2350
GLN15	-	-	-	0.975	0.988	0.947	-	829	434	1580

HIS16	-	-	-	0.967	0.979	0.947	100	-	-	-
ALA17	-	-	-	1	-	-	-	-	-	-
GLU18	-	-	-	1	-	-	-	-	-	-
PRO19	-	-	-	-	-	-	-	-	-	-
GLY20	2.66	2.07	3.41	0.904	0.917	0.889	100	-	-	-
ASN21	-	-	-	1	-	-	-	-	-	-
ALA22	1.91	1.44	2.53	1	-	-	-	-	-	-
GLN23	-	-	-	1	-	-	-	-	-	-
SER24	-	-	-	0.977	0.99	0.95	-	492	167	1450
VAL25	-	-	-	1	-	-	-	-	-	-
LEU26	3.01	1.96	4.62	0.974	0.991	0.931	100	-	-	-
GLU27	-	-	-	1	-	-	-	-	-	-
ALA28	-	-	-	0.992	0.998	0.966	100	-	-	-
ILE29	-	-	-	1	-	-	-	-	-	-
ASP30	-	-	-	1	-	-	-	-	-	-
THR31	-	-	-	0.962	0.978	0.935	-	961	609	1520

TYR32	2.26	1.65	3.09	1	-	-	-	-	-	-
CYS33	-	-	-	0.979	0.985	0.97	-	2690	626	11600
GLU34	-	-	-	0.985	0.991	0.975	100	-	-	-
GLN35	-	-	-	1	-	-	-	-	-	-
LYS36	-	-	-	0.972	0.98	0.961	-	924	684	1250
GLU37	-	-	-	0.94	0.958	0.916	49	-	23.4	103
TRP38	-	-	-	1	-	-	-	-	-	-
ALA39	-	-	-	1	-	-	-	-	-	-
MET40	-	-	-	0.943	0.962	0.914	10	-	-	-
ASN41	-	-	-	0.99	0.996	0.976	-	2000	-	-
VAL42	-	-	-	0.97	0.984	0.947	-	-	-	-
GLY43	-	-	-	-	-	-	-	-	-	-
ASP44	-	-	-	-	-	-	-	-	-	-
LYS45	-	-	-	0.922	0.933	0.908	49	-	36.6	64.5
LYS46	-	-	-	0.978	0.983	0.972	-	935	752	1160
GLY47	-	-	-	-	-	-	-	-	-	-

LYS48	-	-	-	1	-	-	-	-	-	-
ILE49	-	-	-	1	-	-	-	-	-	-
VAL50	-	-	-	1	-	-	-	-	-	-
ASP51	-	-	-	0.987	0.995	0.964	-	2000	-	-
ALA52	-	-	-	1	-	-	-	-	-	-
VAL53	-	-	-	-	-	-	-	-	-	-
ILE54	3.76	2.82	5.01	1	-	-	-	-	-	-
GLN55	-	-	-	0.993	0.999	0.928	-	2000	-	-
GLU56	-	-	-	0.981	0.996	0.924	100	-	-	-
HIS57	-	-	-	0.974	0.982	0.962	-	2000	-	-
GLN58	-	-	-	-	-	-	-	-	-	-
PRO59	-	-	-	-	-	-	-	-	-	-
SER60	-	-	-	0.918	0.935	0.898	10	-	-	-
VAL61	-	-	-	0.959	0.972	0.941	26	-	10.7	61.4
LEU62	-	-	-	0.981	0.985	0.976	-	2000	-	-
LEU63	-	-	-	0.989	0.992	0.986	-	2000	-	-

GLU64	-	-	-	1	-	-	-	-	-	-
LEU65	-	-	-	1	-	-	-	-	-	-
GLY66	-	-	-	0.943	0.951	0.934	10	-	-	-
ALA67	-	-	-	0.986	0.996	0.957	-	-	-	-
TYR68	-	-	-	0.934	0.953	0.91	-	-	-	-
CYS69	4.07	2.46	6.75	1	-	-	-	-	-	-
GLY70	-	-	-	0.971	0.988	0.933	10	-	-	-
TYR71	2.7	1.65	4.4	1	-	-	-	-	-	-
SER72	-	-	-	0.989	0.998	0.933	-	2000	-	-
ALA73	2.89	2.02	4.15	1	-	-	-	-	-	-
VAL74	-	-	-	0.984	0.992	0.966	-	2910	82.9	102000
ARG75	3.51	2.8	4.39	1	-	-	-	-	-	-
MET76	-	-	-	-	-	-	-	-	-	-
ALA77	-	-	-	0.971	0.983	0.95	-	716	416	1240
ARG78	-	-	-	0.976	0.982	0.968	-	2000	-	-
LEU79	-	-	-	1	-	-	-	-	-	-

LEU80	-	-	-	1	-	-	-	-	-	-
SER81	-	-	-	0.896	0.903	0.889	35	-	29.6	42.1
PRO82	-	-	-	-	-	-	-	-	-	-
GLY83	-	-	-	-	-	-	-	-	-	-
ALA84	-	-	-	0.977	0.981	0.972	-	2000	-	-
ARG85	-	-	-	0.967	0.972	0.962	100	-	-	-
LEU86	-	-	-	1	-	-	-	-	-	-
ILE87	-	-	-	0.985	0.989	0.98	100	-	-	-
THR88	2.16	1.86	2.5	1	-	-	-	-	-	-
ILE89	-	-	-	0.979	0.984	0.974	-	2000	-	-
GLU90	-	-	-	0.978	0.982	0.973	-	2000	-	-
ILE91	-	-	-	1	-	-	-	-	-	-
ASN92	2.4	1.78	3.24	1	-	-	-	-	-	-
PRO93	-	-	-	-	-	-	-	-	-	-
ASP94	-	-	-	0.971	0.984	0.945	-	1170	662	2070
CYS95	-	-	-	0.939	0.962	0.903	10	-	-	-

ALA96	-	-	-	0.95	0.97	0.917	-	3590	628	20500
ALA97	-	-	-	1	-	-	-	-	-	-
ILE98	-	-	-	1	-	-	-	-	-	-
THR99	-	-	-	1	-	-	-	-	-	-
GLN100	2.26	1.9	2.69	1	-	-	-	-	-	-
ARG101	-	-	-	0.995	0.999	0.968	-	2000	-	-
MET102	2.57	2.09	3.17	1	-	-	-	0	-	-
VAL103	2.92	2.35	3.62	1	-	-	-	0	-	-
ASP104	2.38	1.98	2.86	1	-	-	-	0	-	-
PHE105	-	-	-	0.991	0.997	0.969	-	2000	-	-
ALA106	-	-	-	1	-	-	-	0	-	-
GLY107	-	-	-	0.954	0.964	0.942	-	0	-	-
VAL108	-	-	-	0.961	0.973	0.943	-	0	-	-
LYS109	-	-	-	0.972	0.982	0.956	-	587	367	938
ASP110	-	-	-	0.951	0.959	0.942	-	2000	-	-
LYS111	-	-	-	0.944	0.955	0.93	10	-	-	-

VAL112	-	-	-	1	-	-	-	-	-	-
THR113	-	-	-	0.954	0.96	0.947	-	-	-	-
LEU114	-	-	-	0.979	0.984	0.973	100	-	-	-
VAL115	-	-	-	1	-	-	-	-	-	-
VAL116	-	-	-	0.982	0.986	0.976	100	-	-	-
GLY117	-	-	-	0.97	0.975	0.963	-	-	-	-
ALA118	-	-	-	1	-	-	-	-	-	-
SER119	-	-	-	0.891	0.926	0.843	10	-	-	-
GLN120	-	-	-	1	-	-	-	-	-	-
ASP121	-	-	-	0.994	0.998	0.984	-	2000	-	-
ILE122	-	-	-	0.976	0.99	0.946	10	-	-	-
ILE123	-	-	-	1	-	-	-	-	-	-
PRO124	-	-	-	-	-	-	-	-	-	-
GLN125	-	-	-	0.939	0.948	0.927	10	-	-	-
LEU126	-	-	-	1	-	-	-	-	-	-
LYS127	-	-	-	1	-	-	-	-	-	-

LYS128	-	-	-	0.895	0.901	0.889	100	-	-	-
LYS129	-	-	-	1	-	-	-	-	-	-
TYR130	-	-	-	0.959	0.97	0.944	100	-	-	-
ASP131	-	-	-	0.948	0.955	0.939	100	-	-	-
VAL132	-	-	-	0.945	0.95	0.94	100	-	-	-
ASP133	-	-	-	0.958	0.963	0.951	100	-	-	-
THR134	-	-	-	0.849	0.857	0.842	-	-	-	-
LEU135	-	-	-	1	-	-	-	-	-	-
ASP136	-	-	-	1	-	-	-	-	-	-
MET137	-	-	-	0.988	0.994	0.975	100	-	-	-
VAL138	-	-	-	1	-	-	-	-	-	-
PHE139	-	-	-	0.972	0.978	0.963	-	1180	921	1520
LEU140	-	-	-	0.989	0.993	0.982	-	2000	-	-
ASP141	-	-	-	0.972	0.981	0.958	100	-	-	-
HIS142	-	-	-	1	-	-	-	-	-	-
TRP143	-	-	-	0.966	0.981	0.939	-	-	-	-

LYS144	-	-	-	1	-	-	-	-	-	-
ASP145	-	-	-	0.988	0.997	0.946	-	1820	208	16000
ARG146	-	-	-	1	-	-	-	-	-	-
TYR147	3.76	2.77	5.1	0.965	0.981	0.938	100	-	-	-
LEU148	-	-	-	0.995	1	0.938	-	2000	-	-
PRO149	-	-	-	-	-	-	-	-	-	-
ASP150	-	-	-	0.992	0.997	0.975	-	2000	-	-
THR151	-	-	-	1	-	-	-	0	-	-
LEU152	-	-	-	1	-	-	-	0	-	-
LEU153	-	-	-	0.979	0.988	0.965	-	735	456	1180
LEU154	-	-	-	1	-	-	-	0	-	-
GLU155	-	-	-	0.993	0.997	0.98	-	2000	-	-
GLU156	3	2.44	3.69	0.978	0.986	0.965	100	-	-	-
CYS157	-	-	-	0.963	0.978	0.939	10	-	-	-
GLY158	-	-	-	0.981	0.989	0.968	-	688	427	1110
LEU159	-	-	-	0.981	0.988	0.969	-	2000	-	-

LEU160	-	-	-	0.977	0.984	0.967	-	1400	943	2080
ARG161	-	-	-	0.979	0.986	0.969	100	-	-	-
LYS162	-	-	-	0.977	0.985	0.965	-	1060	730	1530
GLY163	-	-	-	1	-	-	-	0	-	-
THR164	-	-	-	1	-	-	-	0	-	-
VAL165	-	-	-	0.981	0.985	0.975	-	2000	-	-
LEU166	-	-	-	0.985	0.99	0.98	-	2000	-	-
LEU167	-	-	-	0.982	0.987	0.974	-	10	-	-
ALA168	-	-	-	0.976	0.981	0.969	-	2000	-	-
ASP169	-	-	-	0.982	0.993	0.954	-	3810	315	46100
ASN170	-	-	-	1	-	-	-	0	-	-
VAL171	-	-	-	0.983	0.991	0.968	-	2000	-	-
ILE172	3.75	2.71	5.19	1	-	-	-	-	-	-
CYS173	-	-	-	0.987	0.998	0.918	10	-	-	-
PRO174	-	-	-	-	-	-	-	-	-	-
GLY175	-	-	-	1	-	-	-	-	-	-

ALA176	-	-	-	0.91	0.919	0.901	10	-	-	-
PRO177	-	-	-	-	-	-	-	-	-	-
ASP178	-	-	-	1	-	-	-	-	-	-
PHE179	-	-	-	0.992	0.999	0.947	-	2000	-	-
LEU180	2.7	2.08	3.52	1	-	-	-	0	-	-
ALA181	-	-	-	0.993	0.998	0.969	-	2000	-	-
HIS182	-	-	-	0.942	0.955	0.926	10	-	-	-
VAL183	-	-	-	1	-	-	-	-	-	-
ARG184	-	-	-	1	-	-	-	-	-	-
GLY185	-	-	-	1	-	-	-	-	-	-
SER186	-	-	-	0.939	0.953	0.922	10	-	-	-
SER187	-	-	-	-	-	-	-	-	-	-
CYS188	-	-	-	1	-	-	-	-	-	-
PHE189	-	-	-	1	-	-	-	-	-	-
GLU190	-	-	-	0.958	0.967	0.948	10	-	-	-
CYS191	-	-	-	0.985	0.991	0.973	-	2000	-	-

THR192	-	-	-	0.935	0.943	0.926	10	-	-	-
HIS193	-	-	-	1	-	-	-	-	-	-
TYR194	-	-	-	1	-	-	-	-	-	-
GLN195	-	-	-	0.955	0.96	0.949	10	-	-	-
SER196	-	-	-	1	-	-	-	-	-	-
PHE197	-	-	-	0.972	0.981	0.959	-	1060	747	1500
LEU198	-	-	-	1	-	-	-	-	-	-
GLU199	-	-	-	0.978	0.989	0.956	10	-	-	-
TYR200	-	-	-	1	-	-	-	-	-	-
ARG201	2.77	2.09	3.67	0.987	0.996	0.963	100	-	-	-
GLU202	-	-	-	0.978	0.992	0.938	100	-	-	-
VAL203	-	-	-	0.79	0.803	0.776	-	-	-	-
VAL204	-	-	-	1	-	-	-	-	-	-
ASP205	-	-	-	1	-	-	-	-	-	-
GLY206	-	-	-	0.953	0.964	0.94	10	-	-	-
LEU207	-	-	-	1	-	-	-	-	-	-

GLU208	-	-	-	0.985	0.991	0.975	-	1260	787	2010
LYS209	-	-	-	0.976	0.98	0.97	-	2000	-	-
ALA210	-	-	-	1	-	-	-	-	-	-
ILE211	-	-	-	0.965	0.972	0.957	10	-	-	-
TYR212	-	-	-	0.99	0.994	0.984	-	2000	-	-
LYS213	-	-	-	0.975	0.983	0.965	-	1000	732	1370
GLY214	-	-	-	-	-	-	-	-	-	-
PRO215	-	-	-	-	-	-	-	-	-	-
GLY216	-	-	-	0.38	0.396	0.363	-	652	643	662
SER217	-	-	-	0.161	0.202	0.127	-	730	714	746

SI Table 5. Model-free analysis results for COMT:DNC:Mg^{2+}:Sinefungin complex obtained by in-house scripts calculations. R_{ex} parameter calculated for a magnetic field of 500 MHz.

6. General conclusions and future work

This thesis primarily concerns the use of nuclear magnetic resonance (NMR) spectroscopy to study two ternary complexes of human S-COMT: S-COMT:SAM:DNC:Mg^{2+} and S-COMT:sinefungin:DNC:Mg^{2+}. In Chapter 3, we show that the sinefungin complex has transition state character, so can be considered a transition state analogue. Comparison with the reactant (SAM) complex allows catalytically relevant conformational change in the protein to be studied. To achieve this, firstly, NMR backbone assignments of the two COMT ternary complexes were determined at high level of coverage. In total, 97% of all backbone resonances were assigned in both complexes (95% of $^{1}H_{N}$, 95% of ^{15}N, 98% of $^{13}C_{\alpha}$, 97% of $^{13}C_{\beta}$ and 98% of $^{13}C'$ nuclei). Next, the secondary structure content of S-COMT was predicted by analysing the backbone $^{1}H_{N}$, ^{15}N, $^{13}C_{\alpha}$, $^{13}C_{\beta}$ and $^{13}C'$ chemical shifts of both complexes using the TALOS+ and TALOS-N [1, 2] algorithms. This indicated that the solution conformation is very similar to the protein structure observed in crystals (compared to PDB: 3BWM [3] and then crystals that we have obtained, PDB: 6I3C, 6I3D) and provided confidence in these assignments. The backbone ^{1}H, ^{13}C and ^{15}N chemical shifts for the S-COMT complexes have been deposited in the BioMagResBank (http://www.bmrb.wisc.edu/) under the BMRB accession codes 26848 (S-COMT:SAM:DNC:Mg^{2+} complex) and 26851 (S-COMT:sinefungin:DNC:Mg^{2+} complex).

The structures of both S-COMT complexes were also investigated using X-ray crystallography. The sitting drop vapour diffusion technique was used to grow crystals of the two complexes and data were collected from single cryo frozen crystals at Diamond Light Source. Then, structures were solved by molecular replacement and refined. Final models with resolution of 1.3 Å and 1.4 Å have been deposited with the protein data bank, accession codes 6I3C, 6I3D for the S-COMT:SAM:DNC:Mg^{2+} and S-COMT:sinefungin:DNC:Mg^{2+} complex, respectively. The SAM complex crystallized as a monomer while the sinefungin complex crystallized as a dimer with key active site distances differing by <0.03 Å between two chains.

Equivalent X-ray crystal structures and NMR assignments of the reactant and transition state analogue complexes allowed detailed structural comparison. We have observed that our two new crystal structures are almost superimposable, but notably

show differences in the binding of DNC, with the donor-acceptor distance ~0.1 Å shorter in the sinefungin complex. In the case of NMR assignments, a significant difference in chemical shifts appears for residues located in the active site. This is consistent with active site reorganisation during the reaction and was further investigated with the aid of density functional theory calculations and molecular dynamics simulations. All methods were complementary and led us to the conclusion of active site "compaction" and electrostatic preorganization driven by H-bonding between the transferring methyl group and specific "equatorial" active site residues (see Chapter 3). While this thesis did not cover any kinetic analysis, such measurements, especially using kinetic isotope effects (KIEs), would be an interesting direction for the future work, since reported deuterium and tritium KIEs are large [4, 5]. We propose that KIEs observed on the reaction arise through the equatorial H-bonding we identified. The analysis we have developed to characterize these interactions would then allow e.g. disruption of these interactions through mutagenesis to be correlated with KIEs.

In Chapter 4 we have presented the effect of hydrostatic pressure from 1 bar up to 2500 bar on S-COMT NMR chemical shifts. The majority of resonances shift linearly with pressure in positive nitrogen and positive hydrogen directions (low field ΔHN), indicating that almost the entire polypeptide backbone is sensitive to pressure. A tendency toward low field shifts is correlated with a decrease in hydrogen bond distance between the amide nitrogen atom and the oxygen atom of either water or carbonyl groups. On average, we have found that shifts are larger for alpha helical and coil regions than for beta strands, but no significant change in predicted secondary structure with pressure was observed. This was also confirmed by predictions from TALOS-N [2] and CS-ROSETTA [6] and the linear pressure response in N-H plane indicates no structural transition and simple compression within the folded state. For future studies, it will be interesting to compare these results with high pressure molecular dynamics simulations, which can highlight subtle changes, elevated by pressure and provide a more atomistic description of protein conformational rearrangement.

In Chapter 4 and 5 we showed that S-COMT is a highly ordered and stable protein. This stability may be also achieved due to dimerization. Our preliminary NMR relaxation analyses presented in Chapter 5 are contaminated by fast exchange monomer-dimer equilibrium. Relaxation rates reflect exchange effects, not a single state. Dynamics of the monomer are of interest and one of our proposed ways to achieve that

is through mutagenesis in future work. There are few potential candidates found in a dimer interface observed in the sinefungin X-ray crystal sturcutre that can make hydrogen bonds and/or non-bonded contacts. Firstly, this dimer interface contains a pair of positive charged Lys45 and negative charged Glu190 residues. There is also a pair of tyrosine and threonine (Tyr194 chain A – Thr192 chain B), hydrogen bonds between two histidines (His193 chain A – His193 chain B) and a cysteine hydrogen bonded to glutamine (Gln195 chain A – Cys191 chain B) in the dimer interface that could be disrupted. S-COMT also contains seven cysteines, but we believe that they were reduced under our experimental conditions, as 10 mM DTT (dithiothreitol) reducing agent was included in all samples and 1D proton spectra recorded at the beginning and at the end of a set of experiments confirmed the continuing presence of DTT (see Appendix Figure 8). Another approach to overcome problems associated with dimerization is to record and analyse a set of several relaxation experiments performed at different sample concentrations, so the effect of dimer formation on intramolecular conformational exchange can be monitored as the concentration dependence of the difference between auto- and cross-correlated transverse relaxation rates. Another aspect that may be worth to consider is a constant time Carr-Purcell-Meiboom-Gill (CPMG) relaxation dispersion experiment, which may help to understand conformational exchange in µs-ms timescale and investigate protein equilibrium conformations.

Finally, we have obtained information about reactant and transition state analogue complexes of human S-COMT containing the inhibitor DNC. It would be interesting to now turn to look at physiologically relevant substrates/analogues, for example dopamine, levodopa and similar catecholamines. Also ternary complexes with SAH (product of the reaction) could deliver additional relevant data, which can help to determine how much protein rearrangement is likely to occur as the product is formed after the transition state.

In overall, the initial aims (Chapter 1.4) are covered. We have provided the first NMR backbone assignment of COMT, two crystal structures in high resolution and we have confirmed that compressive motions and electrostatic preorganization occurred for the methyl transfer reaction catalysed by COMT. High pressure NMR and dynamics studies showed that S-COMT is a highly ordered and stable protein. However, relaxation measurements indicated higher order species presented in the sample, most

likely a dimer, which influenced the relaxation rates and led to overestimations. Dimer studies were beyond the scope of this project, as a dimer is not physiologically relevant from the functional point of view.

References

1. Shen, Y., et al., *TALOS+: a hybrid method for predicting protein backbone torsion angles from NMR chemical shifts.* Journal of Biomolecular NMR, 2009. **44**(4): p. 213-23.
2. Shen, Y. and A. Bax, *Protein backbone and sidechain torsion angles predicted from NMR chemical shifts using artificial neural networks.* Journal of biomolecular NMR, 2013. **56**(3): p. 227-241.
3. Rutherford, K., et al., *The 108M polymorph of human catechol O-methyltransferase is prone to deformation at physiological temperatures.* Biochemistry, 2006. **45**(7): p. 2178-2188.
4. Hegazi, M.F., R.T. Borchardt, and R.L. Schowen, . *alpha.-Deuterium and carbon-13 isotope effects for methyl transfer catalyzed by catechol O-methyltransferase. SN2-like transition state.* Journal of the American Chemical Society, 1979. **101**(15): p. 4359-4365.
5. Zhang, J. and J.P. Klinman, *Enzymatic methyl transfer: role of an active site residue in generating active site compaction that correlates with catalytic efficiency.* Journal of the American Chemical Society, 2011. **133**(43): p. 17134-7.
6. Lange, O.F., et al., *Determination of solution structures of proteins up to 40 kDa using CS-Rosetta with sparse NMR data from deuterated samples.* Proceedings of the National Academy of Sciences, USA, 2012. **109**(27): p. 10873-10878.

7. Appendix

1. Amino acid sequence of the human S-COMT, containing a TEV-cleavable N-terminal His-tag:

```
        10         20         30         40         50         60
MHHHHHHENL YFQGDTKEQR ILNHVLQHAE PGNAQSVLEA IDTYCEQKEW AMNVGDKKGK

        70         80         90        100        110        120
IVDAVIQEHQ PSVLLELGAY CGYSAVRMAR LLSPGARLIT IEINPDCAAI TQRMVDFAGV

       130        140        150        160        170        180
KDKVTLVVGA SQDIIPQLKK KYDVDTLDMV FLDHWKDRYL PDTLLLEECG LLRKGTVLLA

       190        200        210        220        230
DNVICPGAPD FLAHVRGSSC FECTHYQSFL EYREVVDGLE KAIYKGPGSE AGP
```

2. Expression of S-COMT.

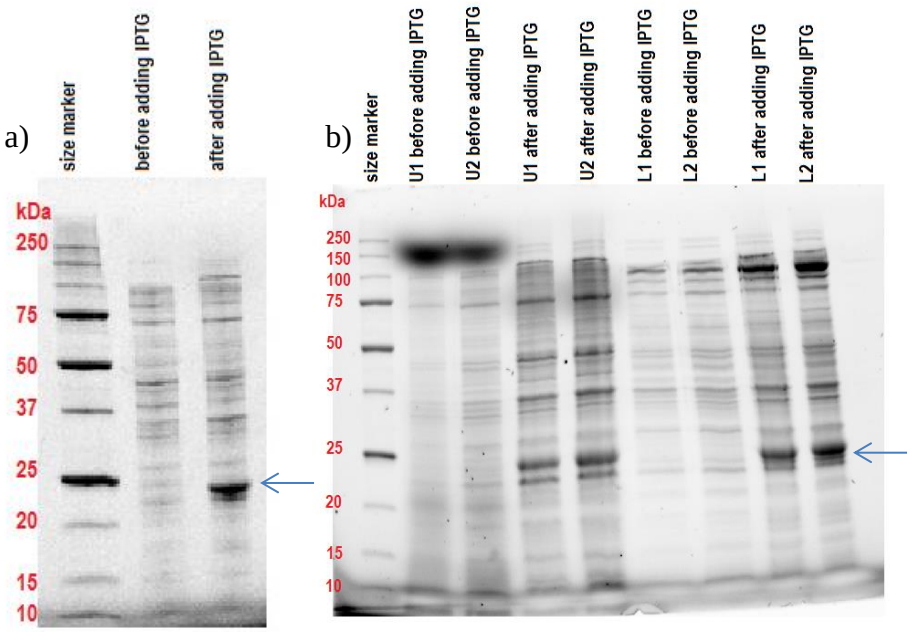

Appendix Figure 1. SDS-PAGE gel containing samples before and after induction with 0.4 mM IPTG of: a) unlabelled rat S-COMT expression, b) unlabelled and ^{15}N labelled human S-COMT. U1, U2 – two samples of unlabelled human S-COMT; L1,L2 – two samples of ^{15}N labelled human S-COMT. The blue arrow indicates the position of COMT.

3. Purification of S-COMT.

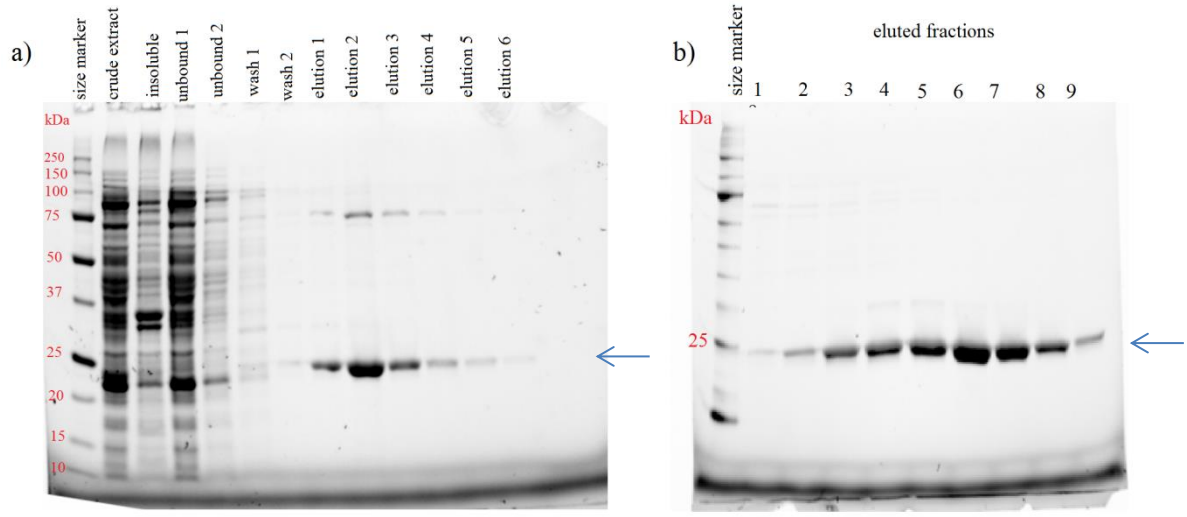

Appendix Figure 2. SDS-PAGE gel of a typical S-COMT purification by a) Ni affinity chromatography performed on His-Trap FF affinity Ni-sepharose column (GE Healthcare) connected to an AKTA purification system; b) size exclusion chromatography performed on 10/300 Superdex 200 GL column (GE Healthcare) connected to an AKTA purification system. The blue arrow indicates the position of COMT.

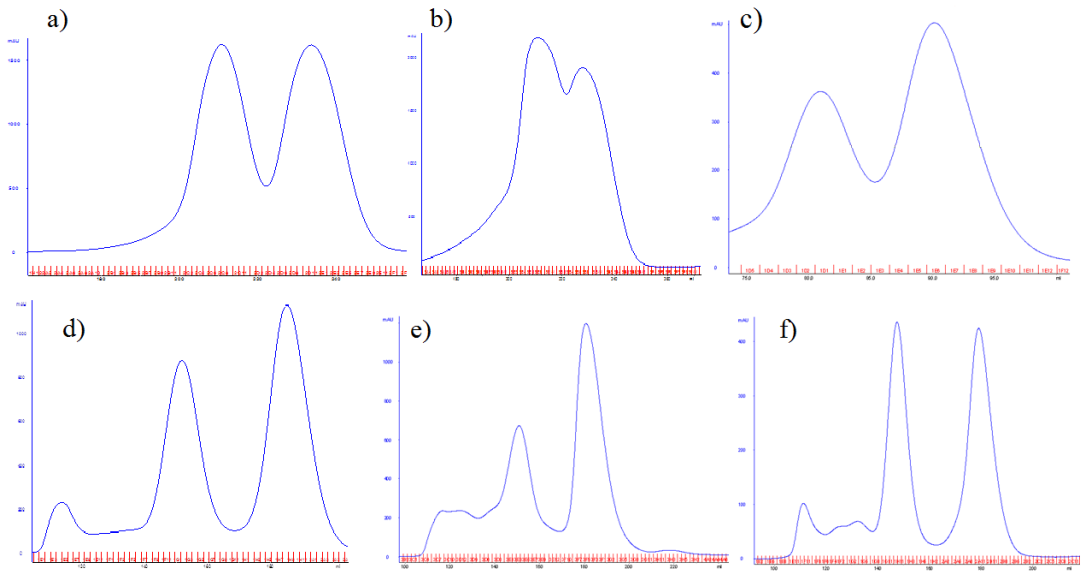

Appendix Figure 3. Chromatograms (280 nm detection) monitoring the size exclusion purification of rat S-COMT (a) and human S-COMT (b-f). Column used: HiLoad 26/60 superdex 200 (a,b); HiLoad 16/60 superdex 200 (c); HiLoad 26/60 superdex 75 (d,e,f). Buffers: 50 mM MOPS pH=7, 2 mM DTT, 0.1 mM EDTA (a); 50 mM MOPS pH=7, 2 mM DTT, 0.1 mM EDTA, 50 mM NaCl (b); 50 mM MOPS pH=7, 2 mM DTT, 150 mM NaCl (c); 50 mM Tris-HCl pH=8, 200 mM NaCl, 10 mM DTT (d,e); 50 mM $NaPO_4$ pH=7.4, 150 mM NaCl (f).

4. Monomer/dimer formation.

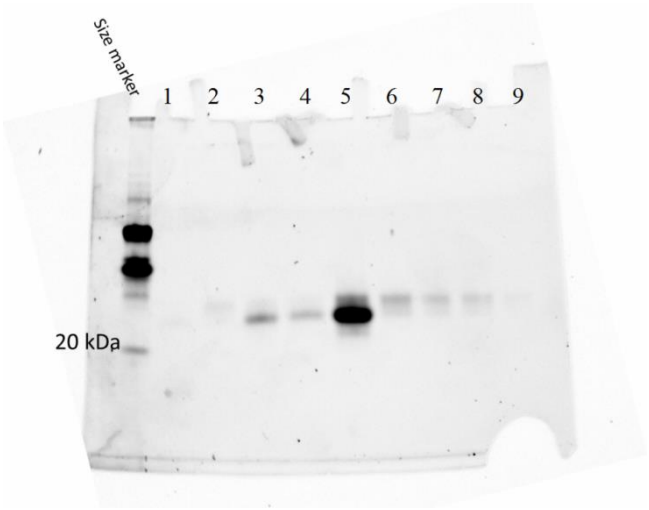

Appendix Figure 4. Native PAGE gel of human S-COMT. 1-9 wells correspond to different concentration of the sample. 1. monomer conc. ~0.015 mg/mL; 2. dimer conc. ~0.015 mg/mL; 3. monomer conc. ~0.14 mg/mL; 4. monomer conc. ~0.07 mg/mL; 5. monomer conc. ~1.4 mg/mL; 6. dimer conc. ~0.06 mg/mL; 7. dimer conc. ~0.045 mg/mL; 8. dimer conc. ~0.03 mg/mL; 9. dimer conc. ~0.02 mg/mL. Concentration estimated using NanoDrop.

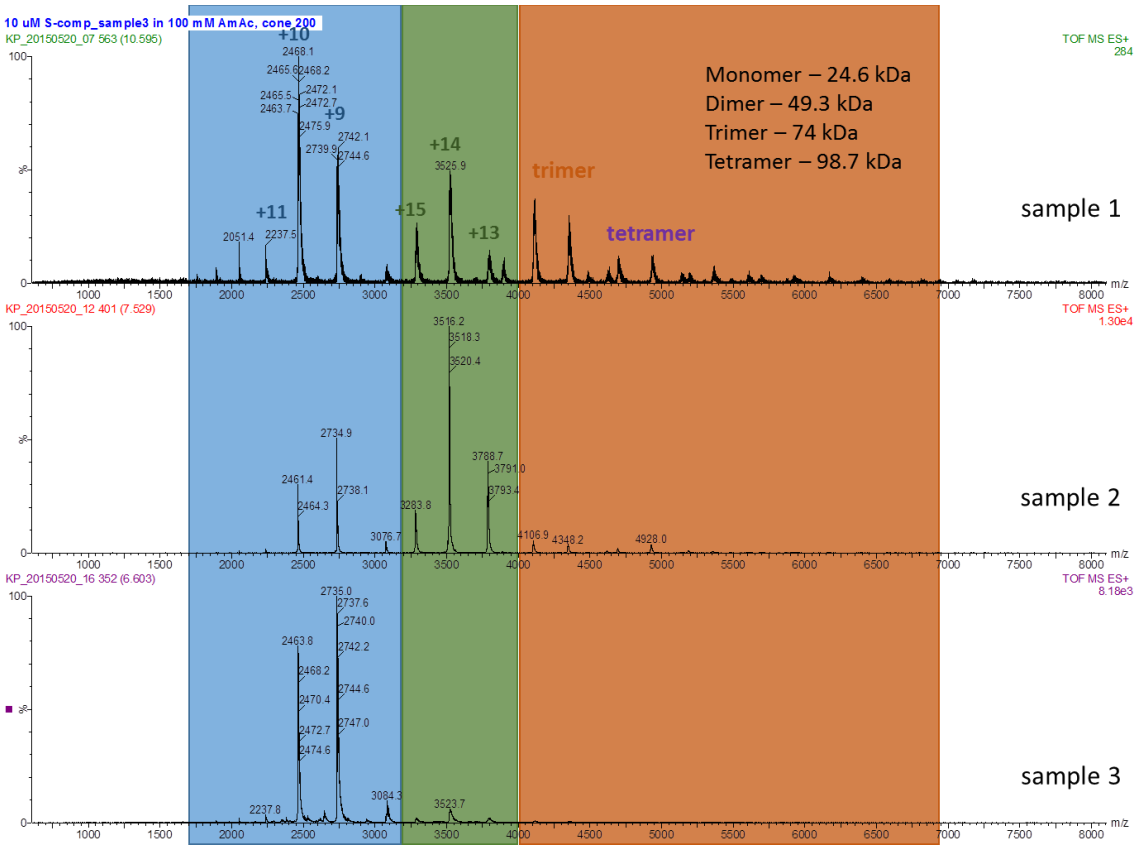

Appendix Figure 5. Mass spectra recorded for three different fractions obtained after size exclusion chromatography of human S-COMT.

5. Ligand interactions.

1. SAM

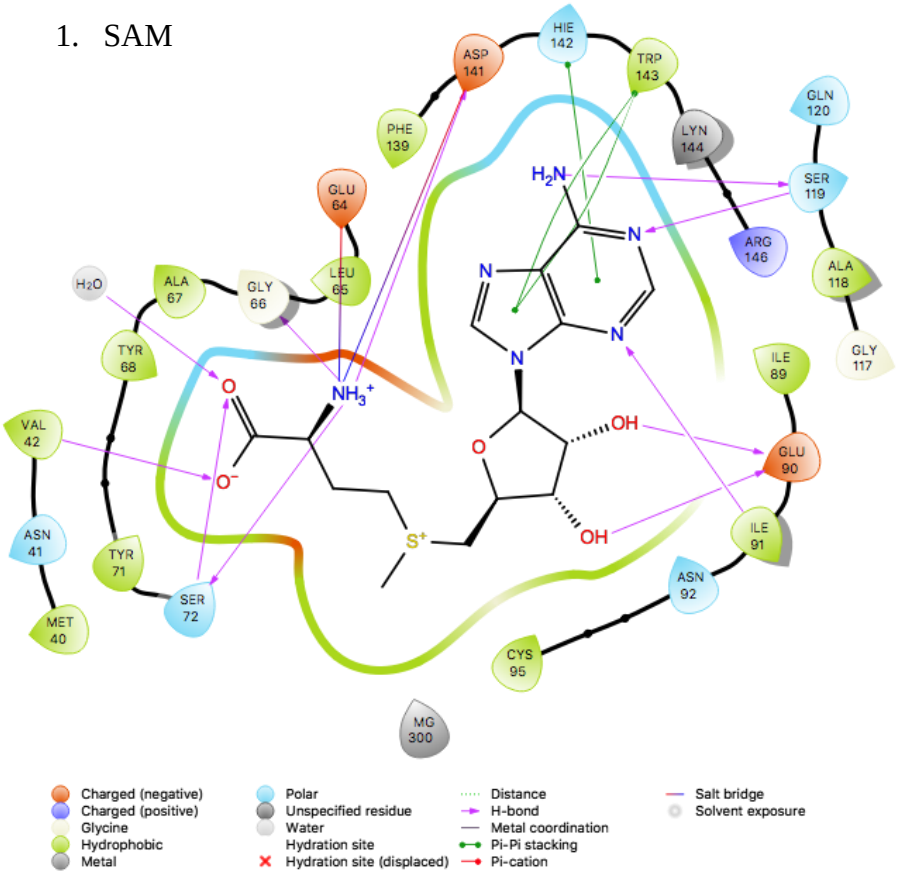

2. DNC

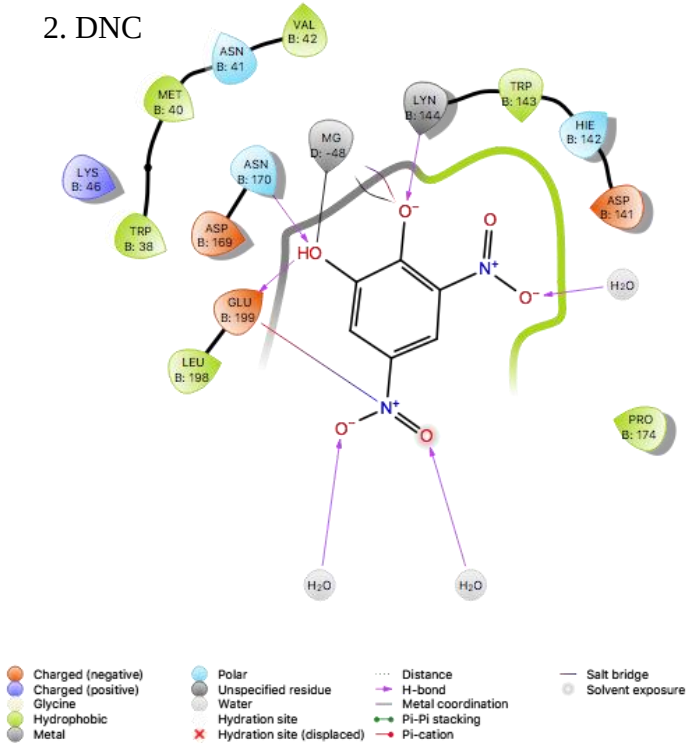

3. Sinefungin

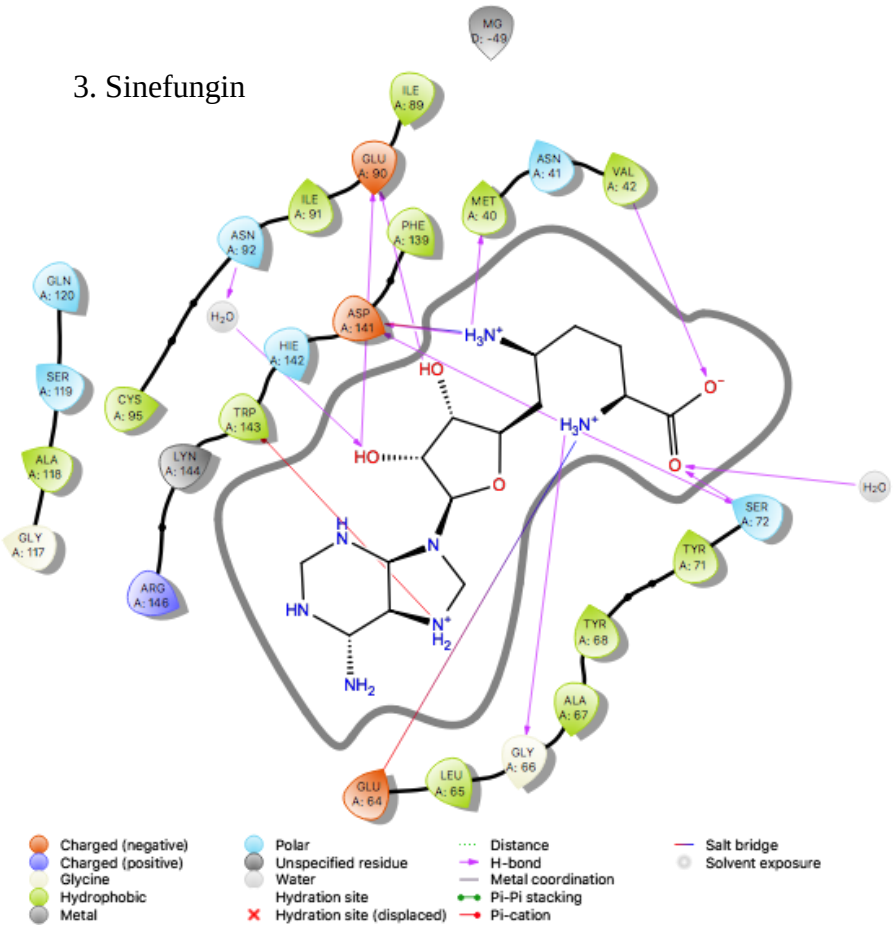

Appendix Figure 6. Ligand interactions between human S-COMT and 1) SAM; 2) DNC; 3) Sinefungin. Rendered using Maestro [1].

6. NMR

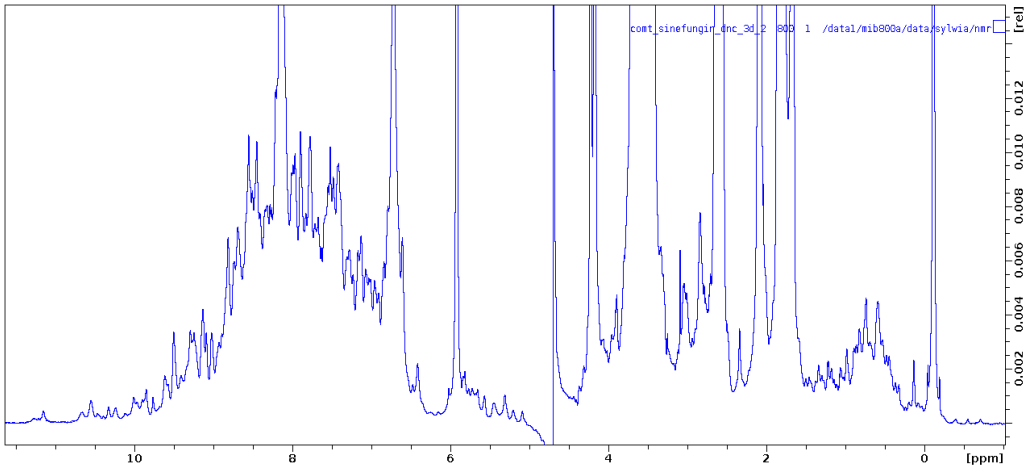

Appendix Figure 7. An example of typical 1D ^{1}H spectrum of human S-COMT:DNC:Mg^{2+}: Sinefungin complex recorded at 800 MHz. The peaks running of the top of the scale between ~0-4 ppm are those from small molecules, e.g. ^{1}H resonances from buffer. The peaks between 11.5 and 6 ppm come from ^{1}H nuclei attached to electron-withdrawing nitrogen or oxygen atoms, whereas all peaks upfield of 4.5 ppm are from carbon-bound protons.

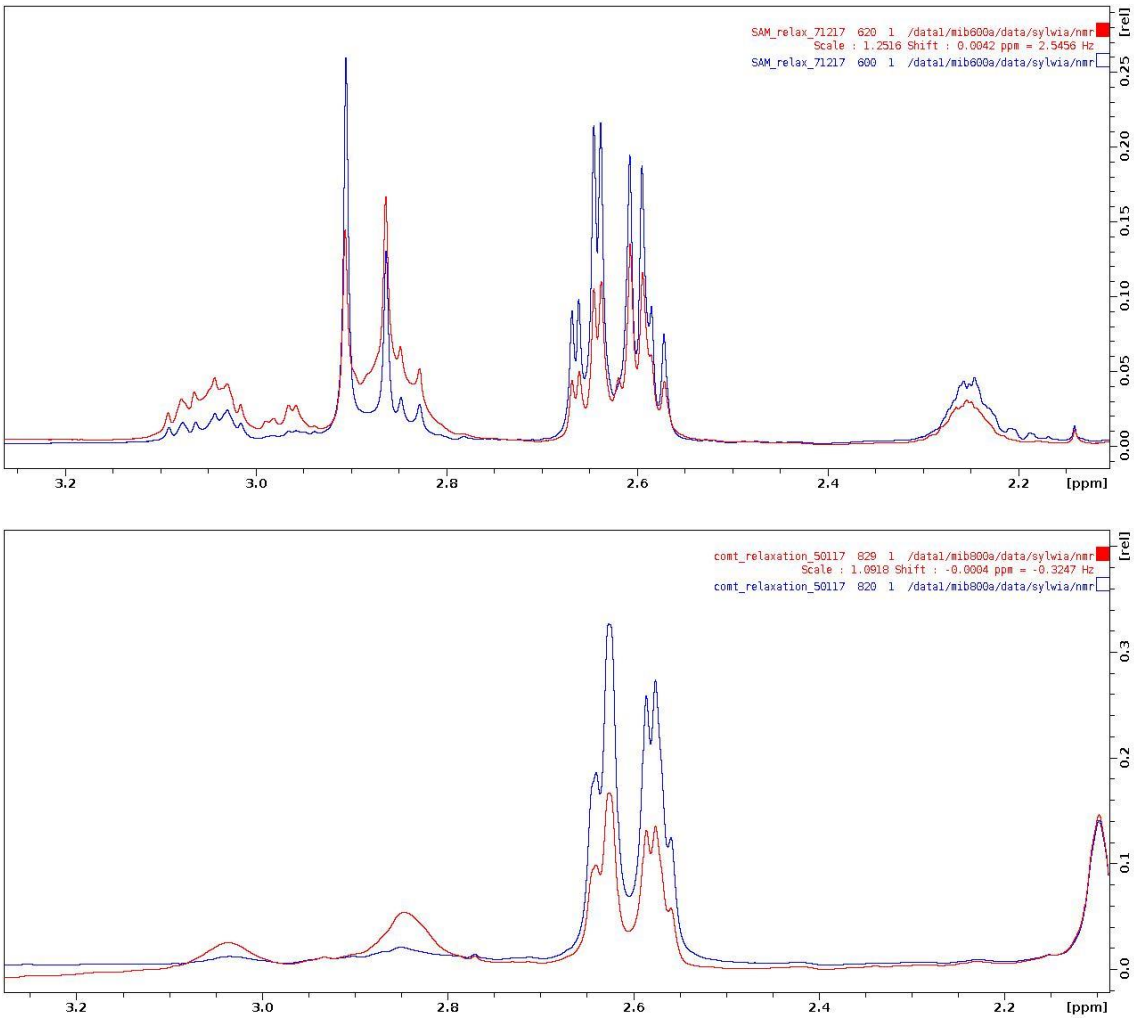

Appendix Figure 8. 1D ^{1}H spectrum of human S-COMT:DNC:Mg^{2+}:SAM complex recorded at 600 MHz (top) and 1D ^{1}H spectrum of human S-COMT:DNC:Mg^{2+}:Sinefungin complex recorded at 800 MHz. DTT peaks visible at ~2.6 ppm. Blue spectra recorded at the beginning of measurements, red spectra recorded at the end. DTT content is decreasing over time, but still present till the end of measurements.

7. Enzyme-ligand complex saturation.

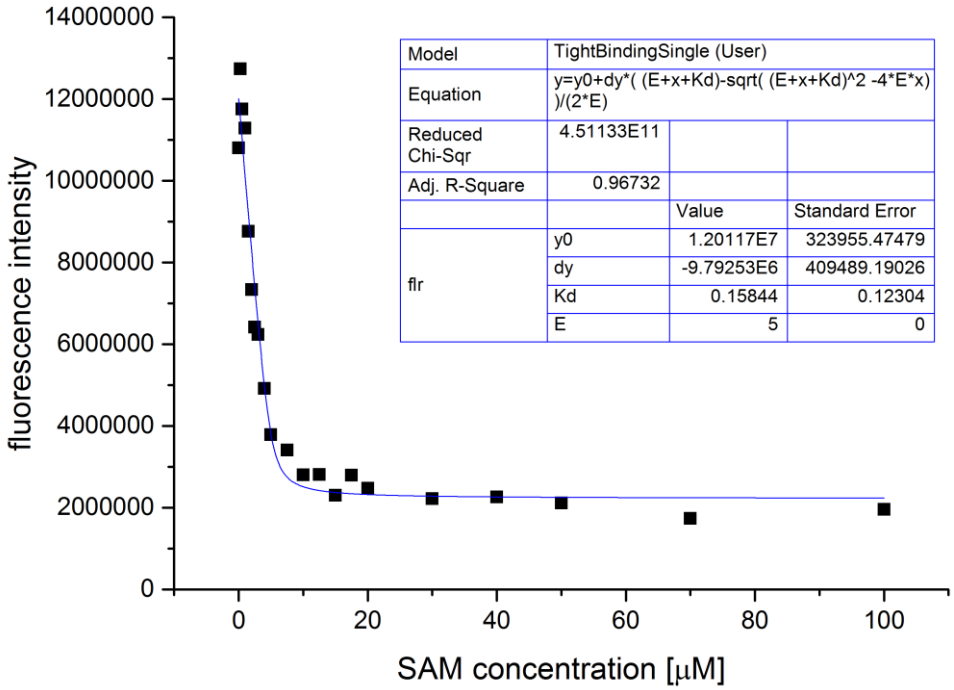

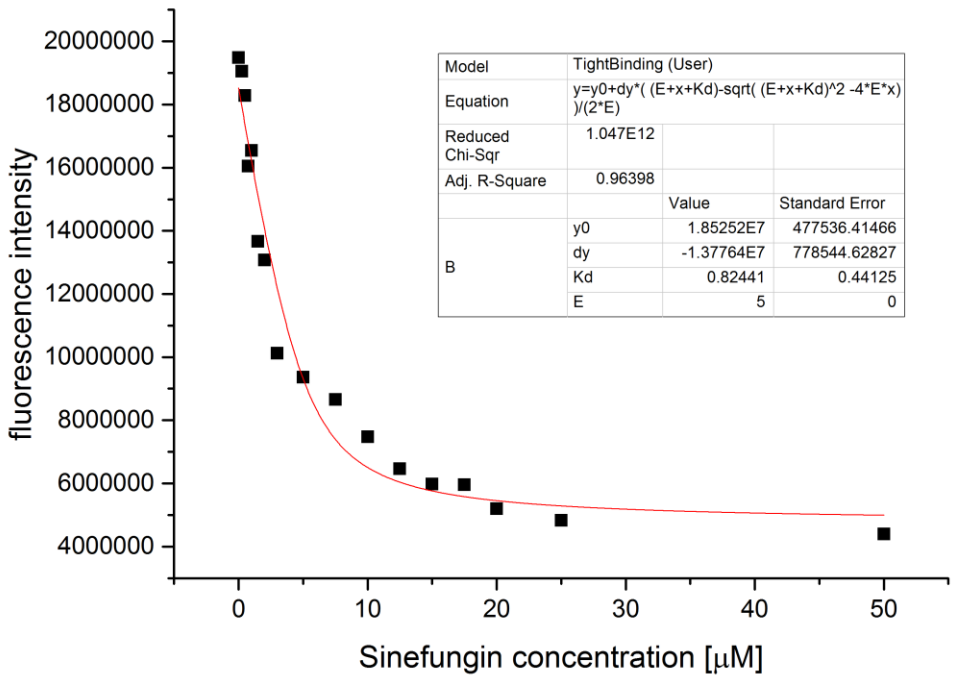

Appendix Figure 9. Saturation curves for COMT complexed with SAM (top) and sinefungin (bottom) in the presence of 7.5 μM DNC in 50 mM Tris-HCl pH = 7.5, 50 mM NaCl, 2 mM $MgCl_2$. Estimated enzyme concentration of 5 μM. Obtained K_d is very tight (sub-μM).

References

1. Release, S., *2: Maestro, Schrödinger, LLC, New York, NY, 2017*. Received: February, 2016. **21**: p. 2018